

**Quantum Chemistry for Spectroscopy – A Tale of  
Three Spins ( $S = 0, \frac{1}{2},$  and  $1$ )**

by

Bryan Matthew Wong

Submitted to the Department of Chemistry  
in partial fulfillment of the requirements for the degree of

Doctor of Philosophy

at the

MASSACHUSETTS INSTITUTE OF TECHNOLOGY

May 2007

© Massachusetts Institute of Technology 2007. All rights reserved.

Author .....  
Department of Chemistry  
May 18, 2007

Certified by .....  
Robert W. Field  
Haslam and Dewey Professor of Chemistry  
Thesis Supervisor

Accepted by .....  
Robert W. Field  
Chairman, Department Committee on Graduate Students

This doctoral thesis has been examined by a Committee of the Department of Chemistry that included

Professor Jianshu Cao \_\_\_\_\_  
(Chairperson)

Professor Troy Van Voorhis \_\_\_\_\_

Professor Robert W. Field \_\_\_\_\_  
(Thesis Supervisor)

# Quantum Chemistry for Spectroscopy – A Tale of Three Spins ( $S = 0, \frac{1}{2},$ and $1$ )

by

Bryan Matthew Wong

Submitted to the Department of Chemistry  
on May 18, 2007, in partial fulfillment of the  
requirements for the degree of  
Doctor of Philosophy

## Abstract

Three special topics in the field of molecular spectroscopy are investigated using a variety of computational techniques. First, large-amplitude vibrational motions on ground-state singlet ( $S_0$ ) potential energy surfaces are analyzed for both the acetylene/vinylidene and the HCN/HNC isomerization systems. Electronic properties such as electric dipole moments and nuclear quadrupole coupling constants are used as diagnostic markers of progress along the isomerization path. Second, the topic of electronically excited triplet states and their relevance to doorway-mediated intersystem crossing for acetylene is considered. A new diabatic characterization of the third triplet electronic state,  $T_3$ , enables a vibrational analysis of data obtained from current and past experiments. The last part of this thesis reviews the techniques and ideas of electron-molecule collisions relevant to Rydberg states of diatomic molecules. Previously developed and current methods of treating the excited Rydberg electron are evaluated and extended. Each of these three topics in molecular spectroscopy is studied using *ab initio* approaches coupled with experimental observations or chemically intuitive models. The unique combination of quantum chemistry and spectroscopy stimulates further developments in both theory and experiment.

Thesis Supervisor: Robert W. Field  
Title: Haslam and Dewey Professor of Chemistry





## Acknowledgments

It is a pleasure to thank those people who have helped me with various aspects of this thesis. First and foremost, I want to express my gratitude to Prof. Robert W. Field for devoting an enormous investment of time and patience to teaching me about the spectroscopy of small molecules. I would like to thank Bob for constantly reminding me that there is often simplicity behind every complexity. His invaluable view and intuition has improved this work in many ways.

In addition, several colleagues have provided support in both professional and personal capacities. Adam H. Steeves deserves recognition for writing most of the *J. Phys. Chem. B* manuscript on large-amplitude motions of  $S_0$  acetylene. Additionally, Dr. Hans A. Bechtel was always available to explain and provide the HCN/HNC nuclear quadrupole coupling constants measured from his experiments. I also owe both Adam and Hans a non-research related acknowledgement for helping me “find Aerosmith” (on two separate occasions) for my computer. I acknowledge Dr. Ryan L. Thom and Prof. John F. Stanton for teaching me about excited states of triplet acetylene. I would also like to thank John for several helpful lessons (in the great state of Texas) on obtaining diabatic parameters from quantum chemistry calculations. Dr. Serhan N. Altunata and Dr. Stephen L. Coy deserve credit for introducing me to electron-molecule scattering techniques. I thank Serhan for explaining the methodological subtleties of scattering theory to me whenever I required his help. I am grateful to Kyle L. Bittinger for extremely qualified help with writing programs in perl. An advantage of working in the Field group is the variety of science that I learned, and I would like to thank all the other group members at M.I.T. during my stay. I would like to express particular thanks to Dr. Kate L. Bechtel and Samuel H. Lipoff for their support during and after my thesis defense. Sam organized the celebration after my thesis defense, and Kate wore the M.I.T. beaver mascot costume during my entire thesis defense (it gets *very* hot in that furry costume). Their encouragement is greatly appreciated.

My last few years at M.I.T. were particularly difficult, and it is appropriate to

express my gratitude to those who prayed for me and gave me invaluable advice. Dr. Sumathy Raman, Dr. Oleg A. Mazyar, and Dr. Andrei A. Golosov all helped me figure out what I should do during these years and what my future plans should be after my time at M.I.T. I am grateful that they also remain close scientific collaborators. Finally, the completion of my education at M.I.T. would not have been possible without my family. Although they did not help me with the scientific details of singlet, triplet, or Rydberg states, they did something far better. They constantly prayed for me and supported me, even when I did not have confidence in myself. Extra special thanks goes to Mom, Dad, and my sister, Bonnie.

*To my family: Mom, Dad, and Bonnie*



# Contents

<b>1</b>	<b>Introduction</b>	<b>23</b>
1.1	Motivation . . . . .	23
1.2	Outline . . . . .	24
<b>2</b>	<b>One-Dimensional Molecular Hamiltonians</b>	<b>29</b>
2.1	Introduction . . . . .	29
2.2	Hamiltonian . . . . .	31
2.3	Eckart Reduced Inertias . . . . .	35
2.4	Pitzer Reduced Inertias . . . . .	37
2.5	Examples and Applications . . . . .	39
2.6	Conclusion . . . . .	46
<b>3</b>	<b>Electronic Signatures of Large-Amplitude Motion in <math>S_0</math> Acetylene</b>	<b>49</b>
3.1	Introduction . . . . .	49
3.2	Hamiltonian . . . . .	52
3.3	Ab Initio Calculations . . . . .	55
3.4	Dipole Moments in the Unsymmetrized Local Mode Basis . . . . .	60
3.5	Local Bending in the Polyad Model . . . . .	62
3.6	Results . . . . .	62
3.7	Evolution of the Dipole Moment . . . . .	64
3.8	Assignment of Large-Amplitude Local Bender States . . . . .	67
3.9	Conclusions . . . . .	70

<b>4</b>	<b>The Hyperfine Structure of HCN and HNC</b>	<b>71</b>
4.1	Introduction . . . . .	71
4.2	Quadrupole Coupling Constants of Nuclei . . . . .	73
4.3	Application to the $\text{HCN} \rightleftharpoons \text{HNC}$ Isomerization System . . . . .	75
4.4	Results for HCN and HNC . . . . .	78
4.5	Conclusion . . . . .	83
<b>5</b>	<b>Valence-Excited States of Triplet Acetylene</b>	<b>85</b>
5.1	Introduction . . . . .	85
5.2	Previous Studies on Triplet Acetylene . . . . .	87
5.3	A New Ab Initio Study of the $T_3$ Surface . . . . .	90
5.4	A Brief Digression on Adiabatic and Diabatic Representations . . . . .	92
5.5	The $T_2/T_3$ Vibronic Model . . . . .	96
5.6	$S_1/T_3$ Vibrational Overlap Integrals . . . . .	99
5.7	Results for $T_3$ Acetylene . . . . .	105
5.8	Conclusion . . . . .	109
<b>6</b>	<b>Computational Techniques for Electron-Molecule Scattering</b>	<b>111</b>
6.1	Introduction . . . . .	111
6.2	Variational Derivation of the K matrix . . . . .	115
6.3	Numerical Evaluation of Integrals . . . . .	120
6.4	Representing the Continuum Functions . . . . .	122
6.5	Additional Computational Details . . . . .	124
6.6	Test Calculations on the $1s\sigma_g 4p\sigma_u \ ^1\Sigma_u^+$ State of $\text{H}_2$ . . . . .	126
6.7	Conclusion . . . . .	128
<b>7</b>	<b>Developments in Electron Scattering for Polar Molecules</b>	<b>131</b>
7.1	Introduction . . . . .	131
7.2	The Electron Scattering Equations . . . . .	133
7.3	A Partial Differential Equation Approach . . . . .	135
7.4	Boundary Conditions Adapted for Long Range Dipoles . . . . .	139

7.5	The Finite Element Approach . . . . .	145
7.6	Extracting the K matrix . . . . .	150
7.7	Conclusion . . . . .	151
<b>8</b>	<b>Conclusion</b>	<b>153</b>
8.1	Summary . . . . .	153
8.2	Future Directions . . . . .	154
<b>A</b>	<b>Expansion of the Internal Coordinate Hamiltonian</b>	<b>157</b>
<b>B</b>	<b>Computer Codes for Calculating Vibrational Overlap Integrals</b>	<b>165</b>
B.1	overlap_integral.m . . . . .	165
B.2	make_overlap_table.m . . . . .	169
B.3	load_acetylene_data.m . . . . .	171
B.4	b_matrix_acetylene.m . . . . .	176
<b>C</b>	<b>Analytical Expressions for One- and Two-Electron Integrals in K matrix Calculations</b>	<b>179</b>
C.1	General Expansion of Cartesian Gaussian Orbitals . . . . .	179
C.2	Overlap Integrals . . . . .	181
C.3	Kinetic Energy Integrals . . . . .	183
C.4	Nuclear Attraction Integrals . . . . .	183
C.5	Electron Repulsion Integrals . . . . .	185





# List of Figures

2-1	Eckart effective inertias (Eq. (2.12)) for six molecules displaying internal rotation compared with those calculated from Pitzer's formulae (Eq. (2.19)). . . . .	42
2-2	The lowest 2,500 eigenvalues for the torsional motion of 1,2-dichloroethane. The eigenvalues obtained from the instantaneous Eckart inertias are considerably larger than those obtained from a constant-valued Pitzer inertia at the <i>trans</i> geometry. . . . .	43
2-3	(a) Relaxed torsional potential and energies for 1,2-dichloroethane obtained at the MP2(full)/6-31G(d) level of theory. Each of the torsional eigenvalues is associated with symmetric (red-colored) and anti-symmetric (green-colored) torsional states. (b) Torsionally averaged Eckart inertias, $\langle I_{\text{Eckart}} \rangle$ , for the lowest 150 torsional states of 1,2-dichloroethane. The broken line indicates the numerical value of $I_{\text{Pitzer}} = 16.37 \text{ amu } \text{\AA}^2$ calculated at the <i>trans</i> global minimum. . . . .	44
2-4	Reduced moment of inertia calculated by the Powell dogleg algorithm for the HCC bending motion of acetylene. The effective inertia increases rapidly near $110^\circ$ when the rightmost hydrogen moves in concert with the leftmost hydrogen to form vinylidene. . . . .	45

3-1	<p>(a) One-dimensional relaxed potential for the acetylene-vinylidene isomerization as a function of the HCC valence bend angle. A transition state structure is labeled by the number 2, and local minima are denoted by numbers 3 and 4. (b) Spatial positions of the acetylene coordinates color-coded to match their corresponding location on the one-dimensional potential. The rightmost hydrogen retraces its path near the transition state but moves in concert with the leftmost hydrogen in the red-colored post transition state 2 regions. . . . .</p>	50
3-2	<p>Dipole moments computed for relaxed geometries as a function of (a) fixed HCC local bend angle and (b) fixed local C–H stretch distance. In Figure 3-2 (a), the schematic diagrams of the bending motion show that when the local bend is excited, the <i>b</i>-axis dipole moment must change sign at <math>\theta = 0</math>. Conversely, the <i>a</i>-axis dipole moment is symmetric about <math>\theta = 0</math> since the active hydrogen is always placed at identical horizontal distances along the <i>a</i>-axis during the (symmetric) local bending motion. In Figure 3-2 (b), the broken line indicates the numerical value of the dipole moment for the CCH equilibrium geometry. The dipole moments for Figures 3-2 (a) and (b) were obtained from the CCSD/aug-cc-pVTZ and MR-AQCC/aug-cc-pVQZ levels of theory, respectively. . . . .</p>	58
3-3	<p>Experimentally derived polyad frequencies for a local CCH bending motion compared with one-dimensional <i>ab initio</i> calculations. The frequencies obtained from the polyad model and the <i>ab initio</i> calculations intersect near 18 quanta of <math>N_{\text{bend}}</math>. Adam H. Steeves is acknowledged for providing the polyad frequencies. . . . .</p>	64

3-4	Vibrationally averaged <i>ab initio</i> dipole moments computed (a) for a local C–H stretch and (b) for a local bend. Since the <i>b</i> -axis dipole moment for the local bend is antisymmetric with respect to the equilibrium bend angle, its vibrational average is exactly zero, and only the vibrational average for the <i>a</i> -axis dipole is displayed. The bottom axis of Figure 3-4 (b) is numbered according to the vibrational level in the fully permutational symmetric isomerization path, and the top axis labels only the symmetric vibrational levels. Both averaged dipole moments are reported relative to the lowest vibrational quantum state.	65
4-1	Dipole moment as a function of the Jacobi angle (defined in Figure 4-3) along an isomerization path from HCN ( $0^\circ$ ) to HNC ( $180^\circ$ ). Dipole moments were calculated at the CCSD(full) level with the aug-cc-pCVTZ basis. . . . .	72
4-2	(a)–(c) Nuclear shapes and nuclear electric quadrupole moments. . . .	75
4-3	Jacobi coordinates for the HNC molecule. . . . .	76
4-4	Dependence of the nuclear quadrupole coupling constant $(eQq)_N$ on a relaxed $\text{HCN} \rightleftharpoons \text{HNC}$ isomerization path. . . . .	77
4-5	Dependence of the nuclear quadrupole coupling constant $(eQq)_D$ on a relaxed $\text{DC}^{15}\text{N} \rightleftharpoons \text{D}^{15}\text{NC}$ isomerization path. The arrows along the horizontal axis indicate molecular geometries where (1) the D atom is directly over the C atom ( $\theta = 60^\circ$ ), (2) the D atom is over the C–N midpoint ( $\theta = 90^\circ$ ), and (3) the D atom is directly over the N atom ( $\theta = 117^\circ$ ). . . . .	78
4-6	(a) One-dimensional relaxed potential for the $\text{HCN} \rightleftharpoons \text{HNC}$ isomerization as a function of the Jacobi angle. The transition state structure is labeled by the number 2, and HCN/HNC minima are denoted by numbers 1 and 3, respectively. (b) Spatial positions of the the HCN/HNC atoms color-coded to match their corresponding location on the one-dimensional potential. . . . .	79

4-7	(a) The 50 lowest vibrational eigenvalues for the $\text{HCN} \rightleftharpoons \text{HNC}$ potential obtained at the CCSD(T)/aug-cc-pVQZ level of theory. Each of the eigenvalues is associated with either HCN (green-colored) or HNC (red-colored) localization. (b) Vibrationally averaged nuclear quadrupole coupling constants for the lowest 50 vibrational states of HCN (green)/HNC (red) energy. . . . .	80
4-8	Calculated and experimental ( $l = 0$ ) vibrational frequencies for HCN and HNC. The lines were fitted using a least squares method which yields <i>ab initio</i> slopes of $710.8 \text{ cm}^{-1}/(\text{HCN bend quantum})$ and $492.1 \text{ cm}^{-1}/(\text{HNC bend quantum})$ and experimental slopes of $685.6 \text{ cm}^{-1}/(\text{HCN bend quantum})$ and $468.4 \text{ cm}^{-1}/(\text{HNC bend quantum})$ . . . . .	81
4-9	Calculated and experimental ( $l = 0$ ) nuclear quadrupole coupling constants for HCN and HNC. The lines were fitted using a least squares method which yields <i>ab initio</i> slopes of $-0.062 \text{ MHz}/(\text{HCN bend quantum})$ and $-0.157 \text{ MHz}/(\text{HNC bend quantum})$ and experimental slopes of $-0.075 \text{ MHz}/(\text{HCN bend quantum})$ and $-0.118 \text{ MHz}/(\text{HNC bend quantum})$ . Dr. Hans A. Bechtel is acknowledged for providing the experimental quadrupole coupling constants. . . . .	82
5-1	Highest occupied molecular orbital for the $S_1 \ ^1A_u$ <i>trans</i> state of acetylene. 86	
5-2	Potential energy curves for <i>cis-trans</i> bending calculated at the EOM-CCSD level with the cc-pVTZ basis. The first excited electronic states are stabilized by bending out of linearity. . . . .	87
5-3	Zeeman anticrossing spectra for the $\nu'_3 = 0 - 3$ vibrational levels of the $\tilde{A} \ ^1A_u$ state. An increase in the number of anticrossings is observed with increasing excitation of the $\nu'_3$ mode. Figures reproduced from Ref. [1]. . . . .	88
5-4	The $\nu_3 (a_g)$ <i>trans</i> -bending normal mode for the $\tilde{A} \ ^1A_u$ state of acetylene. The harmonic vibrational frequency was calculated at the EOM-CCSD level with the cc-pVQZ basis. . . . .	89

5-5	(a) Potential energy curves as a function of the HCCH torsion and (b) intersection of the $T_2/T_3$ surfaces as a function of the HCCH and CCH angles under a $C_2$ symmetry restriction. Energies for both figures were calculated at the EOM-CCSD level with the cc-pVTZ basis. . . . .	90
5-6	Highest occupied molecular orbital for the lowest stationary point on $T_3$ ( ${}^3B$ ). The geometry parameters for this $C_2$ symmetry stationary point are listed in Table 5.1. . . . .	91
5-7	(a) The $\nu_6$ antisymmetric CCH bending normal mode for $T_3$ acetylene ( $\angle H_1C_1C_2 = \theta_{eq} - \Delta\theta$ , $\angle H_2C_2C_1 = \theta_{eq} + \Delta\theta$ ) and (b) adiabatic $T_2/T_3$ surfaces as a function of the HCCH torsional angle and CCH asymmetric bend angle. The $T_2/T_3$ energies were obtained at the EOM-CCSD level with the cc-pVTZ basis. The stationary point on $T_3$ is unstable against increasing $\Delta\theta$ . . . . .	92
5-8	Representative adiabatic and diabatic potential energy curves as a function of the normal coordinate $q$ . The solid adiabatic curves are separated by an energy difference of $\Delta$ at $q = 0$ , but the dotted diabatic curves are allowed to intersect. . . . .	93
5-9	(a)–(d) Adiabatic potential energy curves (Eq. (5.2)) as a function of the normal coordinate $q$ . All potential curves have identical values of $\Delta$ , $\omega_1$ , and $\omega_2$ . As the vibronic coupling parameter $\lambda$ is increased, the curves are better approximated in the diabatic representation. . . . .	94
5-10	Diabatic potential energy curves represented in the new basis of Eq. (5.4). . . . .	95
5-11	(a)–(f) Diabatized vibrational normal modes for the $T_3$ ${}^3B$ state. . . . .	106

6-1	(a) Schematic picture of an excited Rydberg state with high angular momentum, $l$ . When an electron occupies a large Rydberg orbital, the nuclear and electronic motions are largely separable. (b) Depiction of a Rydberg state with low angular momentum. When the Rydberg electron penetrates the ion core, it can exchange energy and angular momentum with the nuclei. . . . .	112
6-2	Schematic diagram of a molecule enclosed by a notional sphere of radius $R$ . Exchange between the scattered and atomic electrons is only important within the sphere. The bound wavefunctions centered on nuclei $Z_A$ and $Z_B$ (only two nuclei are shown for clarity) have negligible amplitude outside the sphere. . . . .	113
6-3	(a)–(b) Analytical continuum functions $f_l(k, r)$ and $(1 - e^{-\lambda r^{l+1}})g_l(k, r)$ with $l = 1$ (crosses). Each of the continuum functions are fit by a linear combination of 9 single-centered Gaussian functions (full curves) for $E = -0.03125$ Hartrees. . . . .	123
6-4	Potential energy curves for the $H_2^+$ ion ground state and the $1s\sigma_g4p\sigma_u$ $^1\Sigma_u^+$ state of $H_2$ . Energies for the $H_2^+$ ion were calculated at the ROHF level with the 6-31G basis, and the solid energy curve is the result of a high level <i>ab initio</i> calculation by Staszewska et al. [2]. The blue data points were obtained from the two-electron $\mathbf{K}$ matrix calculation described in this work. . . . .	127
7-1	CCSD(full) cc-pCVTZ electric dipole moments for the $CaF^+$ ion compared with those obtained from the effective potential of Ref. [3]. Both the CCSD(full) and effective potential dipoles agree with each other near the equilibrium internuclear distance ( $R = 3.54$ Bohrs), but considerable deviations are observed for small and large $R$ . Dr. Stephen L. Coy is acknowledged for providing the dipole moments from the effective potential. . . . .	132

7-2	Coordinate system for a $\text{CaF}^+$ ion used throughout Chapter 7. The $\text{CaF}^+$ ion is aligned along the $z$ -axis with the origin at its center of mass. The orientation of the $z$ -axis is defined such that the dipole moment points towards the positive $z$ -axis. . . . .	137
7-3	Values of $l_{\text{eff}}(l_{\text{eff}} + 1)$ , obtained from Eq. (7.27) as a function of the dipole moment. The solid lines are eigenvalues for $m = 0$ . The dashed and dotted lines correspond to $m = 1$ and 2, respectively. For sufficiently strong dipole moments, $l_{\text{eff}}(l_{\text{eff}} + 1)$ will become negative. . . .	141
7-4	Angular plots of $\text{Re}(\Theta(\theta)\Phi(\phi))$ evaluated for a 8.6863 Debye dipole at the origin. The negative $z$ -axis corresponds to the position of a negative partial charge. Figure 7-4 (a) depicts a $4s\sigma$ orbital which is strongly polarized away from the negative charge, and (b) depicts a $4f\phi$ orbital which resembles a hydrogenic orbital. . . . .	142
7-5	Optimal values of $\alpha(r_c)$ as a function of energy for a $l = 1$ Coulomb potential. The circles at $E > 0$ were determined by integrating Eq. (7.36) using the boundary conditions in Eqs. (7.37)–(7.38). The solid curve is a spline fit to the circles only which smoothly extrapolates to $E < 0$ . . . . .	144
7-6	(a) Deviations between a numerically calculated $l = 2$ Coulomb phase $\beta(E)/\pi$ and its analytical value $\nu - l$ . The dashed curve was obtained using a WKB boundary condition to approximate $\alpha(r_c)$ at the minimum of the effective potential [4]. The solid curve was obtained from the extrapolated boundary condition described in this chapter. (b) Magnified plot of Figure 7-6 (a). . . . .	145

7-7	(a) Four piecewise linear basis functions (solid lines) for the one-dimensional finite element method. A linear combination of them is shown as a broken line. (b) Piecewise linear basis functions in two dimensions. A triangular mesh is plotted in the $xy$ -plane, and the linear combination of basis functions is plotted above it. (For the curious reader, Figure 7-7 (b) depicts a solution to the Helmholtz's differential equation for waves reflecting off a $0.1 \times 0.1$ square in the center.) . . . . .	146
7-8	(a) Boundary conditions for integrating Eqs. (7.22)–(7.23) using a sparse finite element mesh. (b) A more refined version of the triangular mesh shown in Figure 7-8 (a). . . . .	149
8-1	Preliminary six-dimensional <i>ab initio</i> calculations of dipole matrix elements for $S_0$ acetylene. The dipole matrix elements are largest for the lowest members of a pure-bending polyad. Prof. Hua Guo is acknowledged for preparing this figure. . . . .	155
8-2	Individual points angularly distributed around the center of mass of the $\text{CaF}^+$ ion. A negative point charge is placed sequentially at each of these points in order to compute the interaction energy with the polarizable ion. Due to the cylindrical symmetry, only the angular points from $0 \leq \theta \leq \pi$ are unique. . . . .	155



# List of Tables

2.1	Effective moments of inertia obtained from <sup>a</sup> Eq. (2.12), <sup>b</sup> Eq. (2.19), and <sup>c</sup> Ref. [5]. . . . .	40
3.1	(a)–(c): Energy splittings between lowest members of the $g+$ and $u+$ polyads and calculated dipole moments for $N_{\text{bend}} = 14 - 26$ . All energies and energy differences reported are in units of $\text{cm}^{-1}$ . Energies denoted by an asterisk are not well-described in the local mode basis using the Hose-Taylor criterion. The increase in dipole moment is accompanied by decreasing energy differences between the $g+$ and $u+$ polyads. Adam H. Steeves is acknowledged for preparing this table. . . . .	68
4.1	Calculated and experimental ( $l = 0$ ) vibrational frequencies for HCN and HNC. . . . .	81
4.2	Calculated and experimental ( $l = 0$ ) nuclear quadrupole coupling constants for HCN and HNC. Dr. Hans A. Bechtel is acknowledged for providing the experimental quadrupole coupling constants. . . . .	82
5.1	Optimized geometries at the diabatic $T_3$ $\text{C}_2$ minimum. . . . .	98
5.2	<i>Ab initio</i> adiabatic coupling parameters between $T_3$ and $T_2$ with diabatic frequencies of $T_3$ . . . . .	99
5.3	Computed and experimental $S_1$ vibrational frequencies. Harmonic frequencies were calculated at the EOM-CCSD level with the cc-pVQZ basis. . . . .	100

5.4	The $\mathbf{T}$ matrix for the $T_3 \ ^3B$ state determined from an <i>ab initio</i> normal modes analysis and Eq. (5.40). . . . .	106
5.5	Computed diabatic $T_3 \ ^3B$ vibrational frequencies. Vibrational descriptions were based on the $\mathbf{T}$ matrix elements (Table (5.4)), and harmonic frequencies were calculated at the EOM-CCSD level with the cc-pVQZ basis. . . . .	106
5.6	$T_3 \ ^3B$ vibrational levels predicted to lie in the vicinity of $S_1 \ 3\nu_3$ . Five of the overlap integrals are rigorously zero by symmetry. . . . .	107
5.7	Numerical <i>a</i> -axis Coriolis coefficients for $T_3 \ ^3B$ , calculated from an <i>ab initio</i> normal modes analysis. . . . .	108
5.8	Calculated <i>a</i> -axis vibration-rotation interaction coefficients for $T_3 \ ^3B$ . . . . .	109
6.1	Optimized Gaussian exponents and coefficients for representing continuum functions with $l = 1$ and $E = -0.03125$ Hartrees. All exponents, $\alpha_i$ , are in units of Bohr <sup>-2</sup> . . . . .	124

# Chapter 1

## Introduction

### 1.1 Motivation

The formulation of quantum mechanics is one of the greatest scientific achievements of the human intellect. Inspired by *experimental* problems in blackbody radiation, the photoelectric effect, and atomic structure, the ideas of quantum mechanics were first developed in the early twentieth century. (It is interesting that quantum physics started not with a breakdown of Maxwell's or Newton's laws *a priori* but with a need to explain complex experimental phenomena.) Since then, each decade has demonstrated the power of quantum theory to illuminate questions in physics, astronomy, chemistry, and the biological sciences.

Quantum theory has made rapid progress in these fields, particularly in chemistry, because of its power to reduce complicated problems to a set of rules and procedures. However, therein lies a potential pitfall in using quantum mechanics: it is possible to develop increasingly sophisticated approaches and methods but lose sight of its practical value. Consequently, the presented thesis is an endeavor to describe the practical applications of using quantum mechanical methods for understanding complex molecular spectra. While the compilation of spectroscopic data within the last few decades has been enormous, the process of interpreting the available spectra or extracting the various sources of spectroscopic contributions has not been as complete. The surprisingly rich information available from molecular spectra is hidden by its great

complexity. As one moves farther away from the simple picture of vibrational normal modes or the naïve transitions between discrete hydrogenic levels, the more difficult it becomes to understand a molecule’s underlying dynamics. (The Nobel Laureate Francis Crick once described the interpretation of complicated biomolecular spectra as being “like trying to determine the structure of a piano by listening to the sound it made while being dropped down a flight of stairs.”) Fortunately, this complicated situation is the merging ground of experimentalists and theoreticians. On one hand, theoreticians need experimental results to refine incomplete theories; on the other, experimentalists need theoreticians to help disentangle experimental data.

The close connection to spectroscopic experiments is a key concept in this thesis, and as the first part of the title suggests, the principle of using “quantum chemistry *for* spectroscopy” has guided this effort. Although this thesis does not involve any experimental work originating from the author whatsoever, any formal theories that are not connected to measurable experimental quantities are avoided or referenced elsewhere. This choice of presentation is not to undermine the rigorous aspects of quantum chemistry, but rather to reinforce it by comparing their results to real spectroscopic experiments. For this same reason, the presented thesis is highly problem-driven and, as the second part of the title implies, consists of three distinct parts corresponding to the three types of experiments currently performed in the research group of Prof. Robert W. Field. Each of the three parts is self-contained, completely independent of one another, and may actually be read in any order.

## 1.2 Outline

The first part of the thesis, Chapters 2-4, describes large-amplitude vibrational motion on ground-state singlet ( $S_0$ ) potential energy surfaces. The fundamental goal of this part is to develop the diagnostics and interpretive concepts needed to reveal and understand how large-amplitude motions are encoded in the vibration-rotation energy level structure of small, gas-phase, combustion-relevant polyatomic molecules. Specific topics in this first section are as follows:

- Chapter 2 introduces a simple yet accurate method for separating a large-amplitude, low-frequency internal motion from all of the other normal modes in a molecule. Numerical results are presented for several molecules possessing internal large-amplitude motions. These results are compared with those obtained from approximate analytic formulas in the current literature. The techniques in this chapter illustrate most of the ideas that are essential to handle the more complicated situations in the following two chapters.
- Chapter 3 utilizes a one-dimensional local bend model introduced in Chapter 2 to describe the variation of electronic properties of acetylene in excited vibrational levels. Calculations on the  $S_0$  potential energy surface predict an approximately linear dependence of the electric dipole moment on the number of quanta in either the local bending or local stretching excitation. The use of a one-dimensional model for the local bend is justified by comparison to an effective Hamiltonian model which reveals the same decoupling of the large-amplitude bending from other degrees of freedom.
- Chapter 4 outlines preliminary work on the use of nuclear quadrupole hyperfine structure to detect the onset of delocalization on the  $S_0$   $\text{HCN} \rightleftharpoons \text{HNC}$  potential energy surface. Unlike the electric dipole moment,  $\mu$ , where the experimental observable is the magnitude,  $|\mu|$ , and not its sign ( $|\mu|$  is approximately the same for both HCN and HNC), a hyperfine calculation can determine in which potential well the vibrational wavefunction is localized. A preview of hyperfine calculations applied to the isotopically substituted species  $\text{DC}^{15}\text{N}$  and  $\text{D}^{15}\text{NC}$  is presented to illustrate the striking differences from their non-deuterated  $^{14}\text{N}$  isotopomers.

The next part of the thesis, Chapter 5, describes singlet-triplet interactions in acetylene as part of a larger effort to understand intersystem crossing in metastable electronically excited states. Intersystem crossing in acetylene proceeds through a “doorway” state which has been assigned as a low-lying vibrational level of the third triplet electronic state,  $T_3$ . Characterization of this specific  $T_3$  state is an impor-

tant step for preparing future experimental approaches in acetylene photophysics and dynamics.

- Chapter 5 reports a new *ab initio* study of the acetylene  $T_3$  potential energy surface which clarifies the nature of its energy minimum. A unique feature of this chapter is the unconventional combination of non-adiabatic quantum chemistry with previous spectroscopic assignments to assign spectra. The results of this calculation enable tentative assignments of two vibrational levels as possible candidates for the  $T_3$  “doorway” state. This new characterization resolves some of the existing controversies concerning this state and allows a unification of current and past experimental measurements.

The last part of the thesis, Chapters 6-7, introduces the basic techniques and ideas of electron-molecule collisions relevant to Rydberg states. The exchange of energy between electronic and nuclear motions in Rydberg states is one of the most fundamental mechanisms for electron/nuclear interactions. In contrast to the techniques used in the previous chapters, the tools of quantum chemistry generalize poorly for highly excited Rydberg states. On the other hand, experimental Rydberg spectra have an enormous array of closely spaced resonances that are capable of unambiguous spectroscopic assignment. This seems paradoxical at first glance, but as a Rydberg state becomes highly excited, the more it acquires the character of a perturbed hydrogenic state. Consequently, its associated structure is expected to become more regular and predictable. Of course, the world of Rydberg states is not as simple as it may seem. The temporary excitation of the ion core by the Rydberg electron accounts for many classes of “anomalous” (but non-dissociative) observations. In order to study this “simple” two-electron process, one must combine the mature techniques of quantum chemistry with scattering theory.

- Chapter 6 contains a detailed discussion of first attempts to formulate and use a new *ab initio* electron-molecule scattering theory. Based on an early variational derivation of a scattering matrix (which embodies all the information of the

scattering process), the approach taken in this chapter is to incorporate analytical scattering wavefunctions into the numerical algorithms of current quantum chemistry programs. A simple test model system (the  $1s\sigma_g 4p\sigma_u \ ^1\Sigma_u^+$  H<sub>2</sub> Rydberg state) is also presented to illustrate the current progress and developments with this approach.

- Chapter 7 continues with the examination of Rydberg states by presenting the working equations for electron scattering using a finite element approach. The goal of this chapter is to present an alternative method for describing electron-molecule scattering which does not suffer from the linear dependence problems associated with the approaches used in Chapter 6. The necessary equations are presented and gradually generalized for highly polar molecules. It should also be noted that the techniques presented in this chapter are very preliminary and their development is still in progress.

Finally, Chapter 8 concludes this thesis by summarizing its findings and considering the possible continuations of this work. The appendices at the end of this thesis consist of lengthy derivations or computer codes as a reference for the reader. The appendices have been placed at the end to avoid interrupting the main flow of arguments.

In passing and as previously noted, each of the three parts of this thesis is self-contained and may actually be read in any order. For this reason, it may come as no surprise that the actual sequence in which this work was performed is not the same as the order listed in the table of contents. For the curious reader, the actual chronological order in which the work written in this thesis was completed is as follows: Chapter 6 – Summer 2005, Chapter 2 – Winter 2005, Chapter 3 – Spring 2006, Chapter 5 – Winter 2006, Chapter 7 – Spring 2007, and Chapter 4 – Spring 2007.





# Chapter 2

## One-Dimensional Molecular Hamiltonians

This chapter describes a method used to reduce the full Watson Hamiltonian [6] to an effective one-dimensional form. The majority of the work in this chapter resulted from a collaboration with Dr. Ryan L. Thom and was published as an article in the *Journal of Physical Chemistry A* [7].

### 2.1 Introduction

The theoretical study of many topics in molecular spectroscopy is based on the existence of a complete Hamiltonian. Although the Hamiltonian for a system of  $N_n$  nuclei and  $N_e$  electrons can be easily written in rectilinear Cartesian coordinates, the resulting Schrödinger equation is still too complicated to allow an exact solution. Even within the Born-Oppenheimer approximation, a full solution of the nuclear motions alone in large molecules (of more than about a dozen atoms) is difficult. As a result, the conventional approach to computing spectroscopic quantities involves the assumption that the quantum mechanical energies are a sum of four separate contributions corresponding to electronic, vibrational, rotational, and translational motions. Since a complete set of molecular energy levels is rarely available, this independent normal-mode approximation is practical and sometimes reasonable. However, in many cases

a molecule may contain several low-frequency modes which are not well approximated as small-amplitude harmonic oscillations. Common examples of these floppy modes include anharmonic bending modes which involve rather large changes in the angle between two bonds [8]. Uncertainties in how to treat large-amplitude curvilinear motions can give rise to significant errors in spectroscopic calculations.

When a large-amplitude curvilinear motion is present, the nuclear Hamiltonian cannot be separated to quadratic order in both the kinetic and potential energy. In addition, one frequently finds that the bond lengths and angles are functions of the large-amplitude coordinate. As a result, the vibrational frequencies of the small-amplitude modes also vary with the large-amplitude coordinate [9]. This raises complex issues about how one should rigorously define the normal coordinates and separate them from the large-amplitude curvilinear coordinate as well as from the external rotation of the molecule. In many cases there will be more than one large-amplitude mode, and these will all be coupled together as well as to all of the normal modes. The present chapter focuses on the calculation of molecular parameters where only one large-amplitude motion is coupled to the other vibrational modes and to the overall external rotation in molecules. Large asymmetric molecules with internal rotations are presented as “toy models,” but the formalism developed in this work is applicable to any large-amplitude motion. The next chapter employs these methods to show how changes in dipole moments along a large-amplitude bending coordinate provide a method to identify particular vibrational levels via the Stark effect [10].

In the following sections, a rigorous but practical method is introduced to cast the Watson Hamiltonian into an effective one-dimensional form. The only major difficulty in deriving this tractable representation is due to the introduction of a non-uniformly rotating reference frame. The orientation of this reference frame is specified subject to the constraint that the angular momentum of the nuclei as viewed in this frame is minimized – a condition met by the Eckart [11] condition. The introduction of a rotating frame does not result in any complexities when computing the scalar potential energy function, but the transformation of the nuclear kinetic energy operator to this non-uniformly rotating frame can be a difficult problem. This change in coordinates

results in an effective one-dimensional inertia which is described in section 2.2. Several examples of molecules in which the coupling between the large-amplitude motion and overall rotation is complex are presented in section 2.5. Numerical comparisons with other models that describe alternative methods of separating these couplings are also provided. The errors introduced by these other models are analyzed to identify which cases require a higher level treatment.

## 2.2 Hamiltonian

The theory of the internal coordinate path Hamiltonian is expressed in terms of a single large-amplitude coordinate,  $s$ , its conjugate momentum,  $\hat{p}_s (= -i\hbar\partial/\partial s)$ , and the coordinates  $Q_k$  ( $k = 1, 2, \dots, 3N - 7$ ) and momenta  $\hat{P}_k (= -i\hbar\partial/\partial Q_k)$  of the orthogonal small-amplitude vibrational modes. A detailed method for solving this Hamiltonian using a variational method is described by Tew et al. [12] Their formulation is closely related to the reaction path Hamiltonian of Miller, Handy, and Adams [13], with the exception that the internal coordinate path lies on or above the minimum energy path. One of the simplest algorithms to computationally define the minimum energy path is to optimize a saddle point on the potential energy surface and follow the negative gradient of the energy in mass-weighted Cartesian coordinates. However, as Tew et al. have stated, this algorithm is not a numerically sound technique. If the reaction path is not followed with small enough steps, one may not be able to locate the minima accurately at the end of the path. Furthermore, near the saddle point, the optimized geometries may be inaccurate since the first step away from this starting point is necessarily along a vector that does not include any curvature.

The internal coordinate path Hamiltonian used by Tew et al. removes many of these problems by parametrizing a path with a single internal coordinate such as a bond length, a valence bend angle, or in the case of internal rotations, a dihedral angle. The internal coordinate path is defined by keeping a single internal coordinate fixed and minimizing the energy with respect to the other  $3N - 7$  degrees of freedom. An internal coordinate is always well-defined at any point on the path and guarantees a

continuous variation with no numerical complexity. Since the path is parametrized by an internal coordinate and does not follow the mass-weighted gradient, the internal coordinate path Hamiltonian is invariant under atomic isotope substitution within the molecule. All that remains to define the path is the rotational orientation of the molecular geometries along the internal coordinate parametrization. This section demonstrates that the effective inertias for large-amplitude motions should only be calculated in a molecule-fixed axis system in which the coupling is minimized between the motion along the path and the rotations of the molecule.

The quantum mechanical nuclear kinetic energy operator [12] is given by

$$\hat{T} = \frac{1}{2} \sum_{d,e=1}^4 \mu^{1/4} \left( \hat{\Pi}_d - \hat{\pi}_d \right) \mu_{de} \mu^{-1/2} \left( \hat{\Pi}_e - \hat{\pi}_e \right) \mu^{1/4} + \frac{1}{2} \sum_{k=1}^{3N-7} \mu^{1/4} \hat{P}_k \mu^{-1/2} \hat{P}_k \mu^{1/4}. \quad (2.1)$$

$\hat{\Pi}$  and  $\hat{\pi}$  are four-component operators given by

$$\begin{aligned} \hat{\Pi} &= \left( \hat{J}_x, \hat{J}_y, \hat{J}_z, \hat{p}_s \right), \\ \hat{\pi} &= \sum_{k,l=1}^{3N-7} \left( B_{kl,x}(s), B_{kl,y}(s), B_{kl,z}(s), B_{kl,s}(s) \right) Q_k \hat{P}_l, \end{aligned} \quad (2.2)$$

where  $\hat{J}_x$ ,  $\hat{J}_y$ , and  $\hat{J}_z$  are the components of the total angular momentum operator, and  $B_{kl,x}$ ,  $B_{kl,y}$ ,  $B_{kl,z}$ , and  $B_{kl,s}$  are matrices that are functions of the large-amplitude curvilinear coordinate  $s$ . One also requires the following definitions.

$$\begin{aligned} \mu_{de}(s, \mathbf{Q}) &= \sum_{a,b=1}^4 (\mathbf{I}_0 + \mathbf{b})_{da}^{-1} \mathbf{I}_{0ab} (\mathbf{I}_0 + \mathbf{b})_{be}^{-1}, \\ \mu(s, \mathbf{Q}) &= \det(\mu_{de}). \end{aligned} \quad (2.3)$$

In the following definitions,  $i$  and  $\alpha\beta\gamma$  denote the  $i$ th atom and the  $xyz$  Cartesian components respectively. The augmented  $4 \times 4$  symmetric inertia tensor  $\mathbf{I}_0$  is

$$\mathbf{I}_0(s) = \begin{pmatrix} \mathbf{I}_{0\alpha\beta}(s) & \mathbf{I}_{0\alpha s}(s) \\ \mathbf{I}_{0s\beta}(s) & I_{0ss}(s) \end{pmatrix} \quad (2.4)$$

where  $\mathbf{I}_{0\alpha\beta}$  are the elements of the ordinary  $3 \times 3$  Cartesian inertia tensor along the path. The other terms  $I_{0\alpha s}$  ( $= I_{0s\alpha}$ ) and  $I_{0ss}$  are given by

$$\begin{aligned} I_{0\alpha s}(s) &= I_{0s\alpha}(s) = \sum_{i=1}^N \sum_{\beta,\gamma=1}^3 \epsilon_{\alpha\beta\gamma} a_{i\beta}(s) a'_{i\gamma}(s), \\ I_{0ss}(s) &= \sum_{i=1}^N \sum_{\alpha=1}^3 a'_{i\alpha}(s) a'_{i\alpha}(s), \end{aligned} \quad (2.5)$$

where  $\epsilon_{\alpha\beta\gamma}$  is the Levi-Civita antisymmetric tensor. The vectors  $\mathbf{a}_i$  ( $= m_i^{1/2} \mathbf{r}_i$ ) are the mass-weighted Cartesian coordinates of the  $i$ th atom at a point on the path  $s$  with respect to a molecule-fixed axis system, and  $\mathbf{a}'_i = d\mathbf{a}_i/ds$ . All that remains is to define  $\mathbf{B}$  and  $\mathbf{b}$ ; in the following discussion, it is shown that it is not necessary to know the explicit forms of these matrices beyond the facts that  $\mathbf{B}$  is a function of  $s$ , and  $\mathbf{b}$  is a  $4 \times 4$  matrix which is merely linear in  $Q_k$ :

$$\mathbf{B}(s) = \sum_{k=1}^{3N-7} Q_k \mathbf{b}_k(s). \quad (2.6)$$

The exact kinetic energy operator in the full  $3N$  coordinates is too complicated to work with directly, and it is necessary to use various approximations to the Hamiltonian that are manageable and physically insightful. The effective moment of inertia matrix depends weakly on the small-amplitude coordinates  $Q_k$  [14]. Expanding  $\mu_{de}$  in the vibrational normal coordinates and retaining the first term that depends only on  $s$  gives

$$\mu_{de}(s, \mathbf{Q}) = \sum_{a,b=1}^4 (\mathbf{I}_0 + \mathbf{b})_{da}^{-1} \mathbf{I}_{0ab} (\mathbf{I}_0 + \mathbf{b})_{be}^{-1} \approx \mathbf{I}_{0de}^{-1}(s). \quad (2.7)$$

Substituting Eq. (2.7) into Eq. (2.1), and after significant operator algebra (see Appendix A), the approximate kinetic energy operator is given by

$$\begin{aligned} \hat{T} &= \frac{1}{2} \sum_{d,e=1}^4 \mu_{de} \left( \hat{\Pi}_d - \hat{\pi}_d \right) \left( \hat{\Pi}_e - \hat{\pi}_e \right) + \frac{1}{2} \sum_{d=1}^4 \left( \hat{p}_s \mu_{sd} \right) \left( \hat{\Pi}_d - \hat{\pi}_d \right) \\ &+ \frac{1}{2} \mu^{1/4} \left( \hat{p}_s \mu_{ss} \mu^{-1/2} \left( \hat{p}_s \mu^{1/4} \right) \right) + \frac{1}{2} \sum_{k=1}^{3N-7} \hat{P}_k^2, \end{aligned} \quad (2.8)$$

where the operator  $\hat{p}_s$  operates only within the parentheses in Eq. (2.8); that is, the next to last term in Eq. (2.8) is a scalar pseudopotential term. Since the “vibrational angular momentum” terms,  $\hat{\pi}_a$ , are linear in the small-amplitude coordinates,  $Q_k$ , neglecting their contribution to the kinetic energy gives

$$\hat{T} = \frac{1}{2} \sum_{d,e=1}^4 \mu_{de} \hat{\Pi}_d \hat{\Pi}_e + \frac{1}{2} \sum_{d=1}^4 (\hat{p}_s \mu_{sd}) \hat{\Pi}_d + \frac{1}{2} \mu^{1/4} (\hat{p}_s \mu_{ss} \mu^{-1/2} (\hat{p}_s \mu^{1/4})) + \frac{1}{2} \sum_{k=1}^{3N-7} \hat{P}_k^2. \quad (2.9)$$

To remove the terms that couple the total angular momentum with the large-amplitude momentum, one must choose molecule-fixed axes such that  $\mu_{\alpha s} = \mu_{s\alpha} = 0$ . In other words, if the molecule-fixed axes are chosen such that  $I_{0\alpha s} = I_{0s\alpha} = 0$ , the effective inverse moment of inertia matrix  $\mu$  is block diagonal, and the kinetic energy operator becomes

$$\hat{T} = \frac{1}{2} \sum_{d,e=1}^3 \mu_{de} \hat{\Pi}_d \hat{\Pi}_e + \frac{1}{2} \hat{p}_s \mu_{ss} \hat{p}_s + \frac{1}{2} \mu^{1/4} (\hat{p}_s \mu_{ss} \mu^{-1/2} (\hat{p}_s \mu^{1/4})) + \frac{1}{2} \sum_{k=1}^{3N-7} \hat{P}_k^2. \quad (2.10)$$

Eq. (2.10) implicitly requires numerical enforcement of the Eckart conditions

$$\sum_{i=1}^N \mathbf{a}_i(s) \times \mathbf{a}'_i(s) = \mathbf{0}. \quad (2.11)$$

Once the Eckart conditions are satisfied, the effective inverse inertia for the large-amplitude coordinate is given by

$$\mu_{ss}(s) = \left( \sum_{i=1}^N \mathbf{a}'_i(s) \cdot \mathbf{a}'_i(s) \right)^{-1}. \quad (2.12)$$

From this expression, one recognizes that  $\mu_{ss} = I_{0ss}^{-1}$  is Wilson’s [15]  $G$  matrix-element for the large-amplitude curvilinear coordinate. The following section describes the computational procedure for calculating this quantity.

## 2.3 Eckart Reduced Inertias

First the molecular geometries are optimized using a quantum chemistry computational method while holding a selected internal coordinate,  $s$ , fixed. All conformers of the molecule are translated to a reference frame where the origin is at the center of mass. These molecular geometries are then rotated to a reference frame using the internal axis method (IAM) [16]. In the IAM, the axis about which the top executes internal rotation is chosen parallel to one of the coordinate axes. This reference frame is just an intermediate frame that is computationally convenient in order to compute the Eckart axes later.

The torsional angle dependence of all the mass-weighted Cartesian coordinates of the  $i$ th atom in the IAM frame  $(a_{i\xi}, a_{i\eta}, a_{i\zeta})$  is fit to a Fourier series. The corresponding mass-weighted Cartesian coordinates of the  $i$ th atom in the Eckart frame are denoted by  $(a_{ix}, a_{iy}, a_{iz})$ . The orientation of the Eckart axis system relative to the IAM frame can always be expressed in terms of the Euler angles [15]

$$\begin{bmatrix} a_{ix} \\ a_{iy} \\ a_{iz} \end{bmatrix} = \begin{bmatrix} \lambda_{x\xi} & \lambda_{x\eta} & \lambda_{x\zeta} \\ \lambda_{y\xi} & \lambda_{y\eta} & \lambda_{y\zeta} \\ \lambda_{z\xi} & \lambda_{z\eta} & \lambda_{z\zeta} \end{bmatrix} \begin{bmatrix} a_{i\xi} \\ a_{i\eta} \\ a_{i\zeta} \end{bmatrix}, \quad (2.13)$$

where  $\lambda_{\alpha\tau}$  is the direction cosine (which is a function of the Euler angles  $\theta$ ,  $\phi$ , and  $\chi$ ) of the Eckart  $\alpha$ -axis relative to the IAM  $\tau$ -axis. Using a finite difference approximation for  $\mathbf{a}'_i(s)$  gives

$$\mathbf{a}'_i(s_j) \approx \frac{\mathbf{a}_i(s_{j+1}) - \mathbf{a}_i(s_j)}{s_{j+1} - s_j}. \quad (2.14)$$

If the internal coordinate path steps are sufficiently small, the error in estimating  $\mathbf{a}'_i(s)$  will also be small. To minimize these numerical errors, a Fourier interpolation scheme is used to estimate the mass-weighted Cartesian coordinates at several points between each optimized geometry in the IAM frame. Substituting the finite difference approximation into Eq. (2.11) reduces the Eckart equations to

$$\sum_{i=1}^N \mathbf{a}_i(s_j) \times \mathbf{a}_i(s_{j+1}) = \mathbf{0}. \quad (2.15)$$

The three components of this vector equation are

$$\begin{aligned} \sum_{i=1}^N [a_{ix}(s_j) a_{iy}(s_{j+1}) - a_{iy}(s_j) a_{ix}(s_{j+1})] &= 0, \\ \sum_{i=1}^N [a_{iy}(s_j) a_{iz}(s_{j+1}) - a_{iz}(s_j) a_{iy}(s_{j+1})] &= 0, \\ \sum_{i=1}^N [a_{iz}(s_j) a_{ix}(s_{j+1}) - a_{ix}(s_j) a_{iz}(s_{j+1})] &= 0. \end{aligned} \quad (2.16)$$

The initial geometry in the Eckart frame, defined as the point  $s_{j=0}$ , is rotated to an orientation which diagonalizes the inertia tensor. In order to determine the other rotated coordinates at points  $s_{j+1}$ , Eqs. (2.16) are written in terms of the direction cosines which are functions of the Euler angles  $\theta$ ,  $\phi$ , and  $\chi$ . The Cartesian coordinates at points  $s_{j+1}$  in the Eckart frame can be expressed in terms of the coordinates at points  $s_{j+1}$  in the corresponding IAM frame using Eq. (2.13). Therefore,

$$\begin{aligned} [x\xi] \lambda_{y\xi} + [x\eta] \lambda_{y\eta} + [x\zeta] \lambda_{y\zeta} - [y\xi] \lambda_{x\xi} - [y\eta] \lambda_{x\eta} - [y\zeta] \lambda_{x\zeta} &= 0, \\ [y\xi] \lambda_{z\xi} + [y\eta] \lambda_{z\eta} + [y\zeta] \lambda_{z\zeta} - [z\xi] \lambda_{y\xi} - [z\eta] \lambda_{y\eta} - [z\zeta] \lambda_{y\zeta} &= 0, \\ [z\xi] \lambda_{x\xi} + [z\eta] \lambda_{x\eta} + [z\zeta] \lambda_{x\zeta} - [x\xi] \lambda_{z\xi} - [x\eta] \lambda_{z\eta} - [x\zeta] \lambda_{z\zeta} &= 0, \end{aligned} \quad (2.17)$$

where

$$[\alpha\tau] = \sum_{i=1}^N a_{i\alpha}(s_j) a_{i\tau}(s_{j+1}), \quad (2.18)$$

with  $\alpha = x, y$ , or  $z$ , and  $\tau = \xi, \eta$ , or  $\zeta$ . The  $\lambda_{\alpha\tau}$  in Eq. (2.17) are the direction cosine matrix elements evaluated at the  $j + 1$  point. The geometry  $a_{i\alpha}(s_j)$  in the Eckart frame and the geometry  $a_{i\tau}(s_{j+1})$  in the IAM frame are known quantities, so Eq. (2.17) is a set of three simultaneous transcendental equations involving only the three Euler angles. This nonlinear system of equations is solved using the Powell dogleg method [17]. This system of equations is highly nonlinear and can require several



function evaluations to reach convergence. In a computer program available via the Internet [18], analytical Jacobians have been implemented in the dogleg method to maximize computational efficiency. This system of transcendental equations is solved iteratively with initial guesses of the Euler angles at point  $s_{j+1}$  taken from the known Euler angles at point  $s_j$ . After this procedure is carried out for all the geometries  $(a_{i\xi}, a_{i\eta}, a_{i\zeta})$ , a finite difference approximation can be used to obtain  $(a'_{ix}, a'_{iy}, a'_{iz})$  in the Eckart frame, and one has all the information needed to calculate the effective inertia in Eq. (2.12).

## 2.4 Pitzer Reduced Inertias

The conventional approach to computing the effective reduced inertias for internal rotations is through the use of approximate analytical formulae [19, 20, 21]. Pitzer and co-workers have developed several expressions for reduced moments of inertia which approximately separate the coupling of internal rotation from the overall external rotation of a molecule. As recommended by Pitzer, these protocols are only highly accurate when the moments of inertia for overall rotation are independent of the coordinates of internal rotation [20] (for example, any molecule with rigid symmetrical tops like ethane). However, for molecules with one or more asymmetric internal rotors, the external inertia tensor does depend strongly on the internal rotation coordinate, and the Pitzer approximation is less accurate. Section 2.5 gives examples where the conventional Pitzer scheme for estimating the effective inertia can have large differences from inertias obtained by imposing Eckart conditions within the internal coordinate path Hamiltonian formalism. In certain extreme situations, the rotation of one asymmetric rotor from a *trans* to a *gauche* conformation in a massive alkane, for example, can significantly change the principal axes of inertia. Furthermore, Pitzer also argued that if cross terms in the potential energy between internal rotation and vibration are significant, the method of reduced inertias itself may be a crude approximation [20].

The method of calculating the effective moment of inertia with Pitzer's formulas

is well-known [5, 19, 20, 21, 22] and only a brief review of the method is given in this section. Pitzer's expression for the reduced moment of inertia for a single internal rotation is given by

$$I = A - \sum_i \left[ \frac{(\alpha^{iy}U)^2}{M} + \frac{(\beta^i)^2}{I_i} \right], \quad (2.19)$$

where

$$\beta^i = \alpha^{iz}A - \alpha^{ix}B - \alpha^{iy}C + U(\alpha^{i-1,y}r^{i+1} - \alpha^{i+1,y}r^{i-1}). \quad (2.20)$$

The superscripts  $i-1$  and  $i+1$  are cyclic indices such that if  $i=1$ ,  $i-1=3$ , and if  $i=3$ ,  $i+1=1$ . The array

$$\begin{bmatrix} \alpha^{1x} & \alpha^{2x} & \alpha^{3x} \\ \alpha^{1y} & \alpha^{2y} & \alpha^{3y} \\ \alpha^{1z} & \alpha^{2z} & \alpha^{3z} \end{bmatrix} \quad (2.21)$$

is the direction cosines between the axes of the rotating top ( $x, y, z$ ) and the axes of the whole molecule (1, 2, 3). The internal rotation axis is taken as the  $z$ -axis of the top, and the  $x$ -axis passes through the top's center of mass. The axes of the whole molecule are those which pass through the center of mass and diagonalize the inertia tensor. All of Pitzer's expressions are based on the kinetic energy expression of Kassel [23] and Crawford [24], which uses a principal axis method (cutely abbreviated as PAM) [16] for molecular-fixed axes. It should be noted that these and the following expressions give the same results whether one includes or does not include atoms on the axis of rotation as part of the top. The following quantities are defined only with respect to the coordinate system of the top, which is composed of the  $i$ th atom with mass  $m_i$

$$\begin{aligned} A &= \sum_i m_i (x_i^2 + y_i^2), \\ B &= \sum_i m_i x_i z_i, \\ C &= \sum_i m_i y_i z_i, \\ U &= \sum_i m_i x_i. \end{aligned} \quad (2.22)$$

Finally, the components of the vector  $(r^1, r^2, r^3)$  in Eq. (2.20) point from the center of gravity of the whole molecule in the PAM reference frame to the origin of coordinates of the top.

## 2.5 Examples and Applications

In Table 1.1, the results of Eq. (2.12) are compared against Eq. (2.19) for several molecules having a single unsymmetrical torsion. Table (2.1) also gives the parameters characterizing the local minima along the torsional coordinate for each molecule:  $U$  is the torsional potential energy of a local minimum relative to the lowest global one,  $I_{\text{Eckart}}$  is the effective inertia calculated from Eq. (2.12), and  $I_{\text{Pitzer}}$  is the effective inertia calculated from Eq. (2.19). All *ab initio* electronic structure calculations for these molecules were carried out with the Gaussian 03 package [25] using the second order Møller-Plesset perturbation level of theory for all electrons (MP2(full)). All *ab initio* calculations and algorithm developments were performed on a custom-built server at the Sidney-Pacific Residence at the Massachusetts Institute of Technology, which comprises 2 processors ( $2 \times 2.8$  GHz Intel Xeon), with a total of 4 Gb of RAM. The standard 6-31G(d) basis set with the MP2(full) level of theory used in the present work is the same methodology employed in geometry optimizations in Pople's G3 composite procedures [26]. The point of the calculations presented is to provide reasonable and consistent geometries to test the accuracy of other conventional assumptions used in computing effective inertias. The purpose is not to resolve the many open questions regarding how best to calculate *ab initio* torsional potentials on the specific molecules presented as illustrative examples. For each molecule, the torsional potential was calculated by constraining a dihedral angle and optimizing all other internal coordinates to minimize the total energy. Of the six molecules listed in Table 2.1, hydrogen peroxide, 1,2-dichloroethane, and 1-fluoro-2-chloroethane were previously analyzed by Chuang and Truhlar [5]. The last column of Table 2.1 lists the available literature values of Chuang and Truhlar who also used the same Pitzer approximation described in Section 2.4 of the present work. Some attention should

	Torsional Angle (degrees)	U (cm-1)	$I_{\text{Eckart}}^a$ (amu Å <sup>2</sup> )	$I_{\text{Pitzer}}^b$ (amu Å <sup>2</sup> )	$I_{\text{Pitzer}}^c$ (amu Å <sup>2</sup> )
HO–OH					
Minimum 1	121.2°	0	0.4373	0.4357	0.3951
OHC–CHO					
Minimum 1	180.0°	0	4.445	4.985	—
Minimum 2	0.0°	1505	2.818	3.021	—
H <sub>2</sub> CHC–CHCH <sub>2</sub>					
Minimum 1	180.0°	0	5.338	6.236	—
Minimum 2	37.8°	936.8	3.460	4.589	—
FH <sub>2</sub> C–CH <sub>2</sub> F					
Minimum 1	69.0°	0	9.390	8.749	—
Minimum 2	180.0°	74.83	8.490	8.910	—
ClH <sub>2</sub> C–CH <sub>2</sub> F					
Minimum 1	180.0°	0	11.05	11.55	18.37
Minimum 2	65.9°	164.9	11.34	11.59	25.28
ClH <sub>2</sub> C–CH <sub>2</sub> Cl					
Minimum 1	180.0°	0	15.76	16.37	17.56
Minimum 2	68.2°	531.7	15.15	17.84	207.8

Table 2.1: Effective moments of inertia obtained from <sup>a</sup>Eq. (2.12), <sup>b</sup>Eq. (2.19), and <sup>c</sup>Ref. [5].

be drawn to the large deviation of their results from the calculations presented here, especially for the case of 1,2-dichloroethane, ClH<sub>2</sub>C–CH<sub>2</sub>Cl. Extensive theoretical [27, 28, 29, 30] and a few experimental [31, 32] studies have already been carried out on this asymmetric torsional motion. One of the first studies on 1,2-dichloroethane in the current literature is the finite-difference-boundary-value treatment by Chung-Phillips [28]. Her analysis includes an *ab initio* calculation of the relaxed geometries and torsional potential performed at the HF/6-31G\* level of theory. Using the HF/6-31G\* adiabatic potential energy curve, Chung-Phillips calculated one *trans* minimum and two equivalent *gauche* minima with  $I_{\text{Pitzer}}$  values of 16.46 amu Å<sup>2</sup> and 17.93 amu Å<sup>2</sup> respectively. Although the Hartree-Fock method used in her work is not quantitatively accurate, her two values of  $I_{\text{Pitzer}}$  are still in extraordinary agreement with our calculations in Table 2.1. More recently, Ayala and Schlegel have revisited the calculation of  $I_{\text{Pitzer}}$  for 1,2-dichloroethane and found in Section III of their work that the reduced moment of inertia increases only by a factor of 2 (in contrast to Chuang

and Truhlar’s factor of 12) as the twist angle is varied [27]. One of the latest studies on 1,2-dichloroethane torsional motion is from the work of Hnizdo and coworkers who have used the Pitzer formalism to estimate entropies of internal rotation via Monte Carlo simulations [30]. In Figure 2 of their work, they have plotted the variation of  $I_{\text{Pitzer}}^{1/2}$  as a function of the torsional angle, and they obtain results which are in excellent agreement with Figure 2-1 (f) of the present work. The good consistency of the reported results with respect to these three literature values supports the tabulated values, and the method used here for calculating  $I_{\text{Pitzer}}$  appears to be well-justified.

Figure 2-1 compares the Eckart and Pitzer effective inertias for the six molecules listed in Table 2.1. For each figure, both the Eckart and Pitzer inertias were calculated using the same molecular geometries on a regular grid of  $10^\circ$  increments for the torsional angle. An interesting feature of these figures is that both methods yield similar results for  $\text{H}_2\text{O}_2$ , but the differences between the two methods become more significant as the rotating top becomes more asymmetric. Among these calculations, considerable quantitative and qualitative discrepancies are seen between the two methods for 1,3-butadiene. The torsional potential energy surface of 1,3-butadiene has a local minimum near  $40^\circ$  corresponding to a *gauche* configuration. At this value of the torsional angle, the Eckart effective inertia also has a minimum, but this feature is absent in the Pitzer calculations. For the asymmetric torsions studied, it is apparent the Eckart effective inertias show more structure and variation as a function of torsional angle than the corresponding Pitzer inertias.

To demonstrate the effects of using the Eckart and Pitzer formalisms on dynamical properties, a converged set of eigenvalues and eigenvectors are calculated for 1,2-dichloroethane utilizing the one-dimensional kinetic energy operator given by the first three terms of Eq. (2.10). Figure 2-2 compares the lowest 2,500 torsional energies evaluated (1) using the instantaneous Eckart inertias displayed in Figure 2-1 (f), and (2) using only the constant value of the Pitzer inertia at the global *trans* minimum. Both methods give eigenvalues close to each other for torsional quanta less than 50, but the eigenvalues obtained from the instantaneous Eckart calculations are generally much larger than the results derived from the constant Pitzer inertia. The differences

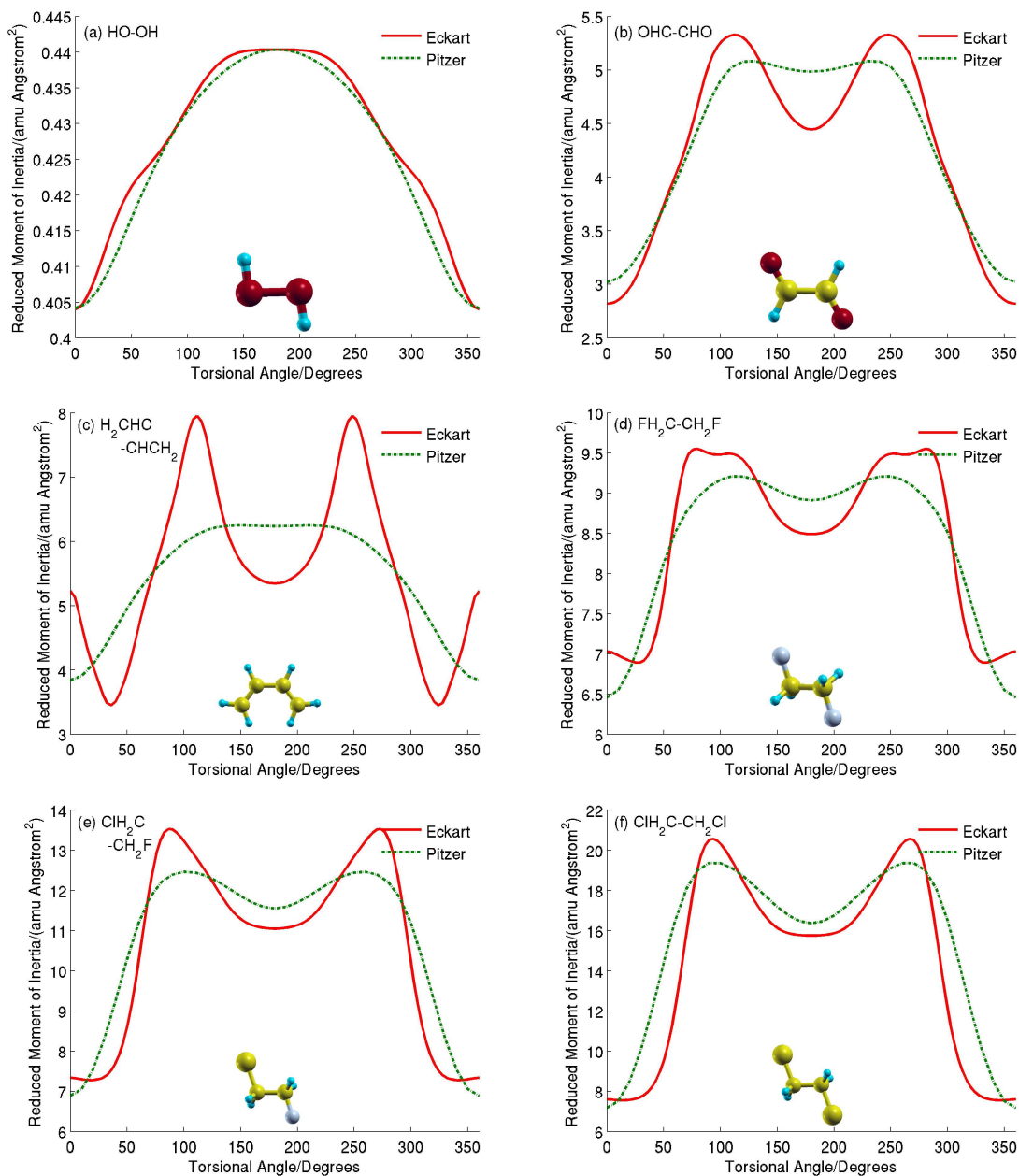


Figure 2-1: Eckart effective inertias (Eq. (2.12)) for six molecules displaying internal rotation compared with those calculated from Pitzer's formulae (Eq. (2.19)).

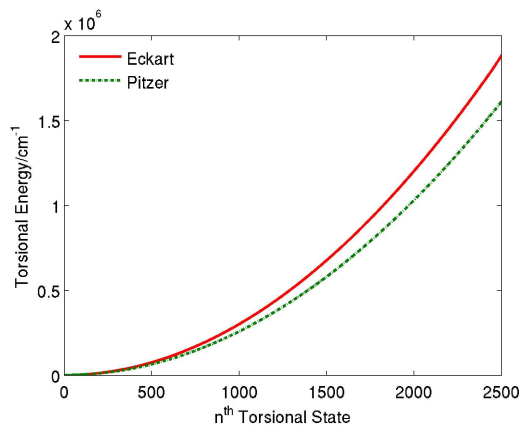


Figure 2-2: The lowest 2,500 eigenvalues for the torsional motion of 1,2-dichloroethane. The eigenvalues obtained from the instantaneous Eckart inertias are considerably larger than those obtained from a constant-valued Pitzer inertia at the *trans* geometry.

between the two methods are even more pronounced when the number of torsional quanta becomes greater than 100, and after 2,500 quanta of the torsion is reached, the Eckart eigenvalues are larger than the Pitzer eigenvalues by more than  $272,000 \text{ cm}^{-1}$ . This discrepancy can be simply understood realizing that the allowed eigenvalues for free rotation in one dimension are  $E_m = m^2 \hbar^2 / 2I$  with  $m = 0, \pm 1, \pm 2, \dots$ . For 1,2-dichloroethane at the simple MP2 level of theory, this free rotation limit is only reached when the number of torsional quanta exceeds 90 and the eigenvalues become doubly degenerate as shown in Figure 2-3 (a). Below the free rotation limit, the torsional wavefunctions have distinct, nondegenerate energies corresponding to alternating symmetric (red-colored) and antisymmetric (green-colored) torsional states.

Figure 2-3 (b) shows the 150 lowest torsionally averaged Eckart inertias,  $\langle I_{\text{Eckart}} \rangle$ , of 1,2-dichloroethane obtained by evaluating the instantaneous Eckart inertias in Figure 2-1 (f) averaged over each of the torsional wavefunctions. The averaged Eckart inertias are also color-coded to match their symmetric (red)/antisymmetric (green) energy levels in Figure 2-3 (a). The dotted horizontal line is the numerical value for the Pitzer effective inertia evaluated at the *trans* global minimum. For  $n < 5$ ,  $\langle I_{\text{Eckart}} \rangle$  does not vary appreciably from  $15.76 \text{ amu } \text{Å}^2$  since the torsional wavefunction is lo-

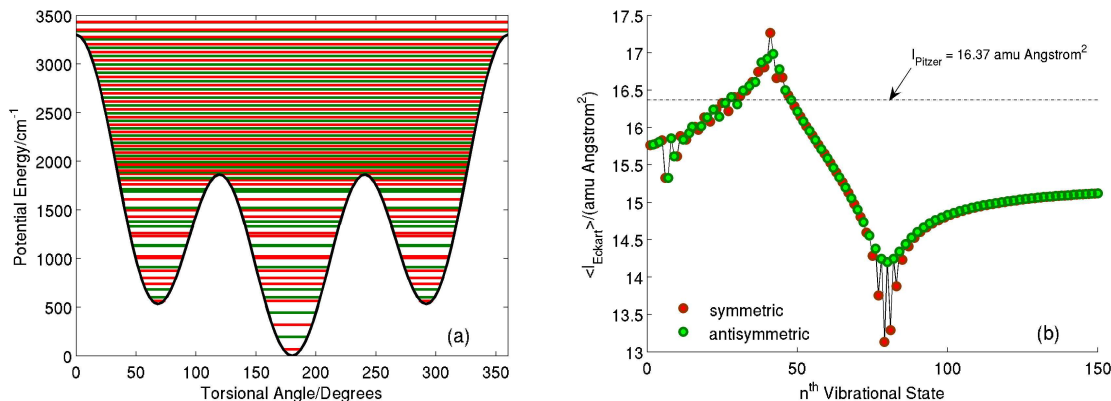


Figure 2-3: (a) Relaxed torsional potential and energies for 1,2-dichloroethane obtained at the MP2(full)/6-31G(d) level of theory. Each of the torsional eigenvalues is associated with symmetric (red-colored) and antisymmetric (green-colored) torsional states. (b) Torsionally averaged Eckart inertias,  $\langle I_{\text{Eckart}} \rangle$ , for the lowest 150 torsional states of 1,2-dichloroethane. The broken line indicates the numerical value of  $I_{\text{Pitzer}} = 16.37 \text{ amu } \text{\AA}^2$  calculated at the *trans* global minimum.

calized in the *trans* global minimum. For  $5 < n < 90$ ,  $\langle I_{\text{Eckart}} \rangle$  varies rapidly since the torsional wavefunction alternates between the two *gauche* local minima and the single *trans* minimum. As discussed previously, the torsion is nearly a free rotation for  $n > 90$ , and  $\langle I_{\text{Eckart}} \rangle$  is approximately constant with a limiting value of approximately  $15.1 \text{ amu } \text{\AA}^2$ . Since the free rotation energy,  $E_m$ , is proportional to  $I^{-1}$ , basing the torsional energies on the larger Pitzer inertia would significantly underestimate the Eckart eigenvalues above the free rotation limit (cf. Figure 2-2).

As a final application, the effective inertia is calculated for the large-amplitude motion describing the isomerization of acetylene to vinylidene. Since the local bender limit of this 1,2-hydrogen rearrangement process is of primary interest, the most intuitive choice for the large-amplitude curvilinear parameter,  $s$ , is the internal HCC bend angle in acetylene. While CC–HH diatom-diatom coordinates are much better suited for describing vinylidene and H-atom orbiting states [33, 34], they are more awkward to use at low energies below the vinylidene isomerization barrier [35, 36, 37]. For this reason, the internal coordinate path was obtained by constraining the HCC angle at  $5^\circ$  increments while optimizing all other internal coordinates to minimize the total energy. The electronic structure calculations for the relaxed molecular geometries of



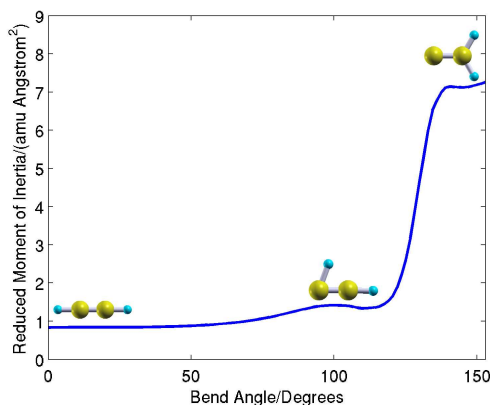


Figure 2-4: Reduced moment of inertia calculated by the Powell dogleg algorithm for the HCC bending motion of acetylene. The effective inertia increases rapidly near  $110^\circ$  when the rightmost hydrogen moves in concert with the leftmost hydrogen to form vinylidene.

acetylene were carried out using the coupled cluster with single and double substitutions level of theory (CCSD). The basis set used at this level of theory was Dunning's augmented correlation consistent triple-zeta basis, aug-cc-pvtz [38]. Figure 2-4 shows the effective inertia as a function of the bend angle up to a final value of  $153^\circ$ , which corresponds to the equilibrium vinylidene geometry. The method of Pitzer cannot be applied to this type of large-amplitude motion, but the effective inertia can still be calculated easily by solving Eq. (2.12) as described in Section 2.3. As shown in Figure 2-4, the isomerization from acetylene to vinylidene involves one hydrogen migrating a large distance off the C–C bond axis while the other hydrogen remains relatively stationary. The transition state structure for the isomerization process emerges when the active hydrogen makes an angle of approximately  $110^\circ$  as measured from the equilibrium linear geometry. Once the HCC bend angle is increased past the transition state structure, large variations in geometries occur as the rightmost hydrogen moves in concert with the leftmost hydrogen, and the C–C triple bond lengthens to a double bond [10]. Since the Eckart inertia is proportional to  $\mathbf{a}'_i(s) \cdot \mathbf{a}'_i(s)$  (cf. Eq. (2.12)), and the geometry changes rapidly past the transition state, the effective inertia is significantly larger for HCC bend angles greater than  $110^\circ$ . In a later paper, this method has been used in conjunction with an effective Hamiltonian model to

describe the Stark effect as a diagnostic tool for assigning excited vibrational states [10].

## 2.6 Conclusion

This chapter has presented a method by which accurate inertias for internal rotations and other large-amplitude motions may be calculated by rigorously separating this large-amplitude motion from the external rotation. It was shown that the conventional Pitzer scheme for estimating the effective inertia can have large differences from the Eckart method, which minimizes the couplings of torsions to rotations. The discrepancies are mostly due to more accurate numerical minimization methods presently available and are not meant to imply a criticism of Pitzer's earlier work, whose approximate analytical formulae were pioneering at the time they were proposed. The source of error in Pitzer's inertia is apparent if one remembers that the Pitzer method is inherently based on a coordinate system used from PAM. If the rotating top has an axis of symmetry, the principal axes of the molecule do not change significantly as the torsional angle is varied. However, if both the rotating top and the frame of the molecule are heavy and asymmetric, the cross terms, which represent the interactions between the two kinds of rotation (cf. Eq. (2.9)), are much larger in PAM/Pitzer's method than in the Eckart frame. In order to correct this inadequacy, it is necessary to go beyond approximate analytical formulae to pursue numerical methods of minimizing these couplings.

It was also shown that the Eckart method is general and applies to other large-amplitude motions such as large variations in angle bends. In a one-dimensional description of the acetylene/vinylidene isomerization, the procedure is essential since it minimizes several of the coupling terms between the large-amplitude bend and the overall rotation. This is particularly important since the relaxed geometries that describe the 1,2-hydrogen rearrangement do not change uniformly along the isomerization path. A user-friendly code for computing the Eckart inertia as a function of the torsional angle is available [18]. These computer programs automatically solve

the nonlinear set of equations in Eq. (2.17) and output the reduced inertias as a function of the torsional angle. All of the examples presented in Table 2.1 are also available as sample inputs for these codes. The Eckart method described in Section 2.3 is recommended as an alternative to the conventional Pitzer method, particularly for molecules with asymmetric internal rotors.



# Chapter 3

## Electronic Signatures of Large-Amplitude Motion in $S_0$ Acetylene

The primary objective of this chapter is to illustrate the use of electronic properties to identify vibrationally excited states of  $S_0$  acetylene. The majority of the work in this chapter resulted from a collaboration with Adam H. Steeves and was published as an article in the *Journal of Physical Chemistry B* [10].

### 3.1 Introduction

The acetylene ( $\text{H-C}\equiv\text{C-H}$ )  $\rightleftharpoons$  vinylidene ( $\text{H}_2\text{C}=\text{C:}$ ) isomerization on the ground electronic potential energy surface exemplifies one of the simplest bond-breaking processes in polyatomic molecules. Numerous spectroscopic studies have been carried out on acetylene [39, 40, 41, 42, 43], with the intent to observe the acetylene  $\rightleftharpoons$  vinylidene isomerization and to confirm theoretical calculations [33, 34, 35, 44, 45, 46, 47]. One of the most recent studies on the spectroscopy of acetylene is that of Jacobson and coworkers [39, 40, 48] who measured  $S_1 \rightarrow S_0$  dispersed fluorescence spectra, which sample vibrational energy levels on the  $S_0$  surface in the energy region up to 15,000  $\text{cm}^{-1}$ . The excited vibrational states in this energy region lie close to the vinylidene

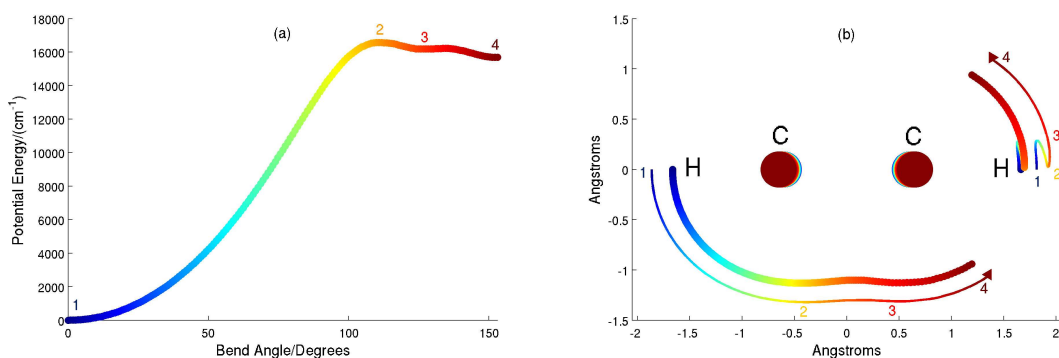


Figure 3-1: (a) One-dimensional relaxed potential for the acetylene-vinylidene isomerization as a function of the HCC valence bend angle. A transition state structure is labeled by the number 2, and local minima are denoted by numbers 3 and 4. (b) Spatial positions of the acetylene coordinates color-coded to match their corresponding location on the one-dimensional potential. The rightmost hydrogen retraces its path near the transition state but moves in concert with the leftmost hydrogen in the red-colored post transition state 2 regions.

minimum (cf. Figure 3-1 (a)). By fitting the spectroscopically assigned levels of the bending modes to an effective two-dimensional Hamiltonian, Jacobson and coworkers were able to show that the vibrational eigenstates of acetylene undergo a *normal-to-local* transition [48, 49, 50, 51, 52, 53, 54, 55, 56, 57]— a behavior in which the normal modes, which describe small deviations from the equilibrium geometry, evolve into local modes where the excitation is isolated in a single CH bond-stretch or a CCH angle-bend. This evolution of vibrational character is of particular interest in acetylene because the local bending vibration bears a strong resemblance to the reaction coordinate for the acetylene  $\rightleftharpoons$  vinylidene isomerization (Figure 3-1 (b)) where one hydrogen migrates a large distance off the C–C bond axis while the other hydrogen remains relatively stationary.

Contrary to the large number of studies on the vibrational overtone spectrum of acetylene, very little information is available regarding the effect of an electric field on the vibrational levels of the  $S_0$  state of this molecule. This is not surprising given that the ground electronic state of acetylene is linear and has  $D_{\infty h}$  symmetry. The definite  $g/u$  symmetry of every rovibrational level dictates that there can be no permanent dipole moment in any eigenstate; furthermore, the inversion symmetry of the molecule

restricts the action of the dipole operator to off-diagonal in the vibrational quantum numbers (see Section 3.4). That is, there is no permanent electric dipole moment in acetylene that can lead to a pure rotational transition. Despite the absence of a permanent vibrational dipole moment, Barnes et al. have analyzed electric field-induced perturbations in  $\nu_1 + 3\nu_3$  and  $\nu_2 + 3\nu_3$  bands of acetylene at fields up to 300 kV/cm [58, 59]. In both cases, the primary effect of the electric field is to mix the optically bright vibrational state with a near-degenerate optically dark level that differs from the bright level by exchanging one quantum of excitation in the symmetric C–H stretching mode  $(\nu_1, g)$  for one quantum of excitation in the antisymmetric C–H stretching mode  $(\nu_3, u)$ , or vice versa. The electric dipole moment function of  $S_0$  acetylene has also been studied by breaking the inversion symmetry through isotopic substitution. Muentner and Laurie first observed the pure rotational transitions of acetylene- $d$  in the ground vibrational state [60]. Matsumura et al. subsequently measured states excited in the CCH and CCD bending vibrations and determined the variation of the dipole moment with excitation in these modes to be 0.046 and -0.0336 D/quanta respectively [61].

In light of these spectroscopic and other theoretical results [62], it was proposed that changes in electronic structure can be used as a universal marker to distinguish the unique local mode vibrational states from the vast majority of normal vibrational eigenstates. In any given energy region, the majority of vibrational states have excitation energy distributed among many small-amplitude, strongly-coupled modes [63]. Because the vibrational energy is distributed throughout the molecule, rather than being directed along one particular large-amplitude coordinate, the average electronic structure does not significantly deviate from that of the equilibrium nuclear configuration. However, for a large-amplitude, local motion, changes in the relative orientations of functional groups in a molecule can cause large changes in the electric dipole moment. The electronic wavefunction is even more severely deformed in the case of chemical isomerization in which bonds are broken and new bonds formed, thereby altering the global electronic structure. Therefore, the measured magnitude of the electric dipole moment can be experimentally used as a measure of progress

along the reaction coordinate.

The following sections utilize the one-dimensional reaction path-like Hamiltonian developed in Chapter 2 to put the predictions of these dipole moments on a quantitative basis. This reduced form of the full seven-dimensional vibrational Hamiltonian is suitable for calculations of vibrationally averaged dipole moments of both local stretching and local bending modes. Although multidimensional potential energy surfaces of acetylene can presently be calculated with excellent accuracy [33, 34, 36, 64, 65], physical insight can be obtained from an effective, one-dimensional *ab initio* calculation. The present approach to this enormous reduction in phase space dimension is based on the observation that the spectroscopic fitting Hamiltonian,  $\mathbf{H}^{\text{eff}}$ , exhibits extremely stable, one-dimensional, pure local bending motions. Therefore, a Hamiltonian parametrized by a single internal coordinate is used in which the relevant large-amplitude motion is decoupled from the other degrees of freedom. Numerical comparisons with other models and experimental data allow the assessment of the physical relevance of this reduction.

## 3.2 Hamiltonian

The theory of the internal coordinate path Hamiltonian and its variational solution has been described by Tew et al. [12] Their parametrization of a large-amplitude motion with a single internal coordinate is based on the work of Hougen, Bunker, and Johns, who were the first workers to include large-amplitude motion in their semi-rigid bender model [8]. Other workers, such as Szalay, have extended this approach to account for non-rigid effects of large-amplitude internal motion in general molecules [66]. The formulation of Tew et al. is closely related to the reaction path Hamiltonian introduced by Miller, Handy, and Adams [13] with the exception that the internal coordinate path need not be exactly parallel to the minimum energy path. When defining a path to parametrize a large-amplitude motion, it should be remembered that the minimum energy path is defined as the steepest descent path from a transition state toward reactants or products [67, 68]. More rigorously, the minimum energy



path can be expressed by the solution of the differential equation

$$\frac{d\mathbf{x}}{d\tilde{s}} = -\frac{\nabla V}{|\nabla V|}, \quad (3.1)$$

where  $\mathbf{x}$  is a  $3N$  component vector of mass-weighted Cartesian coordinates,  $\tilde{s}$  is the path length, and  $V$  is the potential energy of  $N$  nuclear displacement vectors. When the minimum energy path is located in mass-weighted coordinates as written in Eq. (3.1), it is called an intrinsic reaction coordinate [67, 68]. Since the minimum energy path by definition follows the gradient vector of the potential energy, the potential energy at any point on the path can be expanded in terms of the normal coordinates  $Q_k$  up to second order:

$$\hat{V} = V_0(\tilde{s}) + \frac{1}{2} \sum_{k=1}^{3N-7} \omega_k^2(\tilde{s}) Q_k^2, \quad (3.2)$$

where  $\omega_k^2(\tilde{s})$  are the  $3N - 7$  eigenvalues of a projected force constant matrix.

In order to define a minimum energy path, one commences by optimizing a saddle point on the potential energy surface and then follows the negative gradient of the energy in mass-weighted Cartesian coordinates. However, as Tew et al. have stated, this algorithm is not a numerically sound technique. If insufficiently small steps are taken along the reaction path, one may be unable to locate the minimum accurately at the end of the path. Furthermore, near the saddle point, the optimized geometries may be inaccurate since the first step away from this starting point is along a vector defined without reference to any curvature. The internal coordinate path Hamiltonian used in this work removes many of these problems by parametrizing a path with a single internal coordinate such as a bond length or a valence bend angle. This parametrization guarantees a continuous variation with no numerical complexity since the internal coordinate is a geometric variable and is always well-defined at any point on the path. However, since this path is obtained by scanning relaxed points on the potential surface with a user-chosen internal coordinate, the gradient vector of the molecular potential energy has not necessarily been followed. Whereas the minimum energy path potential energy has no term linear in  $Q_k$ , the internal coordinate path

potential must have a linear term:

$$\hat{V} = V_0(s) + \sum_{k=1}^{3N-7} g_k(s) Q_k + \frac{1}{2} \sum_{k=1}^{3N-7} \omega_k^2(s) Q_k^2, \quad (3.3)$$

where  $s$  is a conveniently chosen geometric variable such as an angle, a bond length, or a combination of angles and bond lengths used to parametrize the large-amplitude path. For many cases, the true reaction coordinate can be approximated by a single internal coordinate, and the gradient  $g_k$  will be small if the internal coordinate is approximately in the same direction as  $\tilde{s}$ . In other words, neglecting this gradient term is equivalent to ignoring the minor off-diagonal matrix elements of  $g_k(s) Q_k$  in the small-amplitude harmonic quantum numbers.

In the present work the internal coordinate path method is used with an approximate treatment for the other small-amplitude modes. The approximate expressions and their numerical evaluations have already been reported in Chapter 2. This approach is briefly reviewed here, and only the slight modifications used in the present work will be described in detail. The theory of the internal coordinate path Hamiltonian for an  $N$ -atom molecule is expressed in terms of a single large-amplitude coordinate,  $s$ , its conjugate momentum,  $\hat{p}_s (= -i\hbar\partial/\partial s)$ , and the coordinates  $\mathbf{Q} = \{Q_1, Q_2, \dots, Q_{3N-7}\}$  and momenta  $\hat{\mathbf{P}} = \{\hat{P}_1, \hat{P}_2, \dots, \hat{P}_{3N-7}\} = -i\hbar\{\partial/\partial Q_1, \partial/\partial Q_2, \dots, \partial/\partial Q_{3N-7}\}$  of the orthogonal small-amplitude vibrational modes. The full quantum mechanical kinetic energy operator in these coordinates is given by

$$\hat{T} = \frac{1}{2} \sum_{d,e=1}^4 \mu^{1/4} \left( \hat{\Pi}_d - \hat{\pi}_d \right) \mu_{de} \mu^{-1/2} \left( \hat{\Pi}_e - \hat{\pi}_e \right) \mu^{1/4} + \frac{1}{2} \sum_{k=1}^{3N-7} \mu^{1/4} \hat{P}_k \mu^{-1/2} \hat{P}_k \mu^{1/4}. \quad (3.4)$$

$\hat{\Pi}$  and  $\hat{\pi}$  are four-component operators given by

$$\begin{aligned} \hat{\Pi} &= \left( \hat{J}_x, \hat{J}_y, \hat{J}_z, \hat{p}_s \right), \\ \hat{\pi} &= \sum_{k,l=1}^{3N-7} \left( B_{kl,x}(s), B_{kl,y}(s), B_{kl,z}(s), B_{kl,s}(s) \right) Q_k \hat{P}_l, \end{aligned} \quad (3.5)$$

where  $\hat{J}_x$ ,  $\hat{J}_y$ , and  $\hat{J}_z$  are the components of the total angular momentum operator, and  $B_{kl,x}$ ,  $B_{kl,y}$ ,  $B_{kl,z}$ , and  $B_{kl,s}$  are the ‘‘Coriolis coupling’’ matrices [12] that are functions of the large-amplitude coordinate,  $s$ . The symmetric tensor,  $\mu_{de}$ , and its determinant,  $\mu$ , are also functions of the internal coordinate,  $s$ .

As reported previously [7], the following approximations allow for the computation to be manageable: (1) the effective inertia tensor depends weakly on  $\mathbf{Q}$ , and only the terms that depend on  $s$  are retained; (2) the ‘‘vibrational angular momentum’’ terms,  $\hat{\pi}_\alpha$ , are linear in the small-amplitude coordinates,  $\mathbf{Q}$ , and their contribution to the kinetic energy is neglected; (3) numerically enforcing the Eckart conditions minimizes many of the coupling terms in Eq. (3.1). It follows from these approximations that the kinetic energy operator for total angular momentum  $J = 0$  can be written in the following form (cf. Eq. 10 of Ref. [7]):

$$\hat{T} = \frac{1}{2}\hat{p}_s I_{0ss}^{-1} \hat{p}_s + \frac{1}{2}\mu^{1/4} \left( \hat{p}_s I_{0ss}^{-1} \mu^{-1/2} \left( \hat{p}_s \mu^{1/4} \right) \right) + \frac{1}{2} \sum_{k=1}^{3N-7} \hat{P}_k^2, \quad (3.6)$$

where the scalar terms  $I_{0ss}^{-1}$  and  $\mu$  are given by

$$I_{0ss}^{-1}(s) = \left( \sum_{i=1}^N \mathbf{a}'_i(s) \cdot \mathbf{a}'_i(s) \right)^{-1}, \quad (3.7)$$

$$\mu(s) = I_{0ss}^{-1} \cdot \det(\mathbf{I}_0^{-1}). \quad (3.8)$$

The vectors  $\mathbf{a}_i$  ( $= m_i^{1/2} \mathbf{r}_i$ ) are the mass-weighted Cartesian coordinates of the  $i$ th atom at a point on the path  $s$  with respect to the Eckart axis system, and  $\mathbf{a}'_i = d\mathbf{a}_i/ds$ . Finally, the operator  $\hat{p}_s$  operates only within the parentheses in Eq. (3.6); that is, the next to last term in Eq. (3.6) is a scalar term.

### 3.3 Ab Initio Calculations

All *ab initio* electronic structure calculations for the acetylene-vinylidene isomerization were carried out with the Gaussian 03 package [25]. Extensive theoretical studies

have been carried out on both the global potential energy surface [33, 34] and the one-dimensional minimum energy path [64] in the current literature. One of the most recent theoretical studies on acetylene is the investigation by Zou and Bowman [33]. Their analysis includes several high-level *ab initio* calculations of the six-dimensional potential (seven-dimensional for linear geometries) performed at the coupled cluster with single and double substitutions with perturbative triples (CCSD(T)) level of theory. In their least squares fit of the potential energy surface, they obtained eigenfunctions and eigenvalues of the exact Hamiltonian for zero total angular momentum. The most consistent and accurate *ab initio* energies are from their CCSD(T)/aug-cc-pVTZ calculations which yield a  $15407\text{ cm}^{-1}$  energy difference between the acetylene and vinylidene minima.

Since the goal of this chapter is to obtain an effective one-dimensional cut of a seven-dimensional potential, the intent is not to reproduce Zou and Bowman’s *ab initio* values exactly. Instead, the purpose of this work is to obtain accurate results from a computational method which does not require the evaluation of gradients or Hessians. To this end, the relaxed geometry parameters were analyzed using the CCSD level of theory with Dunning’s augmented correlation consistent triple-zeta basis, aug-cc-pVTZ [38]. The geometry optimizations were carried out with tight convergence criteria with root-mean-square forces within 0.0001 atomic units and root-mean-square displacements within 0.0004 atomic units. CCSD(T) single-point energies were subsequently performed with the cc-pVQZ basis set at the CCSD optimized geometries.

For the acetylene-vinylidene isomerization, the local bender limit of the 1,2-hydrogen rearrangement process is of primary interest. The isomerization coordinate near the linear acetylene global minimum corresponds to an HCC bend-like motion and involves a periodic potential. Therefore, the most appropriate choice for the large-amplitude parameter,  $s$ , is the internal HCC bend angle coordinate. While CC–HH diatom-diatom coordinates are much better suited for describing vinylidene and H-atom orbiting states [33, 34], they are more awkward to use at low energies below the vinylidene isomerization barrier [35, 36, 37]. For this reason, the internal

coordinate path was obtained by constraining the HCC angle at  $5^\circ$  increments while optimizing all other internal coordinates to minimize the total energy. At all intermediate geometries between the  $D_{\infty h}$  acetylene global minimum and the  $C_{2v}$  vinylidene local minimum, molecular symmetry was constrained within the  $C_s$  point group. It should also be remembered that the domain for the valence angle,  $s$ , is  $(0, 2\pi)$ ; that is,  $s = 0$  corresponds to one linear structure ( $H_a C_b C_c H_d$ ), and  $s = \pi$  corresponds to another ( $H_d C_b C_c H_a$ ). The permutational symmetry of the isomerization path with respect to the interchange of the two H atoms ( $P_{ad}$ ) was used to generate additional energies, dipole moments, and geometries. Therefore, the fully symmetric internal coordinate path can be constructed with only the information from vinylidene to acetylene by using permutation group operations in a local frame. The symmetric  $a$ -axis and antisymmetric  $b$ -axis dipole moments of acetylene at the CCSD/aug-cc-pVTZ levels of theory are shown in Figure 3-2 (a). Since all molecular geometries were constrained to lie in a plane, the  $c$ -axis dipole moment is exactly zero and only the  $a$ -axis and  $b$ -axis dipoles are displayed. Finally, each resulting geometry was translated to the center of mass frame, and all energies, dipole moments, and geometries as a function of  $s$  were fit to a Fourier series. In this way, finite differences can be used to solve iteratively for the Euler angles that rotate the Cartesian axes in order to impose the Eckart conditions.

A converged set of eigenvalues and eigenvectors for the one-dimensional Hamiltonian described in Eq. (3.6) were computed using a discrete variable representation [69]. For the acetylene-vinylidene isomerization, the large-amplitude coordinate involves a periodic potential, and the most natural choice for a complete orthogonal set of basis functions is the set of complex exponentials

$$\left\{ \frac{e^{-mis}}{\sqrt{2\pi}}, \dots, \frac{e^{-2is}}{\sqrt{2\pi}}, \frac{e^{-is}}{\sqrt{2\pi}}, \frac{1}{\sqrt{2\pi}}, \frac{e^{is}}{\sqrt{2\pi}}, \frac{e^{2is}}{\sqrt{2\pi}}, \dots, \frac{e^{mis}}{\sqrt{2\pi}} \right\} \quad (3.9)$$

where  $m$  is a positive integer. The scalar functions  $V_0(s)$ ,  $I_{0ss}^{-1}$ ,  $\mu$ , and the dipole moment components can all be fitted to a Fourier series of the form:

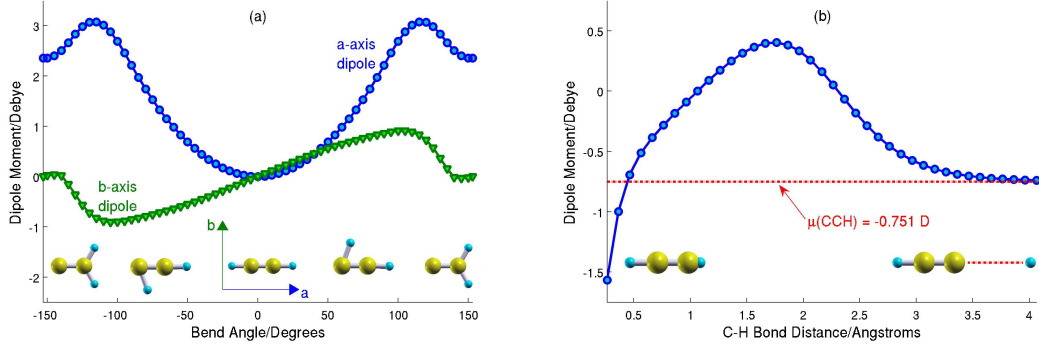


Figure 3-2: Dipole moments computed for relaxed geometries as a function of (a) fixed HCC local bend angle and (b) fixed local C–H stretch distance. In Figure 3-2 (a), the schematic diagrams of the bending motion show that when the local bend is excited, the  $b$ -axis dipole moment must change sign at  $\theta = 0$ . Conversely, the  $a$ -axis dipole moment is symmetric about  $\theta = 0$  since the active hydrogen is always placed at identical horizontal distances along the  $a$ -axis during the (symmetric) local bending motion. In Figure 3-2 (b), the broken line indicates the numerical value of the dipole moment for the CCH equilibrium geometry. The dipole moments for Figures 3-2 (a) and (b) were obtained from the CCSD/aug-cc-pVTZ and MR-AQCC/aug-cc-pVQZ levels of theory, respectively.

$$f(s) = \frac{a_0}{2} + \sum_{j=1}^{[(N-1)/2]} a_j \cos(js) + \sum_{j=1}^{[(N-1)/2]} b_j \sin(js), \quad (3.10)$$

where  $N$  is the number of discrete data points to be fitted, and the square brackets  $[(N-1)/2]$ , denote the largest integer less than or equal to  $(N-1)/2$ . The nonvanishing matrix elements of Eq. (3.10),  $F_{k,k'} = \langle k | f(s) | k' \rangle$ , in the ordered basis listed in Eq. (3.9) are

$$\begin{aligned} F_{k,k} &= \frac{a_0}{2}, \\ F_{k,k+l} &= \frac{a_l + ib_l}{2}, \\ F_{k+l,k} &= F_{k,k+l}^* = \frac{a_l - ib_l}{2}, \end{aligned} \quad (3.11)$$

Since the maximum value of  $l$  is  $\max(j) = [(N-1)/2]$ , the structure of  $\mathbf{F}$  is an  $N$ -diagonal,  $(2m+1) \times (2m+1)$  Hermitian matrix. The matrix representation of  $\hat{p}_s$  is a  $(2m+1) \times (2m+1)$  diagonal matrix with  $[-m\hbar, \dots, -2\hbar, -\hbar, 0, \hbar, 2\hbar, \dots, m\hbar]$  along the diagonal. Using Eqs. (3.10) and (3.11) the kinetic energy, potential energy,

and dipole moment matrix elements were easily obtained from their Fourier series expansion coefficients.

For the local C–H stretch of acetylene, the parameter  $s$  was chosen to be the single bond distance between the carbon and hydrogen atoms undergoing the large-amplitude motion. Unlike the acetylene-vinylidene isomerization, the local stretch is not sufficiently described by a CCSD(T) single-reference electronic configuration especially for large C–H bond distances. The electronic ground state of  $S_0$  acetylene in its equilibrium geometry is qualitatively well described by CCSD(T) in which the carbon-hydrogen  $\sigma$  bond is doubly occupied. However, as the C–H bond is broken, the  $\sigma$  and  $\sigma^*$  orbitals become nearly degenerate, and the entire molecule ( $\text{HCC}\cdot + \text{H}\cdot$ ) becomes a diradical. An accurate description of the potential and dipole moments over this wide range of nuclear geometries requires the use of a multireference electronic wavefunction. Before proceeding with a detailed discussion of our *ab initio* methods for the local C–H stretch, it should be mentioned that Lee and Taylor [70] have proposed the “T1 diagnostic” to determine whether a single-reference-based electron correlation procedure is appropriate. Based on their criterion, if the Euclidean norm of the t1 vector from a CCSD calculation is greater than 0.02, a multireference electron correlation method is necessary. The T1 diagnostic has been computed for the local C–H stretch and was found to be 0.023 at a C–H bond distance of 2.256 Å using a cc-pVQZ basis. On the other hand, the T1 diagnostic for the acetylene-vinylidene transition state is 0.019 using an aug-cc-pVTZ basis, indicating that the isomerization is still qualitatively described by a single-reference configuration.

All multireference-based electronic structure calculations for the local C–H stretch were carried out with the Molpro 2002.6 package [71]. To minimize the errors caused by basis set truncation, the larger aug-cc-pVQZ basis set was used. The complete multireference calculation for each relaxed geometry was comprised of three separate steps. First, the ground-state molecular orbitals were calculated using the restricted Hartree-Fock (RHF) method. Next, to accurately describe the local stretch, configurations occupying the  $\sigma^*$  C–H bond orbital must be included; therefore, the multi-configuration self-consistent field (MCSCF) method with the previous RHF orbitals

as initial guesses for orbital optimization was used. In the MCSCF and subsequent electronic structure calculations, the 10 outermost molecular orbitals were selected as the active space which includes six  $\sigma$  and four  $\pi$  orbital symmetries. The outermost 10 electrons were placed in the active space, while the 4 electrons in the two lowest  $\sigma$  orbitals were kept doubly occupied but still correlated in all configurations. Lastly, to include electron correlation effects not accounted for in MCSCF methods, the final electronic wavefunction was constructed as single and double electronic excitations from MCSCF orbitals using the multireference averaged quadratic coupled cluster (MR-AQCC) [72] method. The MR-AQCC method is essentially a modified multireference procedure which approximately corrects for the size-consistency problem associated with the truncation of electronic excitations. The relaxed MR-AQCC geometries and energies for C–H bond distances ranging from 0.26 Å to 4.06 Å were evaluated in intervals of 0.1 Å. The dipole moment as a function of the local C–H stretch is shown in Figure 3-2 (b). The dotted horizontal line in this figure is the numerical value of the dipole moment for the HCC fragment evaluated at the relaxed MR-AQCC/aug-cc-pVQZ geometry. Each resulting geometry was translated to the center of mass frame, and all energies, dipole moments, and geometries were smoothly fit as a function of  $s$ . All of the matrix elements involving the C–H stretch of acetylene were evaluated using numerical quadrature.

### 3.4 Dipole Moments in the Unsymmetrized Local Mode Basis

The analysis and text in this section are due to Adam H. Steeves and were excerpted from Ref. [10].

As previously noted, the inversion symmetry of acetylene prohibits both the existence of a permanent vibrational dipole moment and the corresponding typical quadratic Stark effect. The one-dimensional calculations are carried out in a space where  $g/u$  symmetry is not conserved. The resulting eigenfunctions are therefore



not eigenfunctions of the inversion operator and may possess permanent vibrational dipole moments. In order to make the comparison with experiment, one must consider the local-mode interpretation of the electric field induced perturbation investigated by Barnes et al. and demonstrate how the local mode limit of vibrational character leads to an effective dipole of the  $g/u$  components.

The matrix element connecting the optically bright and dark field-free eigenstates is an off-diagonal (in vibration) element of the electric dipole operator, or a *transition dipole moment*,  $\langle 04+ | \mu | 04- \rangle$ . The local mode notation can be expressed in terms of the left and right oscillators,

$$|04\pm\rangle = \frac{1}{\sqrt{2}} [|04\rangle \pm |40\rangle], \quad (3.12)$$

where the notation on the right hand side of Eq. (3.12) indicates an unsymmetrized basis state  $|v_{\text{left}}v_{\text{right}}\rangle$ . The dipole matrix element can be re-expressed in the unsymmetrized basis as:

$$\langle 04+ | \mu | 04- \rangle = \frac{1}{2} [\langle 04 | \mu | 04 \rangle - \langle 40 | \mu | 40 \rangle]. \quad (3.13)$$

Since, by symmetry, the two diagonal elements of the dipole operator in the unsymmetrized basis are of the same magnitude but of opposite sign,

$$\langle 04 | \mu | 04 \rangle = - \langle 40 | \mu | 40 \rangle, \quad (3.14)$$

the perturbation matrix element in the symmetrized basis can be expressed as a diagonal matrix element in the left/right basis:

$$\langle 04+ | \mu | 04- \rangle = \langle 04 | \mu | 04 \rangle. \quad (3.15)$$

The transition dipole moment between the vibrational levels that make up the local mode pair can therefore be interpreted as a permanent vibrational dipole moment of an unsymmetrized state excited only in the right (or left) oscillator. Because the

+/- ( $g/u$ ) components have been brought into near degeneracy, each rovibrational level now interacts with the rotational levels differing in  $J$  by one that belong to the *other* member of the local mode pair, through the dipole operator. The inversion symmetry has therefore been effectively broken because the physical consequences of the near degeneracy in the local mode limit are essentially identical to breaking the symmetry of the molecule through other means, e.g. isotopic substitution. That is, when the molecule is excited to a vibrational level that is in the local mode limit, it will exhibit regular quadratic Stark shifts, and it will be possible to excite “pure rotational” transitions.

### 3.5 Local Bending in the Polyad Model

The polyad model is a multi-resonant effective Hamiltonian fitted to an extensive set of spectroscopic data [48, 73, 74, 75, 76]. Although the local bending levels are not directly observed by any of the spectroscopic techniques and therefore not included in the fit, they emerge naturally from the effective Hamiltonian model. The local mode basis for bending levels is more complicated than that for the stretching levels because each CCH oscillator is treated as an isotropic two-dimensional harmonic oscillator and therefore is characterized by a vibrational angular momentum. In the symmetrized local mode basis, a state is labeled  $|v_A^{\ell_A}, v_B^{\ell_B}\rangle_{\mathcal{L}}^{g/u\pm}$ , where  $\ell_{A/B}$  refers to the vibrational angular momenta associated with the left or right local bending mode. While the extreme local bender levels are denoted  $|N_{\text{bend}}^0, 0^0\rangle_{\mathcal{L}}^{g/u\pm}$ , the higher lying levels are formed by removing one quantum of vibration from the highly excited oscillator and placing it in the less excited oscillator, e.g.  $| (N_{\text{bend}} - 1)^1, 1^{-1} \rangle_{\mathcal{L}}^{g/u\pm}$ ,  $| (N_{\text{bend}} - 2)^0, 2^0 \rangle_{\mathcal{L}}^{g/u\pm}$ , etc.

### 3.6 Results

The local-bending behavior that emerges from the polyad model represents a reduction to one dimension of the full spectroscopic effective Hamiltonian. The spectro-

scopic fitting Hamiltonian itself is dimensionally reduced from 7 to 3 by the specification of  $N_{\text{stretch}}$ ,  $N_{\text{bend}}$ ,  $\ell$ , and  $g/u$  symmetry ( $7 - 1 (N_{\text{stretch}}) - 1 (N_{\text{res}} = N_{\text{bend}}) - 1 (\ell = 0) - 1 (g/u) = 3$ ). Similarly, the internal coordinate path treatment of the vibrational level structure reduces the *ab initio* potential energy surface to one dimension.

The agreement between the frequencies calculated from the one-dimensional *ab initio* model and the experimentally determined effective Hamiltonian model is generally good ( $< 20 \text{ cm}^{-1}$ ) in the region where the local-bender is believed to be an accurate description of the lowest members of each polyad (Figure 3-3). For the purpose of comparison with the one-dimensional calculations, the frequency of the local bending vibration was determined from the polyad model by calculating the energy difference between the lowest members of successive *gerade* pure-bending polyads with even values of  $N_{\text{bend}}$ ,  $0_g^+$  and dividing by two. Near 18 quanta of  $N_{\text{bend}}$ , the frequencies calculated from the polyad model and those calculated from the one-dimensional cut through an *ab initio* potential pass through each other. The close match between the vibrational frequencies supports the assertion that both models describe the same class of essentially one-dimensional large-amplitude motion. This agreement is particularly notable since the two calculations arise from drastic reductions in dimension of two very different (empirical vs. *ab initio*) Hamiltonians.

As anticipated from knowledge of the evolution of the vibrational character, the agreement between the two Hamiltonians occurs over a limited range. Below  $N_{\text{bend}} = 10$ , the disagreement between the two models reaches  $50 \text{ cm}^{-1}$ , which is not surprising because the lowest members of the pure-bending polyads are well-described in the normal mode rather than the local mode basis. Above 22 quanta of local bending, the *ab initio* frequency decreases rapidly, to values below  $600 \text{ cm}^{-1}$ , as the bending vibration starts to sample the barrier to isomerization (by tunneling through this barrier), and the approximately stationary hydrogen abruptly starts to migrate off axis to its vinylidene position. This behavior is not captured by the polyad model (because there is nothing barrier-related in the spectroscopic  $\mathbf{H}_{\text{eff}}$ ), in which the vibrational frequency continues to decrease at a relatively constant rate.

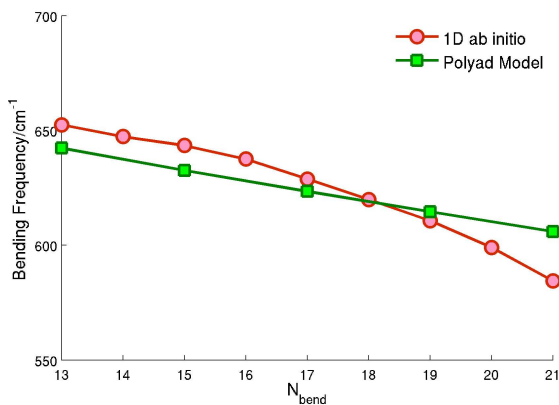


Figure 3-3: Experimentally derived polyad frequencies for a local CCH bending motion compared with one-dimensional *ab initio* calculations. The frequencies obtained from the polyad model and the *ab initio* calculations intersect near 18 quanta of  $N_{\text{bend}}$ . Adam H. Steeves is acknowledged for providing the polyad frequencies.

### 3.7 Evolution of the Dipole Moment

The *ab initio* vibrationally averaged dipole moments associated with the local stretching mode increase approximately linearly and start to decrease near the 11th vibrational state (Figure 3-4 (a)). This trend can be associated with the increasing polarization of the C–H bond as internuclear distance increases. However, as the C–H bond is stretched, the polarization must reach a maximum (cf. Figure 3-2 (b)), and at large internuclear distances the C–H bond must begin to break, leading to more neutral electron distributions for the H atom and HCC fragment ( $\mu = -0.751$  D at the MR-AQCC/aug-cc-pVQZ level of theory). Since the one-dimensional calculations do not preserve *g/u* symmetry and are not eigenfunctions of the inversion operator, the vibrationally averaged dipole moment corresponding to the zero-point vibration is nonzero. As discussed in Section 3.1, the definite *g/u* symmetry of every rovibrational level maintains that the dipole moment of any eigenstate must be zero. In order to make meaningful comparisons to experimental data and other models, vibrationally averaged dipole moments are reported relative to the lowest vibrational quantum state; i.e., the average dipole moments are bounded from below by zero. The present calculations may be compared with the experimental value from Barnes et al. [58] of 0.0696(12) for the dipole matrix element between the  $|04+\rangle$  and  $|04-\rangle$

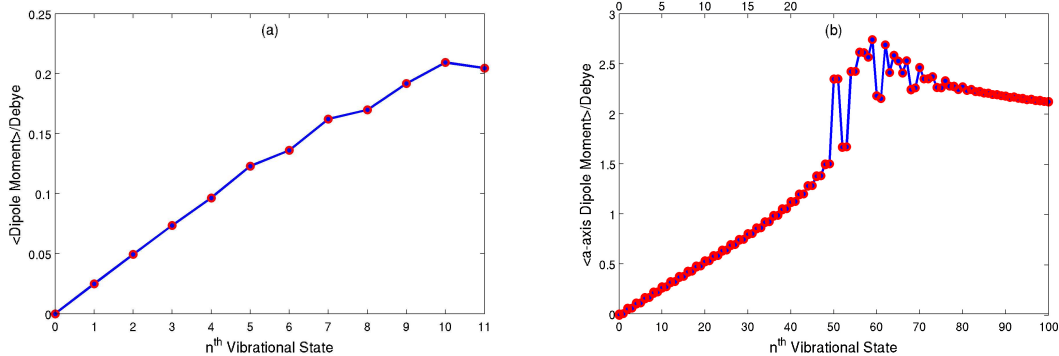


Figure 3-4: Vibrationally averaged *ab initio* dipole moments computed (a) for a local C–H stretch and (b) for a local bend. Since the *b*-axis dipole moment for the local bend is antisymmetric with respect to the equilibrium bend angle, its vibrational average is exactly zero, and only the vibrational average for the *a*-axis dipole is displayed. The bottom axis of Figure 3-4 (b) is numbered according to the vibrational level in the fully permutational symmetric isomerization path, and the top axis labels only the symmetric vibrational levels. Both averaged dipole moments are reported relative to the lowest vibrational quantum state.

local mode stretching states. The calculated value of 0.0966 D is quite reasonable for the one-dimensional model. Some of this discrepancy is due to the fact that the acetylene stretching system, at this level of excitation, is in the intermediate case between the pure normal and pure local mode limits [52]. Experimental evidence that the local mode limit has not been reached is provided by the non-zero difference in vibrational excitation energies between the *g* and *u* states. The difference in energies has been measured to be  $4.133(16) \text{ cm}^{-1}$ . The one-dimensional model will only apply to the pure local mode limit, while excitation of the other C–H bond oscillator must lead to a partial cancellation of the dipole due to its large-amplitude motion. The experimental value embodies this partial cancellation, while the one-dimensional model does not.

Figure 3-4 (b) shows the vibrationally averaged dipole moments for the full permutationally symmetric isomerization path with respect to the interchange of the two H atoms. The bottom axis of Figure 3-4 (b) is numbered according to the vibrational quantum numbers in this symmetric  $\text{H}_a\text{C}_b\text{C}_c\text{H}_d \rightleftharpoons \text{H}_d\text{C}_b\text{C}_c\text{H}_a$  double-well potential. Because of this symmetry, the lowest average dipole moments come in pairs corresponding to nuclear permutational splittings between symmetric and anti-

symmetric vibrational states. Throughout this chapter the numbering scheme at the top axis of Figure 3-4 (b) is used in which only the symmetric vibrational states in the one-dimensional bending model are labeled. It can be seen that the vibrationally averaged dipole moments obey a nearly linear trend up to 22 quanta of vibrational excitation, increasing approximately 0.053 D per quantum of excitation (the slope was determined using a least squares method on the lowest 10 data points). As in the case of the C–H stretching, the calculated value overestimates the value available from experiment. The value of the slope obtained from the relatively low energy excited states of acetylene-*d* by Matsumura et al. [61], 0.046 D is, in a manner similar to that of the C–H stretching modes, not reflective of the pure CCH bending motion. Examination of the normal mode eigenvectors, obtained from an **FG** matrix analysis based on the force constants of Strey and Mills [77], reveals that significant CCD bending motion occurs in the nominally CCH bending mode,  $\nu_5$ . The calculated dipole moment variation, in the linear region, is qualitatively due to the diminishing projection of the C–H bond dipole on the C–C bond axis, leading to an imbalance of the bond dipoles of the two C–H fragments. In the same energy region where the vibrational frequency begins to decrease rapidly, the dipole moment increases more quickly due to increased sampling of the isomerization barrier (3.33 D) and mixing with the vinylidene configuration (2.35 D).

The  $v = 25$  excited vibrational level identified in the calculation clearly deviates from the smooth linear trend of the lower-lying states. This level is associated with the zero-point level of  $S_0$  vinylidene. Near the  $v = 25$  vibrational level, the averaged dipole moments begin to change abruptly since the vibrational wavefunction begins to sample both the acetylene and vinylidene minima. Above this energy, the dipole moment oscillates between acetylene-localized states and values more typical of the isomerization transition state before approaching a constant value of 2.0 D at high local excitation.

## 3.8 Assignment of Large-Amplitude Local Bender States

The analysis and text in this section are due to Adam H. Steeves and were excerpted from Ref. [10].

Although the extreme local bender levels have been the primary focus of this chapter, those that lie at the bottom of each pure-bending polyad, it is important to note that the other members of pure-bending polyads can be described in the local mode basis. Examination of the eigenfunctions obtained from the polyad model reveals a transition at approximately 14 quanta of bending vibration, at which point the lowest member of each pure-bending polyad is best described by a local CCH bending motion [48]. This qualitative change in vibrational character is accompanied by a decreasing energy difference between the lowest members of the  $0_g^+$  and  $0_u^+$  polyads. At  $N_{\text{bend}} = 10$ , this energy difference is  $> 10 \text{ cm}^{-1}$ , but it rapidly decreases to  $< 10^{-3} \text{ cm}^{-1}$  by  $N_{\text{bend}} = 14$ , and  $< 10^{-7} \text{ cm}^{-1}$  by  $N_{\text{bend}} = 22$ . In Table 3.1 (a)–(c) the energy splittings between the lowest members of the  $g+$  and  $u+$  polyads are compared for  $N_{\text{bend}} = 14 - 26$ . These lowest extreme local bender levels form a local mode pair, and the transition dipole that couples them can be viewed as a permanent vibrational dipole moment, as in the case of the acetylene C–H stretching levels discussed in Section 3.7.

The ability to equate the one-dimensional calculation of the dipole moment with the dipole created by imbalance in excitation of oscillators can be used for other predictions. It enables the assignment of dipole moments to any basis state in the local mode limit and therefore allows the calculation of the dipole moment for each eigenstate based on the eigenvectors in the local mode basis. Predictions of the dipole moments for the three lowest energy eigenstates of the  $N_{\text{bend}} = 14 - 26$  polyads are found in Table 3.1 (a)–(c). Predictions are made in the same manner as for the stretching case by neglecting the vibrational angular momentum, i.e.  $\mu(|14^2, 2^{-2}\rangle_{\mathcal{L}}) = \mu(|14^0, 2^0\rangle_{\mathcal{L}})$ . These lowest eigenstates are assigned to the local mode states as  $|N_{\text{bend}}^0, 0^0\rangle_{\mathcal{L}}^{g+}$ ,  $|(N_{\text{bend}} - 1)^1, 1^{-1}\rangle_{\mathcal{L}}^{g+}$ , and  $|(N_{\text{bend}} - 2)^0, 2^0\rangle_{\mathcal{L}}^{g+}$  respec-

$N_{\text{bend}}$	$E \left(  N_{\text{bend}}^0, 0^0 \rangle_{\mathcal{L}}^{g+} \right)$	$E(g+) - E(u+)$	$\mu$ (D)
14	8972.1	$-1 \times 10^{-4}$	0.85
16	10236.9	$-3 \times 10^{-5}$	1.02
18	11485.0	$-4 \times 10^{-6}$	1.20
20	12717.4	$-4 \times 10^{-7}$	1.36
22	13934.9	$-4 \times 10^{-8}$	1.55
24	15137.9	$-1 \times 10^{-9}$	1.77
26	16327.1	$3 \times 10^{-10}$	2.28

$N_{\text{bend}}$	$E \left(  (N_{\text{bend}} - 1)^1, 1^{-1} \rangle_{\mathcal{L}}^{g+} \right)$	$E(g+) - E(u+)$	$\mu$ (D)
14	9070.0*	-9	—
16	10352.4*	$-4 \times 10^{-2}$	—
18	11605.7	$6 \times 10^{-5}$	1.01
20	12844.8	$7 \times 10^{-5}$	1.18
22	14070.2	$8 \times 10^{-6}$	1.36
24	15289.9	$3 \times 10^{-7}$	1.54
26	16480.1	$-8 \times 10^{-8}$	1.76

$N_{\text{bend}}$	$E \left(  (N_{\text{bend}} - 2)^0, 2^0 \rangle_{\mathcal{L}}^{g+} \right)$	$E(g+) - E(u+)$	$\mu$ (D)
14	9037.0*	$-4 \times 10^{-2}$	—
16	10315.6	$3 \times 10^{-3}$	0.78
18	11574.7	$2 \times 10^{-4}$	0.93
20	12815.7	$-8 \times 10^{-6}$	1.07
22	14040.2	$-2 \times 10^{-6}$	1.20
24	15249.3	$-1 \times 10^{-7}$	1.39
26	16443.9	$1 \times 10^{-8}$	1.54

Table 3.1: (a)–(c): Energy splittings between lowest members of the  $g+$  and  $u+$  polyads and calculated dipole moments for  $N_{\text{bend}} = 14 - 26$ . All energies and energy differences reported are in units of  $\text{cm}^{-1}$ . Energies denoted by an asterisk are not well-described in the local mode basis using the Hose-Taylor criterion. The increase in dipole moment is accompanied by decreasing energy differences between the  $g+$  and  $u+$  polyads. Adam H. Steeves is acknowledged for preparing this table.



tively, although only the lowest energy state in the  $N_{\text{bend}} = 14$  polyad can be assigned based on the Hose-Taylor criterion [78]. As one moves towards the center of each polyad, the local mode model describes each eigenstate less well. That is, the eigenstates contain larger contributions from several local mode basis states, including those with smaller differences in excitation between the two oscillators. This trend causes the dipole moment to decrease faster than linearly inside a given polyad, although at high excitation ( $N_{\text{bend}} \sim 22$ ) all of the listed states are described well by the local mode basis.

The shape of the  $a$ -axis dipole moment function strongly resembles that of the potential energy surface. The maximum value of the  $a$ -axis dipole is reached near the transition state of the isomerization reaction, before the approximately stationary hydrogen begins to move off axis to form vinylidene. The near transition state configuration represents the largest distortion of the electronic wavefunction. This is ideal for performing high-resolution experiments because the larger dipole moments are more readily observable via laser Stark spectroscopy. Even more useful is the ability to identify particular vibrational levels based on the predictions of variation in electronic structure. While electronic signatures of only two one-dimensional motions have been described, vibrational states that do not consist of these special motions are expected to be highly dynamically mixed. The ergodic nature of the highly mixed vibrational levels imply that they will remain essentially silent to Stark effect measurements, except in the case of accidental near degeneracies. The large-amplitude states will be the only states with significant, regular Stark activity.

In addition, the dipole moments will help assign members of the  $|N_{\text{bend}}, 0\rangle_{\mathcal{L}}^{g/u\pm}$ ,  $|N_{\text{bend}} - 1, 1\rangle_{\mathcal{L}}^{g/u\pm}$ ,  $|N_{\text{bend}} - 2, 2\rangle_{\mathcal{L}}^{g/u\pm}$ , etc. family of states. This information is essential because once the energies of such assigned states are obtained from spectra, the one-dimensional local mode potential can be experimentally refined. The relative energies of the  $\left\{ |N_{\text{bend}}, 0\rangle_{\mathcal{L}}^{g/u\pm}, |N_{\text{bend}} - 1, 1\rangle_{\mathcal{L}}^{g/u\pm}, |N_{\text{bend}} - 2, 2\rangle_{\mathcal{L}}^{g/u\pm} \right\}$  and  $\left\{ |N_{\text{bend}} + 1, 0\rangle_{\mathcal{L}}^{g/u\pm}, |N_{\text{bend}}, 1\rangle_{\mathcal{L}}^{g/u\pm}, |N_{\text{bend}} - 1, 2\rangle_{\mathcal{L}}^{g/u\pm} \right\}$  etc. groups of local mode states, supplemented by measured dipole moments, provide direct experimental characterization of the reaction coordinate near the barrier maximum.

## 3.9 Conclusions

A one-dimensional reduction of the full seven-dimensional *ab initio*  $S_0$  potential energy surface of  $C_2H_2$  was explored, and it was found that it strongly resembles the one-dimensional, local bending reduction of the empirical spectroscopic pure-bend effective Hamiltonian. These reductions in dimension occur when the large-amplitude motion decouples from the other nuclear motions as a result of anharmonic detuning from resonance. A comparison between the computed frequencies of the one-dimensional *ab initio* potential and those of the spectroscopic effective Hamiltonian, the parameters of which are refined against experimental data, exhibits good agreement for the local bending motion. The results of Section 3.6 strongly indicate reduction of both *ab initio* and spectroscopic Hamiltonians to the same one-dimensional potential even though the two Hamiltonians are derived from completely different formalisms. This is particularly noteworthy since the spectroscopic effective Hamiltonian does not explicitly specify the displacement coordinates of the stable, one-dimensional, localized, motion, but this one-dimensional path is explicitly defined in the reaction path Hamiltonian. More importantly, the large-amplitude local vibrations which lead to changes in the electronic properties of acetylene, permits a transition dipole between the two nearly degenerate  $g/u$  eigenstates associated with the local mode. This near-degeneracy of the local mode pair, which indicates that the  $g/u$  symmetry is ready to be broken, is a hallmark of local mode behavior. The large changes in dipole moments along the local bending coordinate provide a method to identify particular vibrational levels via the Stark effect. The dipole moment values computed from the *ab initio* one-dimensional potential will be useful in distinguishing extreme local mode states from the vastly more strongly mixed isoenergetic states.

# Chapter 4

## The Hyperfine Structure of HCN and HNC

This chapter describes ongoing work pertaining to the nuclear quadrupole hyperfine structures of HCN, HNC, and their isotopomers. The majority of the work in this chapter resulted from a collaboration with Dr. Hans A. Bechtel.

### 4.1 Introduction

Similar to the acetylene  $\rightleftharpoons$  vinylidene system described in Chapter 3, the primary objective for studying the HCN  $\rightleftharpoons$  HNC isomerization is to observe vibrational states proximal to a barrier maximum. These highly excited vibrational states have amplitude localized along the minimum energy isomerization path and therefore reveal features of the potential energy surface that control intramolecular dynamics. As in the acetylene  $\rightleftharpoons$  vinylidene isomerization, the magnitude of the electric dipole moment is also an effective diagnostic for identifying delocalized states between the HCN and HNC regions of the potential. Indeed, Bowman et al. [62] have already performed three dimensional *ab initio* calculations on the dipole moment and showed that isomerizing vibrational states possess significantly smaller dipole moments than localized HCN or HNC states. Figure 4-1 depicts the electric dipole moment along an optimized HCN  $\rightleftharpoons$  HNC isomerization path. At the endpoints of this path, the

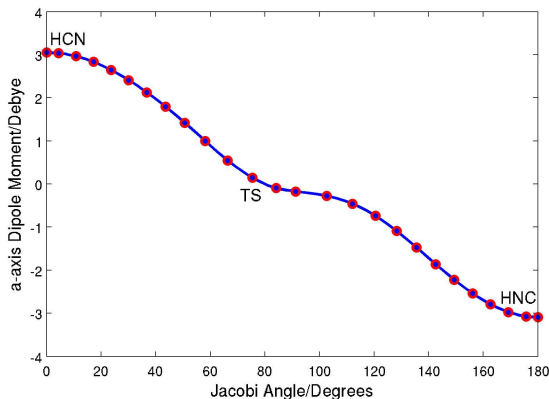


Figure 4-1: Dipole moment as a function of the Jacobi angle (defined in Figure 4-3) along an isomerization path from HCN ( $0^\circ$ ) to HNC ( $180^\circ$ ). Dipole moments were calculated at the CCSD(full) level with the aug-cc-pCVTZ basis.

HCN and HNC dipoles are nearly equal in magnitude but opposite in sign, with the dipole moment function changing sign near the transition state. Since delocalized isomerization states sample both HCN and HNC configurations, their vibrationally averaged dipoles are nearly zero. Consequently, Stark effect measurements of dipole moments in vibrationally excited states are direct experimental observables related to the extent of delocalization.

Another electronic property useful in identifying isomerization states is nuclear quadrupole hyperfine interactions. Hyperfine structure originates from the nuclear quadrupole moment of a (spherically asymmetric) nucleus interacting with the electric field gradient due to the electronic wavefunction. For both HCN and HNC, only the  $^{14}\text{N}$  nitrogen nucleus possesses a nuclear quadrupole moment, and the nuclear quadrupole coupling constants are highly sensitive to which isomer is measured. Qualitatively, the change in nuclear quadrupole hyperfine structure for HCN/HNC is due to variations in the distances and angles between atoms bonded with the  $^{14}\text{N}$  nucleus. Consequently, hyperfine structure measurements provide another probe to identify the onset of delocalization.

In this chapter, the results of recent and new *ab initio* nuclear quadrupole hyperfine calculations are presented to complement the current experimental data on the  $\text{HCN} \rightleftharpoons \text{HNC}$  system. The following section begins with a brief description of

nuclear quadrupole structure, and the subsequent sections provide a detailed account of the computational steps involved in obtaining the current results. Comparisons to available experimental data are provided throughout, and preliminary hyperfine calculations applied to the isotopically substituted species DC<sup>15</sup>N and D<sup>15</sup>NC are also presented.

## 4.2 Quadrupole Coupling Constants of Nuclei

In a molecule, the electric field gradient  $\mathbf{q}_J$  at the site of a nucleus  $J$  is given by the second derivatives of the potential  $V$  with respect to the Cartesian coordinates. Accordingly,  $\mathbf{q}_J$  is a symmetric second rank tensor with Cartesian components  $q_{xx,J} = \partial^2 V / \partial x^2$ ,  $q_{xy,J} = \partial^2 V / \partial x \partial y$ , etc. Given the electronic wavefunction,  $\psi$ , the electric field gradient component at a particular nucleus  $J$ ,  $q_{xy,J}$ , is given by a sum of nuclear and electronic terms [79]:

$$\begin{aligned} q_{xy,J} &= q_{xy,J}^{\text{nucl}} + q_{xy,J}^{\text{elec}} \\ &= e \sum_{I \neq J} \frac{Z_I (3x_{IJ}y_{IJ} - r_{IJ}^2)}{r_{IJ}^5} - e \langle \psi | \sum_i \frac{3x_{iJ}y_{iJ} - r_{iJ}^2}{r_{iJ}^5} | \psi \rangle \end{aligned} \quad (4.1)$$

where  $e$  is the charge of an electron,  $Z_I$  is the charge on nucleus  $I$ , and  $i$  labels the electrons. The first term adds a positive contribution from all the other nuclei in the molecule, and the second term is the negative contribution from the electrons  $i$ . The coordinate system in which the Cartesian form of the tensor is diagonal is called the principal axis system. From Eq. (4.1), the Cartesian tensor is traceless ( $q_{xx} + q_{yy} + q_{zz} = 0$ ), and therefore, only two components are independent in the principal axis system. These two independent components are conventionally taken to be  $q_{zz}$  and the asymmetry parameter,  $\eta = (q_{xx} - q_{yy}) / q_{zz}$  [79]. The principal component,  $q_{zz}$ , follows from simplification of Eq. (4.1):

$$\begin{aligned}
q_{zz,J} &= e \sum_{I \neq J} \frac{Z_I (3z_{IJ}^2 - r_{IJ}^2)}{r_{IJ}^5} - e \langle \psi | \sum_i \frac{3z_{iJ}^2 - r_{iJ}^2}{r_{iJ}^5} | \psi \rangle \\
&= e \sum_{I \neq J} \frac{Z_I (3 \cos^2 \theta_I - 1)}{r_{IJ}^3} - e \langle \psi | \sum_i \frac{3 \cos^2 \theta_i - 1}{r_{iJ}^3} | \psi \rangle
\end{aligned} \tag{4.2}$$

where  $\theta_I$  and  $\theta_i$  are the angles between the  $z$  axis and nucleus  $I$  and electron  $i$ , respectively.

The quantity determined from experimental data is the nuclear quadrupole coupling constant  $\chi_{zz}$ , which is usually measured in units of MHz and directly proportional to  $q_{zz}$ :

$$\chi_{zz} = eQq_{zz}/h \tag{4.3}$$

where  $e$  is the charge of an electron,  $h$  is Planck's constant, and  $Q$  is the scalar quadrupole moment of the nucleus. The nuclear electric quadrupole moment is usually defined as [80, 81, 82]:

$$Q = \iiint \rho r^2 (3 \cos^2 \theta - 1) d\tau \tag{4.4}$$

where  $\rho$  is the (positive) nuclear charge density, and the integral is taken over the volume of the nucleus. The coordinate system is such that the origin is at the center of mass of the nucleus and the  $z$  axis ( $\theta$  is the angle between  $r$  and this axis) is taken along the spin axis of the nucleus. The nuclear quadrupole moment qualitatively describes the spheroidal shape of positive nuclear charge, and only nuclei with spin  $I \geq 1$  have nonzero nuclear electric quadrupole moments. The magnitude and sign of the nuclear quadrupole moment indicates the shape of the atomic nucleus. For example, a zero value of  $eQ$  indicates a spherically symmetric charge distribution and no quadrupole moment (Figure 4-2 (a)). A positive sign indicates that the asymmetric distribution of protons is such that there is an elongation along the body  $z$  axis, and a prolate spheroid results (Figure 4-2 (b)). Finally if the asymmetric distribution of protons is such that a flattening of the nucleus along the  $x$  and  $y$  axes occurs, an oblate spheroid is produced (Figure 4-2 (c)). Since the nuclear quadrupole coupling

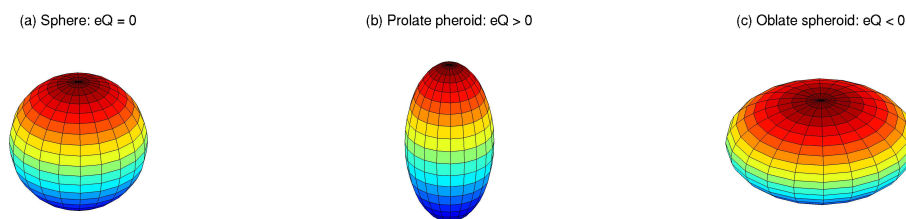


Figure 4-2: (a)–(c) Nuclear shapes and nuclear electric quadrupole moments.

constant,  $\chi$ , is directly related to the asphericity of the electronic density at the probe nucleus, the prediction of  $\chi$  allows an estimation of the  $p\pi$  and  $p\sigma$  bonding within the molecule.

### 4.3 Application to the $\text{HCN} \rightleftharpoons \text{HNC}$ Isomerization System

From the second term in Eq. (4.2), the calculation of nuclear quadrupole coupling constants involves an expectation value of the electric field gradient at the nucleus. Due to the dependence on the electronic environment close to the nucleus of interest, an accurate calculation of quadrupole coupling constants puts strict demands on the basis set and, to a lesser degree, the level of electron correlation. Unlike the *ab initio* calculations for acetylene described in Chapter 3, the correlation consistent basis sets of Dunning and coworkers [38] are not suited for accurate calculations of quadrupole coupling constants. As it is the region close to the nucleus of interest that needs to be accurately described, the use of large core-valence basis sets is necessary. Furthermore, the inclusion of diffuse functions in the basis set is essential to correctly calculate the dependence of the nuclear quadrupole couplings on large changes in geometry, such as a hydrogen atom migration.

For the  $\text{HCN} \rightleftharpoons \text{HNC}$  isomerization, all electric field gradients at the  $^{14}\text{N}$  nucleus were obtained from analytical gradient expressions at the CCSD(full) level with all the core orbitals correlated (analytical evaluation of CCSD(T) electric field gradients is presently not available). All geometry optimizations and electric field gradients

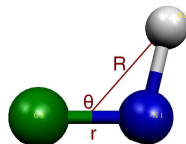


Figure 4-3: Jacobi coordinates for the HNC molecule.

utilized the augmented core-valence triple zeta basis set (aug-cc-pCVTZ) for the C and N atoms, and a normal aug-cc-pVTZ basis set for the H atom was used. The use of core-valence functions provided a significant improvement on the  $(eQq)_N$  couplings for HCN and particularly for the HNC minimum (0.2229 MHz with aug-cc-pVTZ vs. 0.3366 MHz with aug-cc-pCVTZ). The one-dimensional  $\text{HCN} \rightleftharpoons \text{HNC}$  quadrupole coupling constants were calculated by choosing a grid of 24 values of the Jacobi angles between the HCN ( $\theta = 0$ ) and HNC ( $\theta = \pi$ ) isomers and optimizing all other internal coordinates to minimize the total energy. The Jacobi coordinates used in the present work are shown in Figure 4-3, where  $R$  is the distance of the H atom from the center of mass of the CN fragment,  $r$  is the C-N distance, and  $\theta$  is the angle between the two Jacobi vectors  $R$  and  $r$ .

Figure 4-4 shows the principal component of the quadrupole coupling constant tensor,  $(eQq)_N$ , along the optimized isomerization path from HCN to HNC. For HCN, the (not vibrationally averaged) quadrupole coupling constant is large and negative,  $(eQq)_N = -4.72$  MHz, whereas for HNC, it is small and positive  $(eQq)_N = 0.34$  MHz. The most recent *ab initio* calculations by Pd and Chandra [83] on HNC also predict a small nuclear quadrupole coupling constant,  $-313 \text{ kHz} \geq (eQq)_N \geq -288 \text{ kHz}$ , but of the wrong sign. Unlike the dipole moment,  $\mu$ , where the experimental observable is the magnitude,  $|\mu|$ , and not its sign ( $|\mu| \sim 3$  Debye for both HCN and HNC), a hyperfine splitting measurement can determine in which potential well the vibrational wavefunction is localized.

The hyperfine structures of  $\text{DC}^{15}\text{N}$  and  $\text{D}^{15}\text{NC}$ , on the other hand, are slightly more complicated. In these deuterated isotopomers, only the deuteron has a quadrupole moment ( $I_D = 1$ ) while both the  $^{15}\text{N}$  and  $^{12}\text{C}$  nuclei do not ( $I_{^{15}\text{N}} = I_{^{12}\text{C}} = 1/2$ ). Figure



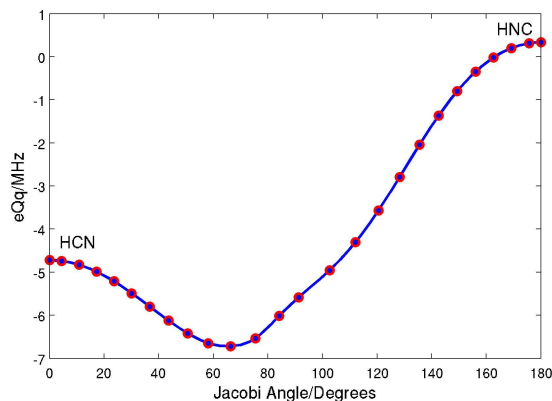


Figure 4-4: Dependence of the nuclear quadrupole coupling constant  $(eQq)_N$  on a relaxed  $\text{HCN} \rightleftharpoons \text{HNC}$  isomerization path.

4-5 shows the quadrupole coupling constant  $(eQq)_D$  along the relaxed isomerization path from  $\text{DC}^{15}\text{N}$  to  $\text{D}^{15}\text{NC}$ . In contrast to the  $\text{HCN} \rightleftharpoons \text{HNC}$  isomerization, the quadrupole coupling constants for both  $\text{DC}^{15}\text{N}$  and  $\text{D}^{15}\text{NC}$  are small, positive, and nearly equal:  $(eQq)_{\text{DC}^{15}\text{N}} = 0.22$  MHz and  $(eQq)_{\text{D}^{15}\text{NC}} = 0.29$  MHz. Figure 4-5 also shows the quadrupole coupling constant,  $(eQq)_D$ , possesses a local maximum in the vicinity of the isomerization transition state. The striking differences between Figures 4-4 and 4-5 can be explained in terms of the chemical environment experienced by the quadrupolar nucleus. The quadrupole coupling,  $eQq$ , reflects the anisotropy of the molecular electric field at the position of the probe nucleus. Therefore, if the nucleus is located in a highly symmetric chemical environment, the electric field gradient is small. Near the transition state, the deuterium is positioned close to the center of the  $\text{C}^{15}\text{N}$  bond and experiences a fairly symmetrical field (the electronegativities of both C and N are fairly equal), and the electric field gradient is nearly zero as shown in Figure 4-5. Consequently, a plot of  $(eQq)_D$  as a function of Jacobi angle is nearly symmetrical about the transition state point. In contrast, the  $^{14}\text{N}$  probe nucleus in the  $\text{HCN} \rightleftharpoons \text{HNC}$  system is bound to two atoms when the molecule is only localized in the HNC well; when the isomerization is localized in the HCN well, the  $^{14}\text{N}$  nucleus is found on the periphery of the molecule where the molecular fields are highly anisotropic and field gradients are large ( $(eQq)_N = -4.72$  MHz).

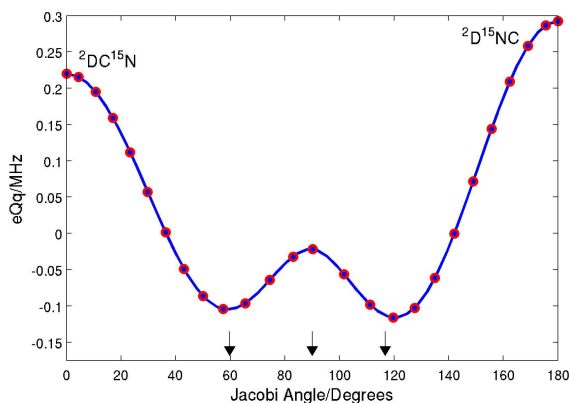


Figure 4-5: Dependence of the nuclear quadrupole coupling constant ( $eQq$ )<sub>D</sub> on a relaxed  $DC^{15}N \rightleftharpoons D^{15}NC$  isomerization path. The arrows along the horizontal axis indicate molecular geometries where (1) the D atom is directly over the C atom ( $\theta = 60^\circ$ ), (2) the D atom is over the C–N midpoint ( $\theta = 90^\circ$ ), and (3) the D atom is directly over the N atom ( $\theta = 117^\circ$ ).

## 4.4 Results for HCN and HNC

In order to make meaningful comparisons with experimental data, the ( $eQq$ )<sub>N</sub> constants in Figure 4-4 must be averaged over vibrational wavefunctions obtained from a reasonable potential. Accordingly, CCSD(T) calculations of single-point energies were performed with the aug-cc-pVQZ basis set at the CCSD(full) optimized geometries described in Section 4.3. Since the aug-cc-pVQZ basis set does not allow for a full description of core correlation effects, all of the CCSD(T) single-point energies presented in this section have all of the core orbitals frozen. At the CCSD(T) level of theory, the relative energy of the HNC isomer calculated with respect to the HCN isomer is  $5,168 \text{ cm}^{-1}$ , and the barrier height is  $16,648 \text{ cm}^{-1}$ . The  $HCN \rightleftharpoons HNC$  isomerization potential relative to the HCN global minimum is shown in Figure 4-6 (a), and the corresponding molecular geometries are shown in Figure 4-6 (b). Motion on the one-dimensional  $HCN \rightleftharpoons HNC$  potential surface is relatively simple – after the transition state (labeled “2”) is traversed, the hydrogen atom moves in a smaller circle due to the slightly more electronegative nitrogen nucleus.

Like the acetylene  $\rightleftharpoons$  vinylidene system described in Chapter 3, the  $HCN \rightleftharpoons HNC$  isomerization involves a periodic potential. Therefore, the complete periodic

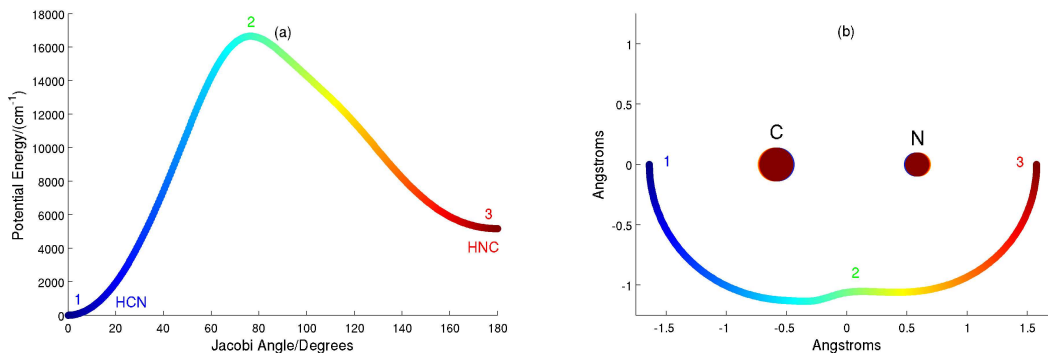


Figure 4-6: (a) One-dimensional relaxed potential for the  $\text{HCN} \rightleftharpoons \text{HNC}$  isomerization as a function of the Jacobi angle. The transition state structure is labeled by the number 2, and HCN/HNC minima are denoted by numbers 1 and 3, respectively. (b) Spatial positions of the the HCN/HNC atoms color-coded to match their corresponding location on the one-dimensional potential.

isomerization path can be constructed with only the information about the path from HCN to HNC by using permutation group operations in a local frame. Each resulting geometry was translated to a center of mass frame, and all Cartesian components as a function of the Jacobi angle were fit to a Fourier series. Finite differences were then used on the fitted geometries to align the molecule along an Eckart frame as described in Chapter 2. Finally, the kinetic energy, potential energy, and quadrupole moment matrix elements were obtained from their Fourier series expansion coefficients using Eqs. (3.10) and (3.11), and the one-dimensional Hamiltonian in Eq. (3.6) was diagonalized in a basis of complex exponentials. The lowest 50 eigenenergies obtained from this procedure are presented in Figure 4-7 (a) superimposed on the  $\text{HCN} \rightleftharpoons \text{HNC}$  isomerization potential. The green lines indicate vibrational wavefunctions which are localized in the HCN potential well, and the red lines represent wavefunctions localized in the HNC well. Assignments were based on the expectation values of the Jacobi angle until this metric became useless at energies far above the transition state.

Figure 4-7 (b) shows the variation of the 50 lowest vibrationally averaged  $\langle eQq \rangle_N$  coupling constants,  $\langle (eQq)_N \rangle$ , color-coded to match their HCN (green)/HNC (red) energy levels in Figure 4-7 (a). For  $n < 9$ ,  $\langle (eQq)_N \rangle$  varies linearly since the vibrational wavefunction is localized in the HCN global minimum. After the HCN bending energy exceeds  $5,168 \text{ cm}^{-1}$  ( $9 < n < 50$ ),  $\langle (eQq)_N \rangle$  varies rapidly between two limits

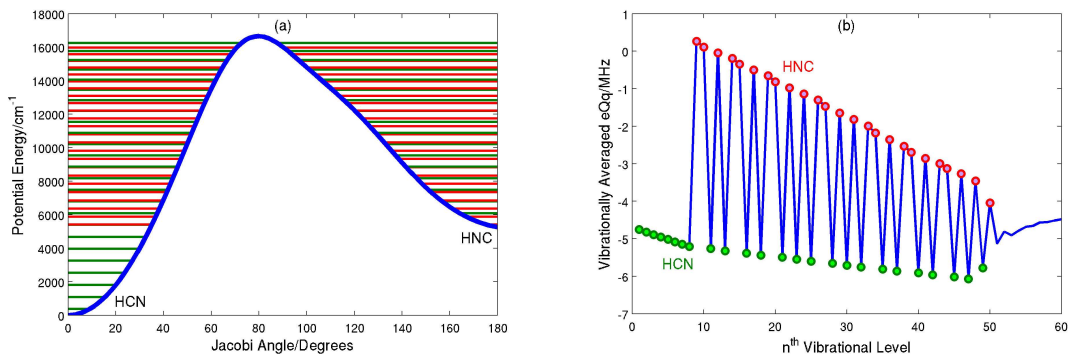


Figure 4-7: (a) The 50 lowest vibrational eigenvalues for the  $\text{HCN} \rightleftharpoons \text{HNC}$  potential obtained at the CCSD(T)/aug-cc-pVQZ level of theory. Each of the eigenvalues is associated with either HCN (green-colored) or HNC (red-colored) localization. (b) Vibrationally averaged nuclear quadrupole coupling constants for the lowest 50 vibrational states of HCN (green)/HNC (red) energy.

since the vibrational wavefunction alternates its localization between the local HNC minimum and the global HCN minimum. Once the bending energy surpasses  $16,648 \text{ cm}^{-1}$  ( $n > 50$ ), the hydrogen migration becomes nearly a free rotation and  $\langle (eQq)_N \rangle$  is approximately constant with a limiting value of approximately  $-4.5 \text{ MHz}$ . Figure 4-8 and Table 4.1 compare bending frequencies between the one-dimensional *ab initio* model and the experimentally determined ( $l = 0$ ) frequencies for both HCN and HNC [84, 85]. Only the experimental frequencies for even quanta in the bend are presented since vibrations with odd quanta are currently not available. The agreement between the frequencies is good, and both the HCN and HNC data obey a linear trend with  $710.8 \text{ cm}^{-1}/(\text{HCN bend quantum})$  and  $492.1 \text{ cm}^{-1}/(\text{HNC bend quantum})$  respectively (the experimental data gives smaller slopes of  $685.6 \text{ cm}^{-1}/(\text{HCN bend quantum})$  and  $468.4 \text{ cm}^{-1}/(\text{HNC bend quantum})$ ). Similarly, Figure 4-9 and Table 4.2 present the dependence of the vibrationally averaged  $(eQq)_N$  values as a function of vibrational excitation for both HCN and HNC. Experimental quadrupole coupling constants were taken from both Bechtel et al. [86] and experiments currently in progress. The vibrationally averaged quadrupole coupling constants also obey a nearly linear trend with  $-0.062 \text{ MHz}/(\text{HCN bend quantum})$  and  $-0.157 \text{ MHz}/(\text{HNC bend quantum})$ . These values are in fair agreement with the experimental findings of Bechtel and coworkers who measure coupling constants of  $-0.075 \text{ MHz}/(\text{HCN bend quantum})$  and  $-0.118$

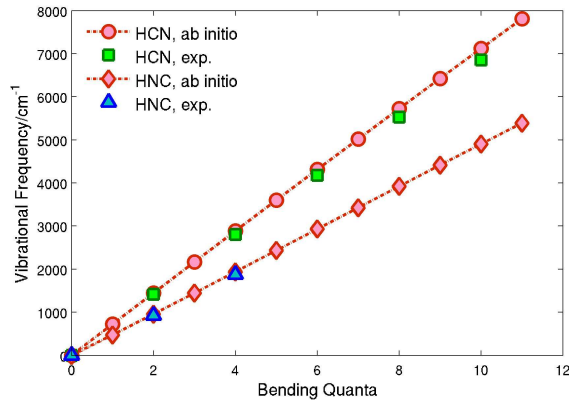


Figure 4-8: Calculated and experimental ( $l = 0$ ) vibrational frequencies for HCN and HNC. The lines were fitted using a least squares method which yields *ab initio* slopes of  $710.8 \text{ cm}^{-1}/(\text{HCN bend quantum})$  and  $492.1 \text{ cm}^{-1}/(\text{HNC bend quantum})$  and experimental slopes of  $685.6 \text{ cm}^{-1}/(\text{HCN bend quantum})$  and  $468.4 \text{ cm}^{-1}/(\text{HNC bend quantum})$ .

Bend Quanta ( $\nu_1, \nu_2, \nu_3$ )	Calculated ( $\text{cm}^{-1}$ )	Experimental ( $\text{cm}^{-1}$ ) [84, 85]
HCN (0,0,0)	0	0
HCN (0,1,0)	724.57	–
HCN (0,2,0)	1447.94	1411.41
HCN (0,3,0)	2168.77	–
HCN (0,4,0)	2886.86	2802.96
HCN (0,5,0)	3602.04	–
HCN (0,6,0)	4313.98	4174.61
HCN (0,7,0)	5022.32	–
HCN (0,8,0)	5726.71	5525.81
HCN (0,9,0)	6426.90	–
HCN (0,10,0)	7122.61	6855.53
<hr/>		
HNC (0,0,0)	0	0
HNC (0,1,0)	473.63	–
HNC (0,2,0)	956.35	926.51
HNC (0,3,0)	1444.99	–
HNC (0,4,0)	1938.04	1873.74

Table 4.1: Calculated and experimental ( $l = 0$ ) vibrational frequencies for HCN and HNC.

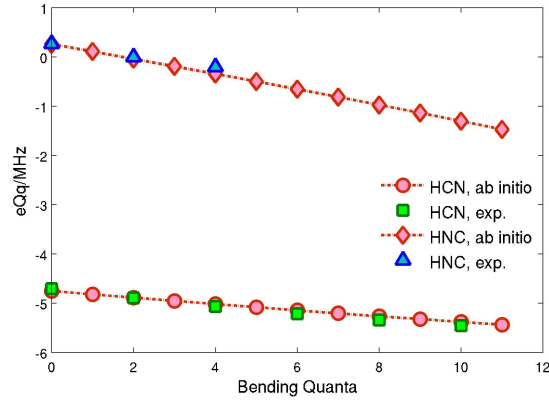


Figure 4-9: Calculated and experimental ( $l = 0$ ) nuclear quadrupole coupling constants for HCN and HNC. The lines were fitted using a least squares method which yields *ab initio* slopes of  $-0.062$  MHz/(HCN bend quantum) and  $-0.157$  MHz/(HNC bend quantum) and experimental slopes of  $-0.075$  MHz/(HCN bend quantum) and  $-0.118$  MHz/(HNC bend quantum). Dr. Hans A. Bechtel is acknowledged for providing the experimental quadrupole coupling constants.

Bend Quanta ( $\nu_1, \nu_2, \nu_3$ )	Calculated (MHz)	Experimental (MHz) [86]
HCN (0,0,0)	-4.7545	-4.7084
HCN (0,1,0)	-4.8223	—
HCN (0,2,0)	-4.8887	-4.8966
HCN (0,3,0)	-4.9543	—
HCN (0,4,0)	-5.0189	-5.0699
HCN (0,5,0)	-5.0822	—
HCN (0,6,0)	-5.1444	-5.2175
HCN (0,7,0)	-5.2054	—
HCN (0,8,0)	-5.2654	-5.3485
HCN (0,9,0)	-5.3242	—
HCN (0,10,0)	-5.3818	-5.4579
HNC (0,0,0)	0.2607	0.2641
HNC (0,1,0)	0.1094	—
HNC (0,2,0)	-0.0418	0.0000
HNC (0,3,0)	-0.1933	—
HNC (0,4,0)	-0.3459	-0.2066

Table 4.2: Calculated and experimental ( $l = 0$ ) nuclear quadrupole coupling constants for HCN and HNC. Dr. Hans A. Bechtel is acknowledged for providing the experimental quadrupole coupling constants.

MHz/(HNC bend quantum). Further studies on higher vibrational states and hyperfine measurements on other isotopomers are currently in progress.

## 4.5 Conclusion

This chapter has demonstrated that the hyperfine structures of HCN and HNC are considerably different and can be used as a sensitive probe for the onset of isomerization. In particular, it was shown that the calculated nuclear quadrupole coupling constants at the CCSD(full) level change significantly, even with minor changes in the geometry. Consequently, comparisons with the available experimental data indicate that it is not sufficient to study only the HCN/HNC minima, and vibrational averaging of the entire isomerization path is necessary.

In addition, to obtain quantitative agreement with experiment, it appears that large core valence basis sets are necessary to describe the electric field gradients at the nuclei of interest. Using these basis sets for the DC<sup>15</sup>N and C<sup>15</sup>NC isotopomers, small coupling constants were calculated, which arise from the nearly symmetrical chemical environment experienced by the deuteron nucleus during the isomerization process. On the other hand, the large <sup>14</sup>N quadrupole coupling constant, in the vicinity of the HCN potential well, makes it an ideal system for millimeter wave spectroscopic studies. Furthermore, the direct comparison between vibrationally averaged  $(eQq)_N$  values with available experimental data demonstrates that the nuclear quadrupole couplings can be adequately predicted by *ab initio* quantum chemical methods. It is clear, however, that it may be necessary to consider the anharmonic couplings to the other modes in order to obtain better estimates of vibrationally averaged quantities.





# Chapter 5

## Valence-Excited States of Triplet Acetylene

This chapter describes a characterization of singlet-triplet interactions relevant to intersystem crossing between  $T_3$ , the third excited triplet state, and  $\tilde{A} \ ^1A_u$ , the first excited singlet state of acetylene. The majority of the work in this chapter resulted from a collaboration with Dr. Ryan L. Thom and Prof. John F. Stanton. A manuscript presenting this work was published as an article in the *Journal of Chemical Physics* [87].

### 5.1 Introduction

The spectroscopic and theoretical characterizations of acetylene in its ground electronic state have been the focus of several years of research [33, 34, 39, 40, 41, 42, 43, 48]. Due to the enormous experimental and theoretical attention it has received, combined with the simplicity of the molecule, acetylene is among the best understood tetra-atomic systems. Despite these numerous studies, relatively little attention has focused on the low-lying triplet excited electronic states of  $C_2H_2$ . As discussed in Chapter 3, acetylene in its ground electronic state ( $\tilde{X} \ ^1\Sigma_g^+$ ) is linear in its equilibrium geometry with an electronic configuration of  $(1\sigma_g)^2 (1\sigma_u)^2 (2\sigma_g)^2 (2\sigma_u)^2 (3\sigma_g)^2 (1\pi_u)^4$ . The lowest valence-excited electronic states result from an excitation to a  $\pi$  anti-

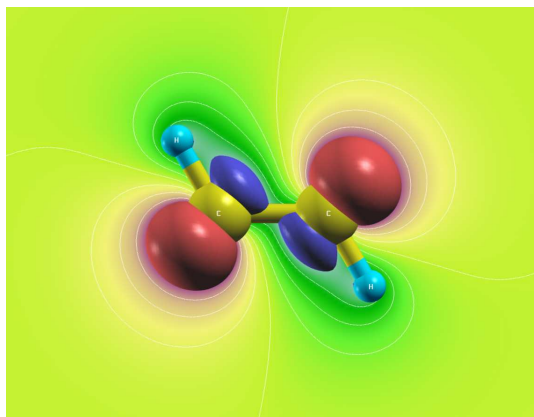


Figure 5-1: Highest occupied molecular orbital for the  $S_1 \ ^1A_u$  *trans* state of acetylene.

bonding orbital within the  $\pi^4 \rightarrow \pi^3\pi^*$  manifold. As a result, these orbital excitations in acetylene are stabilized by having both CCH bond angles bend out of linearity. For example, the first excited singlet state of acetylene ( $\tilde{A} \ ^1A_u$ ) is *trans* bent, and Figure 5-1 depicts the highest occupied molecular orbital for this optimized geometry. Figure 5-2 shows the potential energy surfaces for several low-lying acetylene electronic states, all constrained to planar geometry and plotted as a function of the CCH bend coordinate. From Figure 5-2, the first triplet potential surface ( $T_1$ ) possesses stable minima in both *trans*- and *cis*-bent geometries, denoted by  $^3B_u$  and  $^3B_2$  respectively. The second triplet state ( $T_2$ ) also supports both *trans*- and *cis*- minima ( $^3B_u$  and  $^3B_2$  respectively) with the *cis* stationary point being more stable. The stationary points on the  $T_3$  surface are not well characterized but play an important role for interpreting the Zeeman anticrossing (ZAC) measurements by Dupré and coworkers [1, 88, 89, 90], described further in Section 5.2.

In this chapter, a new *ab initio* study of the acetylene  $T_3$  potential surface is reported, which clarifies the nature of its energy minimum. The resulting equilibrium geometries and diabatic force constants enable an analysis of interactions between  $T_3$  vibrational levels which are energetically near the  $3\nu_3$  vibrational level on the  $S_1$  excited singlet state. The following sections describe theoretical assignments and comparisons with experimental data to resolve some of the existing controversies concerning the photophysics of this  $T_3$  state.

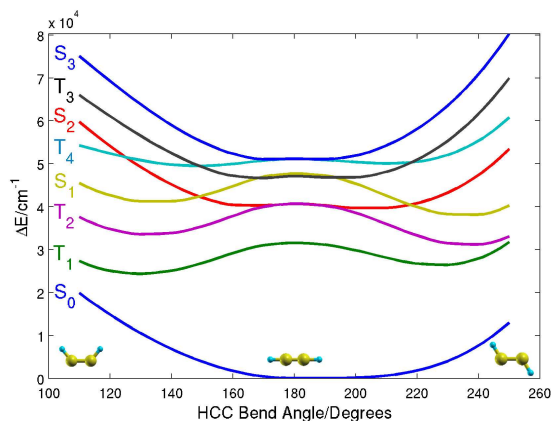


Figure 5-2: Potential energy curves for *cis* – *trans* bending calculated at the EOM-CCSD level with the cc-pVTZ basis. The first excited electronic states are stabilized by bending out of linearity.

## 5.2 Previous Studies on Triplet Acetylene

One of the many unanswered questions regarding triplet states concerns the anomalous behavior of the Zeeman anticrossing (ZAC) density of  $\tilde{A}^1A_u$  acetylene as a function of excitation energy, reported by Dupré and coworkers [1, 88, 89, 90]. In a ZAC measurement, a single  $S_1$  rovibrational level is excited, and the fluorescence is monitored while the strength of an external magnetic field is scanned. States containing triplet electronic state character have a magnetic dipole moment and therefore respond strongly to the external magnetic field. When a triplet state is tuned into degeneracy with the fluorescing bright state, it mixes dark-state character into the bright state, resulting in a decrement to the fluorescence signal (Figure 5-3). The resulting ZAC spectrum measured by Dupré et al. was recorded with 0 – 3 quanta in the *trans* bending normal mode  $\nu_3$  of the  $\tilde{A}^1A_u$  state (cf. Figure 5-4), covering an energy range of 42,200 – 45,300  $\text{cm}^{-1}$  above the zero-point level of the  $S_0$  ground state. As shown in Figure 5-3, the acetylene ZAC spectra showed a dramatic increase in the number of anticrossings with increasing excitation of the  $\tilde{A}^1A_u \nu_3$  mode; however, none of the observed anticrossings could be assigned to triplet states of definite vibrational and rotational ( $K_a, N$ ) quantum numbers. The results of Dupré et al. clearly imply that the increase in the density of detectable anticrossings is attributed to a sudden increase in  $S_1 - T_i$  coupling strength ( $i = 1, 2, \text{ or } 3$ ). In 1996, the

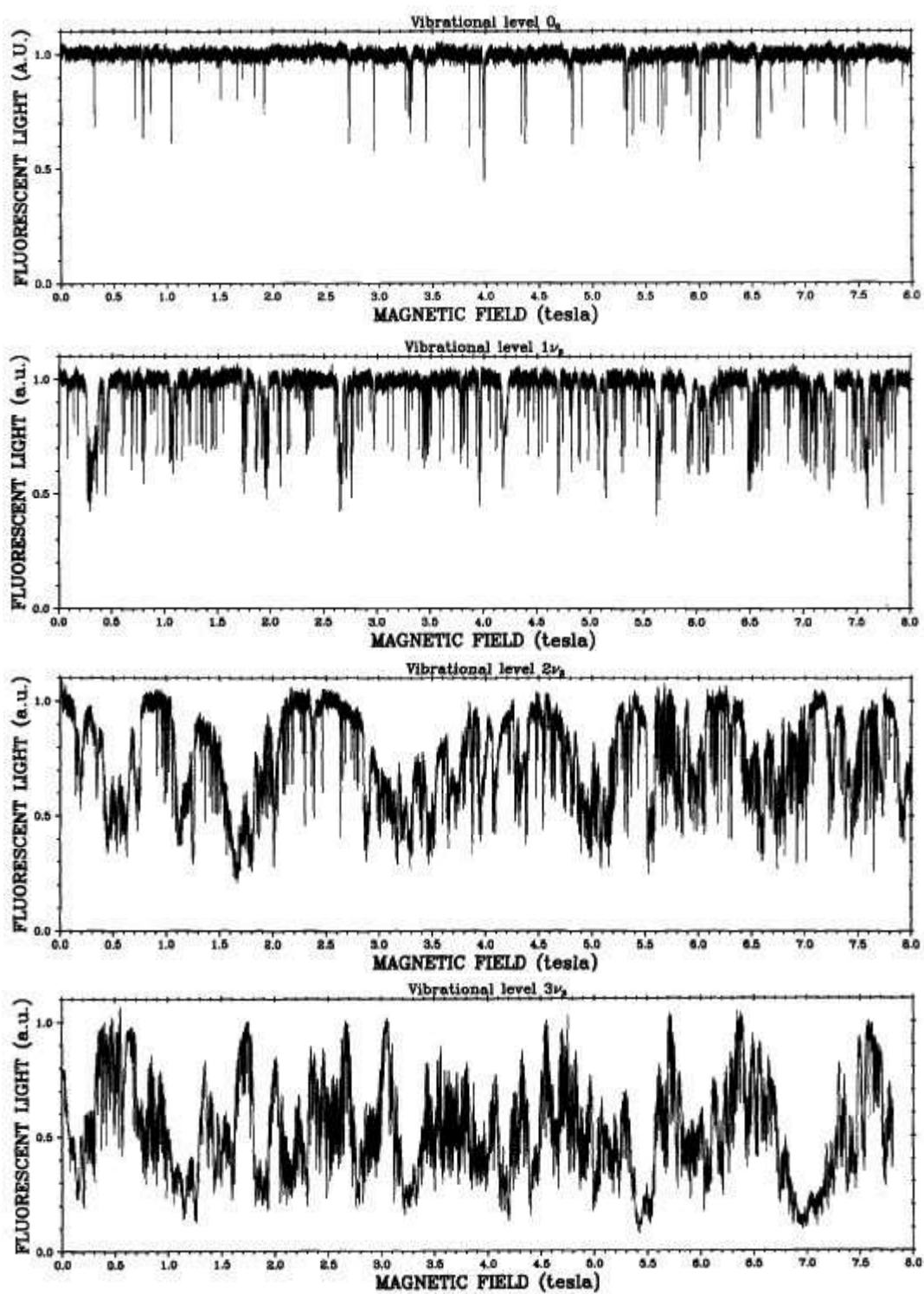


Figure 5-3: Zeeman anticrossing spectra for the  $\nu'_3 = 0 - 3$  vibrational levels of the  $\tilde{A}^1A_u$  state. An increase in the number of anticrossings is observed with increasing excitation of the  $\nu'_3$  mode. Figures reproduced from Ref. [1].

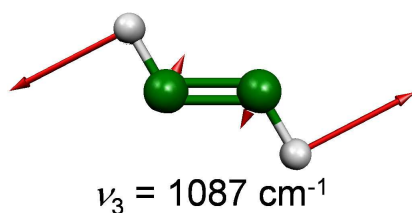


Figure 5-4: The  $\nu_3$  ( $a_g$ ) *trans*-bending normal mode for the  $\tilde{A}^1A_u$  state of acetylene. The harmonic vibrational frequency was calculated at the EOM-CCSD level with the cc-pVQZ basis.

anomalous ZAC density was partially addressed in the work by Vacek et al. [91] and Sherrill et al. [92] who concluded that the  $T_1$  and  $T_2$  states are not candidates for the triplet coupling state since they are energetically too low and outside the experimental ZAC window. Consequently, several studies [93, 94, 95] have focused on the third triplet electronic state ( $T_3$ ) as the most likely candidate for providing the special “doorway” to coupling with the  $3\nu_3$  vibrational level of  $S_1$ . One of the most extensive analyses attempting to assign the triplet perturbers of  $S_1$   $3\nu_3$  is the work by Mishra and coworkers [96] who simultaneously recorded ultraviolet laser-induced fluorescence (UV-LIF) and surface electron ejection by laser excited metastables (SEELEM) spectra in the  $45,300 \text{ cm}^{-1}$  region. One of the key results of that work is the identification of a rotational series of triplet levels which were fitted using a deperturbation model.

In contrast to the several experimental studies in the literature, *ab initio* electronic structure calculations have been slow in characterizing the location and nature of the minimum of the  $T_3$  potential energy surface. Cui et al. [97, 98] were only able to locate a transition state (saddle point), with one imaginary normal-mode frequency along an antisymmetric CCH bending coordinate (see Figures 5-7 (a)–(b)). More recently, Ventura et al. [99] performed extended multireference electron correlation calculations on all four of the lowest-lying acetylene triplet potential energy surfaces. These authors were the first researchers to report a genuine minimum (no imaginary frequencies) belonging to the  $T_3$  surface. Although Ventura et al. give an optimized geometry for this equilibrium structure (which has a similar geometry to the saddle

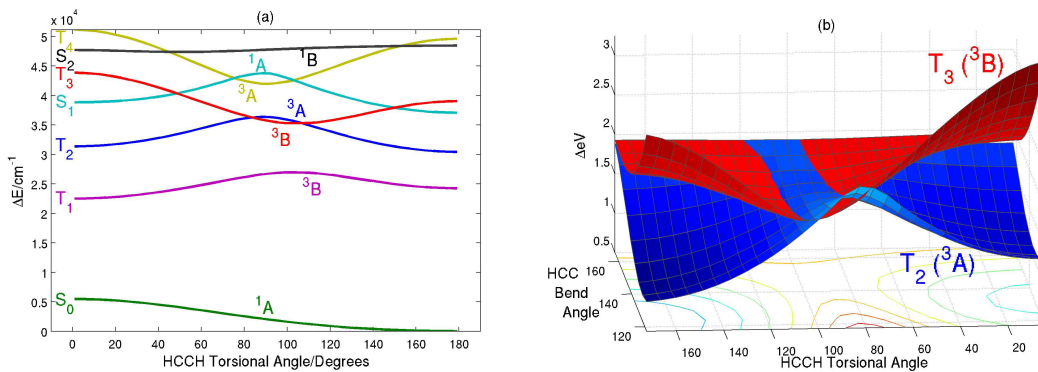


Figure 5-5: (a) Potential energy curves as a function of the HCCH torsion and (b) intersection of the  $T_2/T_3$  surfaces as a function of the HCCH and CCH angles under a  $C_2$  symmetry restriction. Energies for both figures were calculated at the EOM-CCSD level with the cc-pVTZ basis.

point of Cui et al.), the usefulness of their findings is reduced since they provided no normal mode vibrational frequencies or eigenvectors. The location and nature of a  $T_3$  minimum is controversial since the two seams of  $T_2/T_3$  intersections lie very close to the predicted  $T_3$  stationary point. Figures 5-5 (a)–(b) illustrate the complicated crossings of the  $T_2/T_3$  surfaces and show that  $T_3$  is stabilized relative to the Cui et al. saddle point by an out-of-plane torsional angle. This complicated topography accounts for the difficulties encountered in locating stationary points.

### 5.3 A New Ab Initio Study of the $T_3$ Surface

Both the ZAC measurement and the deperturbation model used to interpret the UV-LIF/SEELM dataset provide estimates of spin-orbit matrix elements between  $S_1$  and  $T_3$  perturbors. The deperturbation model and Hamiltonian fit from Refs. [87, 96, 95] yield a  $3\nu_3 S_1 \sim T_3$  coupling matrix element of  $0.126 \text{ cm}^{-1}$ . To an excellent approximation, this matrix element factors into a product of a purely electronic matrix element of the spin-orbit operator and a vibrational overlap integral. An *ab initio* calculation has already been carried out for  $T_3$  acetylene by Cui et al. [97, 98], who computed  $\mathbf{H}^{\text{SO}}$  between  $S_1$  and  $T_3$  at several nuclear configurations. At the minimum of the seam of intersection in  $C_2$  symmetry between the  $S_1$  and  $T_3$  surfaces,

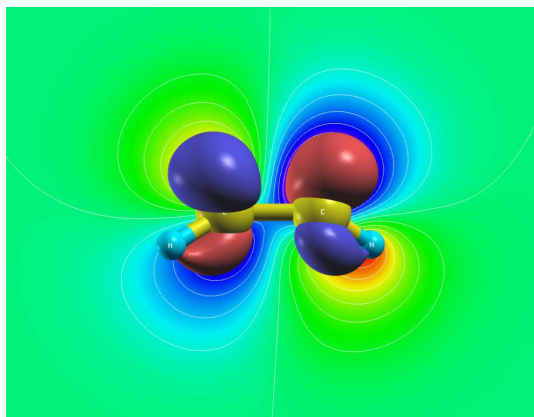


Figure 5-6: Highest occupied molecular orbital for the lowest stationary point on  $T_3$  ( ${}^3B$ ). The geometry parameters for this  $C_2$  symmetry stationary point are listed in Table 5.1.

this matrix element (i.e.,  $\langle \Psi(S=0, M_S=0) | \mathbf{H}^{\text{SO}} | \Psi(S=1, M_S=1) \rangle$ ) is  $13.7 \text{ cm}^{-1}$ . This value yields a vibrational overlap integral for the  $T_3$  perturber of approximately  $0.126/13.7 = 0.01$ .

The vibrational overlap integral is calculable if the geometry and force field near the minimum of the respective electronic states can be estimated. In order to shed light on the nature of the  $T_3$  potential energy surface, with a view to producing an accurate estimate of this crucial vibrational overlap integral, new *ab initio* calculations were carried out. Geometries and harmonic frequencies of stationary points on  $T_3$  were optimized using the equation of motion coupled cluster with singles and doubles (EOM-CCSD) method. In this work, the correlation-consistent basis sets of Dunning [38] denoted by cc-pVXZ, where X stands for D (double), T (triple), or Q (quadruple) zeta quality, were used. All EOM-CCSD calculations were performed using the ACES II set of programs [100] with analytic gradients for both geometry and harmonic frequency calculations.

Vibrational frequency calculations using the EOM-CCSD approach and cc-pVQZ basis indicate that all the stationary points on  $T_3$  are not local minima on the potential energy surface. The  $C_{2h}$  and  $C_{2v}$  structures on  $T_3$  have one and two imaginary frequencies, respectively. The lowest stationary point on  $T_3$  was found with  $C_2$  symmetry (see Figure 5-6) but has one imaginary frequency along an antisymmetric CCH



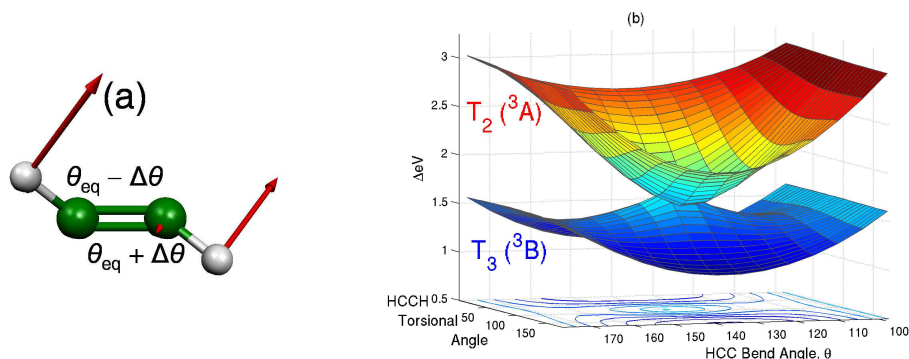


Figure 5-7: (a) The  $\nu_6$  antisymmetric CCH bending normal mode for  $T_3$  acetylene ( $\angle\text{H}_1\text{C}_1\text{C}_2 = \theta_{\text{eq}} - \Delta\theta$ ,  $\angle\text{H}_2\text{C}_2\text{C}_1 = \theta_{\text{eq}} + \Delta\theta$ ) and (b) adiabatic  $T_2/T_3$  surfaces as a function of the HCCH torsional angle and CCH asymmetric bend angle. The  $T_2/T_3$  energies were obtained at the EOM-CCSD level with the cc-pVTZ basis. The stationary point on  $T_3$  is unstable against increasing  $\Delta\theta$ .

bending coordinate. In addition, it was found that both  $T_2$  and  $T_3$  cross at a geometry which is very close to this  $T_3$   $\text{C}_2$  point. In Figures 5-7 (a)–(b), the effect of antisymmetric bending on  $T_2$  and  $T_3$  is shown. Near the  $T_3$   $\text{C}_2$  stationary point, the energy decreases on antisymmetric bending for the lower state ( $T_3$ ) and increases for the upper one ( $T_2$ ). The small energy difference between  $T_2$  and  $T_3$  in Figure 5-7 (b) clearly shows that these two states are better described as coupled surfaces in a diabatic representation.

## 5.4 A Brief Digression on Adiabatic and Diabatic Representations

Before proceeding with a detailed analysis of the  $T_2/T_3$  diabatization, it is helpful to first consider a simple example of a model Hamiltonian which contains vibrational-electronic (vibronic) couplings between electronic states with the vibrational normal modes. One way to visualize the adiabatic and diabatic states is to look at a one-dimensional slice of Figure 5-7 (b) along the asymmetric bending coordinate. In Figure 5-8, the solid lines represent two typical potential energy curves for different adiabatic electronic states that one would obtain from a quantum chemistry ap-



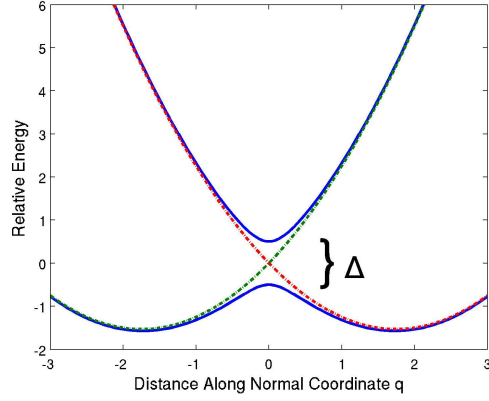


Figure 5-8: Representative adiabatic and diabatic potential energy curves as a function of the normal coordinate  $q$ . The solid adiabatic curves are separated by an energy difference of  $\Delta$  at  $q = 0$ , but the dotted diabatic curves are allowed to intersect.

proach. Unlike the adiabatic states, the potential energy curves of the diabatic states depicted in Figure 5-8 are allowed to cross. Qualitatively, the diabatic states are chosen such that the character of the excited state remains constant throughout a geometric distortion. A simple model for the one-dimensional curves in Figure 5-8 can be constructed with the following two by two Hamiltonian

$$\hat{U}_{\text{diabatic}} = \begin{pmatrix} \frac{1}{2}\omega_1 q^2 - \lambda q & \frac{\Delta}{2} \\ \frac{\Delta}{2} & \frac{1}{2}\omega_2 q^2 + \lambda q \end{pmatrix}. \quad (5.1)$$

One can see that the dotted diabatic curves plotted in Figure 5-8 are the diagonal elements of this diabatic Hamiltonian; i.e., they are both linearly displaced harmonic oscillators. The variable  $\Delta$  is the energy difference between the two electronic states at  $q = 0$ ,  $\omega_1$  and  $\omega_2$  are the harmonic frequencies of the diabatic states, and  $\lambda$  is the vibronic coupling coefficient. Diagonalizing  $\hat{U}_{\text{diabatic}}$  yields the following adiabatic potential curves

$$E^\pm(q) = \frac{1}{4}\omega_1 q^2 + \frac{1}{4}\omega_2 q^2 \pm \frac{1}{2} \left[ \left( \frac{1}{2}\omega_1 q^2 + \frac{1}{2}\omega_2 q^2 \right)^2 - (\omega_1 q^2 - 2\lambda q)(\omega_2 q^2 + 2\lambda q) + \Delta^2 \right]^{1/2}. \quad (5.2)$$

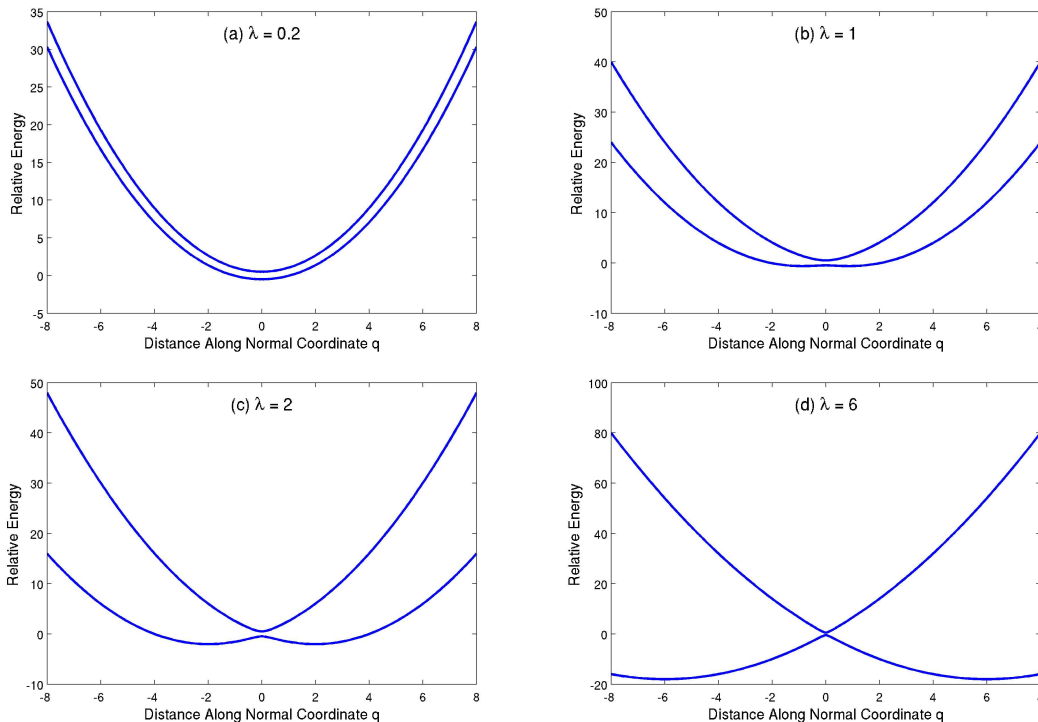


Figure 5-9: (a)–(d) Adiabatic potential energy curves (Eq. (5.2)) as a function of the normal coordinate  $q$ . All potential curves have identical values of  $\Delta$ ,  $\omega_1$ , and  $\omega_2$ . As the vibronic coupling parameter  $\lambda$  is increased, the curves are better approximated in the diabatic representation.

The adiabatic potentials are plotted in Figure 5-8, where  $\Delta$  is the energy difference between them (setting  $q = 0$  in Eq. (5.2) gives  $E^\pm(q = 0) = \pm\Delta/2$  as promised). Clearly, it is the vibronic couplings in  $\hat{U}_{\text{diabatic}}$  which are responsible for the sharpness of the avoided crossing at  $q = 0$  between the close-lying adiabatic states. To illustrate this point, the adiabatic potential curves along the normal coordinate  $q$  for different values of  $\lambda$  (but identical values of  $\Delta$ ,  $\omega_1$ , and  $\omega_2$ ) are plotted in Figures 5-9 (a)–(d). The two adiabatic potentials can be well approximated as independent surfaces when  $\lambda = 0.2$ , and the Born-Oppenheimer adiabatic approximation is applicable. However as the vibronic coupling coefficient is increased, the two excited state curves are more accurately modeled as coupled surfaces, and a diabatic representation is more appropriate.

Although the discussion so far has been phrased in terms of the particular diabatic basis in which Eq. (5.1) is expressed, the choice of diabatic basis is ultimately

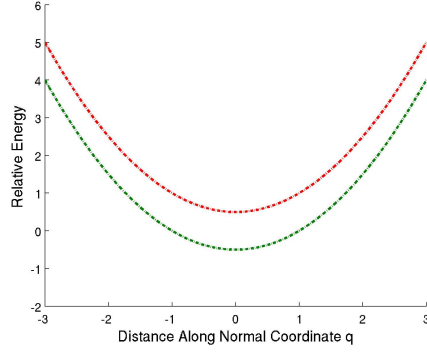


Figure 5-10: Diabatic potential energy curves represented in the new basis of Eq. (5.4).

immaterial. For example, consider another diabatic basis that is obtained from the previous basis by the unitary matrix

$$\mathbf{S} = \frac{1}{\sqrt{2}} \begin{pmatrix} 1 & 1 \\ 1 & -1 \end{pmatrix}. \quad (5.3)$$

The Hamiltonian in this new diabatic basis is obtained by performing the same unitary transformation on the old Hamiltonian

$$\begin{aligned} \hat{\mathbf{U}}_{\text{diabatic}}^{\text{new}} &= \mathbf{S}^{-1} \hat{\mathbf{U}}_{\text{diabatic}} \mathbf{S} \\ &= \begin{pmatrix} \frac{\omega_1 + \omega_2}{4} q^2 + \frac{\Delta}{2} & \frac{\omega_1 - \omega_2}{4} q^2 - \lambda q \\ \frac{\omega_1 - \omega_2}{4} q^2 - \lambda q & \frac{\omega_1 + \omega_2}{4} q^2 - \frac{\Delta}{2} \end{pmatrix}. \end{aligned} \quad (5.4)$$

Once again, the new diabatic states are the diagonal elements of  $\hat{\mathbf{U}}_{\text{diabatic}}^{\text{new}}$  which are plotted in Figure 5-10. Although the new diabatic states look considerably different than the curves plotted in Figure 5-8, diagonalization of  $\hat{\mathbf{U}}_{\text{diabatic}}^{\text{new}}$  still yields the *same* adiabatic potential curves depicted in Figure 5-8 and also mathematically expressed in Eq. (5.2) (the adiabatic potentials must be the same since the eigenvalues are invariant under a unitary transformation). Evidently, the old diabatic basis states shown in Figure 5-8 are equally as valid as the new diabatic basis states in Figure 5-10 since they both preserve the same adiabatic eigenvalues. The only criterion for the diabatic states is that they preserve their character upon geometric distortion, a

behavior which is still clearly demonstrated in Figure 5-10. Consequently, the choice of a diabatic basis is completely arbitrary and not unique; in practice, the basis which is chosen is usually the one in which the electronic states can be computed with the least amount of effort. In the next section, the diabatic basis in which Eq. (5.4) is expressed will be utilized to obtain the (non-imaginary) diabatic frequencies of  $T_2/T_3$  acetylene.

## 5.5 The $T_2/T_3$ Vibronic Model

To treat the interactions between  $T_2$  and  $T_3$ , a two-dimensional diabatic model was used in which the  $T_3$  and  $T_2$  electronic states are coupled by the two nontotally symmetric modes,  $\nu_5$  (antisymmetric CC stretch) and  $\nu_6$  (antisymmetric CCH bend) (see Figures 5-11 (e)–(f)). To estimate the adiabatic couplings, the diabatic electronic Hamiltonian matrix  $\hat{\mathbf{U}}$  is written in the basis spanned by  $\phi_1$  and  $\phi_2$ , which are the diabatic wavefunctions associated with  $T_3$  and  $T_2$ , respectively. Within the harmonic approximation, the diabatic potential energy curves  $U_{11}$  and  $U_{22}$  expressed in the dimensionless normal coordinates  $q = (\omega/\hbar)^{1/2}Q$  are given by

$$U_{11} = \langle \phi_1 | \mathbf{U} | \phi_1 \rangle = \frac{1}{2}\omega_5 q_5^2 + \frac{1}{2}\omega_6 q_6^2, \quad (5.5)$$

$$U_{22} = \langle \phi_2 | \mathbf{U} | \phi_2 \rangle = \frac{1}{2}\omega_5 q_5^2 + \frac{1}{2}\omega_6 q_6^2 + \Delta, \quad (5.6)$$

where  $\Delta$  is the vertical excitation energy between the  $T_3$  and  $T_2$  states at the reference  $C_2$  saddle point on the  $T_3$  surface. In Eq. (5.5), mode  $\nu_5$  is assumed to have the same diabatic frequency ( $\omega_5$ ) on the  $T_3$  and  $T_2$  diabatic surfaces [101, 102]. This assumption is quite reasonable given that the potential energy surfaces for  $T_2$  and  $T_3$  are symmetrical about the plane  $\angle HCC = \theta_{\text{eq}} = 137^\circ$  in Figure 5-7 (b) (i.e., the local minima on the lower surface have the same curvature). Similarly, mode  $\nu_6$  is assumed to have the same diabatic frequency ( $\omega_6$ ) on the  $T_3$  and  $T_2$  diabatic surfaces. By choosing  $\omega_5$  (or  $\omega_6$ ) to have the same frequency on the  $T_3$  and  $T_2$  diabatic surfaces, the diabatic frequencies obtained from the basis in which Eq. (5.4) is expressed

will be the same as the diabatic frequencies resulting from the different basis of Eq. (5.1). As a result, the vibrational overlap analysis in Section (5.6), which relies on the numerical values of the diabatic frequencies, will be unchanged even if a different diabatic basis is chosen.

Since  $T_3$  and  $T_2$  are now diabatic, they are coupled by the adiabatic vibronic coupling operator  $U_{12}$  which can be expanded in a Taylor series in  $q_5$  and  $q_6$  [103, 104, 105]:

$$U_{12} = U_{21} = \langle \phi_1 | \mathbf{U} | \phi_2 \rangle = \lambda_5 q_5 + \lambda_6 q_6 + \lambda'_5 q_5^3 + \lambda'_6 q_6^3 + \dots \approx \lambda_5 q_5 + \lambda_6 q_6, \quad (5.7)$$

where only the terms linear in  $q_5$  and  $q_6$  in Eq. (5.7) are retained.

To make contact with properties obtained from quantum chemistry codes, one must switch to the adiabatic representation. The two-dimensional adiabatic potential surfaces  $E^+(q_5; q_6)$  and  $E^-(q_5; q_6)$ , are obtained by diagonalization of the diabatic electronic Hamiltonian matrix

$$\begin{pmatrix} U_{11} & U_{12} \\ U_{21} & U_{22} \end{pmatrix} = \begin{pmatrix} \frac{1}{2}\omega_5 q_5^2 + \frac{1}{2}\omega_6 q_6^2 & \lambda_5 q_5 + \lambda_6 q_6 \\ \lambda_5 q_5 + \lambda_6 q_6 & \frac{1}{2}\omega_5 q_5^2 + \frac{1}{2}\omega_6 q_6^2 + \Delta \end{pmatrix}. \quad (5.8)$$

The two roots of this Hamiltonian, which represent the adiabatic energy curves, are

$$E^\pm(q_5, q_6) = \frac{1}{2}(\omega_5 q_5^2 + \omega_6 q_6^2 + \Delta) \pm \frac{\Delta}{2} \left[ 1 + \frac{4(\lambda_5 q_5 + \lambda_6 q_6)^2}{\Delta^2} \right]^{1/2}, \quad (5.9)$$

where  $E^+$  and  $E^-$  are the adiabatic potential energy surfaces of the  $T_2$  and  $T_3$  states, respectively. Therefore, the second derivative of each of these roots yields the adiabatic harmonic frequencies  $\Omega_5^\pm$  and  $\Omega_6^\pm$ :

$$\Omega_5^\pm = \left[ \frac{\partial^2 E^\pm(q_5, q_6)}{\partial q_5^2} \right]_{q_5=q_6=0} = \omega_5 \pm \frac{2\lambda_5^2}{\Delta}, \quad (5.10)$$

$$\Omega_6^\pm = \left[ \frac{\partial^2 E^\pm(q_5, q_6)}{\partial q_6^2} \right]_{q_5=q_6=0} = \omega_6 \pm \frac{2\lambda_6^2}{\Delta}. \quad (5.11)$$

	pVDZ	pVTZ	pVQZ	Ventura, et al. [99]
$r_{\text{CC}}(\text{\AA})$	1.381	1.349	1.347	1.352
$R_{\text{CH}}(\text{\AA})$	1.101	1.075	1.077	1.079
$\theta_{\text{CCH}}(^{\circ})$	132.6	137.4	137.3	138.7
$\tau_{\text{HCCH}}(^{\circ})$	104.7	104.6	104.5	106.1

Table 5.1: Optimized geometries at the diabatic  $T_3$   $\text{C}_2$  minimum.

The anharmonic cubic and quartic terms can be similarly obtained by differentiating Eq. (5.9) with higher order derivatives, but only the harmonic terms are retained in this treatment. Using Eqs. (5.10) and (5.11), the diabatic frequencies  $\omega_5$  and  $\omega_6$  are given by

$$\omega_5 = \frac{\Omega_5^+ + \Omega_5^-}{2}, \quad (5.12)$$

$$\omega_6 = \frac{\Omega_6^+ + \Omega_6^-}{2}, \quad (5.13)$$

and the adiabatic vibronic coupling coefficients are then given by

$$|\lambda_5| = \frac{[\Delta (\Omega_5^+ - \Omega_5^-)]^{1/2}}{2}, \quad (5.14)$$

$$|\lambda_6| = \frac{[\Delta (\Omega_6^+ - \Omega_6^-)]^{1/2}}{2}. \quad (5.15)$$

To utilize this diabatic model one must calculate, using quantum chemistry methods, the following adiabatic quantities:  $\Delta$ ,  $\Omega_5^{\pm}$ , and  $\Omega_6^{\pm}$ . Utilizing the EOM-CCSD method, the geometries for the  $\text{C}_2$  saddle point on the  $T_3$  surface are collected in Table 5.1, with previous results from the literature for comparison. A general decrease in bond lengths and increase in bond angles is observed with larger basis set size. However, when the basis set increases from cc-pVTZ to cc-pVQZ, the difference in geometry is relatively small within the EOM-CCSD approach. The pVQZ results of Table 5.1 agree well with the MR-AQCC (TQ)-extrapolated values from Ventura, et al. [99]

	pVDZ	pVTZ	pVQZ
$\Delta$ (eV)	0.0461	0.0296	0.0281
$ \lambda_5 $ (eV)	0.0308	0.0226	0.0220
$ \lambda_6 $ (eV)	1.101	1.075	1.024
$\omega_5$ ( $cm^{-1}$ )	2965.0	3041.7	3036.5
$\omega_6$ ( $cm^{-1}$ )	474.6	370.4	397.6

Table 5.2: *Ab initio* adiabatic coupling parameters between  $T_3$  and  $T_2$  with diabatic frequencies of  $T_3$ .

## 5.6 $S_1/T_3$ Vibrational Overlap Integrals

The computed parameters for the adiabatic vibronic couplings between  $T_3$  and  $T_2$  were obtained using Eqs. (5.14) and (5.15), and are listed in Table 5.2. The diabatic frequencies of  $T_3$ ,  $\omega_5$  and  $\omega_6$ , (rescaled to conventional mass-weighted normal coordinates) are also listed. Within all basis sets, the  $\nu_6$  mode, which corresponds to the antisymmetric CCH bend, provides the stronger coupling between  $T_3$  and  $T_2$ .

Now the non-imaginary harmonic frequencies and force constants about the diabaticized  $T_3$  minimum can be used to compute vibrational overlap integrals with  $S_1$   $3\nu_3$ . In order to minimize errors and maintain consistency within the calculation, the harmonic frequencies and force constants for  $S_1$  were recomputed within the EOM-CCSD approach. Table 5.3 lists the normal modes and calculated frequencies for  $S_1$  (It is worth mentioning that the EOM-CCSD approach is not strictly appropriate for calculating  $S_1$  properties because of the multireference character of the reference ground state wavefunction. This is reflected in the calculated  $\nu_4$  frequency of  $641.5$   $cm^{-1}$  which is noticeably smaller than  $765$   $cm^{-1}$  obtained from experiment. The  $S_1$  vibrational frequencies obtained using other approaches are currently being investigated by Prof. John F. Stanton and Bryan M. Wong.) The calculation also establishes an electronic energy separation ( $S_1 - T_3$ ) of  $0.0012211$  Hartree =  $270$   $cm^{-1}$  using the cc-pVQZ basis.

The vibrational overlap integrals between  $T_3$  and  $S_1$   $3\nu_3$  can be calculated within the harmonic oscillator approximation using the multidimensional generating function formalism developed by Sharp and Rosenstock [108] and extended by several other authors [109, 110]. The original manuscript by Sharp and Rosenstock, it should

Mode	Predominant Character	Calculated (cm <sup>-1</sup> )	Exp. (cm <sup>-1</sup> ) [106, 107]
$\nu_1 (a_g)$	Symmetric CH stretch	3113.8	3004
$\nu_2 (a_g)$	CC stretch	1504.0	1420
$\nu_3 (a_g)$	Symmetric CCH bend	1087.3	1064
$\nu_4 (a_u)$	Out-of-plane torsion	641.5	765
$\nu_5 (b_u)$	Antisymmetric CH stretch	3091.4	2914
$\nu_6 (b_u)$	Antisymmetric CCH bend	732.4	785

Table 5.3: Computed and experimental  $S_1$  vibrational frequencies. Harmonic frequencies were calculated at the EOM-CCSD level with the cc-pVQZ basis.

be noted, contains a few typographical errors, so it is helpful to review and list the corrected formulae in the present work. The following equations use the same nomenclature introduced by Sharp and Rosenstock to clearly distinguish the corrected expressions from the original misprints.

The vibrational overlap integral between the nuclear wavefunction of the initial state  $\psi'(\mathbf{m})$  and the nuclear wavefunction of the final state  $\psi(\mathbf{n})$  is defined by

$$I(\mathbf{m}, \mathbf{n}) = \mathfrak{N} \int \psi'(\mathbf{m}) \psi(\mathbf{n}) d\mathbf{Q}, \quad (5.16)$$

where  $\mathfrak{N}$  is a normalization constant,  $\mathbf{Q}$  is a  $3N - 6$  dimensional column vector of normal coordinates, and  $\mathbf{m}$  and  $\mathbf{n}$  are  $3N - 6$  dimensional vectors which contain the vibrational quanta in each of the  $3N - 6$  oscillators; i.e.

$$\mathbf{m} = (m_1, m_2, \dots, m_{3N-6}). \quad (5.17)$$

The main complication in performing the integration in Eq. (5.16) arises from the fact that  $\psi'(\mathbf{m})$  and  $\psi(\mathbf{n})$  are described in different sets of normal coordinates. In general, the normal coordinates of  $\psi'(\mathbf{m})$  and  $\psi(\mathbf{n})$  have different equilibrium structures and vibrational frequencies; therefore, the normal modes of one state are a complicated combination of modes of the other. Duschinsky [111] suggested a linear transformation (aptly named the Duschinsky transformation) between the initial and final state coordinates according to

$$\mathbf{Q}' = \mathbf{J}\mathbf{Q} + \mathbf{K}, \quad (5.18)$$



where the Duschinsky rotation matrix  $\mathbf{J}$  describes the projection of the normal coordinate basis vectors of the initial state onto those of the final state, and  $\mathbf{K}$  relates the difference in molecular geometry between initial and final states

$$\mathbf{J} = (\mathbf{L}')^{-1} \mathbf{L}, \quad (5.19)$$

$$\mathbf{K} = (\mathbf{L}')^{-1} \mathbf{R}, \quad (5.20)$$

In Eqs. (5.19)–(5.20)  $\mathbf{L}$  is the matrix which relates the normal mode coordinates  $\mathbf{Q}$  to the  $3N - 6$  dimensional column vector of internal displacement coordinates  $\mathbf{S}$ ; i.e. bond lengths, bond angles, and torsional angles measured with respect to the equilibrium reference configuration:

$$\mathbf{S} = \mathbf{L}\mathbf{Q}. \quad (5.21)$$

In Eq. (5.20),  $\mathbf{R}$  is the  $3N - 6$  dimensional vector whose components are the changes in equilibrium position from the initial to the final states  $\mathbf{R} = \mathbf{R}_{\text{eq}} - \mathbf{R}'_{\text{eq}}$ . A lengthy derivation by Sharp and Rosenstock yields the desired vibrational overlap integrals,  $I(\mathbf{m}, \mathbf{n})$ , as coefficients in the power series

$$\sum_{\mathbf{m}} \sum_{\mathbf{n}} \mathbf{T}^{\mathbf{m}} \mathbf{U}^{\mathbf{n}} (2^{\mathbf{m}} 2^{\mathbf{n}} / \mathbf{m}! \mathbf{n}!)^{1/2} I(\mathbf{m}, \mathbf{n}) = I_0 \exp(\mathbf{T}^{\dagger} \mathbf{A} \mathbf{T} + \mathbf{T}^{\dagger} \mathbf{B} + \mathbf{U}^{\dagger} \mathbf{C} \mathbf{U} + \mathbf{U}^{\dagger} \mathbf{D} + \mathbf{U}^{\dagger} \mathbf{E} \mathbf{T}). \quad (5.22)$$

A misprint occurs in Eq. (22) of Ref. [108] where the root of the fraction in the left hand side of the equation is missing. The corrected version is printed above. Eq. (5.22) is written in the extremely compact notation of Ref. [108] which requires further explanation. The shorthand notation introduced by Sharp and Rosenstock is

$$\mathbf{m}! = \prod_{i=1}^{3N-6} m_i!, \quad (5.23)$$

$$2^{\mathbf{m}} = \prod_{i=1}^{3N-6} 2^{m_i}, \quad (5.24)$$

$$\mathbf{T}^{\mathbf{m}} = \prod_{i=1}^{3N-6} (T_i)^{m_i}, \quad (5.25)$$

In addition, the vectors  $\mathbf{T}$  and  $\mathbf{U}$  each contain  $3N - 6$  dummy summation variables; i.e.,  $\mathbf{T} = (T_1, T_2, \dots, T_{3N-6})$  and  $\mathbf{U} = (U_1, U_2, \dots, U_{3N-6})$ . The other quantities in Eq. (5.22) are derived from the Duschinsky transformation as follows:

$$\mathbf{A} = 2\Gamma'^{1/2} \mathbf{J} (\mathbf{J}^\dagger \Gamma' \mathbf{J} + \Gamma)^{-1} \mathbf{J}^\dagger \Gamma'^{1/2} - \mathbf{1}, \quad (5.26)$$

$$\mathbf{B} = -2\Gamma'^{1/2} \left[ \mathbf{J} (\mathbf{J}^\dagger \Gamma' \mathbf{J} + \Gamma)^{-1} \mathbf{J}^\dagger \Gamma' - \mathbf{1} \right] \mathbf{K}, \quad (5.27)$$

$$\mathbf{C} = 2\Gamma^{1/2} (\mathbf{J}^\dagger \Gamma' \mathbf{J} + \Gamma)^{-1} \Gamma^{1/2} - \mathbf{1}, \quad (5.28)$$

$$\mathbf{D} = -2\Gamma^{1/2} (\mathbf{J}^\dagger \Gamma' \mathbf{J} + \Gamma)^{-1} \mathbf{J}^\dagger \Gamma' \mathbf{K}, \quad (5.29)$$

$$\mathbf{E} = 4\Gamma^{1/2} (\mathbf{J}^\dagger \Gamma' \mathbf{J} + \Gamma)^{-1} \mathbf{J}^\dagger \Gamma'^{1/2}. \quad (5.30)$$

where  $\Gamma'$  and  $\Gamma$  are diagonal  $(3N - 6) \times (3N - 6)$  matrices containing the initial and final normal mode frequencies ( $\omega_i/\hbar$ ) in units of  $\text{amu}^{-1} \text{ \AA}^{-2}$ , respectively:

$$\Gamma = \begin{pmatrix} \frac{\omega_1}{\hbar} & \dots & 0 \\ & \frac{\omega_2}{\hbar} & \vdots \\ \vdots & & \ddots \\ 0 & \dots & \frac{\omega_{3N-6}}{\hbar} \end{pmatrix}, \quad (5.31)$$

The normalization factor  $I_0$  is given by

$$\begin{aligned} I_0 &= I(0, 0) \\ &= [\det(\Gamma \Gamma') 4^{3N-6}]^{1/4} [\det \mathbf{J} (\mathbf{J}^\dagger \Gamma' \mathbf{J} + \Gamma)]^{-1/2} \\ &\quad \times \exp \left[ -\frac{1}{2} \mathbf{K}^\dagger \Gamma' \mathbf{K} + \frac{1}{2} \mathbf{K}^\dagger \Gamma' \mathbf{J} (\mathbf{J}^\dagger \Gamma' \mathbf{J} + \Gamma)^{-1} \mathbf{J}^\dagger \Gamma' \mathbf{K} \right]. \end{aligned} \quad (5.32)$$

An additional misprint occurs in Eq. (21) of Ref. [108] where the exponent of

$\det(\mathbf{\Gamma}\mathbf{\Gamma}')$  is incorrect. The corrected version is given by Eq. (5.32) above.

Eq. (5.32) is the main result of Sharp and Rosenstock: to calculate an overlap integral,  $I(\mathbf{m}, \mathbf{n})$ , the respective sets of quantum numbers  $\mathbf{m}$  and  $\mathbf{n}$  are substituted in Eq. (5.32), and the coefficients of terms at the left and right hand sides with identical powers of the dummy variables  $\mathbf{U}$  and  $\mathbf{T}$  are compared. Unfortunately, the complexity of the occurring expressions grows rapidly with increasing quantum numbers, and the procedure of expanding and comparing both sides of Eq. (5.32) becomes extremely tedious. For the present study of  $S_1/T_3$  vibrational overlaps, a computer algebra system was used to obtain the overlap integrals directly by differentiating the Sharp and Rosenstock generating function with respect to the dummy variables  $\mathbf{T}$  and  $\mathbf{U}$ :

$$I(\mathbf{m}, \mathbf{n}) = I_0 (2^{\mathbf{m}} 2^{\mathbf{n}} \mathbf{m}! \mathbf{n}!)^{-1/2} \times \prod_{i=1}^{3N-6} \frac{\partial^{m_i}}{\partial T_i^{m_i}} \frac{\partial^{n_i}}{\partial U_i^{n_i}} \exp(\mathbf{T}^\dagger \mathbf{A} \mathbf{T} + \mathbf{T}^\dagger \mathbf{B} + \mathbf{U}^\dagger \mathbf{C} \mathbf{U} + \mathbf{U}^\dagger \mathbf{D} + \mathbf{U}^\dagger \mathbf{E} \mathbf{T}) \Big|_{\mathbf{T}=\mathbf{U}=0}. \quad (5.33)$$

Eq. (5.33) follows directly from the power series definition of  $I(\mathbf{m}, \mathbf{n})$  expressed in Eq. (5.32). In a computer program available via the Internet [112], the symbolic differentiation method has been implemented to calculate vibrational overlap integrals given  $\mathbf{L}'$ ,  $\mathbf{L}$ ,  $\mathbf{R}'_{\text{eq}}$ ,  $\mathbf{R}_{\text{eq}}$ ,  $\mathbf{m}$ , and  $\mathbf{n}$  as inputs for any general molecule. The user-friendly code and sample inputs for the present  $S_1/T_3$  study are further documented in Appendix B.

All that remains is to describe how one may obtain the  $\mathbf{L}$  matrix found in Eqs. (5.19)–(5.20). From the  $\mathbf{FG}$  method of Wilson, Decius, and Cross, [15] the  $\mathbf{L}$  matrix is the transformation which simultaneously diagonalizes the  $\mathbf{G}$  (internal coordinate momentum coupling) and  $\mathbf{F}$  (internal coordinate force constant) matrices:

$$\mathbf{L}^\dagger \mathbf{G}^{-1} \mathbf{L} = \mathbf{1}, \quad (5.34)$$

$$\mathbf{L}^\dagger \mathbf{F} \mathbf{L} = \hbar^2 \mathbf{\Gamma}^2. \quad (5.35)$$

The  $\mathbf{L}$  matrix naturally emerges from a normal mode analysis when the Wilson  $\mathbf{F}$

matrix is expressed in internal coordinates (i.e. force constants corresponding to motions directed along valence coordinates). However, the  $\mathbf{F}$  matrix is not a quantity which is conventionally computed from *ab initio* computer codes. Instead, a  $3N \times 3N$  Hessian matrix,  $\mathbf{F}_{\text{cart}}$ , which includes the second partial derivatives of the potential  $V$  with respect to mass-weighted Cartesian displacement of the atoms is produced:

$$(F_{\text{cart}})_{ij} = \frac{1}{(m_i m_j)^{1/2}} \frac{\partial^2 V}{\partial \xi_i \partial \xi_j}, \quad (5.36)$$

where  $\xi_1, \xi_2, \xi_3, \dots, \xi_{3N}$  are the displacements in Cartesian coordinates  $\Delta x_1, \Delta y_1, \Delta z_1, \dots, \Delta z_N$ , and  $m_i$  is the mass of the atom to which  $\xi_i$  refers. This  $3N \times 3N$  Hessian matrix is usually expressed in a basis where the six zero frequency coordinates (three translational and three rotational coordinates) have already been projected out. The diagonalization of the projected  $\mathbf{F}_{\text{cart}}$  matrix produces  $3N - 6$ ,  $3N$ -dimensional eigenvectors which describe each normal coordinate in terms of mass-weighted Cartesian nuclear displacements. These  $3N - 6$  eigenvectors can be combined to form the  $3N \times (3N - 6)$   $\mathbf{l}$  matrix:

$$l_{ik} = \frac{\partial m_i^{1/2} \xi_i}{\partial Q_k}. \quad (5.37)$$

Therefore, the  $\mathbf{L}$  matrix can be obtained from the equation

$$\mathbf{L} = \mathbf{B}\mathbf{M}^{-1/2}\mathbf{l}, \quad (5.38)$$

where  $\mathbf{M}$  is a diagonal  $3N \times 3N$  matrix of atom masses  $m_i$ , and  $\mathbf{B}$  is a  $(3N - 6) \times 3N$  matrix which relates the internal coordinates  $S_t$  to the nuclear Cartesian displacements:

$$B_{tk} = \frac{\partial S_t}{\partial \xi_k} \quad (5.39)$$

The  $\mathbf{B}$  matrix is solely dependent on the equilibrium geometry, and its elements are derived in Eqs. (3), (5)–(7), and (21)–(24) in Section 4-1 of Ref. [15] for bond stretching, valence angle bending, and torsion respectively (the sets of elements  $B_{tk}$  are denoted by the vector quantities  $\mathbf{s}_{t\alpha}$  in Ref. [15]). The computer source codes,

also documented in Appendix B, automatically calculate the  $\mathbf{B}$  and  $\mathbf{L}$  matrices in internal coordinates for acetylene given the equilibrium geometries and  $\mathbf{I}$  matrices in Cartesian coordinates.

## 5.7 Results for $T_3$ Acetylene

The  $\mathbf{L}$  matrix described in Section 5.6 describes the relative contributions of each internal coordinate motion to each of the normal mode coordinates. The same information is expressed more clearly by the orthogonal matrix  $\mathbf{T}$  (not to be confused with the vector  $\mathbf{T}$  in Eqs. (5.22) and (5.25)) defined by

$$\mathbf{T} = \mathbf{G}^{-1/2}\mathbf{L} \quad (5.40)$$

where  $\mathbf{G}$  is the traditional Wilson's  $\mathbf{G}$  matrix (effective inverse mass matrix) whose elements are defined by

$$G_{tt'} = \sum_{i=1}^{3N} \frac{1}{m_i} B_{ti} B_{t'i} \quad (5.41)$$

The  $\mathbf{T}$  matrix for the  $T_3$   ${}^3B$  stationary point is presented in Table 5.4, and Table 5.5 lists the symmetries, dominant characters, and frequencies as determined from the *ab initio* and  $\mathbf{T}$  matrix analysis. It is important to note that the mode ordering in Table 5.5 for  $T_3$  is different than the mode ordering in Table 5.3 for the  $S_1$  state (i.e.,  $\nu_2$  labels a torsional motion in  $T_3$  but labels a CC stretch in the  $S_1$  state). The normal mode vibrations for the  $T_3$   ${}^3B$  stationary point are also shown in Figure 5-11. It is interesting to note in Table 5.4 that both  $\nu_2$  and  $\nu_3$  involve a strong mixing between the HCCH torsion and CC stretch modes. Of the two, the higher frequency  $\nu_2$  mode contains the larger percentage of torsional vibration.

Table 5.6 lists the  $T_3$  vibrational states, the harmonic energies of which are predicted to fall within approximately  $100 \text{ cm}^{-1}$  of  $S_1$   $3\nu_3$ , along with their calculated overlaps with  $S_1$   $3\nu_3$ . In addition to the vibrational overlap measurement for the  $S_1 \sim T_3$  perturbation discussed earlier in Section 5.3, the magnitude of the vibrationally averaged rotational constant,  $A_\nu$ , is also an important quantity to consider

	$\nu_1$	$\nu_2$	$\nu_3$	$\nu_4$	$\nu_5$	$\nu_6$
$R_{C_1C_2}$	0.1130	0.5203	0.8454	0.0416	0.0000	0.0000
$r_{C_1H_1}$	-0.7023	0.0583	0.0576	0.0074	-0.6978	0.1146
$r_{C_2H_2}$	-0.7023	0.0583	0.0576	0.0074	0.6978	-0.1146
$\theta_{H_1C_1C_2}$	-0.0017	0.0875	-0.0191	-0.7014	-0.1146	-0.6978
$\theta_{H_2C_2C_1}$	-0.0017	0.0875	-0.0191	-0.7014	0.1146	0.6978
$\tau_{H_1C_1C_2H_2}$	-0.0279	-0.8409	0.5271	-0.1191	0.0000	0.0000

Table 5.4: The  $\mathbf{T}$  matrix for the  $T_3$   $^3B$  state determined from an *ab initio* normal modes analysis and Eq. (5.40).

Mode	Predominant Character	Calculated ( $\text{cm}^{-1}$ )
$\nu_1$ (a)	Symmetric CH stretch	3225.88
$\nu_2$ (a)	Torsion	1626.90
$\nu_3$ (a)	CC stretch	1411.96
$\nu_4$ (a)	Symmetric CCH bend	653.04
$\nu_5$ (b)	Antisymmetric CH stretch	3036.48
$\nu_6$ (b)	Antisymmetric CCH bend	397.56

Table 5.5: Computed diabatic  $T_3$   $^3B$  vibrational frequencies. Vibrational descriptions were based on the  $\mathbf{T}$  matrix elements (Table (5.4)), and harmonic frequencies were calculated at the EOM-CCSD level with the cc-pVQZ basis.

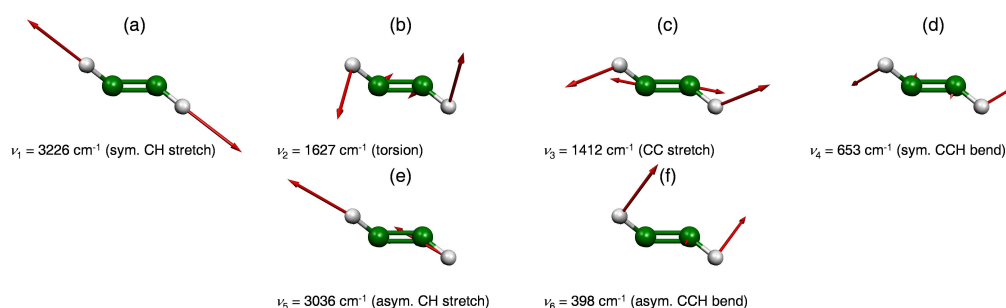


Figure 5-11: (a)–(f) Diabatized vibrational normal modes for the  $T_3$   $^3B$  state.

Vibrational Level	$E - E(3\nu_3)$ (cm <sup>-1</sup> )	$\langle \psi   S_1 3\nu_3 \rangle$	$A_\nu$ (cm <sup>-1</sup> )
$\nu_2 + 2\nu_4 + \nu_6$	-108	0	24.62
$\nu_3 + 3\nu_4$	-68	0.12	28.82
$\nu_3 + 5\nu_6$	-39	0	11.25
$4\nu_4 + 2\nu_6$	-32	-0.062	26.86
$\nu_5 + \nu_6$	-5	-0.0037	19.19
$\nu_4 + 7\nu_6$	-3	0	9.29
$\nu_2 + \nu_3 + \nu_6$	-3	0	20.05
$\nu_2 + \nu_4 + 3\nu_6$	+34	0	18.09
$2\nu_3 + \nu_4$	+38	0.015	24.25
$\nu_3 + 2\nu_4 + 2\nu_6$	+74	0.011	22.29
$3\nu_4 + 4\nu_6$	+110	0.017	20.33

Table 5.6:  $T_3$   ${}^3B$  vibrational levels predicted to lie in the vicinity of  $S_1 3\nu_3$ . Five of the overlap integrals are rigorously zero by symmetry.

for assigning  $T_3$  levels nearly degenerate with  $S_1$  levels. In order to estimate  $A_\nu$  for  $T_3$ , a second-order perturbative treatment can be used which gives the vibrational dependence of  $A_\nu$  by the power series

$$A_\nu = A_e - \sum_r \alpha_r^A (\nu_r + 1/2) + \dots \quad (5.42)$$

Using the optimized geometry parameters in Table 5.1, the equilibrium  $A$  rotational constant,  $A_e$ , is 19.95 cm<sup>-1</sup>. The result for  $\alpha_r^A$  in the harmonic limit is [113]

$$-\alpha_r^A = \frac{2A_0^2}{\omega_r} \left[ \sum_\xi \frac{3(a_r^{A\xi})^2}{4I_{\xi,\xi}} + \sum_{s \neq r} (\zeta_{r,s}^\alpha)^2 \frac{(3\omega_r^2 + \omega_s^2)}{\omega_r^2 - \omega_s^2} \right], \quad (5.43)$$

where

$$a_r^{\alpha\beta} = \left( \frac{\partial I_{\alpha\beta}}{\partial Q_r} \right)_e = \sum_{\gamma,\delta,\varepsilon} 2\epsilon_{\alpha\gamma\varepsilon} \epsilon_{\beta\delta\varepsilon} \sum_i m_i^{1/2} r_{i\gamma} l_{i\delta,r}, \quad (5.44)$$

The variables  $\epsilon_{\alpha\gamma\varepsilon}$  and  $\epsilon_{\beta\delta\varepsilon}$  are the conventional Levi-Civita antisymmetric tensors, and the constants denoted  $\zeta_{r,s}^\alpha$  are the Coriolis coefficients that define the components of vibrational angular momentum in terms of the normal coordinates and their conjugate momenta:

$$\pi^\alpha = \sum_{r,s} \zeta_{r,s}^\alpha Q_r P_s. \quad (5.45)$$

	$\nu_1$	$\nu_2$	$\nu_3$	$\nu_4$	$\nu_5$	$\nu_6$
$\nu_1$	0					
$\nu_2$	0	0				
$\nu_3$	0	0	0			
$\nu_4$	0	0	0	0		
$\nu_5$	0.0093	0.3776	-0.2387	0.0241	0	
$\nu_6$	0.0288	-0.7470	0.4913	-0.0166	0	0

Table 5.7: Numerical  $a$ -axis Coriolis coefficients for  $T_3$   ${}^3B$ , calculated from an *ab initio* normal modes analysis.

The Coriolis coefficients are listed in Table 5.7 and can be calculated directly from the  $\mathbf{l}$ -matrix components:

$$\zeta_{r,s}^\alpha = \sum_{\beta,\gamma,i} \epsilon_{\alpha\beta\gamma} l_{\beta i,r} l_{\gamma i,s}. \quad (5.46)$$

Using the parameters from the  $T_3$  *ab initio* normal mode analysis, the  $\alpha$  coefficients in Eq. (5.43) can be computed and are given in Table 5.8. The relative magnitudes of  $\alpha_4$  and  $\alpha_6$  show that  $A_\nu$  is strongly affected by levels involving the  $\nu_4$  symmetric bending and  $\nu_6$  antisymmetric bending modes. Specifically, excitation of  $\nu_4$  results in a dramatic decrease in  $A_\nu$ , while excitation of  $\nu_6$  dramatically increases  $A_\nu$ . An examination of Table 5.6 yields three  $T_3$  vibrational states lying between 38 and 111  $\text{cm}^{-1}$  from  $S_1$   $3\nu_3$  with an appropriate vibrational overlap ( $\sim 0.01$ ) with the observed triplet perturber. Of all the computed quantities, the energy is expected to be the least accurate, owing both to error in the *ab initio* energy itself and the neglect of anharmonicity. The overlap integrals, on the other hand, are expected to be much less sensitive to inaccuracies in the computed frequencies. The vibrational state  $2\nu_3 + \nu_4$ , with a reasonable  $A_\nu$  value of 24.45  $\text{cm}^{-1}$ , is predicted to lie only 38.0  $\text{cm}^{-1}$  higher in energy than  $S_1$   $3\nu_3$ . A higher-energy state at 110.4  $\text{cm}^{-1}$  from  $S_1$   $3\nu_3$ ,  $3\nu_4 + 4\nu_6$ , is predicted to possess an  $A_\nu$  value closest to that required for the observed simultaneous perturbation of  $S_1$   $3\nu_3$   $K = 0$  and  $K = 1$  (see Refs. [87, 95]). Therefore, the vibrational levels  $2\nu_3 + \nu_4$  and  $3\nu_4 + 4\nu_6$  can be tentatively proposed as leading candidates for the assignment of the  $T_3$  perturber.



	$\alpha_1$	$\alpha_2$	$\alpha_3$	$\alpha_4$	$\alpha_5$	$\alpha_6$
Eq. (5.43)	-0.25	-0.71	-0.40	-2.49	-0.25	+2.03

Table 5.8: Calculated  $a$ -axis vibration-rotation interaction coefficients for  $T_3$   $^3B$ .

## 5.8 Conclusion

In this chapter, a new *ab initio* characterization of the acetylene  $T_3$  potential energy surface for the  $^3B$  stationary point was completed. By accounting for the adiabatic interactions with the  $T_2$  surface, diabaticized harmonic frequencies and force constants about the diabatic  $T_3$  minimum were obtained. These quantities enable the calculation of harmonic vibrational overlap integrals with the  $3\nu_3$  vibrational level of  $S_1$  for the entire manifold of low-lying  $T_3$  vibrational states. On the basis of this analysis, a small number of  $T_3$  states that lie in the energetic region of  $S_1$   $3\nu_3$  were found to possess overlaps of the correct magnitude for the triplet perturber of this level. Two of these, the  $2\nu_3 + 3\nu_4$  and  $3\nu_4 + 4\nu_6$  levels, are predicted to possess a rotational structure consistent with the observed perturbations of  $S_1$   $3\nu_3$  at both  $K = 0$  and 1, unifying UV-LIF/SEELEM measurements with a much earlier Zeeman anticrossing observation. Experiments are currently in progress to locate additional  $T_3$  levels with the goal of adding more experimental calibrations of the  $T_3$  diabatic potential energy surface and  $S_1 \sim T_3$  and  $T_3 \sim T_{1,2}$  spin-orbit coupling strengths.



# Chapter 6

## Computational Techniques for Electron-Molecule Scattering

This chapter presents a first and early attempt to formulate a new *ab initio* electron-molecule scattering theory relevant to molecular Rydberg states. The majority of the work in this chapter resulted from a collaboration with Dr. Serhan N. Altunata, and certain sections were published in an article in the *Journal of Chemical Physics* [114].

### 6.1 Introduction

Molecular Rydberg states, in which one electron has been excited into a large-radius hydrogenic-like orbital, possess several unique properties compared to conventional ground state molecules. When an electron has been excited into an orbital with a large mean radius, the electron can be considered to be moving independently of the non-point charge nature of the molecular ion core. Consequently, the electron-ionic core system has the general character of a hydrogenic system where an uncorrelated Rydberg electron only experiences the positive charge of the core (Figure 6-1 (a)). Accordingly, the energy of the electron-ionic core system follows the Rydberg formula and can be expressed as a sum of two terms:

$$E(\nu^+, N^+, n, l, m_l) = I(\nu^+, N^+) - \frac{R_H}{(n - \mu_l)^2}, \quad (6.1)$$

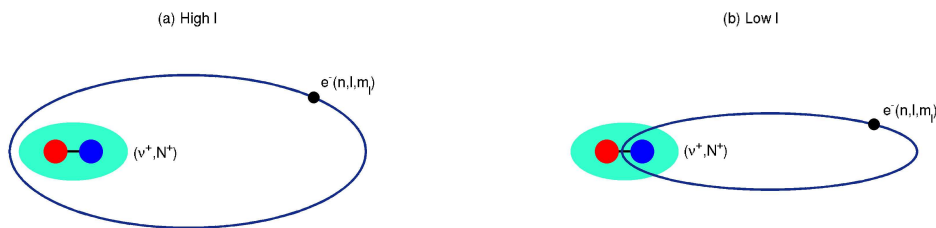


Figure 6-1: (a) Schematic picture of an excited Rydberg state with high angular momentum,  $l$ . When an electron occupies a large Rydberg orbital, the nuclear and electronic motions are largely separable. (b) Depiction of a Rydberg state with low angular momentum. When the Rydberg electron penetrates the ion core, it can exchange energy and angular momentum with the nuclei.

where  $R_H$  is the Rydberg constant ( $= 2.1798736 \times 10^{-18} \text{J}$ ),  $I$  is the ionization energy, and  $(\nu^+, N^+)$  are vibration and rotation quantum numbers of the ionic core. Specifically,  $I(\nu^+, N^+)$  is the energy required to ionize the neutral molecule from the lowest vibration-rotation state to produce the  $(\nu^+, N^+)$  state of the cation. Each Rydberg series converges to an ionization energy associated with a particular ionic core state. The parameters which characterize the Rydberg electron motion are the hydrogenic quantum numbers  $n$ ,  $l$ ,  $m_l$ , and a correction term  $\mu_l$  called the quantum defect. The quantum defect,  $\mu_l$ , is the phase shift of the Rydberg radial wavefunction relative to its hydrogenic form. Qualitatively,  $\mu_l$  measures the penetration of the Rydberg electron into the region of the ionic core. The phase shift is usually larger (greater penetration) for low  $l$ -values because the repulsive centrifugal potential has the form  $l(l+1)/(2r^2)$ .

The modified Rydberg formula as written in Eq. (6.1) is only a zero-order model since it describes the limiting case where there is no interaction between the Rydberg electron and the ion core. When the Rydberg electron penetrates the ion core, the wavefunction can no longer be described as a hydrogenic orbital since it experiences nonlocal exchange and correlation interactions with the core electrons (Figure 6-1 (b)). Consequently, the Rydberg electron quantum numbers do not correspond to operators that commute with the exact Hamiltonian, and the various Rydberg series can become

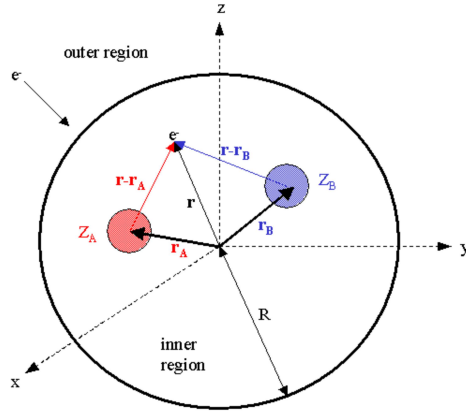


Figure 6-2: Schematic diagram of a molecule enclosed by a notional sphere of radius  $R$ . Exchange between the scattered and atomic electrons is only important within the sphere. The bound wavefunctions centered on nuclei  $Z_A$  and  $Z_B$  (only two nuclei are shown for clarity) have negligible amplitude outside the sphere.

mixed. This mixing of Rydberg series can be associated with the semiclassical picture of a Rydberg electron following a classical trajectory into the core region, exchanging energy and angular momentum, and emerging with different quantum numbers while simultaneously causing a change in the core quantum numbers. Rigorously describing this inelastic process in a quantum mechanical scattering framework is the principal task of multichannel quantum defect theory (MQDT).

The scattering formalism of MQDT was originally introduced by Seaton [115, 116] and was extended for molecular systems by Fano [117], Jungen [118], and Greene [119]. Quantum defect theory begins with the simple idea that each Rydberg series and its associated ionization continuum forms a single “channel” labeled by the quantum numbers of the Rydberg electron and the ion core. In other words, a channel describes an initial or final state of the scattering process. In contrast to calculations of bound-state wavefunctions, MQDT methods partition the configuration space of the scattering electron into two regions separated by a notional spherical boundary with radius  $r = R$ . An illustration of the division of configuration space is shown in Figure 6-2. The sphere is centered at the center of mass of the molecular target. The radius,  $R$ , of this sphere is chosen large enough to approximately enclose the molecular charge cloud. In the internal region,  $r < R$ , electron exchange and inter-electron correlation are significant, and the combination of the target molecule and the scattered electron

acts similarly to a bound state. Conversely, in the external region,  $r > R$ , electron exchange is negligible, and the scattered electron moves in the coulombic potential of the target molecule. Specifically, the long range radial solution for the scattered electron must satisfy the differential equation:

$$\left[ -\frac{1}{2} \frac{d^2}{dr^2} + \frac{l(l+1)}{2r^2} - \frac{Z}{r} + V(r) \right] \psi(r) = \frac{k^2}{2} \psi(r), \quad r > R, \quad (6.2)$$

where the energy  $E = k^2/2$  is specified in advance, and  $V$  may include higher multipolar terms present in some problems. For arbitrary positive or negative energy, quantum defect theory is based on the analytical properties of the regular and irregular solutions of Eq. (6.2), denoted by  $f(k, r)$  and  $g(k, r)$  respectively. These scattering or continuum functions are centered about the center of mass of the molecular target and must have significant amplitude on the spherical boundary. Their presence accounts for the escape of the scattered electron to the external region and yields the correct asymptotic behavior of the collision wavefunctions. The general wavefunction can therefore be expressed by the superposition of  $f(k, r)$  and  $g(k, r)$  in terms of the scattering reaction matrix  $\mathbf{K}$  [120]:

$$\Psi = \sum_j Y^{(j)} \sum_i |i\rangle [f_i(k, r) \delta_{ij} - g_i(k, r) K_{ij}], \quad (6.3)$$

where  $i$  and  $j$  represent particular channels, and  $Y^{(j)}$  is the wavefunction of the ion core multiplied by the angular parts of the Rydberg electron wavefunction. The off-diagonal matrix elements of  $\mathbf{K}$  represent the strength of the mixing between the various channels. As shown by Seaton [115, 116], one can define the matrix

$$\mu_{ij} = \frac{1}{\pi} \tan^{-1}(K_{ij}), \quad (6.4)$$

where  $\mu_{ij}$  are the elements of the quantum defect matrix. The matrix elements  $\mu_{ij}$  are the multichannel analogue of the one-dimensional quantum defect in Eq. (6.1). It is important to point out that the  $\mathbf{K}$  matrix is valid both below and above any ionization threshold, and the MQDT treatment is able to treat both ionization continua and

bound Rydberg states within a single formalism.

The following sections outline a recent and an early attempt to derive and calculate a multi-electron reaction matrix,  $\mathbf{K}$ , based on a variational formalism. It is not the intent of this chapter to give an exhaustive review of the derivation or to include the numerous calculations which have been carried out with this method. Such information can be found in Refs. [114, 121] and also in Appendix C. The purpose of this chapter is to provide a pedagogical exposition of the technical aspects of the method, and the expert reader should refer to Chapter 6 of Ref. [121] for a complete derivation of the multi-electron  $\mathbf{K}$  matrix. This chapter concludes with the calculation of the single channel reaction matrix for the  $1s\sigma_g4p\sigma_u\ ^1\Sigma_u^+$  Rydberg state of  $\text{H}_2$  as an example and first test of the theory.

## 6.2 Variational Derivation of the $\mathbf{K}$ matrix

The basic concept of the multichannel  $\mathbf{K}$  matrix theory derived in Ref. [121] is most easily illustrated by the simple one channel scattering of a spinless particle by a spherically symmetric potential  $V(r)$ . Only the one channel situation is considered in this chapter since this significantly simplifies the derivation and notation of Ref. [121]; furthermore, the more technical aspects of the multichannel case are already explained in Ref. [121], so presenting the full theoretical details would be unnecessary. All of the derivations in this section are presented to give a clear explanation and to highlight the analogies with the multichannel case.

The single channel radial Schrödinger equation in atomic units can be written as

$$\hat{\mathbf{L}}u(r) = 0, \quad (6.5)$$

with

$$\hat{\mathbf{L}} = -\frac{1}{2} \frac{d^2}{dr^2} + V(r) - \frac{k^2}{2}, \quad (6.6)$$

where  $\lim_{r \rightarrow \infty} V(r) = 0$  and the energy  $E = k^2/2$ . From the definition of  $\hat{\mathbf{L}}$  one can

define the function  $\mathcal{L}$ :

$$\mathcal{L} = \int_0^\infty u^*(r) \hat{\mathbf{L}}u(r) dr. \quad (6.7)$$

The boundary conditions assumed for  $u(r)$  are

$$u(0) = 0, \quad (6.8)$$

$$\lim_{r \rightarrow \infty} u(r) = f(kr) + Kg(kr), \quad (6.9)$$

where  $f$  and  $g$  are two linearly independent solutions of the radial Schrödinger equation, and the coefficient of the latter is the  $\mathbf{K}$  matrix which is just a  $1 \times 1$  matrix in this one channel case.

When  $u(r)$  is an exact solution of the radial Schrodinger equation, the functional  $\mathcal{L}$  vanishes. The change in the functional  $\mathcal{L}$  as the exact  $u(r)$  is varied can be examined by replacing  $u(r)$  by a trial solution,  $u_t(r)$ , satisfying the same boundary conditions specified by Eqs. (6.8)–(6.9). Specifically,  $u_t(r)$  is defined by

$$\delta u(r) = u_t(r) - u(r), \quad (6.10)$$

with the boundary conditions

$$\delta u(0) = 0, \quad (6.11)$$

$$\lim_{r \rightarrow \infty} \delta u(r) = \delta Kg(kr). \quad (6.12)$$

Carrying out the variation of  $\mathcal{L}$  gives

$$\begin{aligned} \delta \mathcal{L} &= \int_0^\infty [u^*(r) + \delta u^*(r)] \hat{\mathbf{L}}[u(r) + \delta u(r)] dr \\ &= \int_0^\infty u^*(r) \hat{\mathbf{L}}\delta u(r) dr + \int_0^\infty \delta u^*(r) \hat{\mathbf{L}}u(r) dr. \end{aligned} \quad (6.13)$$

where the last step follows from the definition that  $u(r)$  is an exact solution to the Schrödinger equation,  $\hat{\mathbf{L}}u(r) = 0$ . The first term in Eq. (6.13) can be expanded by using integration by parts twice:



$$\begin{aligned}
\int_0^\infty u^*(r) \hat{\mathbf{L}} \delta u(r) dr &= \int_0^\infty u^*(r) \left[ -\frac{1}{2} \frac{d^2}{dr^2} + V(r) - \frac{k^2}{2} \right] \delta u(r) dr \\
&= -\frac{1}{2} \left\{ u^*(r) \frac{d[\delta u(r)]}{dr} - \frac{du^*(r)}{dr} \delta u(r) \right\} \Big|_0^\infty \\
&\quad + \int_0^\infty \delta u(r) \left[ -\frac{1}{2} \frac{d^2}{dr^2} + V(r) - \frac{k^2}{2} \right] u^*(r) dr \\
&= -\frac{1}{2} \left\{ u^*(r) \frac{d[\delta u(r)]}{dr} - \frac{du^*(r)}{dr} \delta u(r) \right\} \Big|_0^\infty,
\end{aligned} \tag{6.14}$$

where the last step follows from the definition that  $u^*(r)$  is an exact solution to the Schrödinger equation,  $\hat{\mathbf{L}}^* u^*(r) = \hat{\mathbf{L}} u^*(r) = 0$ . The limits in Eq. (6.14) can be evaluated using the boundary conditions in Eqs. (6.8)–(6.9), (6.11)–(6.12), and their derivatives:

$$\lim_{r \rightarrow \infty} \frac{d[\delta u(r)]}{dr} = \delta K \frac{dg(kr)}{dr}, \tag{6.15}$$

$$\lim_{r \rightarrow \infty} \frac{du(r)}{dr} = \frac{df(kr)}{dr} + K \frac{dg(kr)}{dr}. \tag{6.16}$$

Therefore,

$$\begin{aligned}
&\int_0^\infty u^*(r) \hat{\mathbf{L}} \delta u(r) dr \\
&= -\frac{1}{2} \left\{ [f(kr) + Kg(kr)] \delta K \frac{dg(kr)}{dr} - \left[ \frac{df(kr)}{dr} + K \frac{dg(kr)}{dr} \right] \delta K g(kr) \right\} \\
&= -\frac{k}{2} \delta K \left[ f(x) \frac{dg(x)}{dx} - g(x) \frac{df(x)}{dx} \right],
\end{aligned} \tag{6.17}$$

where the last step follows from a change in variables,  $x = kr$ . From the theory of differential equations, the last term in brackets expressed in Eq. (6.17) is the Wronskian of  $f$  and  $g$ . When the wavefunctions are normalized to the energy in Rydberg units, which is the convention taken in Ref. [121], the Wronskian is equal to  $1/\pi$ , and Eq. (6.17) becomes

$$\int_0^\infty u^*(r) \hat{\mathbf{L}} \delta u(r) dr = -\frac{k}{2\pi} \delta K. \tag{6.18}$$

Substituting Eq. (6.18) in Eq. (6.13) gives

$$\delta\mathcal{L} = -\frac{k}{2\pi}\delta K + \int_0^\infty \delta u^*(r) \hat{\mathbf{L}}\delta u(r) dr. \quad (6.19)$$

Eq. (6.19) expresses the exact value of  $\mathbf{K}$  in terms of the approximate value of the functional  $\mathcal{L}$  and a term which is second order in the error in the wavefunction. Setting  $\delta\mathcal{L} = 0$  and substituting Eq. (6.10) in Eq. (6.19) gives

$$K = K_t + \frac{2\pi}{k} \int_0^\infty u_t^*(r) \hat{\mathbf{L}}u_t(r) dr, \quad (6.20)$$

where the label “ $t$ ” refers to a trial state or matrix. Eq. (6.20) can be solved explicitly for a trial wavefunction that contains the linear trial coefficients  $c_i$ . The strategy is to choose a trial function of the form

$$u_t(r) = f(k, r) + Kg(k, r) + \sum_{i=1}^n c_i\phi_i(r), \quad (6.21)$$

where  $\{\phi_i(r)\}$  are a set of unspecified, real, square-integrable energy independent basis functions. In order to keep the same notation as the work presented in Ref. [121], Eq. (6.21) can be expressed more compactly by relabeling the basis functions  $f(k, r)$ ,  $g(k, r)$ , and  $\phi_i(r)$  into a single set  $\{\phi_i(r)\}$ ,  $i = 0, \dots, n+1$  with  $\phi_0 = f(k, r)$ ,  $\phi_1 = g(k, r)$ , and  $c_1 = K$ . Using this convention, Eq. (6.21) becomes

$$u_t(r) = \phi_0(r) + \sum_{i=1}^{n+1} c_i\phi_i(r), \quad (6.22)$$

Substituting  $u_t(r)$  into the variational expression of Eq. (6.20) gives (after some manipulation):

$$K = \frac{2\pi}{k} \left[ \int_0^\infty \phi_0^*(r) \hat{\mathbf{L}}\phi_0(r) dr + \sum_{i=1}^{n+1} c_i^* \int_0^\infty \phi_i^*(r) \hat{\mathbf{L}}\phi_0(r) dr \right. \\ \left. + \sum_{i=1}^{n+1} c_i \int_0^\infty \phi_0^*(r) \hat{\mathbf{L}}\phi_i(r) dr + \sum_{i,j=1}^{n+1} c_i^* c_j \int_0^\infty \phi_i^*(r) \hat{\mathbf{L}}\phi_j(r) dr \right] \quad (6.23)$$

or in matrix notation

$$K = \frac{2\pi}{k} (\mathbf{m}_{00} + \mathbf{c}^\dagger \mathbf{m}_0 + \mathbf{m}_0^\dagger \mathbf{c} + \mathbf{c}^\dagger \mathbf{m} \mathbf{c}), \quad (6.24)$$

with

$$\mathbf{m}_{00} = \int_0^\infty \phi_0^*(r) \hat{\mathbf{L}} \phi_0(r) dr, \quad (6.25)$$

$$(\mathbf{m}_0)_i = \int_0^\infty \phi_i^*(r) \hat{\mathbf{L}} \phi_0(r) dr, \quad (6.26)$$

$$(\mathbf{m})_{ij} = \int_0^\infty \phi_i^*(r) \hat{\mathbf{L}} \phi_j(r) dr, \quad (6.27)$$

and  $\mathbf{c}$  is a column vector of the  $n + 1$  linear trial coefficients  $c_i$ . Eqs. (6.25)–(6.27) define the free-free  $1 \times 1$  matrix  $\mathbf{m}_{00}$ , the bound-free  $N \times 1$  matrix  $\mathbf{m}_0$ , and the bound-bound  $N \times N$  matrix  $\mathbf{m}$ . An optimization of Eq. (6.24) with respect to the expansion coefficients  $\mathbf{c}$  is determined from the condition:

$$\frac{\partial K}{\partial c_i} = 0, \quad i = 1, \dots, n + 1, \quad (6.28)$$

The result of this condition on Eq. (6.24) gives

$$\mathbf{c} = -\mathbf{m}^{-1} \mathbf{m}_0, \quad (6.29)$$

Substituting this result into Eq. (6.24) finally yields

$$\begin{aligned} K &= \frac{2\pi}{k} \left[ \mathbf{m}_{00} + (-\mathbf{m}^{-1} \mathbf{m}_0)^\dagger \mathbf{m}_0 + \mathbf{m}_0^\dagger (-\mathbf{m}^{-1} \mathbf{m}_0) \right. \\ &\quad \left. + (-\mathbf{m}^{-1} \mathbf{m}_0)^\dagger \mathbf{m} (-\mathbf{m}^{-1} \mathbf{m}_0) \right] \\ &= \frac{2\pi}{k} (\mathbf{m}_{00} - \mathbf{m}_0^\dagger \mathbf{m}^{-1} \mathbf{m}_0). \end{aligned} \quad (6.30)$$

This single channel equation is completely analogous to the generalized multi-channel  $\mathbf{K}$  matrix expression in Eq. (6.2.73) of Ref. [121] which is given by

$$\mathbf{K}_{\text{var}} = 2\pi \mathbf{B}_0^{-1} (\mathbf{m}_{00} - \mathbf{m}_{10}^\dagger \mathbf{m}_{11}^{-1} \mathbf{m}_{10}) \mathbf{B}_0^{-1}. \quad (6.31)$$

The additional matrix  $\mathbf{B}_0$  in the multichannel case arises from the normalization of the  $f(k, r)$  and  $g(k, r)$  functions with the ion core molecular basis. In the multichannel case, the matrices  $\mathbf{m}_{00}$ ,  $\mathbf{m}_{10}$ , and  $\mathbf{m}_{11}$  are no longer integrals between one-electron functions; instead they represent an integration between antisymmetrized products of bound  $N$ -electron ion core orbitals,  $\Theta$ , and the free scattered electron,  $\phi_0$  or  $\phi_1$ . For example, the elements of  $\mathbf{m}_{00}$  are defined as

$$(\mathbf{m}_{00})^{pq} = \int_{r_1 \cdots r_{N+1} < R} \{A [\Theta_p^* \phi_{0,p}^*]\} \hat{\mathbf{L}} \{A [\Theta_q \phi_{0,q}]\} dr_1 \cdots dr_{N+1}, \quad (6.32)$$

where the multidimensional integration is always confined within the spherical volume of radius  $R$  (cf. Figure 6-2). In Eq. (6.32),  $A$  is the antisymmetrizing operator, and the indices  $p$  and  $q$  represent all the quantum numbers needed to represent the internal state of the ion core target. The matrices  $\mathbf{m}_{10}$  and  $\mathbf{m}_{11}$  are defined similarly.

### 6.3 Numerical Evaluation of Integrals

The variational form of the  $\mathbf{K}$  matrix is reduced to the evaluation of matrix elements that can be classified as either free-free, bound-free, or bound-bound, depending on whether two, one, or zero scattering basis functions appear in the integrals. However, since the integration is carried out over the finite volume of the  $\mathbf{K}$  matrix sphere, the computation of the one- and two-electron integrals is significantly more difficult than their infinite-volume counterparts. Slater-type orbitals have been used in previous work [122, 123] for atomic and diatomic systems, but their applicability to general scattering problems incurs the enormous computational cost of numerical evaluation of Hamiltonian matrix elements. For polyatomic molecular systems, several atom-centered basis functions must be used, and the computation becomes prohibitively time consuming if numerical algorithms are implemented. Consequently, Cartesian Gaussian-type functions and linear combinations of Gaussians have become widely used as bound state basis set orbitals in molecular scattering theory [124]. Although it is relatively easy to describe the bound state target orbitals with Gaussian-type

functions, the choice of the continuum basis set is more difficult. The continuum basis must be a good approximation to the  $f(k, r)$  and  $g(k, r)$  functions, which are both oscillatory and have significant amplitude on the  $\mathbf{K}$  matrix sphere. Fortunately, a basis set of orthogonal continuum functions can be replaced by a fit to several diffuse Gaussian-type functions (described further in the following section). This approach reduces the problem of multidimensional numerical integration to a sum of Gaussian integrals; however, the remaining complication is the non-trivial computation of the individual matrix elements over a finite volume. These matrix elements, or integrals, must be evaluated accurately and efficiently in order to obtain reliable theoretical predictions for *ab initio* calculations of generic molecular systems.

It should be mentioned that the efficient evaluation of molecular integrals for bound-state calculations has been a topic of many studies for as long as 50 years [125, 126, 127, 128, 129]. Most notably, the high efficiency of the Head-Gordon and Pople algorithm has allowed current programs to evaluate two-electron integrals dynamically in computer memory as needed [130]. To capitalize on the high efficiency of these algorithms, the most practical modification needed to incorporate existing electronic structure programs into the  $\mathbf{K}$  matrix calculation is to subtract the contribution from the outer region of the  $\mathbf{K}$  matrix sphere from the integrals calculated over all space. In the present work, the PSI 3.2.2 software package was used to generate the integrals over all space for up to  $k$ -type ( $l = 9$ ) angular momentum basis sets [131]. Since it is assumed that the bound target basis functions have negligible amplitude outside the  $\mathbf{K}$  matrix sphere, the only matrix elements which need to be modified in the PSI 3.2.2 output are those integrations involving two or more continuum orbitals. Morgan, Gillan, Tennyson, and Chen have briefly discussed how one might proceed to evaluate the continuum integrations in Ref. [124], but they did not present a full derivation. Closed form analytic expressions for the one- and two-electron integrals of Cartesian Gaussian orbitals outside the  $\mathbf{K}$  matrix sphere are given in Ref. [114] and Appendix C. These integrals, which are (cutely) called “tail integrals,” are evaluated as finite summations over standard functions; hence, the results are accurate within computer precision.

## 6.4 Representing the Continuum Functions

With the completion of an efficient and accurate integral program, all of the necessary routines to calculate the  $\mathbf{K}$  matrix can be carried out on a computer. The calculation commences with the computation of occupied and virtual orbitals of the target ion using standard quantum chemistry techniques. During early testing of the present work, it was sufficient to use a single Hartree Fock configuration representation of the lowest electronic state of the molecule. The self consistent field program from the PSI 3.2.2 suite solves the Hartree Fock procedure and provides the orbital expansion coefficients. Next, a customized routine solves the differential equation in Eq. (6.2) for the numerical continuum basis functions  $f_l(k, r)$  and  $g_l(k, r)$  with the energy  $E = k^2/2$ , and angular momentum  $l$  specified in advance by the user. Each of the radial continuum basis functions are then fit to a linear combination of Gaussians of the form

$$\sum_i c_i r^l \exp(-\alpha_i r^2). \quad (6.33)$$

Since each of the continuum basis functions is a solution to the partial wave differential equation (cf. Eq. (6.2)), the angular momentum quantum number  $l$ , by definition, is conserved. Consequently, both  $f_l(k, r)$  and  $g_l(k, r)$  must be fit to Gaussians all sharing the same center, which is usually taken as the center of mass of the molecule. In this way, each of the Gaussians which comprise the linear combination can be multiplied by the same spherical harmonic in order for the entire expansion to still be an eigenfunction of  $\hat{\mathbf{L}}$ . Fitting the radial continuum basis functions by a set of Gaussians is extremely difficult since one must represent a large number of nodes with nodeless Gaussian functions expanded about a single center (see Figures 6-3 (a)–(b)). The procedure used to obtain the Gaussian exponents was performed by numerically minimizing the function

$$F_l(\alpha_1, \dots, \alpha_n) = \sum_k \left[ \sum_i^n c_i r_k^l \exp(-\alpha_i r_k^2) - \phi_l(r_k) \right]^2. \quad (6.34)$$

The radial coordinate  $r_k$  spans a dense grid of points over which the continuum

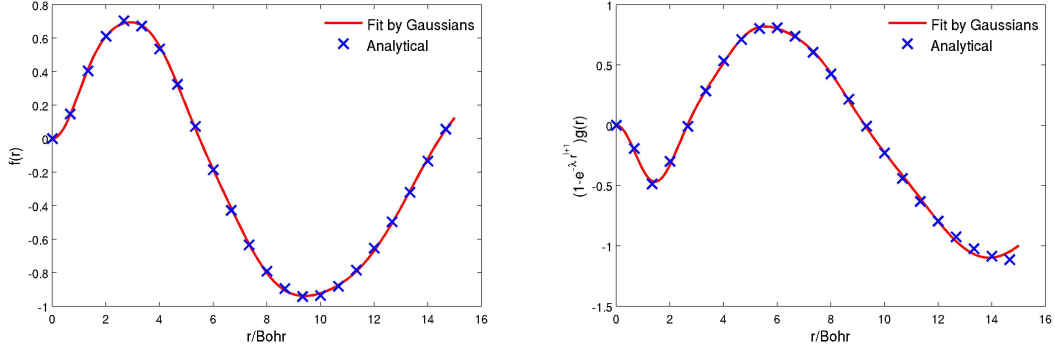


Figure 6-3: (a)–(b) Analytical continuum functions  $f_l(k, r)$  and  $\left(1 - e^{-\lambda r^{l+1}}\right) g_l(k, r)$  with  $l = 1$  (crosses). Each of the continuum functions are fit by a linear combination of 9 single-centered Gaussian functions (full curves) for  $E = -0.03125$  Hartrees.

function  $\phi_l (= f_l(r, k)$  or  $g_l(r, k))$  is to be fitted. This minimization is highly nonlinear and makes the final fit very sensitive to the initial guess of exponents. In the present work, it was empirically found that a geometric series of the form [132]

$$\alpha_i = 0.016 \times 1.39^i, \quad i = 1, 2, 3, \dots, n, \quad (6.35)$$

was found to provide initial guesses which significantly minimized computer time for both  $f_l(k, r)$  and  $g_l(k, r)$ . Using these starting exponents, the coefficients  $c_i$  are determined by an automated least squares fit to  $\phi_l$  using the grid points  $r_k$ . Next, the minimum of  $F_l(\alpha_1, \dots, \alpha_n)$ , using the  $n$   $\alpha_i$  as variational parameters, is obtained using a Powell dogleg algorithm very similar to the methods described in Chapter 2. After this procedure is carried out, the coefficients  $c_i$  are updated by fitting to  $\phi_l$  using the new exponents. The Powell dogleg method to update the  $\alpha_i$  exponents is then repeated using the new coefficients  $c_i$  and old  $\alpha_i$  exponents as initial guesses. The cyclic process of using the least squares fit for  $c_i$  and the Powell dogleg method for  $\alpha_i$  is repeated until convergence is reached.

The quality of the Gaussian basis sets for representing  $f_l(k, r)$  and  $g_l(k, r)$  each with  $l = 1$  and energy  $E = -0.03125$  Hartrees can be seen in Figures 6-3 (a)–(b). The  $g_l(k, r)$  function, which must be regular at  $r = 0$  for a practical numerical implementation, is multiplied by the cut-off function  $\left(1 - e^{-\lambda r^{l+1}}\right)$  which removes the singularity

$i$	$f_l(k, r)$		$(1 - e^{-\lambda r^{l+1}}) g_l(k, r)$	
	$\alpha_i$ exponents	$c_i$ coefficients	$\alpha_i$ exponents	$c_i$ coefficients
1	0.015982	0.32159	0.021174	-1.57293
2	0.024189	-2.83213	0.029195	8.05589
3	0.033825	9.04025	0.040072	-20.38274
4	0.046443	-17.42405	0.054798	35.54647
5	0.063458	24.42726	0.074561	-47.01195
6	0.086156	-25.62546	0.100944	48.25637
7	0.116873	19.94605	0.136341	-37.51221
8	0.158115	-10.25389	0.184532	20.04671
9	0.217796	2.74745	0.254361	-5.99542

Table 6.1: Optimized Gaussian exponents and coefficients for representing continuum functions with  $l = 1$  and  $E = -0.03125$  Hartrees. All exponents,  $\alpha_i$ , are in units of Bohr<sup>-2</sup>.

at the origin and approaches unity for large  $r$ . The curves labeled with crosses represent the actual continuum functions, and the full curves are their approximations by a linear combination of 9 single center Gaussians. Table 6.1 gives the Gaussian exponents  $\alpha_i$  and coefficients  $c_i$  for the fits to the continuum functions. From the figures, the difference between the continuum functions and their approximations is hardly noticeable.

## 6.5 Additional Computational Details

After a numerical fit representing the continuum bases is achieved, the spherical harmonic Gaussians in Eq. (6.33) are converted to their Cartesian Gaussian counterparts using Eq. (C.36) in Appendix C. This additional step is necessary since all the one- and two-electron “tail integrals” are most easily computed in a Cartesian Gaussian basis. It is important to note at this point that all the bound and continuum functions should be constructed to be orthogonal since this greatly simplifies the evaluation of the Hamiltonian matrix elements. Therefore, a customized module reads a set of bound molecular orbital expansion coefficients, a pair of continuum functions, and generates an orthogonal orbital set using a Schmidt orthogonalization procedure. This results in the continuum orbitals picking up bound orbital compo-



nents – a feature that can cause practical linear dependence problems at the four index transformation stage if the coefficients produced are large [133].

Next, all the one- and two-electron integrals for the scattering calculation are generated using a highly vectorized code which evaluates the “tail integral” expressions in Appendix C. The most computationally expensive step in the scattering calculation is the evaluation of the two-electron integrals:

$$\langle ij|kl\rangle = \int \int \chi_i^*(\mathbf{r}_1) \chi_j(\mathbf{r}_1) \frac{1}{|\mathbf{r}_1 - \mathbf{r}_2|} \chi_k^*(\mathbf{r}_2) \chi_l(\mathbf{r}_2) d\mathbf{r}_1 d\mathbf{r}_2. \quad (6.36)$$

As written, the computation of the two-electron matrix elements would require  $n^4$  six-dimensional integrals, where  $n$  is the number of atomic centered functions. This is exceedingly expensive in terms of computer time even for small molecules. Since all of the orbitals are real (this is only true for  $m_l = 0$  scattering states, which is the only case studied in the next section), the complex conjugation has no effect, and orbitals  $i$  and  $j$  or  $k$  and  $l$  can be interchanged to obtain the same integral. Furthermore, the orbitals associated with electron 1 can be swapped with those associated with electron 2. Therefore, the two-electron integrals have approximately eightfold symmetry:

$$\begin{aligned} \langle ij|kl\rangle &= \langle ji|kl\rangle \\ &= \langle ij|lk\rangle \\ &= \langle ji|lk\rangle \\ &= \langle kl|ij\rangle \\ &= \langle lk|ij\rangle \\ &= \langle kl|ji\rangle \\ &= \langle lk|ji\rangle. \end{aligned} \quad (6.37)$$

The approximately eightfold symmetry saves significant computer time since only about one in eight of the two-electron integrals are unique and must be computed (the exact number of unique two-electron integrals is actually  $n(n+1)(2+n(n+1))/8$ ).

Once these atomic integrals are available, a four index transformation program

multiplies them by combinations of molecular orbital coefficients:

$$\langle st|uv\rangle = \sum_{i,j,k,l} c_{is}c_{jt} \langle ij|kl\rangle c_{ku}c_{lv}, \quad (6.38)$$

where  $c_{jt}$  are the atomic function coefficients,  $\{i, j, k, l\}$  are atomic centered functions, and  $\{s, t, u, v\}$  are molecular orbitals. The two-electron integral transformation as written in Eq. (6.38) requires  $n^8$  arithmetic operations where  $n$  is the number of atomic centered functions. Using the summation restructuring scheme of Yoshimine [134], the integral transformation was reduced to  $n^5$  arithmetic operations in the current codes. After this computationally expensive step, another module generates configuration state functions with the appropriate spin and symmetries for the system under study. Finally, the Hamiltonian matrix elements are evaluated, and the  $\mathbf{m}_{00}$ ,  $\mathbf{m}_{10}$ , and  $\mathbf{m}_{11}$  matrices are formed to complete the calculation of the  $\mathbf{K}$  matrix.

## 6.6 Test Calculations on the $1s\sigma_g4p\sigma_u \ ^1\Sigma_u^+$ State of $\mathbf{H}_2$

As a simple and first test of the variational  $\mathbf{K}$  matrix theory, calculations were carried out on the  $1s\sigma_g4p\sigma_u \ ^1\Sigma_u^+$  Rydberg state for the two-electron  $\mathbf{H}_2$  molecule. Only a single channel was included in the calculation, and the one-electron ion core was approximated as a single Slater determinant. Accordingly, the ion core was calculated at the restricted open shell Hartree Fock (ROHF) level with the standard 6-31G basis set [135]. All bound type configurations ( $\phi_i$  in Eq. (6.21)) were obtained by placing an additional electron in the lowest three  $\sigma_u$  virtual orbitals of the ion core. In this way, configurations of the form  $1s\sigma_gnp\sigma_u$  were generated to finally construct an overall state with  $^1\Sigma_u$  symmetry.

Next, the two-electron reaction matrix  $\mathbf{K}$  was generated as a function of energy by calculating the  $\mathbf{m}_{00}$ ,  $\mathbf{m}_{10}$ , and  $\mathbf{m}_{11}$  matrices over a grid of energy points. Using the definition in Eq. (6.4), the quantum defects were produced from the  $\mathbf{K}$  matrix and subsequently used in Eq. (6.1) to determine the potential energy curve for the

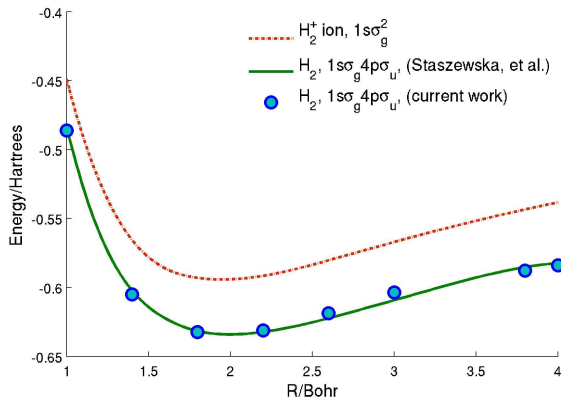


Figure 6-4: Potential energy curves for the  $\text{H}_2^+$  ion ground state and the  $1s\sigma_g 4p\sigma_u$   ${}^1\Sigma_u^+$  state of  $\text{H}_2$ . Energies for the  $\text{H}_2^+$  ion were calculated at the ROHF level with the 6-31G basis, and the solid energy curve is the result of a high level *ab initio* calculation by Staszewska et al. [2]. The blue data points were obtained from the two-electron  $\mathbf{K}$  matrix calculation described in this work.

$1s\sigma_g 4p\sigma_u$   ${}^1\Sigma_u^+$  electronic state of  $\text{H}_2$ . In Figure 6-4, the results of this work are compared to the high level calculation reported by Staszewska et al. in Ref. [2]. Good agreement between this work and the previous high-level calculation is observed in the vicinity of the equilibrium internuclear distance; however, the deviations become more significant at larger internuclear distances. It seems reasonable to expect these deviations since the ROHF wavefunction is a poor approximation for large electronic distances [135].

It should be mentioned at this point that additional test calculations on  $\text{H}_2$  were subsequently performed using basis sets of triple zeta quality. These larger basis sets generate more  $\sigma_u$  virtual orbitals of the ion core which must be orthogonalized to the continuum functions. Consequently, severe problems of linear dependence were encountered due to the increased number of target wavefunctions which must be orthogonalized to the continuum basis. Several authors have also reported serious problems with linear dependence for electron collisions with polyatomic molecules [133, 136, 137, 138, 139, 140, 141]. It may be possible to use the results of the Schmidt procedure to remove functions from the basis, but tests with the existing codes showed that this did not work well. Until this complicated issue is addressed in the current methods, one cannot be completely definitive about the simple calculation

presented in Figure 6-4 (or even possibly, the methodology involved). Nevertheless, the approaches described in this chapter and in Ref. [121] are a useful guide for future calculations aimed at incorporating scattering theories with conventional bound state methods.

## 6.7 Conclusion

This chapter has described a large and complex software package which was initially used to carry out *ab initio* calculations on electron scattering by molecular targets. All of the programs in this package were based on a variational determination of the  $\mathbf{K}$  matrix which embodies the information on the scattering process. The most computationally intensive step in the scattering calculation is the computation of coulomb and exchange integrals within a finite spherical volume. Rather than modify highly efficient codes for molecular integral evaluation, subtracting the outer or tail regions permits the evaluation of Hamiltonian matrix elements within the required finite spherical volume. Thus, the implementation of the current approach, exploiting current bound-state software packages, is straightforward and practical. Furthermore, the proposed scheme of using single center Gaussian functions to represent the continuum electron fits conveniently within the framework developed in this work. A detailed numerical analysis of the nonlinear fit to Gaussians and the final computation of the  $\mathbf{K}$  matrix for the  $1s\sigma_g4p\sigma_u$   $^1\Sigma_u^+$  state of  $\text{H}_2$  provide a first test of the approximations and expressions.

Inherent in all computer packages of this type is the need to extend it to larger and more complicated molecular targets. However, difficulties in further development of this program suite arise due to linear dependence problems between the target and continuum wavefunctions. As discussed in the previous sections, the use of larger basis sets for the ion target lead to significant overlap with the continuum functions, resulting in noninvertible overlap matrices or unusually large coefficients at the four index transformation stage. This is not surprising since single-centered continuum functions are a fairly crude approximation for molecules possessing anisotropic po-

tentials (such as large dipoles or polar polyatomic targets). Numerically solving for the continuum functions directly (as opposed to a nonlinear fit and subsequent orthogonalization) from a multi-electron potential may solve the current difficulties. The use of finite element numerical functions to represent the continuum for polar molecules is an ongoing work and the subject of the next chapter.



# Chapter 7

## Developments in Electron Scattering for Polar Molecules

This chapter outlines preliminary work on an electron-molecule scattering approach for Rydberg states of highly polar diatomics. The majority of the work presented in this chapter is currently in progress and still in development.

### 7.1 Introduction

Electronic structure calculations to determine excited state potential energy curves for heavy atom systems are difficult. Due to the large number of inner shell electrons which can give rise to numerous interactions, applying the standard quantum chemistry methods to these systems is sometimes not feasible. As discussed in the previous chapter, the tools of conventional quantum chemistry mostly rely on variational approaches that minimize variables (usually the total energy) subject to constraints, and therefore generalize poorly to highly excited states. Not surprisingly, it is only within the last twenty years that techniques for excited state calculations have begun to achieve the same accuracy as their ground state counterparts [142, 143, 144, 145]. Unfortunately, this type of accuracy usually comes with great computational expense.

One of the many examples where *ab initio* calculations have progressed slowly is the prediction of the electronic spectrum for the alkaline earth halides. The alkaline

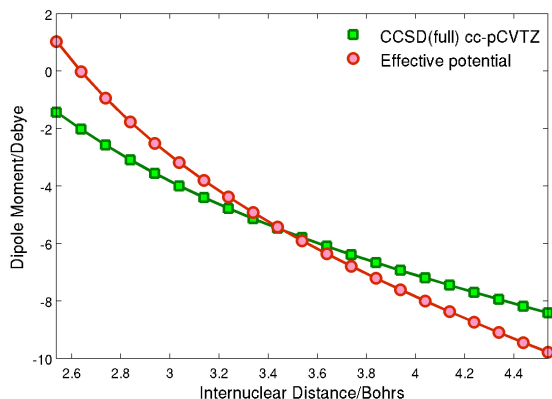


Figure 7-1: CCSD(full) cc-pCVTZ electric dipole moments for the  $\text{CaF}^+$  ion compared with those obtained from the effective potential of Ref. [3]. Both the CCSD(full) and effective potential dipoles agree with each other near the equilibrium internuclear distance ( $R = 3.54$  Bohr), but considerable deviations are observed for small and large  $R$ . Dr. Stephen L. Coy is acknowledged for providing the dipole moments from the effective potential.

earth halides are prototypes of highly polar diatomic molecules possessing a single nonbonding electron. Accordingly, this nominally unpaired electron moves in the field of an ionic closed-shell core containing a metal  $M^{2+}$  ion and a halogen  $X^-$  ion. This zero-order picture has been the starting point for several experimental and theoretical studies [146, 147, 148, 149, 150] on the CaF molecule. Recently, a tractable approach to treat the Rydberg electronic structure of CaF utilized an effective potential to represent the ion core, and included parameters fitted to experimental data [3]. The fact that this effective potential was able to predict the Rydberg energies in a semi-quantitative way validated the zero-order picture of a nonbonding electron moving around a closed-shell ion core. On closer inspection, however, the effective potential approach is inaccurate on two accounts. First, although the study in Ref. [3] is *ab initio* in character, an empirical polarization potential to approximate electron exchange is used as a necessary ingredient in their approach. Second, and related to the first, the phenomenological polarization potential incorrectly predicts the electric dipole moment of the  $\text{CaF}^+$  ion as a function of the internuclear distance,  $R$ . Figure 7-1 depicts the dipole moment obtained from the effective potential of Ref. [3] and compares it with a high-level CCSD(full) calculation using a cc-pCVTZ basis recently



published for the Ca atom [151]. An inspection of the dipole moment reveals that the effective potential is not quantitatively accurate in the small or large  $R$  limit.

The natural solution to this problem is to re-solve the MQDT equations using a multi-electron *ab initio* approach. By invoking the rigorous methods of quantum chemical techniques, it is possible to fix the incorrect dipole dependence on internuclear distance and also eliminate any empirical parameters at the same time. The following sections describe preliminary and ongoing steps to incorporate multi-electron methods within an MQDT approach.

## 7.2 The Electron Scattering Equations

The full Hamiltonian for the scattering of an electron by a non-rotating diatomic molecule is given by

$$\hat{H} = \hat{H}_{\text{ion}}(\mathbf{r}_1, \dots, \mathbf{r}_{N-1}) + V_{\text{int}}(\mathbf{r}_1, \dots, \mathbf{r}_N) - \frac{1}{2} \nabla_{\mathbf{r}_N}^2. \quad (7.1)$$

where the scattered electron is denoted by the subscript  $N$ , and the diatomic ion has  $N - 1$  electrons with positions  $\mathbf{r}_i$  and 2 nuclei with positions  $\mathbf{R}_i$  and charge  $Z_i$ :

$$\begin{aligned} \hat{H}_{\text{ion}} = & -\frac{1}{2} \sum_{i=1}^{N-1} \nabla_{\mathbf{r}_i}^2 - \frac{1}{2} \sum_{i=1}^2 \nabla_{\mathbf{R}_i}^2 - \sum_{i=1}^{N-1} \sum_{j=1}^2 \frac{Z_j}{|\mathbf{r}_i - \mathbf{R}_j|} + \sum_{i>j}^2 \frac{Z_i Z_j}{|\mathbf{R}_i - \mathbf{R}_j|} \\ & + \sum_{i>j}^{N-1} \frac{1}{|\mathbf{r}_i - \mathbf{r}_j|}. \end{aligned} \quad (7.2)$$

The term  $V_{\text{int}}$  is given by

$$V_{\text{int}} = - \sum_{i=1}^2 \frac{Z_i}{|\mathbf{r}_N - \mathbf{R}_i|} + \sum_{i=1}^{N-1} \frac{1}{|\mathbf{r}_N - \mathbf{r}_i|}. \quad (7.3)$$

In the fixed-nuclei approximation, the electronic problem can be treated alone, and the ion wavefunctions,  $\Phi_\gamma(\mathbf{x}_1, \dots, \mathbf{x}_{N-1}, R)$ , satisfy

$$\left( \hat{H}_{\text{ion}} - E_\gamma \right) \Phi_\gamma(\mathbf{x}_1, \dots, \mathbf{x}_{N-1}, R) = 0, \quad (7.4)$$

where the  $\mathbf{x}$  coordinate includes both space and spin, and  $R$  is the internuclear distance. The subscript  $\gamma$  represents the set of quantum numbers that fully describe an eigenstate of the ion. The total wavefunction  $\Psi(\mathbf{x}_1, \dots, \mathbf{x}_N, R)$  can be expanded in terms of the ion eigenfunctions:

$$\Psi(\mathbf{x}_1, \dots, \mathbf{x}_N, R) = A \sum_{\gamma} \Phi_{\gamma}(\mathbf{x}_1, \dots, \mathbf{x}_{N-1}, R) F_{\gamma}(\mathbf{x}_N), \quad (7.5)$$

where  $A$  is the antisymmetrizing operator and  $F_{\gamma}(\mathbf{x}_N)$  is the scattered electron function. The sum over  $\gamma$  allows different configurations of the target ion and scattered electron to contribute. When only the ground state wavefunction in this expansion is retained (which is the only case considered in this chapter), the static exchange approximation is obtained:

$$\Psi(\mathbf{x}_1, \dots, \mathbf{x}_N, R) = A \Phi(\mathbf{x}_1, \dots, \mathbf{x}_{N-1}, R) F(\mathbf{x}_N). \quad (7.6)$$

Since only closed shell ions are treated in this chapter, one can reduce Eq. (7.5) further by assuming the ion wavefunction,  $\Phi(\mathbf{x}_1, \dots, \mathbf{x}_{N-1}, R)$ , is known in the Hartree-Fock approximation to be a single determinant:

$$\Phi(\mathbf{x}_1, \dots, \mathbf{x}_{N-1}, R) = \frac{1}{\sqrt{(N-1)!}} |U_1(\mathbf{x}_1) \cdots U_{N-1}(\mathbf{x}_{N-1})|, \quad (7.7)$$

where the  $U_i(\mathbf{x}_i)$  are single-electron ion orbital functions. Substituting Eq. (7.7) into Eq. (7.6) and using the properties of Slater determinants [135], one can show that  $F(\mathbf{r})$  satisfies the integro-differential equation

$$\left[ -\frac{1}{2} \nabla^2 - \frac{1}{2} k^2 + V_s(\mathbf{r}) \right] F(\mathbf{r}) = \sum_{\alpha=1}^{N_{\text{occ}}} \left[ \int U_{\alpha}^*(\mathbf{s}) \frac{1}{|\mathbf{r}-\mathbf{s}|} F(\mathbf{s}) d\mathbf{s} \right] U_{\alpha}(\mathbf{r}), \quad (7.8)$$

where the static potential  $V_s(\mathbf{r})$  is

$$V_s(\mathbf{r}) = \sum_{\alpha=1}^{N_{\text{occ}}} \int U_{\alpha}^*(\mathbf{s}) \frac{1}{|\mathbf{r}-\mathbf{s}|} U_{\alpha}(\mathbf{s}) d\mathbf{s} + \sum_{i=1}^2 \frac{Z_i}{|\mathbf{r}-\mathbf{R}_i|}, \quad (7.9)$$

and

$$\frac{1}{2}k^2 = E - E_0, \quad (7.10)$$

with  $E_0$  being the ground state energy of the ion.

Eqs. (7.8)–(7.9) treat the evaluation of the scattered electron function within the framework of the static exchange approximation. Specifically, the local and nonlocal interactions of the scattered electron with the ion core are included, but correlation is completely neglected. The neglected correlation terms can be included approximately by adding a polarization potential to  $V_s$  of the form

$$V_{\text{pol}} = -\frac{1}{2r^4} (\alpha_0 + \alpha_2 P_2(\cos \theta)), \quad (7.11)$$

where  $\alpha_0$  and  $\alpha_2$  are the totally symmetric and nontotally symmetric components of the polarizability tensor which can be calculated using *ab initio* electronic structure codes. The additional  $V_{\text{pol}}$  term approximately accounts for any contribution coming from the distortion of the ion orbitals due to the perturbative effect of the impinging electron.

### 7.3 A Partial Differential Equation Approach

The single-electron ion orbital functions,  $U_\alpha(\mathbf{r})$ , can be obtained from conventional electronic structure programs in a basis set of Cartesian Gaussians. On the other hand, the evaluation of the continuum function  $F(\mathbf{r})$  as a function of  $k$  in Eq. (7.8) is more difficult. As discussed in Chapter 6,  $F(\mathbf{r})$ , oscillates significantly as a function of radial distance and does not even approach 0 as  $r \rightarrow \infty$  when the scattered electron energy exceeds the ionization energy. Consequently, Gaussian-type basis sets are not well-suited to approximate the free-particle wavefunction  $F(\mathbf{r})$  at large distances. Furthermore, some diatomics have highly polar ionic cores, which imply that the continuum function  $F(\mathbf{r})$  has some multi-center character; therefore, the nonlinear fits by single-center Gaussians discussed in Chapter 6 are not applicable. For these reasons, a partial differential equation (PDE) approach adapted to diatomics

is currently being used to solve Eq. (7.8). The necessary equations and methods are described in the present and following sections.

The integro-differential expression in Eq. (7.9) can be implemented in a PDE solver by rewriting it as

$$\left[ -\frac{1}{2}\nabla^2 - \frac{1}{2}k^2 + V_s(\mathbf{r}) \right] F(\mathbf{r}) = \sum_{\alpha=1}^{N_{\text{occ}}} W_{\alpha}(\mathbf{r}) U_{\alpha}(\mathbf{r}), \quad (7.12)$$

where  $W_{\alpha}(\mathbf{r})$  is the exchange integral

$$W_{\alpha}(\mathbf{r}) = \int U_{\alpha}^*(\mathbf{s}) \frac{1}{|\mathbf{r} - \mathbf{s}|} F(\mathbf{s}) d\mathbf{s}, \quad \alpha = 1, \dots, N_{\text{occ}}. \quad (7.13)$$

A useful property to remember is that the Coulomb potential is the Green's function of the Laplacian:

$$\nabla_{\mathbf{r}}^2 \frac{1}{|\mathbf{r} - \mathbf{s}|} = -4\pi\delta(\mathbf{r} - \mathbf{s}). \quad (7.14)$$

Therefore, when  $W_{\alpha}(\mathbf{r})$  is acted upon by the  $\nabla^2$  operator, one obtains

$$\begin{aligned} \nabla_{\mathbf{r}}^2 W_{\alpha}(\mathbf{r}) &= \int U_{\alpha}^*(\mathbf{s}) \nabla_{\mathbf{r}}^2 \frac{1}{|\mathbf{r} - \mathbf{s}|} F(\mathbf{s}) d\mathbf{s} \\ &= \int U_{\alpha}^*(\mathbf{s}) [-4\pi\delta(\mathbf{r} - \mathbf{s})] F(\mathbf{s}) d\mathbf{s} \\ &= -4\pi U_{\alpha}^*(\mathbf{r}) F(\mathbf{r}), \quad \alpha = 1, \dots, N_{\text{occ}}. \end{aligned} \quad (7.15)$$

Thus, Eq. (7.12) combined with Eq. (7.15) is a system of  $N_{\text{occ}} + 1$  coupled, three-dimensional PDE's for the scattering function  $F(\mathbf{r})$  and the exchange kernels  $W_{\alpha}(\mathbf{r})$ . It is important to note that this set of equations has no integral terms but must be solved simultaneously. If this PDE approach is confined to diatomic systems, the cylindrical symmetry can be used to reduce the dimensionality of the PDE system. For example, Figure 7-2 shows the coordinate system for a  $\text{CaF}^+$  ion aligned along the  $z$ -axis. The origin of the coordinate system is located at the center of mass of the  $\text{CaF}^+$  ion, and the orientation of the diatomic is chosen such that the dipole moment points towards the positive  $z$ -axis. Since  $m$  is a good quantum number, the azimuthal dependence is exactly separable in this coordinate system, and one can write:

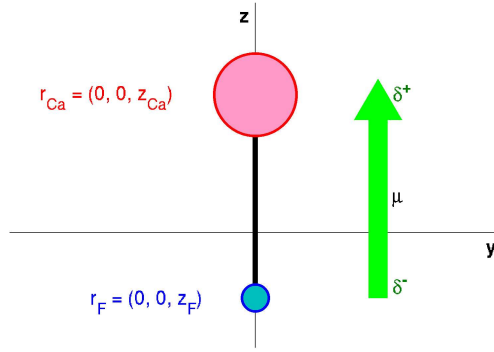


Figure 7-2: Coordinate system for a  $\text{CaF}^+$  ion used throughout Chapter 7. The  $\text{CaF}^+$  ion is aligned along the  $z$ -axis with the origin at its center of mass. The orientation of the  $z$ -axis is defined such that the dipole moment points towards the positive  $z$ -axis.

$$F^{(m)}(\mathbf{r}) = \frac{f^{(m)}(\mathbf{v})}{r\sqrt{1-\eta^2}} \frac{e^{im\phi}}{\sqrt{2\pi}}, \quad (7.16)$$

and

$$U_\alpha(\mathbf{r}) = \frac{u_\alpha(\mathbf{v})}{r\sqrt{1-\eta^2}} \frac{e^{im_\alpha\phi}}{\sqrt{2\pi}}, \quad (7.17)$$

where  $\eta = \cos\theta$ , and the vector  $\mathbf{v}$  has two components given by  $\mathbf{v} = (r, \eta)$ . The azimuthal quantum numbers  $m$  and  $m_\alpha$  are restricted to integer values, i.e., 0 for  $\sigma$  orbitals,  $\pm 1$  for  $\pi$  orbitals,  $\pm 2$  for  $\delta$  orbitals, etc.

The Laplacian in the  $(r, \eta, \phi)$  coordinates is given by

$$\nabla^2 = \frac{1}{r^2} \frac{\partial}{\partial r} \left( r^2 \frac{\partial}{\partial r} \right) + \frac{1}{r^2} \frac{\partial}{\partial \eta} \left[ (1-\eta^2) \frac{\partial}{\partial \eta} \right] + \frac{1}{r^2(1-\eta^2)} \frac{\partial^2}{\partial \phi^2}. \quad (7.18)$$

Substituting this form of the Laplacian in Eq. (7.12) and using the definition in Eq. (7.17) gives, after significant manipulation,

$$\begin{aligned}
& \left( \frac{1}{2} \left[ \frac{1}{\sqrt{1-\eta^2}} \frac{\partial^2}{\partial r^2} f^{(m)}(\mathbf{v}) + \frac{f^{(m)}(\mathbf{v})}{r^2 (1-\eta^2)^{3/2}} + \frac{\sqrt{1-\eta^2}}{r^2} \frac{\partial^2}{\partial \eta^2} f^{(m)}(\mathbf{v}) \right. \right. \\
& \quad \left. \left. - \frac{m^2 f^{(m)}(\mathbf{v})}{r^2 (1-\eta^2)^{3/2}} \right] + \frac{1}{2} \frac{k^2 f^{(m)}(\mathbf{v})}{\sqrt{1-\eta^2}} \right) e^{im\phi} \\
& = V(\mathbf{v}) \frac{f^{(m)}(\mathbf{v})}{\sqrt{1-\eta^2}} e^{im\phi} - \sum_{\alpha=1}^{N_{\text{occ}}} W_{\alpha}^{(m)}(\mathbf{r}) \frac{u_{\alpha}(\mathbf{v})}{\sqrt{1-\eta^2}} e^{im_{\alpha}\phi}.
\end{aligned} \tag{7.19}$$

Substituting Eqs. (7.16) and (7.17) in Eq. (7.15) gives

$$\nabla_{\mathbf{r}}^2 W_{\alpha}^{(m)}(\mathbf{r}) = -2 \frac{u_{\alpha}^*(\mathbf{v}) f^{(m)}(\mathbf{v})}{r^2 (1-\eta^2)} e^{i(m-m_{\alpha})\phi}, \quad \alpha = 1, \dots, N_{\text{occ}}. \tag{7.20}$$

One can also use cylindrical symmetry to define the following:

$$W_{\alpha}^{(m)}(\mathbf{r}) = \frac{w_{\alpha}^{(m)}(\mathbf{v})}{r \sqrt{1-\eta^2}} e^{i(m-m_{\alpha})\phi}. \tag{7.21}$$

Substituting this definition in Eqs. (7.19)–(7.20), and after even more manipulation, one finally obtains

$$\begin{aligned}
& \frac{\partial^2}{\partial r^2} \frac{f^{(m)}(\mathbf{v})}{1-\eta^2} + \frac{(1-m^2) f^{(m)}(\mathbf{v})}{r^2 (1-\eta^2)^2} + \frac{\partial^2}{\partial \eta^2} \frac{f^{(m)}(\mathbf{v})}{r^2} + \frac{k^2 f^{(m)}(\mathbf{v})}{1-\eta^2} \\
& = 2V(\mathbf{v}) \frac{f^{(m)}(\mathbf{v})}{1-\eta^2} - \sum_{\alpha=1}^{N_{\text{occ}}} \frac{2w_{\alpha}^{(m)}(\mathbf{v}) u_{\alpha}(\mathbf{v})}{r (1-\eta^2)^{3/2}},
\end{aligned} \tag{7.22}$$

and

$$\begin{aligned}
& \frac{\partial^2}{\partial r^2} \frac{w_{\alpha}^{(m)}(\mathbf{v})}{1-\eta^2} + \frac{[1-(m-m_{\alpha})^2] w_{\alpha}^{(m)}(\mathbf{v})}{r^2 (1-\eta^2)^2} + \frac{\partial^2}{\partial \eta^2} \frac{w_{\alpha}^{(m)}(\mathbf{v})}{r^2} \\
& = -\frac{2u_{\alpha}^*(\mathbf{v}) f^{(m)}(\mathbf{v})}{r (1-\eta^2)^{3/2}}, \quad \alpha = 1, \dots, N_{\text{occ}}.
\end{aligned} \tag{7.23}$$

Therefore, by exploiting the cylindrical symmetry, the original  $N_{\text{occ}}+1$  coupled, three-dimensional PDE's have been reduced to a system of  $N_{\text{occ}}+1$  coupled, two-dimensional PDE's in Eqs. (7.22)–(7.23).

## 7.4 Boundary Conditions Adapted for Long Range Dipoles

The basic principle of the MQDT method, as mentioned in Chapter 6, maintains that the asymptotic behavior of  $F(\mathbf{r})$  in Eq. (7.16) must be represented by a superposition of the regular and irregular solutions,  $f(E, r)$  and  $g(E, r)$ , of the Schrödinger equation. Once these two outer region functions are known, they can be smoothly matched to the continuum function,  $F(\mathbf{r})$ , inside the  $\mathbf{K}$  matrix sphere. Consequently, the MQDT method relies on an accurate knowledge of the  $f(E, r)$  and  $g(E, r)$  base pairs for arbitrary positive or negative energy. However, since the diatomics considered in this chapter have large electric dipole moments, one must additionally consider the long-range effect of the dipole field on the  $f(E, r)$  and  $g(E, r)$  functions. Following the example of Yoo and Greene [4], to improve convergence issues, it is necessary to modify the conventional  $f(E, r)$  and  $g(E, r)$  functions for the dipole interaction.

In the asymptotic limit,  $r \gg R$ , a multipole expansion can be performed to obtain the potential of the ion in powers of  $1/r$ . Using the coordinate system defined in Figure 7-2, the first two terms in the multipole expansion yield [152]

$$V = -\frac{1}{r} - \frac{|\mu| \cos \theta}{r^2}, \quad (7.24)$$

where  $|\mu|$  is the magnitude of the dipole moment and  $\theta$  is the polar angle from the  $z$ -axis. Therefore, the Schrödinger equation for the Rydberg electron in the large  $r$  limit is

$$\left( -\frac{1}{2} \nabla^2 - \frac{1}{r} - \frac{|\mu| \cos \theta}{r^2} - E \right) F(r, \theta, \phi) = 0, \quad r \gg R. \quad (7.25)$$

When the Laplacian is expressed in spherical coordinates, the solution to Eq. (7.25) is still exactly separable in the form:

$$F(r, \theta, \phi) = R(r) \Theta(\theta) \Phi(\phi). \quad (7.26)$$

After some effort, one obtains separate angular and radial equations:

$$\frac{1}{\sin \theta} \frac{d}{d\theta} \left( \sin \theta \frac{d\Theta(\theta)}{d\theta} \right) + \left[ l_{\text{eff}}(l_{\text{eff}} + 1) + 2|\mu| \cos \theta - \frac{m^2}{\sin^2 \theta} \right] \Theta(\theta) = 0, \quad (7.27)$$

and

$$\frac{1}{r^2} \frac{d}{dr} \left( r^2 \frac{dR(r)}{dr} \right) + \frac{2}{r} R(r) - \frac{l_{\text{eff}}(l_{\text{eff}} + 1)}{r^2} R(r) + 2ER(r) = 0, \quad (7.28)$$

where  $m$  is the same integer value as specified in Eq. (7.16), and  $l_{\text{eff}}(l_{\text{eff}} + 1)$  is the separation constant

Both Eqs. (7.27) and (7.28) are solved simultaneously in two steps. First, the eigenvalues,  $-l_{\text{eff}}(l_{\text{eff}} + 1)$ , and the eigenfunctions,  $\Theta(\theta)$ , of Eq. (7.27) are found for a given value of  $E$  and  $m$ . Once the eigenvalue  $-l_{\text{eff}}(l_{\text{eff}} + 1)$  is obtained, Eq. (7.28) can be integrated numerically, and depending on the boundary conditions imposed, the regular solution,  $f(E, r)$ , or the irregular solution,  $g(E, r)$ , will be obtained. Eq. (7.27) is solved efficiently by expanding  $\Theta(\theta)\Phi(\phi)$  in terms of spherical harmonics:

$$\Theta(\theta) \Phi(\phi) = \sum_{k=m}^{\infty} f_k^m Y_k^m(\theta, \phi). \quad (7.29)$$

Using properties of the spherical harmonics and the Wigner  $3j$  symbols, the eigenvalues  $-l_{\text{eff}}(l_{\text{eff}} + 1)$  and coefficients  $f_k^m$  can be obtained by diagonalizing a symmetric tridiagonal matrix,  $\mathbf{F}$ , with elements given by [153]:

$$F_{i,i} = -i(i+1), \quad (7.30)$$

$$F_{i,i+1} = F_{i+1,i} = 2|\mu| \left[ \frac{(i+m+1)(i-m+1)}{(2i+1)(2i+3)} \right]^{1/2}, \quad (7.31)$$

which are modified from the original expressions of Ref. [153] to follow the specific form of Eq. (7.27). Since the eigenvalues  $-l_{\text{eff}}(l_{\text{eff}} + 1)$  depend on both  $|\mu|$  and  $m$ ,  $l_{\text{eff}}$  is not an integer in general. Actually, for sufficiently strong dipole moments,  $l_{\text{eff}}(l_{\text{eff}} + 1)$  may become negative, and therefore,  $l_{\text{eff}}$  will be imaginary. For example,



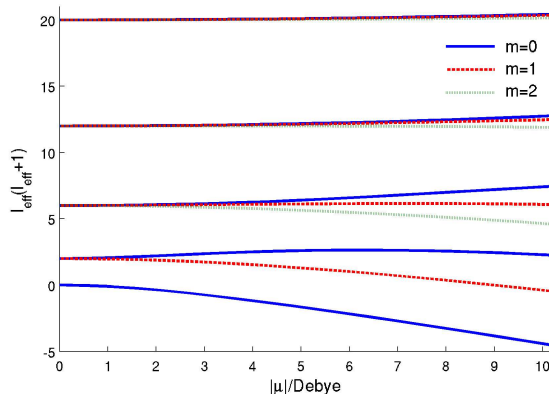


Figure 7-3: Values of  $l_{\text{eff}}(l_{\text{eff}} + 1)$ , obtained from Eq. (7.27) as a function of the dipole moment. The solid lines are eigenvalues for  $m = 0$ . The dashed and dotted lines correspond to  $m = 1$  and  $2$ , respectively. For sufficiently strong dipole moments,  $l_{\text{eff}}(l_{\text{eff}} + 1)$  will become negative.

the first few  $l_{\text{eff}}(l_{\text{eff}} + 1)$  values for  $m = 0, 1$ , and  $2$  are shown as functions of  $|\mu|$  in Figure 7-3. When  $l_{\text{eff}}(l_{\text{eff}} + 1)$  is sufficiently negative, the potential including the centrifugal term will become attractive. Figures 7-4 (a)–(b) show two plots of orbitals obtained from Eq. (7.27) with a 8.6863 Debye dipole located at the origin (the  $\text{CaF}^+$  ion at its equilibrium internuclear distance has a dipole moment of 8.6863 Debye at the CCSD(full) level with the cc-pCVTZ basis). For low  $l$  and  $m$ , there is strong polarization away from the negative charge, but the hydrogenic orbitals are recovered for higher  $l$  and  $m$  values.

Once  $-l_{\text{eff}}(l_{\text{eff}} + 1)$  has been obtained for a given energy and  $m$  value, Eq. (7.28) can, in principle, be integrated to give  $f(E, r)$  and  $g(E, r)$ . Unfortunately, the solution of Eq. (7.28) for use in quantum defect theory studies is, in practice, quite complicated and still a topic of active research [154, 155, 156, 157, 158]. This difficulty arises because quantum defect theory relies on long-range solutions which vary smoothly with energy and radius. When the initial conditions for Eq. (7.28) are poorly chosen, the quantum defect parameters oscillate uncontrollably as a function of energy (see, for example, Figure 7-6 (a)). Yoo and Greene [4] were the first researchers to describe a method which eliminates the energy dependence in the basis functions. Recently, Jungen and Texier proposed an alternative algorithm based on a third order WKB



Figure 7-4: Angular plots of  $\text{Re}(\Theta(\theta)\Phi(\phi))$  evaluated for a 8.6863 Debye dipole at the origin. The negative  $z$ -axis corresponds to the position of a negative partial charge. Figure 7-4 (a) depicts a  $4s\sigma$  orbital which is strongly polarized away from the negative charge, and (b) depicts a  $4f\phi$  orbital which resembles a hydrogenic orbital.

method [154]. The technical details of their approach can be found in Refs. [4] and [154], and only the equations adapted to the dipole case in this chapter will be described in detail.

The expression in Eq. (7.28) can be reduced to a form required in Ref. [4] by defining the reduced radial function  $R(r) = u(r)/r$ . Substituting this definition in Eq. (7.28) gives

$$\left[ \frac{d^2}{dr^2} + k^2(r) \right] u(r) = 0, \quad (7.32)$$

where

$$k^2(r) = E + \frac{2}{r} - \frac{l_{\text{eff}}(l_{\text{eff}} + 1)}{r^2}. \quad (7.33)$$

In Eq. (7.33), Rydberg units are used with  $E = 2E_{\text{a.u.}}$ . The linearly independent regular and irregular functions of Eq. (7.32) can be expressed exactly in the forms

$$f(E, r) = \sqrt{\frac{1}{\pi}} \alpha(E, r) \sin \left[ \int_0^r \alpha^{-2}(E, r') dr' \right], \quad (7.34)$$

and

$$g(E, r) = -\sqrt{\frac{1}{\pi}} \alpha(E, r) \cos \left[ \int_0^r \alpha^{-2}(E, r') dr' \right], \quad (7.35)$$

where  $f(E, r)$  and  $g(E, r)$  are energy-normalized in Rydberg units. The amplitude function  $\alpha(E, r)$  satisfies the differential equation

$$\frac{d^2\alpha(r)}{dr^2} + k^2(r)\alpha(r) = \alpha^{-3}(r). \quad (7.36)$$

Therefore, obtaining  $f(E, r)$  and  $g(E, r)$  amounts to solving Eq. (7.36) and substituting the result into the definitions in Eqs. (7.34)–(7.35). It is important to note that the solution of Eq.(7.36) in itself does not guarantee that the energy dependences will be minimized. Their purpose in Ref. [4] is to provide the boundary conditions  $\alpha(r_c)$  and  $\alpha'(r_c)$  at a radius  $r_c$ , which minimizes the oscillations as a function of energy. The solution proposed by Yoo and Greene is to choose  $r_c$  at the potential minimum or at a small radius if the potential has no minimum. After a lengthy derivation, the numerical values of  $\alpha(r_c)$  and  $\alpha'(r_c)$  can be obtained by integrating Eq. (7.36) inward from a large radius,  $r_f$ , (around 1000 Bohrs) using the boundary conditions:

$$\alpha(r_f) = k^{-1/2}(r_f), \quad E > 0, \quad (7.37)$$

$$\alpha'(r_f) = \frac{d}{dr} [k^{-1/2}(r)]_{r_f}, \quad E > 0. \quad (7.38)$$

This procedure is carried out at several values of  $E > 0$ , and the data points are fitted and extrapolated to negative energies below threshold. Figure 7-5 illustrates this procedure for a Coulomb potential with  $l = 1$ . The values of  $\alpha(r_c)$  are determined at positive energies using Eqs. (7.37)–(7.38), and are fitted to a spline which smoothly extrapolates to negative energies. A similar procedure is used for  $\alpha'(r_c)$ .

Once this procedure is finished, one has all the necessary boundary conditions to integrate Eq. (7.36) smoothly for arbitrary energy. The accuracy of this procedure is best illustrated by plotting the “accumulated phase”  $\beta(E)/\pi$  defined by

$$\beta(E)/\pi = \frac{1}{\pi} \int_0^\infty \alpha^{-2}(E, r) dr. \quad (7.39)$$

The oscillations of  $\beta(E)$  qualitatively measure the energy-dependence of the basis functions  $f(E, r)$  and  $g(E, r)$  (see Eqs. (7.34)–(7.35)). When the basis functions  $f(E, r)$  and  $g(E, r)$  are strongly energy-dependent, this translates into large oscillations in  $\beta(E)$ , which one would like to diminish as much as possible. Figures

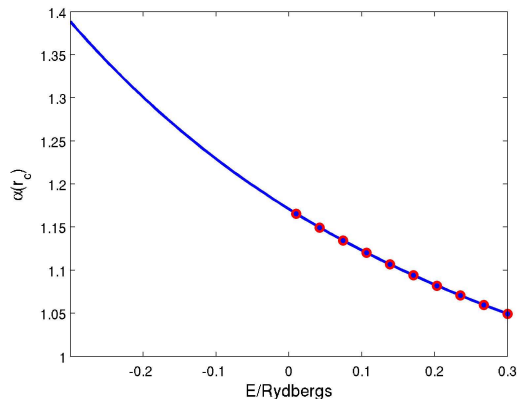


Figure 7-5: Optimal values of  $\alpha(r_c)$  as a function of energy for a  $l = 1$  Coulomb potential. The circles at  $E > 0$  were determined by integrating Eq. (7.36) using the boundary conditions in Eqs. (7.37)–(7.38). The solid curve is a spline fit to the circles only which smoothly extrapolates to  $E < 0$ .

7-6 (a)–(b) show plots of  $\beta(E)$  as a function of energy for a pure  $l = 2$  Coulomb potential. The accumulated phase  $\beta(E)/\pi$  is analytically known for the Coulomb potential and is given by  $\beta_{\text{Coulomb}}(E)/\pi = \nu - l = (-E)^{-1/2} - l$  in Rydberg units [4]. Therefore, by plotting the deviation from the analytically known accumulated phase,  $\beta(E)/\pi - (\nu - l)$ , one can compare the quality of various numerical methods. Figure 7-6 (a) shows deviations,  $\beta(E)/\pi - (\nu - l)$ , calculated from the extrapolation procedure described previously (full curves) and using a zero-order WKB approximation for  $\alpha(r_c)$  and  $\alpha'(r_c)$  described in Ref. [4] (broken curves). At the energies  $\nu = n$  with  $n$  an integer, the deviation for both methods is exactly zero, as they must be since these are true bound state eigenvalues of the Coulomb potential ( $E = -1/n^2$ ). However, it is apparent in Figure 7-6 (a) that the deviations are very small for the extrapolation procedure in comparison to the larger oscillations obtained with a WKB method. In fact, the oscillations from the extrapolation procedure are unnoticeable in Figure 7-6 (a), and one must magnify the vertical scale by an order of magnitude to observe them in Figure 7-6 (b). Therefore, by enforcing these optimal boundary conditions in Eq. (7.36), the functions  $f(E, r)$  and  $g(E, r)$  can be obtained as smooth and weakly-dependent functions of the energy. For these reasons, the extrapolation procedure described here (along with the solution to Eq. (7.27)) is currently be-

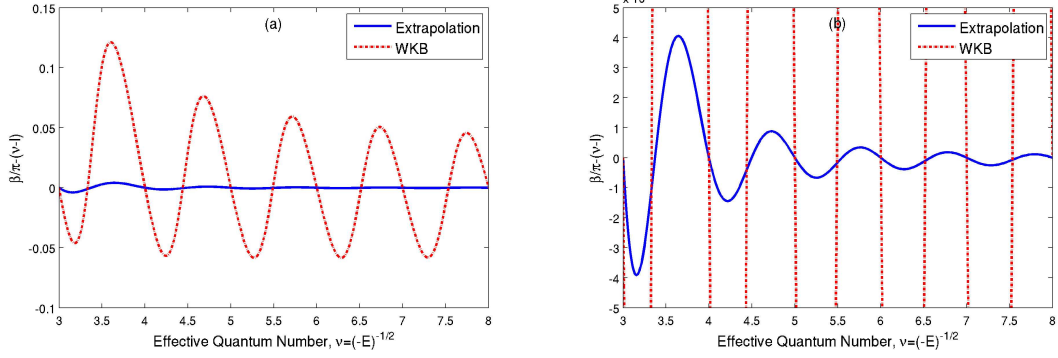


Figure 7-6: (a) Deviations between a numerically calculated  $l = 2$  Coulomb phase  $\beta(E)/\pi$  and its analytical value  $\nu - l$ . The dashed curve was obtained using a WKB boundary condition to approximate  $\alpha(r_c)$  at the minimum of the effective potential [4]. The solid curve was obtained from the extrapolated boundary condition described in this chapter. (b) Magnified plot of Figure 7-6 (a).

ing used to obtain an optimal set of continuum functions incorporating the dipole interaction.

## 7.5 The Finite Element Approach

Now that the PDE's are specified (Section 7.3) and their boundary conditions known (Section 7.4), one can finally discuss their numerical solution. The coupled, two-dimensional system of PDE's in Eqs. (7.22)–(7.23) subject to the complicated boundary conditions of Section 7.4 are most easily solved using finite element methods. The central idea of the finite element method is the use of simple basis sets which are localized only within small regions. Therefore, by using many “elements” over which the basis functions are defined, it is possible to reproduce very complex features of the differential equation solution. This basic idea is most easily understood in the following one-dimensional example. The simplest basis sets in one dimension are piecewise linear functions  $F_k$  whose value is 1 at  $x_k$  and 0 at every  $x_j$  where  $j \neq k$ ; i.e.,

$$F_k(x) = \begin{cases} \frac{x-x_{k-1}}{x_k-x_{k-1}}, & \text{if } x \in [x_{k-1}, x_k], \\ \frac{x_{k+1}-x}{x_{k+1}-x_k}, & \text{if } x \in [x_k, x_{k+1}], \\ 0, & \text{otherwise.} \end{cases} \quad (7.40)$$

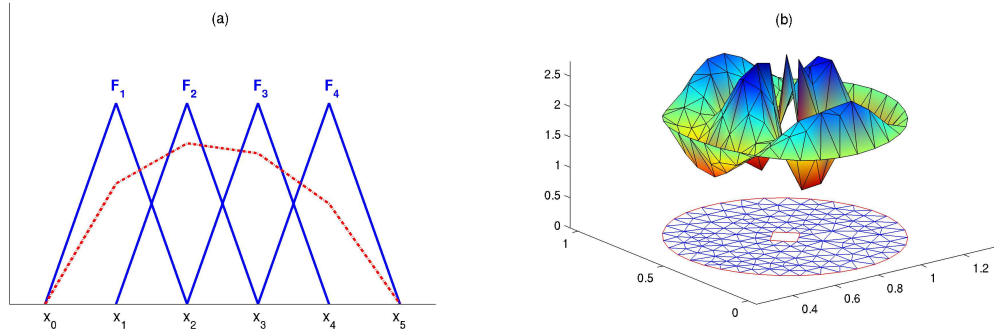


Figure 7-7: (a) Four piecewise linear basis functions (solid lines) for the one-dimensional finite element method. A linear combination of them is shown as a broken line. (b) Piecewise linear basis functions in two dimensions. A triangular mesh is plotted in the  $xy$ -plane, and the linear combination of basis functions is plotted above it. (For the curious reader, Figure 7-7 (b) depicts a solution to the Helmholtz's differential equation for waves reflecting off a  $0.1 \times 0.1$  square in the center.)

for  $k = 1, \dots, n$ . Four of these piecewise linear basis functions localized on four grid points are shown in Figure 7-7 (a). Each triangular basis function,  $F_k(x)$  (full lines), only has an overlap with its neighboring functions,  $F_{k-1}(x)$  and  $F_{k+1}(x)$ . In this way, a linear combination of these basis functions can be used to approximate any continuous function (broken line). This discretization is more delicate in two dimensions since the domain may have a complicated geometry. Analogous to the one-dimensional case, the two-dimensional domain can be split into small triangles. Next, the function can then be approximated by its value on each triangle as depicted in Figure 7-7 (b). The algorithms in two-dimensions are more complicated since the value on a given triangle depends on the value on the neighboring triangles (in one dimension, the value at a point depends only on the values of the left and right functions).

Fortunately, due to their widespread use in mechanical engineering, several finite element solvers are currently available which can mesh any geometry to solve PDE's automatically. The finite element software used in the current work utilizes the MATLAB PDE Toolbox developed by COMSOL Ltd. In order to use the capabilities of the software, the  $N$  coupled PDE's must be written in the somewhat awkward form:

$$-\nabla \cdot (\mathbf{c} \otimes \nabla \mathbf{u}) + \mathbf{a} \mathbf{u} = \mathbf{f}, \quad (7.41)$$

where  $\mathbf{c}$  is an  $N$ -by- $N$ -by-2-by-2 tensor. In the notation of the MATLAB PDE Toolbox, the expression  $\nabla \cdot (\mathbf{c} \otimes \nabla \mathbf{u})$  refers to the  $N \times 1$  matrix with  $(i, 1)$ -component

$$\sum_{j=1}^N \left( \frac{\partial}{\partial x} c_{i,j,1,1} \frac{\partial}{\partial x} + \frac{\partial}{\partial x} c_{i,j,1,2} \frac{\partial}{\partial y} + \frac{\partial}{\partial y} c_{i,j,2,1} \frac{\partial}{\partial x} + \frac{\partial}{\partial y} c_{i,j,2,2} \frac{\partial}{\partial y} \right) u_j. \quad (7.42)$$

The variable,  $\mathbf{a}$ , denotes an  $N \times N$  matrix, and both  $\mathbf{u}$  and  $\mathbf{f}$  are column vectors of length  $N$ . For the special case of the electron scattering PDE's specified in Eqs. (7.22)–(7.23), the  $\mathbf{c}$  tensor is diagonal with elements

$$c_{i,j,k,l} = -\delta_{i,j} \begin{pmatrix} \frac{1}{1-\eta^2} & 0 \\ 0 & \frac{1}{r^2} \end{pmatrix}, \quad (7.43)$$

and  $\mathbf{a}$  is given by the symmetric  $(N_{\text{occ}} + 1) \times (N_{\text{occ}} + 1)$  matrix

$$\mathbf{a} = \begin{pmatrix} \frac{1-m^2}{r^2(1-\eta^2)^2} + \frac{k^2-2V(\mathbf{v})}{1-\eta^2} & \frac{2u_1(\mathbf{v})}{r(1-\eta^2)^{3/2}} & \frac{2u_2(\mathbf{v})}{r(1-\eta^2)^{3/2}} & \cdots & \frac{2u_{N_{\text{occ}}}(\mathbf{v})}{r(1-\eta^2)^{3/2}} \\ \frac{2u_1(\mathbf{v})}{r(1-\eta^2)^{3/2}} & \frac{1-(m-m_1)^2}{r^2(1-\eta^2)^2} & 0 & \cdots & 0 \\ \frac{2u_2(\mathbf{v})}{r(1-\eta^2)^{3/2}} & 0 & \frac{1-(m-m_2)^2}{r^2(1-\eta^2)^2} & \cdots & 0 \\ \vdots & \vdots & \vdots & \ddots & \vdots \\ \frac{2u_{N_{\text{occ}}}(\mathbf{v})}{r(1-\eta^2)^{3/2}} & 0 & 0 & \cdots & \frac{1-(m-m_{N_{\text{occ}}})^2}{r^2(1-\eta^2)^2} \end{pmatrix}. \quad (7.44)$$

In addition,  $\mathbf{u}$  is the  $(N_{\text{occ}} + 1)$  column vector given by

$$\mathbf{u} = \begin{pmatrix} f^{(m)}(\mathbf{v}) \\ w_1^{(m)}(\mathbf{v}) \\ w_2^{(m)}(\mathbf{v}) \\ \vdots \\ w_{N_{\text{occ}}}^{(m)}(\mathbf{v}) \end{pmatrix}, \quad (7.45)$$

and  $\mathbf{f}$  is a  $(N_{\text{occ}} + 1)$  column vector of zeros.

Based on the definitions in Eqs. (7.16)–(7.17), the boundary conditions for the system of PDE's at  $\eta = 1$  and  $\eta = -1$  are given by

$$w_{\alpha}^{(m)}(r, \eta = 1) = w_{\alpha}^{(m)}(r, \eta = -1) = 0, \quad \alpha = 1, \dots, N_{\text{occ}}, \quad (7.46)$$

$$f^{(m)}(r, \eta = 1) = f^{(m)}(r, \eta = -1) = 0, \quad (7.47)$$

and the boundary conditions at  $r = 0$  and  $r = \rho$ , where  $\rho$  is taken large enough to approximately enclose the molecular charge cloud, are

$$w_{\alpha}^{(m)}(r = 0, \eta) = w_{\alpha}^{(m)}(r = \rho, \eta) = 0, \quad \alpha = 1, \dots, N_{\text{occ}}, \quad (7.48)$$

$$f^{(m)}(r = 0, \eta) = 0 \text{ and } f^{(m)}(r = \rho, \eta) = \text{constant} \times \sqrt{1 - \eta^2} \Theta(\eta), \quad (7.49)$$

where  $\Theta(\eta)$  is the solution to Eq. (7.27) expressed in the coordinate  $\eta = \cos(\theta)$ . The last condition in Eq. (7.49) reflects the MQDT principle that at large  $r$ , the scattered electron wavefunction must be described as a dipolar spherical harmonic. In the language of the MATLAB PDE Toolbox, the boundary conditions must be written in the form

$$\mathbf{h}\mathbf{u} = \mathbf{r}, \quad (7.50)$$

where  $\mathbf{h}$ , for the present case, is a  $(N_{\text{occ}} + 1) \times (N_{\text{occ}} + 1)$  diagonal matrix of ones, and  $\mathbf{r}$  is the  $(N_{\text{occ}} + 1)$  column vector given by

$$\mathbf{r} = \begin{pmatrix} \text{constant} \times \sqrt{1 - \eta^2} \Theta(\eta) \\ 0 \\ 0 \\ \vdots \\ 0 \end{pmatrix}. \quad (7.51)$$

Therefore, one can envisage Eqs. (7.22)–(7.23) being integrated in a rectangle with boundary conditions shown in Figures 7-8 (a)–(b).

All that remains to complete the finite element approach is to obtain  $V(\mathbf{v})$  and



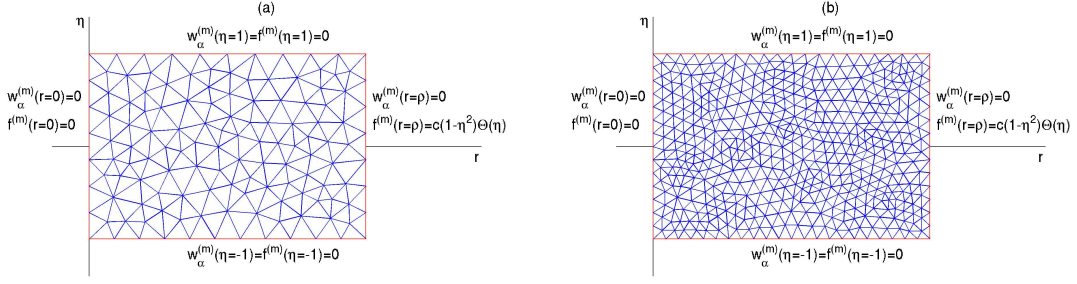


Figure 7-8: (a) Boundary conditions for integrating Eqs. (7.22)–(7.23) using a sparse finite element mesh. (b) A more refined version of the triangular mesh shown in Figure 7-8 (a).

$u(\mathbf{v})$ . It is important to note that the entire derivation in Section 7.3 relies on expressing both  $V(\mathbf{v})$  and  $u(\mathbf{v})$  in terms of cylindrically symmetric functions with the form  $f(r, \eta)e^{im\phi}$ . Unfortunately, none of the widely used quantum chemistry codes use complex-valued basis functions to express the bound orbitals  $u(\mathbf{v})$ . Instead, these programs perform calculations with Cartesian Gaussians of the form

$$x_A^l y_A^m z_A^n e^{-\alpha r_A^2}, \quad (7.52)$$

where  $x_A$ ,  $y_A$ , and  $z_A$  are the components of a position vector  $r_A$  relative to  $A$  ( $r_A = r - A$ ), and  $l$ ,  $m$ , and  $n$  are integers. Without going into further details here, one must transform the Cartesian orbitals  $u(\mathbf{v})$  to pure cylindrical functions using the properties of the spherical harmonics. The procedure for obtaining  $V(\mathbf{v})$  is to convert both terms in Eq. (7.9) to pure cylindrical functions. The second term in Eq. (7.9) is easily converted:

$$\sum_{i=1}^2 \frac{Z_i}{|\mathbf{r} - \mathbf{R}_i|} = \sum_{i=1}^2 \frac{Z_i}{\sqrt{r^2 - 2z_i r \eta + z_j^2}}. \quad (7.53)$$

The integral term in Eq. (7.9) can be calculated analytically using Cartesian Gaussians [126], and the final result, which is a function of the scattered electron coordinate  $\mathbf{r}$ , can be converted to pure cylindrical functions as in Eq. (7.53).

## 7.6 Extracting the $\mathbf{K}$ matrix

Since the  $\Theta_l(\theta)$  solutions of Eq. (7.27) form a complete set, the finite element solutions,  $f_l^{(m)}(\mathbf{v})$ , can be expanded as

$$\frac{f_l^{(m)}(\mathbf{v})}{r\sqrt{1-\eta^2}} = \frac{f_l^{(m)}(r, \theta)}{r \sin \theta} = \sum_{l'} f_{l'}^{(m)}(r) \Theta_{l'}(\theta), \quad (7.54)$$

where  $f_l^{(m)}(\mathbf{v})$  denotes a particular solution from the finite element method with the boundary condition  $f_l^{(m)}(r = \rho, \eta) = \text{constant} \times \sqrt{1-\eta^2} \Theta_l(\eta)$ . In Eq. (7.54),  $f_{l'}^{(m)}(r)$  is only a function of  $r$ . Multiplying both sides of Eq. (7.54) by  $\Theta_l(\theta) \sin \theta$  gives

$$\frac{f_l^{(m)}(r, \theta) \Theta_l(\theta)}{r} = \sum_{l'} f_{l'}^{(m)}(r) \Theta_{l'}(\theta) \Theta_l(\theta) \sin \theta. \quad (7.55)$$

Since the solutions to Eq. (7.27),  $\Theta_l(\theta)$ , are also orthogonal with the weighting function  $\sin \theta$ , both sides of Eq. (7.55) can be integrated to give

$$f_l^{(m)}(r) = \int_0^\pi \frac{f_l^{(m)}(r, \theta) \Theta_l(\theta)}{r} d\theta. \quad (7.56)$$

The MQDT method gives an additional equation for  $f_l^{(m)}(r, \theta)$ :

$$\begin{aligned} \frac{f_l^{(m)}(\mathbf{v})}{r\sqrt{1-\eta^2}} &= \frac{f_l^{(m)}(r, \theta)}{r \sin \theta} \\ &= \sum_{l'} \left[ A_{l,l'} \frac{f_{l'}(E, r)}{r} + B_{l,l'} \frac{g_{l'}(E, r)}{r} \right] \Theta_{l'}(\theta), \quad r \gg R, \end{aligned} \quad (7.57)$$

where the scattering reaction matrix  $\mathbf{K}$ , is given by

$$\mathbf{K} = \mathbf{A}^{-1} \mathbf{B}. \quad (7.58)$$

Comparing Eqs. (7.54) and (7.57) gives

$$f_{l'}^{(m)}(r) = A_{l,l'} \frac{f_{l'}(E, r)}{r} + B_{l,l'} \frac{g_{l'}(E, r)}{r}, \quad r \gg R. \quad (7.59)$$

Substituting the result of Eq. (7.56) in Eq. (7.59) gives

$$\int_0^\pi f_l^{(m)}(r, \theta) \Theta_l(\theta) d\theta = A_{l,l'} f_l(E, r) + B_{l,l'} g_l(E, r), \quad r \gg R. \quad (7.60)$$

The continuum functions  $f_l(E, r)$  and  $g_l(E, r)$  can be calculated using the methods described in Section 7.4. The integral on the left hand side of Eq. (7.60) can also be computed once the solution  $f_l^{(m)}(r, \theta)$  is obtained from the finite element method. Therefore, to determine the matrix elements  $A_{l,l'}$  and  $B_{l,l'}$  (and hence  $\mathbf{K}$ ), one can choose two large values of  $r$ , such as  $r = \rho$  and  $r = \rho - \Delta r$ , and evaluate Eq. (7.60). For a given value of  $l$ , this procedure results in two equations with two unknowns which can be solved simultaneously to obtain  $A_{l,l'}$  and  $B_{l,l'}$ . The remaining matrix elements  $A_{l,l'}$  and  $B_{l,l'}$  can be obtained by re-solving the finite element equations for different values of  $l$  and performing the previously described procedure. This finally completes the method for determining the  $\mathbf{K}$  matrix from a multi-electron approach.

## 7.7 Conclusion

This chapter has thoroughly described a procedure to obtain the reaction matrix  $\mathbf{K}$  for electron scattering in highly polar diatomics. The technique makes use of transforming an integro-differential equation to a system of two-dimensional PDE's which have no integral terms. A numerical method to reduce the energy-dependent oscillations and dipole interactions of the continuum functions is also presented for use in the current study. The resulting equations and boundary conditions are particularly suited for widely available finite element solvers. Finally, the methods outlined in this chapter are currently in the finishing stages of completion and further applications are forthcoming.



# Chapter 8

## Conclusion

### 8.1 Summary

The physical properties of three very different chemical systems have been considered in this thesis: (1) large-amplitude vibrations on ground-state singlet surfaces, (2) the photophysics of electronically excited triplet states germane to doorway-mediated intersystem crossing, and (3) electron-molecule collisions of Rydberg states. On a practical level, each of these separate chemical systems requires a completely different computational approach to describe their complicated nature. On a conceptual level, however, these studies share a common philosophical framework: all of these examples are closely connected to experimental observables or have some connection to chemically intuitive models. For example, Chapters 2–4 illustrate the intuitive idea that when a large-amplitude motion alters a molecular geometry, the electronic structure of the molecule changes as well. This change in electronic structure conveys barrier-relevant information to the spectroscopist. Chapter 5 demonstrates the use of a simple two-dimensional model to decouple two electronically excited triplet states. This simple but powerful model suggests a plausible vibrational assignment in the dense forest of other nearly degenerate vibrational states. Chapters 6–7, which seem to address the most complicated of all the systems presented here, are actually based on the simplest idea: Rydberg states can be described as hydrogenic orbitals because scattering is a *localized* process. The strong electron-nuclear interactions occur during

a short period of time and are confined to a limited region of space. It is these localized interactions which alter a Rydberg electron's global trajectory in free space and provide a mechanism for energy exchange between the Rydberg electron and the ion core. The simple intuitive models coupled with the rigorous theoretical approaches presented in these studies make them useful tools for further developments in both theory and experiment.

## 8.2 Future Directions

Although this thesis has utilized the rigorous tools of quantum chemistry to describe various spectroscopic properties, it would be deceptive to state that these studies are now complete. For instance, the one-dimensional dipole moments presented in Chapter 3 provide insight into the local-bending dipoles but do not capture any dependencies on other anharmonic or Coriolis couplings. For this reason, the one-dimensional dipole moments of vibrationally excited acetylene are currently being compared with full-dimensional *ab initio* calculations from Prof. Hua Guo at the University of New Mexico (Figure 8-1). Similar to the one-dimensional calculation, the preliminary full-dimensional calculations show exceptionally large dipole moments for the lowest members of a pure-bending polyad.

On a more practical note, the vibrationally excited levels of  $S_0$  acetylene must be experimentally accessed through stimulated emission pumping (SEP) from selected vibrational levels of the trans-bent  $S_1$  excited state of acetylene (cf. Figure 5-1). Consequently, a comprehensive understanding of the anharmonic and Coriolis couplings on the  $S_1$  surface is necessary to experimentally locate special eigenstates that can serve as "local-bender plucks" for  $S_0$  local-bender states. The characterization of the acetylene  $S_1$  surface is an ongoing collaboration with Prof. John F. Stanton at the University of Texas at Austin.

Finally, the techniques outlined in Chapter 7 are in their final stages of development and would be the first *ab initio* (as opposed to an effective potential) MQDT study on the CaF molecule. A less ambitious approach to this problem is to refine

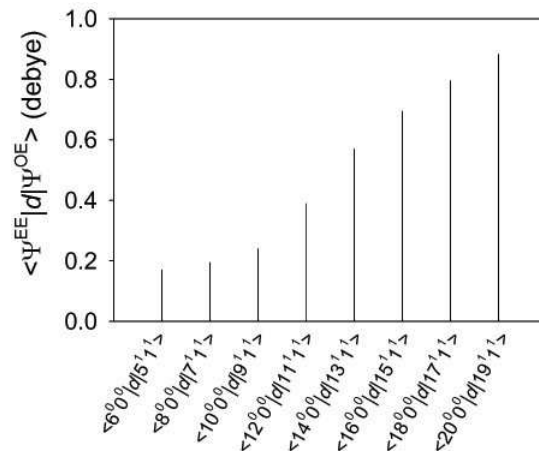


Figure 8-1: Preliminary six-dimensional *ab initio* calculations of dipole matrix elements for  $S_0$  acetylene. The dipole matrix elements are largest for the lowest members of a pure-bending polyad. Prof. Hua Guo is acknowledged for preparing this figure.

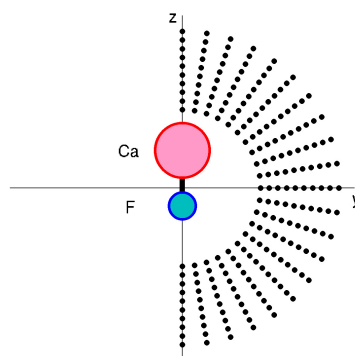


Figure 8-2: Individual points angularly distributed around the center of mass of the  $\text{CaF}^+$  ion. A negative point charge is placed sequentially at each of these points in order to compute the interaction energy with the polarizable ion. Due to the cylindrical symmetry, only the angular points from  $0 \leq \theta \leq \pi$  are unique.

the parameters in the effective potential using *ab initio* calculations and re-calculate the MQDT equations with this new effective potential. The strategy is to adjust the parameters to fit *ab initio* energies of point charges angularly distributed around the  $\text{CaF}^+$  ion (Figure 8-2). Once this fit is finished, these parameters can be modified and compared with experimental data. This approach of refining the effective potential is an ongoing collaboration with Dr. Stephen L. Coy.



# Appendix A

## Expansion of the Internal Coordinate Hamiltonian

This appendix contains a detailed derivation of Eq. (2.8) in Chapter 2.

The quantum mechanical kinetic energy operator for the motion of the nuclei is given by

$$\hat{T} = \frac{1}{2} \sum_{d,e=1}^4 \mu^{1/4} \left( \hat{\Pi}_d - \hat{\pi}_d \right) \mu_{de} \mu^{-1/2} \left( \hat{\Pi}_e - \hat{\pi}_e \right) \mu^{1/4} + \frac{1}{2} \sum_{k=1}^{3N-7} \mu^{1/4} \hat{P}_k \mu^{-1/2} \hat{P}_k \mu^{1/4}. \quad (\text{A.1})$$

This expression can be expanded into the following form:

$$\begin{aligned} \hat{T} &= \frac{1}{2} \mu^{1/4} \sum_{d,e=1}^3 \left( \hat{\Pi}_d - \hat{\pi}_d \right) \mu_{de} \mu^{-1/2} \left( \hat{\Pi}_e - \hat{\pi}_e \right) \mu^{1/4} \\ &\quad + \frac{1}{2} \mu^{1/4} \sum_{d=1}^3 \left( \hat{\Pi}_d - \hat{\pi}_d \right) \mu_{ds} \mu^{-1/2} \left( \hat{p}_s - \hat{\pi}_s \right) \mu^{1/4} \\ &\quad + \frac{1}{2} \mu^{1/4} \sum_{d=1}^3 \left( \hat{p}_s - \hat{\pi}_s \right) \mu_{sd} \mu^{-1/2} \left( \hat{\Pi}_d - \hat{\pi}_d \right) \mu^{1/4} \\ &\quad + \frac{1}{2} \mu^{1/4} \left( \hat{p}_s - \hat{\pi}_s \right) \mu_{ss} \mu^{-1/2} \left( \hat{p}_s - \hat{\pi}_s \right) \mu^{1/4} + \frac{1}{2} \mu^{1/4} \sum_{k=1}^{3N-7} \hat{P}_k \mu^{-1/2} \hat{P}_k \mu^{1/4}, \end{aligned} \quad (\text{A.2})$$

where the variable “s” has been used in place of the subscript “4” for notational convenience in the previous expression. If  $\mu_{de}$  and  $\mu$  are expanded in the vibrational

normal coordinates and only the first term depending on  $s$  is retained (cf. Eq. (2.7)), then  $\mu_{de}$  and  $\mu$  are solely functions of  $s$ , and the following commutation properties hold:

$$\left[ \hat{\Pi}_a, \mu_{de} \right] = \left[ \hat{\Pi}_a, \mu \right] = 0, \quad (a = 1, 2, 3) \text{ and } (d, e = 1, 2, 3, 4), \quad (\text{A.3})$$

$$\left[ \hat{\pi}_a, \mu_{de} \right] = \left[ \hat{\pi}_a, \mu \right] = 0, \quad (a = 1, 2, 3, 4) \text{ and } (d, e = 1, 2, 3, 4), \quad (\text{A.4})$$

$$\left[ \hat{P}_k, \mu \right] = 0, \quad (\text{A.5})$$

$$\left[ \mu_{de}, \mu \right] = 0, \quad (d, e = 1, 2, 3, 4). \quad (\text{A.6})$$

Using these commutation rules in Eq. (A.2) gives

$$\begin{aligned} \hat{T} &= \frac{1}{2} \sum_{d,e=1}^3 \mu_{de} \left( \hat{\Pi}_d - \hat{\pi}_d \right) \left( \hat{\Pi}_e - \hat{\pi}_e \right) \\ &+ \frac{1}{2} \mu^{-1/4} \sum_{d=1}^3 \mu_{ds} \left( \hat{\Pi}_d - \hat{\pi}_d \right) \left( \hat{p}_s - \hat{\pi}_s \right) \mu^{1/4} \\ &+ \frac{1}{2} \mu^{1/4} \sum_{d=1}^3 \left( \hat{p}_s - \hat{\pi}_s \right) \mu_{sd} \mu^{-1/4} \left( \hat{\Pi}_d - \hat{\pi}_d \right) \\ &+ \frac{1}{2} \mu^{1/4} \left( \hat{p}_s - \hat{\pi}_s \right) \mu_{ss} \mu^{-1/2} \left( \hat{p}_s - \hat{\pi}_s \right) \mu^{1/4} + \frac{1}{2} \sum_{k=1}^{3N-7} \hat{P}_k^2. \end{aligned} \quad (\text{A.7})$$

The notation of Eq. (A.7) can be condensed further by defining the operators

$$\hat{J}_a = \hat{\Pi}_a - \hat{\pi}_a, \quad (a = 1, 2, 3), \quad (\text{A.8})$$

$$\hat{J}_s = \hat{p}_s - \hat{\pi}_s, \quad (\text{A.9})$$

which obey the commutation rules

$$\left[ \hat{J}_a, \hat{J}_s \right] = 0, \quad (a = 1, 2, 3), \quad (\text{A.10})$$

$$\left[ \hat{J}_a, \mu_{de} \right] = \left[ \hat{J}_a, \mu \right] = 0, \quad (a = 1, 2, 3) \text{ and } (d, e = 1, 2, 3, 4). \quad (\text{A.11})$$

Using definitions (A.8)–(A.9), Eq. (A.7) can be rearranged in the following form

$$\begin{aligned} \hat{T} = & \frac{1}{2} \sum_{d,e=1}^3 \mu_{de} \hat{J}_d \hat{J}_e + \frac{1}{2} \mu^{-1/4} \sum_{d=1}^3 \mu_{ds} \hat{J}_d \hat{J}_s \mu^{1/4} + \frac{1}{2} \mu^{1/4} \sum_{d=1}^3 \hat{J}_s \mu_{sd} \mu^{-1/4} \hat{J}_d \\ & + \frac{1}{2} \mu^{1/4} \hat{J}_s \mu_{ss} \mu^{-1/2} \hat{J}_s \mu^{1/4} + \frac{1}{2} \sum_{k=1}^{3N-7} \hat{P}_k^2. \end{aligned} \quad (\text{A.12})$$

Since  $\hat{J}_s$  does not commute with  $\mu_{de}$  or  $\mu$ , Eq. (A.12) can be written in terms of commutators between  $\hat{J}_s$ ,  $\mu_{de}$ , and  $\mu$ ,

$$\begin{aligned} \hat{T} = & \frac{1}{2} \sum_{d,e=1}^3 \mu_{de} \hat{J}_d \hat{J}_e + \frac{1}{2} \mu^{-1/4} \sum_{d=1}^3 \mu_{ds} \hat{J}_d \left( \left[ \hat{J}_s, \mu^{1/4} \right] + \mu^{1/4} \hat{J}_s \right) \\ & + \frac{1}{2} \mu^{1/4} \sum_{d=1}^3 \left( \left[ \hat{J}_s, \mu_{sd} \mu^{-1/4} \right] + \mu_{sd} \mu^{-1/4} \hat{J}_s \right) \hat{J}_d \\ & + \frac{1}{2} \mu^{1/4} \hat{J}_s \mu_{ss} \mu^{-1/2} \hat{J}_s \mu^{1/4} + \frac{1}{2} \sum_{k=1}^{3N-7} \hat{P}_k^2. \end{aligned} \quad (\text{A.13})$$

Using commutator Eqs. (A.10)–(A.11) in Eq. (A.13) gives

$$\begin{aligned} \hat{T} = & \frac{1}{2} \sum_{d,e=1}^3 \mu_{de} \hat{J}_d \hat{J}_e + \frac{1}{2} \mu^{-1/4} \sum_{d=1}^3 \mu_{ds} \left[ \hat{J}_s, \mu^{1/4} \right] \hat{J}_d + \frac{1}{2} \sum_{d=1}^3 \mu_{ds} \hat{J}_d \hat{J}_s \\ & + \frac{1}{2} \mu^{1/4} \sum_{d=1}^3 \left[ \hat{J}_s, \mu_{sd} \mu^{-1/4} \right] \hat{J}_d + \frac{1}{2} \sum_{d=1}^3 \mu_{sd} \hat{J}_s \hat{J}_d \\ & + \frac{1}{2} \mu^{1/4} \hat{J}_s \mu_{ss} \mu^{-1/2} \hat{J}_s \mu^{1/4} + \frac{1}{2} \sum_{k=1}^{3N-7} \hat{P}_k^2. \end{aligned} \quad (\text{A.14})$$

The second commutator in Eq. (A.14) can be simplified using the commutation identity

$$\left[ \hat{A}, \hat{B} \hat{C} \right] = \left[ \hat{A}, \hat{B} \right] \hat{C} + \hat{B} \left[ \hat{A}, \hat{C} \right]. \quad (\text{A.15})$$

Therefore,

$$\begin{aligned}
\hat{T} &= \frac{1}{2} \sum_{d,e=1}^3 \mu_{de} \hat{J}_d \hat{J}_e + \frac{1}{2} \sum_{d=1}^3 \mu_{ds} \hat{J}_d \hat{J}_s + \frac{1}{2} \sum_{d=1}^3 \mu_{sd} \hat{J}_s \hat{J}_d \\
&+ \frac{1}{2} \mu^{-1/4} \sum_{d=1}^3 \mu_{ds} \left[ \hat{J}_s, \mu^{1/4} \right] \hat{J}_d + \frac{1}{2} \mu^{1/4} \sum_{d=1}^3 \left[ \hat{J}_s, \mu_{sd} \right] \mu^{-1/4} \hat{J}_d \\
&+ \frac{1}{2} \mu^{1/4} \sum_{d=1}^3 \mu_{sd} \left[ \hat{J}_s, \mu^{-1/4} \right] \hat{J}_d + \frac{1}{2} \mu^{1/4} \hat{J}_s \mu_{ss} \mu^{-1/2} \hat{J}_s \mu^{1/4} + \frac{1}{2} \sum_{k=1}^{3N-7} \hat{P}_k^2.
\end{aligned} \tag{A.16}$$

The second to last term in Eq. (A.16) can be expanded in the following form:

$$\begin{aligned}
&\frac{1}{2} \mu^{1/4} \hat{J}_s \mu_{ss} \mu^{-1/2} \hat{J}_s \mu^{1/4} \\
&= \frac{1}{2} \mu^{1/4} \hat{J}_s \mu_{ss} \mu^{-1/2} \left( \left[ \hat{J}_s, \mu^{1/4} \right] + \mu^{1/4} \hat{J}_s \right) \\
&= \frac{1}{2} \mu^{1/4} \hat{J}_s \mu_{ss} \mu^{-1/2} \left[ \hat{J}_s, \mu^{1/4} \right] + \frac{1}{2} \mu^{1/4} \hat{J}_s \mu_{ss} \mu^{-1/4} \hat{J}_s \\
&= \frac{1}{2} \mu^{1/4} \left( \left[ \hat{J}_s, \mu_{ss} \mu^{-1/2} \left[ \hat{J}_s, \mu^{1/4} \right] \right] + \mu_{ss} \mu^{-1/2} \left[ \hat{J}_s, \mu^{1/4} \right] \hat{J}_s \right) \\
&\quad + \frac{1}{2} \mu^{1/4} \left( \left[ \hat{J}_s, \mu_{ss} \mu^{-1/4} \right] + \mu_{ss} \mu^{-1/4} \hat{J}_s \right) \hat{J}_s \\
&= \frac{1}{2} \mu^{1/4} \left[ \hat{J}_s, \mu_{ss} \mu^{-1/2} \left[ \hat{J}_s, \mu^{1/4} \right] \right] + \frac{1}{2} \mu_{ss} \mu^{-1/4} \left[ \hat{J}_s, \mu^{1/4} \right] \hat{J}_s \\
&\quad + \frac{1}{2} \mu^{1/4} \left[ \hat{J}_s, \mu_{ss} \mu^{-1/4} \right] \hat{J}_s + \frac{1}{2} \mu_{ss} \hat{J}_s \hat{J}_s \\
&= \frac{1}{2} \mu^{1/4} \left[ \hat{J}_s, \mu_{ss} \mu^{-1/2} \left[ \hat{J}_s, \mu^{1/4} \right] \right] + \frac{1}{2} \mu_{ss} \mu^{-1/4} \left[ \hat{J}_s, \mu^{1/4} \right] \hat{J}_s \\
&\quad + \frac{1}{2} \mu^{1/4} \left[ \hat{J}_s, \mu_{ss} \right] \mu^{-1/4} \hat{J}_s + \frac{1}{2} \mu^{1/4} \mu_{ss} \left[ \hat{J}_s, \mu^{-1/4} \right] \hat{J}_s + \frac{1}{2} \mu_{ss} \hat{J}_s \hat{J}_s.
\end{aligned} \tag{A.17}$$

Substituting Eq. (A.17) in Eq. (A.16) and collecting terms gives

$$\begin{aligned}
\hat{T} &= \frac{1}{2} \sum_{d,e=1}^4 \mu_{de} \hat{J}_d \hat{J}_e + \frac{1}{2} \mu^{-1/4} \sum_{d=1}^4 \mu_{ds} \left[ \hat{J}_s, \mu^{1/4} \right] \hat{J}_d \\
&+ \frac{1}{2} \mu^{1/4} \sum_{d=1}^4 \left[ \hat{J}_s, \mu_{sd} \right] \mu^{-1/4} \hat{J}_d + \frac{1}{2} \mu^{1/4} \sum_{d=1}^4 \mu_{sd} \left[ \hat{J}_s, \mu^{-1/4} \right] \hat{J}_d \\
&+ \frac{1}{2} \mu^{1/4} \left[ \hat{J}_s, \mu_{ss} \mu^{-1/2} \left[ \hat{J}_s, \mu^{1/4} \right] \right] + \frac{1}{2} \sum_{k=1}^{3N-7} \hat{P}_k^2.
\end{aligned} \tag{A.18}$$

The second term in Eq. (A.18) can be rearranged using the commutation identity in

Eq. (A.15)

$$\begin{aligned}
& \frac{1}{2}\mu^{-1/4} \sum_{d=1}^4 \mu_{ds} \left[ \hat{J}_s, \mu^{1/4} \right] \hat{J}_d \\
&= \frac{1}{2} \sum_{d=1}^4 \mu_{ds} \mu^{-1/4} \left[ \hat{J}_s, \mu^{1/4} \right] \hat{J}_d \\
&= \frac{1}{2} \sum_{d=1}^4 \mu_{ds} \left[ \hat{J}_s, 1 \right] \hat{J}_d - \frac{1}{2} \sum_{d=1}^4 \mu_{ds} \left[ \hat{J}_s, \mu^{-1/4} \right] \mu^{1/4} \hat{J}_d \\
&= -\frac{1}{2} \sum_{d=1}^4 \mu_{ds} \left[ \hat{J}_s, \mu^{-1/4} \right] \mu^{1/4} \hat{J}_d.
\end{aligned} \tag{A.19}$$

Substituting Eq. (A.19) in Eq. (A.18) gives

$$\begin{aligned}
\hat{T} &= \frac{1}{2} \sum_{d,e=1}^4 \mu_{de} \hat{J}_d \hat{J}_e - \frac{1}{2} \sum_{d=1}^4 \mu_{ds} \left[ \hat{J}_s, \mu^{-1/4} \right] \mu^{1/4} \hat{J}_d \\
&+ \frac{1}{2} \mu^{1/4} \sum_{d=1}^4 \left[ \hat{J}_s, \mu_{sd} \right] \mu^{-1/4} \hat{J}_d + \frac{1}{2} \mu^{1/4} \sum_{d=1}^4 \mu_{sd} \left[ \hat{J}_s, \mu^{-1/4} \right] \hat{J}_d \\
&+ \frac{1}{2} \mu^{1/4} \left[ \hat{J}_s, \mu_{ss} \mu^{-1/2} \left[ \hat{J}_s, \mu^{1/4} \right] \right] + \frac{1}{2} \sum_{k=1}^{3N-7} \hat{P}_k^2.
\end{aligned} \tag{A.20}$$

The commutators in Eq. (A.20) can be significantly simplified using Eq. (A.9) and commutator Eq. (A.4). For example,

$$\begin{aligned}
\left[ \hat{J}_s, \mu \right] &= [\hat{p}_s - \hat{\pi}_s, \mu] \\
&= [\hat{p}_s, \mu] - [\hat{\pi}_s, \mu] \\
&= [\hat{p}_s, \mu].
\end{aligned} \tag{A.21}$$

Commutators involving  $\mu_{sd}$  and other functions of  $\mu$  are similar. Re-expressing Eq. (A.20) in terms of the original operators defined in Eqs. (A.8)–(A.9) gives

$$\begin{aligned}
\hat{T} &= \frac{1}{2} \sum_{d,e=1}^4 \mu_{de} \left( \hat{\Pi}_d - \hat{\pi}_d \right) \left( \hat{\Pi}_e - \hat{\pi}_e \right) - \frac{1}{2} \sum_{d=1}^4 \mu_{ds} [\hat{p}_s, \mu^{-1/4}] \mu^{1/4} \left( \hat{\Pi}_d - \hat{\pi}_d \right) \\
&+ \frac{1}{2} \mu^{1/4} \sum_{d=1}^4 [\hat{p}_s, \mu_{sd}] \mu^{-1/4} \left( \hat{\Pi}_d - \hat{\pi}_d \right) \\
&+ \frac{1}{2} \mu^{1/4} \sum_{d=1}^4 \mu_{sd} [\hat{p}_s, \mu^{-1/4}] \left( \hat{\Pi}_d - \hat{\pi}_d \right) + \frac{1}{2} \mu^{1/4} [\hat{p}_s, \mu_{ss} \mu^{-1/2}] [\hat{p}_s, \mu^{1/4}] \\
&+ \frac{1}{2} \sum_{k=1}^{3N-7} \hat{P}_k^2.
\end{aligned} \tag{A.22}$$

To simplify Eq. (A.22) even further one must remember that  $\hat{p}_s = -i\hbar\partial/\partial s$  is a differential operator, and commutators such as  $[\hat{p}_s, \mu^{-1/4}]$  can be written as

$$\begin{aligned}
[\hat{p}_s, \mu^{-1/4}] &= \hat{p}_s \mu^{-1/4} - \mu^{-1/4} \hat{p}_s \\
&= (\hat{p}_s \mu^{-1/4}) + \mu^{-1/4} \hat{p}_s - \mu^{-1/4} \hat{p}_s \\
&= (\hat{p}_s \mu^{-1/4}),
\end{aligned} \tag{A.23}$$

where the product rule was used in the second step since  $\hat{p}_s$  is an operator which operates on some function to the right; that is, the operator  $\hat{p}_s$  operates only within the parentheses. Therefore, remembering the previous convention, one can replace all the commutators in Eq. (A.22) with parentheses:

$$\begin{aligned}
\hat{T} &= \frac{1}{2} \sum_{d,e=1}^4 \mu_{de} \left( \hat{\Pi}_d - \hat{\pi}_d \right) \left( \hat{\Pi}_e - \hat{\pi}_e \right) - \frac{1}{2} \sum_{d=1}^4 \mu_{ds} (\hat{p}_s, \mu^{-1/4}) \mu^{1/4} \left( \hat{\Pi}_d - \hat{\pi}_d \right) \\
&+ \frac{1}{2} \mu^{1/4} \sum_{d=1}^4 (\hat{p}_s, \mu_{sd}) \mu^{-1/4} \left( \hat{\Pi}_d - \hat{\pi}_d \right) \\
&+ \frac{1}{2} \mu^{1/4} \sum_{d=1}^4 \mu_{sd} (\hat{p}_s, \mu^{-1/4}) \left( \hat{\Pi}_d - \hat{\pi}_d \right) + \frac{1}{2} \mu^{1/4} (\hat{p}_s, \mu_{ss} \mu^{-1/2}) (\hat{p}_s, \mu^{1/4}) \\
&+ \frac{1}{2} \sum_{k=1}^{3N-7} \hat{P}_k^2.
\end{aligned} \tag{A.24}$$

Since the tensor  $\mu_{de}$  is symmetric,  $\mu_{ds} = \mu_{sd}$ . Furthermore, since the quantities within

parentheses in Eq. (A.24) are solely functions of  $s$ , they commute with  $\mu$ , and the second and fourth terms of Eq. (A.24) cancel. Simplifying Eq. (A.24) finally yields

$$\begin{aligned} \hat{T} = & \frac{1}{2} \sum_{d,e=1}^4 \mu_{de} \left( \hat{\Pi}_d - \hat{\pi}_d \right) \left( \hat{\Pi}_e - \hat{\pi}_e \right) + \frac{1}{2} \sum_{d=1}^4 (\hat{p}_s \mu_{sd}) \left( \hat{\Pi}_d - \hat{\pi}_d \right) \\ & + \frac{1}{2} \mu^{1/4} \left( \hat{p}_s \mu_{ss} \mu^{-1/2} \left( \hat{p}_s \mu^{1/4} \right) \right) + \frac{1}{2} \sum_{k=1}^{3N-7} \hat{P}_k^2, \end{aligned} \tag{A.25}$$

which is Eq. (2.8) in Chapter 2 as promised.





# Appendix B

## Computer Codes for Calculating Vibrational Overlap Integrals

This appendix contains source codes for calculating the vibrational overlap integrals described in Chapter 5. The MATLAB m-file **overlap\_integral.m** can calculate vibrational overlap integrals for any general molecule given  $L'$ ,  $L$ ,  $R'_{eq}$ ,  $R_{eq}$ ,  $m$ , and  $n$  as inputs. The m-file **make\_overlap\_table.m** demonstrates how to use **overlap\_integral.m** by generating Table 5.6 as a sample output. The m-files **b\_matrix\_acetylene.m** and **load\_acetylene\_data.m** are specific to acetylene and are required by **make\_overlap\_table.m** to run correctly. All files in this appendix are available via the Internet [112] and were successfully tested on MATLAB Version 7.3 with the Symbolic Math Toolbox.

### B.1 **overlap\_integral.m**

```
1 function overlap=overlap_integral(L_prime,L,R_eq_prime,R_eq,...
    omega_prime,omega,m,n)
%
% This function (overlap_integral.m) calculates the vibrational
% overlap integral between two nuclear wavefunctions using the
% formalism developed by Sharp and Rosenstock (J. Chem. Phys.,
% 41:3453, 1964). This function requires the MATLAB Symbolic
```

```

% Toolbox in order to run correctly and needs the following data
% as inputs:
10 %
% L_prime: (3N-6)x(3N-6) L matrix of the initial vibrational
% state. The L matrix relates the normal mode coordinates to the
% internal displacement coordinates and is defined in Eq. (9) of
% Sharp and Rosenstock.
%
% L: (3N-6)x(3N-6) L matrix of the final vibrational state. See
% description for L_prime.
%
20 % R_eq_prime: (3N-6)x1 column vector whose components are the
% equilibrium internal coordinates of the initial state. The
% ordering of the (3N-6) components must correspond with the
% (3N-6) rows of L_prime.
%
% R_eq: (3N-6)x1 column vector whose components are the
% equilibrium internal coordinates of the final state. The
% ordering of the (3N-6) components must correspond with the
% (3N-6) rows of L.
%
30 % omega_prime: 1x(3N-6) row vector whose components are the
% normal mode frequencies of the initial state. The frequencies
% must be in units of (omega_prime/hbar): amu(-1)*Angstrom(-2).
% The ordering of the (3N-6) components must correspond with the
% (3N-6) columns of L_prime.
%
% omega: 1x(3N-6) row vector whose components are the normal mode
% frequencies of the final state. The frequencies must be in
% units of (omega/hbar): amu(-1)*Angstrom(-2). The ordering of
% the (3N-6) components must correspond with the (3N-6) columns
% of L.
40 %
% m: 1x(3N-6) row vector whose components are the vibrational
% quanta in each of the (3N-6) oscillators of the initial state.
% The ordering of the (3N-6) components must correspond with the
% (3N-6) columns of omega_prime.
%
% n: 1x(3N-6) row vector whose components are the vibrational
% quanta in each of the (3N-6) oscillators of the final state.
% The ordering of the (3N-6) components must correspond with the
% (3N-6) columns of omega.
50
R=R_eq-R_eq_prime; % Eq. (8) of Sharp and Rosenstock

```

```

J=inv(L_prime)*L; % Eq. (11) of Sharp and Rosenstock
K=inv(L_prime)*R; % Eq. (11) of Sharp and Rosenstock

gamma_prime=diag(omega_prime);
% (3N-6)x(3N-6) diagonal matrix of initial frequencies
gamma=diag(omega);
% (3N-6)x(3N-6) diagonal matrix of final frequencies
60
Z=J'*gamma_prime*J+gamma;
% This quantity appears several times in Eqs. (21a) - (21e) of
% Sharp and Rosenstock. This variable is computed here once to
% save some computer time and simplify the following lines of
% code.

A=2*sqrt(gamma_prime)*J*inv(Z)*J'*sqrt(gamma_prime)...
-eye(length(omega));
% Eq. (21a) of Sharp and Rosenstock
70 B=-2*sqrt(gamma_prime)*(J*inv(Z)*J'*gamma_prime...
-eye(length(omega)))*K;
% Eq. (21b) of Sharp and Rosenstock
C=2*sqrt(gamma)*inv(Z)*sqrt(gamma)-eye(length(omega));
% Eq. (21c) of Sharp and Rosenstock
D=-2*sqrt(gamma)*inv(Z)*J'*gamma_prime*K;
% Eq. (21d) of Sharp and Rosenstock
E=4*sqrt(gamma)*inv(Z)*J'*sqrt(gamma_prime);
% Eq. (21e) of Sharp and Rosenstock

80 for i=1:length(m)

    T(i,1)=sym(['t' num2str(i)],'real');
    % initialize the T vector (Eq. (22) of Sharp and Rosenstock))
    % with (3N-6) dummy symbolic variables

    U(i,1)=sym(['u' num2str(i)],'real');
    % initialize the U vector (Eq. (22) of Sharp and Rosenstock))
    % with (3N-6) dummy symbolic variables

90 end

f=exp(T'*A*T+T'*B+U'*C*U+U'*D+U'*E*T);
% generating function from the right hand side of Eq. (22) of
% Sharp and Rosenstock

for i=1:length(m)

```

```

    f=diff(f,T(i),m(i));
    f=subs(f,T(i),0);
100    % take the m(i)-order derivative of the generating function
    % with respect to each of the (3N-6) dummy variables in T

    f=diff(f,U(i),n(i));
    f=subs(f,U(i),0);
    % take the n(i)-order derivative of the generating function
    % with respect to each of the (3N-6) dummy variables in U

end

110  f=f/sqrt(prod(2.^(m+n).*factorial(m).*factorial(n)));
    % divide the generating function with the left hand side of Eq.
    % (22) of Sharp and Rosenstock

    I_0=2^(length(m)/2)*det(gamma*gamma_prime)^(1/4)...
        /sqrt(det(J*Z))*exp(-1/2*K'*gamma_prime*K+1/2*K'...
        *gamma_prime*J*inv(Z)*J'*gamma_prime*K);
    % normalization factor for the overlap integral (Eq. (21) of
    % Sharp and Rosenstock). This variable is the corrected version
    % of Eq. (21) in Sharp and Rosenstock which contains a misprint.
120  overlap=I_0*f;
    % overlap integral

```

## B.2 make\_overlap\_table.m

```
1 function make_overlap_table

% This function (make_overlap_table.m) demonstrates how to use
% the MATLAB m-files load_acetylene_data.m, b_matrix_acetylene.m,
% and overlap_integral.m by generating Table V taken from (R. L.
% Thom, B. M. Wong, R. W. Field, and J. F. Stanton. J. Chem.
% Phys., 126:184307, 2007).

[L_internal_s1,L_internal_t3,R_eq_s1,R_eq_t3,omega_s1,...
10  omega_t3]=load_acetylene_data;
% load data for the S1 and T3 states of acetylene

m_s1=[0 0 3 0 0 0];
% 3 quanta in mode v3 for the S1 state of acetylene. Since the
% harmonic frequencies of S1 (outputted by load_acetylene_data.m)
% are in ascending numerical order, the components of m_s1
% correspond to the mode numbering scheme: [v4,v6,v3,v2,v5,v1].

n_t3_matrix=[1,2,0,1,0,0;
20  0,3,1,0,0,0;
  5,0,1,0,0,0;
  2,4,0,0,0,0;
  1,0,0,0,1,0;
  7,1,0,0,0,0;
  1,0,1,1,0,0;
  3,1,0,1,0,0;
  0,1,2,0,0,0;
  2,2,1,0,0,0;
  4,3,0,0,0,0];
30 % matrix of vibrational quantum numbers for T3 which fall within
% approximately 100 cm-1 of 3v3 S1. Since the harmonic
% frequencies of T3 (outputted by load_acetylene_data.m) are in
% ascending numerical order, the columns of n_t3 correspond to
% the mode numbering scheme: [v6,v4,v3,v2,v5,v1].

for i=1:length(n_t3_matrix(:,1))

  overlap(i)=overlap_integral(L_internal_s1,L_internal_t3,...
40  R_eq_s1,R_eq_t3,omega_s1,omega_t3,m_s1,n_t3_matrix(i,:));
% calculate the overlap integral between 3v3 S1 and each of
% the rows of n_t3_matrix
```

```

end

disp('-----')
disp('  Vibrational Level    Overlap with S1 3v3')

disp(' (v1 v2 v3 v4 v5 v6)')
disp('-----')
50 fprintf(1, '  %2.0f %2.0f %2.0f %2.0f %2.0f %2.0f %16.4f \n',...
    [n_t3_matrix(:, [6,4,3,2,5,1])]; overlap)
disp('-----')
% display the vibrational quantum numbers and overlaps in a table

```

## B.3 load\_acetylene\_data.m

```
1 function [L_internal_s1,L_internal_t3,R_eq_s1,R_eq_t3,...
    omega_s1,omega_t3]=load_acetylene_data
    %
    % This function (load_acetylene_data.m) processes and outputs the
    % data needed by overlap_integral.m to calculate vibrational
    % overlap integrals between the S1 and T3 states of acetylene.
    % This function requires the MATLAB m-file b_matrix_acetylene.m
    % in order to run correctly and outputs the following data:
    %
10 % L_internal_s1: 6x6 L matrix for the S1 state of acetylene
    % (atoms labeled by H3-C1-C2-H4, where H3 is bonded to C1, and H4
    % is bonded to C2). The ordering of the 6 rows correspond to the
    % following internal coordinates: (1) C2-C1 bond distance, (2)
    % H3-C1 bond distance, (3) H4-C2 bond distance, (4) H3-C1-C2
    % angle, (5) H4-C2-C1 angle, and (6) H3-C1-C2-H4 torsional angle.
    %
    % L_internal_t3: 6x6 L matrix for the T3 state of acetylene. The
    % atom labels and the internal coordinate ordering are the same
    % as the rows which comprise L_internal_s1.
20 %
    % R_eq_s1: 6x1 column vector whose components are the equilibrium
    % internal coordinates of the S1 state. The ordering of the 6
    % components correspond to the 6 rows of L_internal_s1.
    %
    % R_eq_t3: 6x1 column vector whose components are the equilibrium
    % internal coordinates of the T3 state. The ordering of the 6
    % components correspond to the 6 rows of L_internal_t3.
    %
    % omega_s1: 1x6 row vector containing the harmonic frequencies of
30 % S1 (in ascending order) in units of amu(-1)*Angstroms(-2)
    %
    % omega_t3: 1x6 row vector containing the harmonic frequencies of
    % T3 (in ascending order) in units of amu(-1)*Angstroms(-2)

    hbar=1.05457266e-34;
    amu=1.6605402e-27;
    lightspeed=299792458e2;
    angstrom=0.529177249;

40 conversion=lightspeed/hbar*amu*1e-20;
```

```

m_C=12; % mass of carbon in amus
m_H=1.007825035; % mass of hydrogen in amus

zmat_s1=angstrom*[1.2563457714    0.2243278705    0.0000000000
-1.2563457714   -0.2243278705    0.0000000000
 2.6953689580   -1.2450027117    0.0000000000
-2.6953689580    1.2450027117    0.0000000000];
% Cartesian coordinates of the S1 state in Angstroms. The rows in
50 % zmat_s1 correspond to the atoms C1, C2, H3, and H4 where H3 is
% bonded to C1, and H4 is bonded to C2.

zmat_t3=angstrom*[1.2639239709    0.1462769266   -0.0654251864
-1.2639239709   -0.1462769266   -0.0654251864
 2.8768155828   -0.7652103906    0.7790064839
-2.8768155828    0.7652103906    0.7790064839];
% Cartesian coordinates of the T3 state in Angstroms. The rows in
% zmat_t3 correspond to the atoms C1, C2, H3, and H4 where H3 is
% bonded to C1, and H4 is bonded to C2.

60 N=length(zmat_s1(:,1)); % number of atoms

e12_s1=zmat_s1(2,:)-zmat_s1(1,:);
R_eq_s1(1,1)=norm(e12_s1); % C2-C1 bond length for S1
e12_s1=e12_s1/R_eq_s1(1,1); % unit vector from C1 to C2 for S1
e21_s1=-e12_s1; % unit vector from C2 to C1 for S1

e13_s1=zmat_s1(3,:)-zmat_s1(1,:);
R_eq_s1(2,1)=norm(e13_s1); % H3-C1 bond length for S1
70 e13_s1=e13_s1/R_eq_s1(2,1); % unit vector from C1 to H3 for S1
e31_s1=-e13_s1; % unit vector from H3 to C1 for S1

e24_s1=zmat_s1(4,:)-zmat_s1(2,:);
R_eq_s1(3,1)=norm(e24_s1); % H4-C2 bond length for S1
e24_s1=e24_s1/R_eq_s1(3,1); % unit vector from C2 to H4 for S1

R_eq_s1(4,1)=acos(dot(e13_s1,e12_s1));
% H3-C1-C2 angle in radians for S1
R_eq_s1(5,1)=acos(dot(e21_s1,e24_s1));
80 % H4-C2-C1 angle in radians for S1

R_eq_s1(6,1)=acos(dot(cross(e31_s1,e12_s1),...
    cross(e12_s1,e24_s1))/(sin(R_eq_s1(4,1))*sin(R_eq_s1(5,1))));
% H3-C1-C2-H4 torsional angle in radians for S1

e12_t3=zmat_t3(2,:)-zmat_t3(1,:);

```



```

R_eq_t3(1,1)=norm(e12_t3); % C2-C1 bond length for T3
e12_t3=e12_t3/R_eq_t3(1,1); % unit vector from C1 to C2 for T3
e21_t3=-e12_t3; % unit vector from C2 to C1 for T3
90
e13_t3=zmat_t3(3,:)-zmat_t3(1,:);
R_eq_t3(2,1)=norm(e13_t3); % H3-C1 bond length for T3
e13_t3=e13_t3/R_eq_t3(2,1); % unit vector from C1 to H3 for T3
e31_t3=-e13_t3; % unit vector from H3 to C1 for T3

e24_t3=zmat_t3(4,:)-zmat_t3(2,:);
R_eq_t3(3,1)=norm(e24_t3); % H4-C2 bond length for T3
e24_t3=e24_t3/R_eq_t3(3,1); % unit vector from C2 to H4 for T3

100 R_eq_t3(4,1)=acos(dot(e13_t3,e12_t3));
% H3-C1-C2 angle in radians for T3
R_eq_t3(5,1)=acos(dot(e21_t3,e24_t3));
% H4-C2-C1 angle in radians for T3

R_eq_t3(6,1)=acos(dot(cross(e31_t3,e12_t3),...
    cross(e12_t3,e24_t3))/(sin(R_eq_t3(4,1))*sin(R_eq_t3(5,1))));
% H3-C1-C2-H4 torsional angle in radians for T3

omega_s1_cm=[641.5243555793 732.4065268561 1087.2531708330 ...
110 1503.9932895188 3091.3722518386 3113.8218266995];
omega_s1=conversion*omega_s1_cm;
% harmonic frequencies of S1 in amu(-1) Angstroms(-2)

omega_t3_cm=[397.5591668938 653.0417221433 1411.9585215773 ...
1626.8956207661 3036.4846162879 3225.8838136171];
omega_t3=conversion*omega_t3_cm;
% harmonic frequencies of T3 in amu(-1) Angstroms(-2)

L_cart_s1=[0.0000000000 0.0000000000 0.1968227203
120 0.0000000000 0.0000000000 0.1968227203
0.0000000000 0.0000000000 -0.6791618487
0.0000000000 0.0000000000 -0.6791618487
0.1356965875 0.1425679465 0.0000000000
0.1356965875 0.1425679465 0.0000000000
-0.4682383473 -0.4919488458 0.0000000000
-0.4682383473 -0.4919488458 0.0000000000
0.0620248472 0.3805824000 0.0000000000
-0.0620248472 -0.3805824000 0.0000000000
-0.4490122073 -0.3869082486 0.0000000000
130 0.4490122073 0.3869082486 0.0000000000
0.6756377137 0.0839708460 0.0000000000

```

```

-0.6756377137      -0.0839708460      0.0000000000
 0.1888498906      -0.0282541255      0.0000000000
-0.1888498906      0.0282541255      0.0000000000
 0.1425679465      -0.1356965875      0.0000000000
 0.1425679465      -0.1356965875      0.0000000000
-0.4919488458      0.4682383473      0.0000000000
-0.4919488458      0.4682383473      0.0000000000
 0.1704280896      -0.1223824165      0.0000000000
140  -0.1704280896      0.1223824165      0.0000000000
      -0.4850244785      0.4698170555      0.0000000000
      0.4850244785      -0.4698170555      0.0000000000];
% mass weighted Cartesian normal mode eigenvector l matrix for
% S1; this is from the standard output of ACES II which outputs
% this matrix in 3 columns corresponding to x, y, and z

L_cart_t3=[0.0869087881      0.1318727780      -0.2712668339
 0.0869087881      0.1318727780      0.2712668339
-0.2998898354      -0.4550438058      0.3232212234
150  -0.2998898354      -0.4550438058      -0.3232212234
      0.0845920890      0.2869702881      -0.1107145827
      -0.0845920890      -0.2869702881      -0.1107145827
      -0.3900441432      -0.3164640929      0.3820347598
      0.3900441432      0.3164640929      0.3820347598
      0.5610259535      0.1842498836      0.0714344622
      -0.5610259535      -0.1842498836      0.0714344622
      0.1814546585      -0.2291594167      -0.2464937041
      -0.1814546585      0.2291594167      -0.2464937041
      0.3684818408      -0.1988277097      -0.1241176044
160  -0.3684818408      0.1988277097      -0.1241176044
      0.1164649336      0.3351008493      0.4282835920
      -0.1164649336      -0.3351008493      0.4282835920
      0.1739955891      -0.0658689303      0.0342824442
      0.1739955891      -0.0658689303      -0.0342824442
      -0.6003939268      0.2272891279      -0.2282067440
      -0.6003939268      0.2272891279      0.2282067440
      0.1943913023      -0.0785119452      0.0772877889
      -0.1943913023      0.0785119452      0.0772877889
      -0.5394169319      0.2966135359      -0.2666913529
170  0.5394169319      -0.2966135359      -0.2666913529];
% mass weighted Cartesian normal mode eigenvector l matrix for
% T3; this is from the standard output of ACES II which outputs
% this matrix in 3 columns corresponding to x, y, and z

L_cart_s1=reshape(L_cart_s1',[3*N,3*N-6]);
% reshape the S1 l matrix to the standard 3N x (3N-6) size

```

```

L_cart_t3=reshape(L_cart_t3',[3*N,3*N-6]);
% reshape the T3 l matrix to the standard 3N x (3N-6) size

180  inv_sqrt_M=diag(kron(1./sqrt([m_C,m_C,m_H,m_H]),ones(1,3)));
% diagonal 3N x 3N matrix containing the reciprocal square roots
% of the atom masses

B_s1=b_matrix_acetylene(zmat_s1); % B matrix for S1
B_t3=b_matrix_acetylene(zmat_t3); % B matrix for T3

L_internal_s1=B_s1*inv_sqrt_M*L_cart_s1; % L matrix for S1
L_internal_t3=B_t3*inv_sqrt_M*L_cart_t3; % L matrix for T3

```

## B.4 b\_matrix\_acetylene.m

```
1  function B=b_matrix_acetylene(zmat)
   %
   % This function (b_matrix_acetylene.m) processes and outputs the
   % B matrix for acetylene. Expressions for the B matrix elements
   % were taken from Section 4-1 of (E. B. Wilson Jr., J. C. Decius,
   % and P. C. Cross. Molecular Vibrations: The Theory of Infrared
   % and Raman Vibrational Spectra. Dover Publications: New York,
   % 1955). This function only requires the z matrix (zmat) in
10  % Cartesian coordinates. The rows in zmat must correspond to the
   % atoms C1, C2, H3, and H4 where H3 is bonded to C1, and H4 is
   % bonded to C2.
   %
   % The 6 rows of the outputted B matrix correspond to the
   % following internal coordinates: (1) C2-C1 bond distance, (2)
   % H3-C1 bond distance, (3) H4-C2 bond distance, (4) H3-C1-C2
   % angle, (5) H4-C2-C1 angle, and (6) H3-C1-C2-H4 torsional angle.

   N=length(zmat(:,1));
   % initialize N to be the number of atoms

20  B=zeros(3*N-6,3*N);
   % initialize (3N-6)x(3N) B matrix with zeros

   e12=zmat(2,:)-zmat(1,:);
   e12=e12/norm(e12); % unit vector from C1 to C2
   e21=-e12; % unit vector from C2 to C1

   B(1,1:6)=[e21,e12];
   % first row of B matrix (Eq. (3) from Wilson et. al)

30  e13=zmat(3,:)-zmat(1,:);
   e13=e13/norm(e13); % unit vector from C1 to H3
   e31=-e13; % unit vector from H3 to C1

   B(2,[1:3,7:9])=[e31,e13];
   % second row of B matrix (Eq. (3) from Wilson et. al)

   e24=zmat(4,:)-zmat(2,:);
   e24=e24/norm(e24); % unit vector from C2 to H4
40  e42=-e24; % unit vector from H4 to C2
```

```

B(3,[4:6,10:12])=[e42,e24];
% third row of B matrix (Eq. (3) from Wilson et. al)

r13=norm(zmat(3,:)-zmat(1,:)); % H3-C1 bond length
r12=norm(zmat(2,:)-zmat(1,:)); % C1-C2 bond length
phi=acos(dot(e13,e12)); % H3-C1-C2 angle in radians

B(4,1:9)=[((r13-r12*cos(phi))*e13...
50   +(r12-r13*cos(phi))*e12)/(r13*r12*sin(phi)),...
   (cos(phi)*e12-e13)/(r12*sin(phi)),...
   (cos(phi)*e13-e12)/(r13*sin(phi))];
% fourth row of B matrix (Eqs. (5)-(7) from Wilson et. al)

r21=norm(zmat(1,:)-zmat(2,:)); % C1-C2 bond length
r24=norm(zmat(4,:)-zmat(2,:)); % H4-C2 bond length
phi=acos(dot(e21,e24)); % H4-C2-C1 angle in radians

B(5,[1:6,10:12])=[(cos(phi)*e21-e24)/(r21*sin(phi)),...
60   ((r21-r24*cos(phi))*e21...
   +(r24-r21*cos(phi))*e24)/(r21*r24*sin(phi)),...
   (cos(phi)*e24-e21)/(r24*sin(phi))];
% fifth row of B matrix (Eqs. (5)-(7) from Wilson et. al)

r31=r13; % C1-H3 bond length
r42=r24; % C2-H4 bond length
phi1=acos(dot(e13,e12)); % H3-C1-C2 angle in radians
phi2=acos(dot(e21,e24)); % H4-C2-C1 angle in radians

70 B(6,:)=[(r12-r31*cos(phi1))/(r12*r31*sin(phi1))...
   *cross(e31,e12)/sin(phi1)+cos(phi2)/(r12*sin(phi2))...
   *cross(e42,e21)/sin(phi2),...
   (r21-r42*cos(phi2))/(r21*r42*sin(phi2))...
   *cross(e42,e21)/sin(phi2)+cos(phi1)/(r21*sin(phi1))...
   *cross(e31,e12)/sin(phi1),...
   -cross(e31,e12)/(r31*(sin(phi1))^2),...
   -cross(e42,e21)/(r42*(sin(phi2))^2)];
% sixth row of B matrix (Eqs. (21)-(24) from Wilson et. al)

```



# Appendix C

## Analytical Expressions for One- and Two-Electron Integrals in K matrix Calculations

This appendix contains closed-form analytical expressions for one- and two-electron integrals between Cartesian Gaussians outside a finite spherical region of space. The majority of the work in this appendix resulted from a collaboration with Dr. Serhan N. Altunata and was published as an article in the *Journal of Chemical Physics* [114].

### C.1 General Expansion of Cartesian Gaussian Orbitals

A general unnormalized Cartesian Gaussian Orbital (CGO) centered at point  $\mathbf{R}_P = (X_P, Y_P, Z_P)$  is given by

$$\chi_P(p, q, r, a) = x_P^p y_P^q z_P^r e^{-ar_P^2}, \quad (\text{C.1})$$

where  $x_P$ ,  $y_P$ , and  $z_P$  are Cartesian components relative to the point  $\mathbf{R}_P$  where  $\mathbf{r}_P = (x_P, y_P, z_P) = (x - X_P, y - Y_P, z - Z_P)$ , and  $p$ ,  $q$ , and  $r$  are integers greater

than or equal to zero. The multipole expansion of this unnormalized CGO about the origin of the  $(x, y, z)$  coordinate system is given by [159]

$$\chi_P(p, q, r, a) = \sum_{l=0}^{\infty} \sum_{m=-l}^l C_{pqra}^{lm}(r) Y_{l,m}(\hat{\mathbf{r}}), \quad (\text{C.2})$$

where the direction  $\hat{\mathbf{r}}$  specifies the angular spherical coordinates  $\theta$  and  $\phi$ , which uniquely define the coordinate system of the spherical harmonic. The spherical harmonics used in the present work follow the conventional phase choice

$$Y_{l,-m} = (-1)^m Y_{l,m}^*. \quad (\text{C.3})$$

The radial function  $C_{pqra}^{lm}(r)$  is derived from a Rayleigh expansion which leads to

$$C_{pqra}^{lm}(r) = 4\pi e^{-a(r^2 + R_P^2)} \sum_{i,j,k} A_{ijk}^{pqr} r^{i+j+k} \sum_{l',m'} i_{l'}(2aR_P r) Y_{l',m'}^*(\hat{\mathbf{R}}_P) \times \sum_{L,M} B_{ijk}^{LM} \langle Y_{l,m} | Y_{L,M} | Y_{l',m'} \rangle, \quad (\text{C.4})$$

which is slightly modified from the expression given by Le Rouzo. The real constant  $A_{ijk}^{pqr}$  is obtained from the polynomial expansion

$$(x - X_P)^p (y - Y_P)^q (z - Z_P)^r = \sum_{i,j,k=0}^{i+j+k \leq p+q+r} A_{ijk}^{pqr} x^i y^j z^k. \quad (\text{C.5})$$

The function,  $i_l$ , is a modified spherical Bessel function of the first kind and of order  $l$ . The complex constant  $B_{ijk}^{LM}$  is given by the expression [160]

$$(-1)^M B_{IJK}^{LM*} = \sqrt{\frac{2L+1}{4\pi} \frac{(L-|M|)!}{(L+|M|)!}} I_\phi(I, J, M) I_\theta(I+J, K, L, M), \quad (\text{C.6})$$

which is modified from Mathar's original expression to follow the phase choice in Eq. (C.3). The integrals  $I_\phi$  and  $I_\theta$  are given by



$$I_\phi = \frac{\pi}{2^{I+J-1}} i^J \sum_{\sigma=\max(0,(I+J-M)/2)}^{\min(I,(I+J-M)/2)} (-1)^{(I+J-M)/2-\sigma} \binom{I}{\sigma} \binom{J}{{(I+J-M)/2-\sigma}}, \quad (\text{C.7})$$

and

$$I_\theta = \frac{2^{L+1}}{(L-|M|)!} \sum_{v=0}^{[(L-|M|)/2]} \left(\frac{1}{2} - v\right)_L \binom{L-|M|}{2v} \times \sum_{\sigma=0}^{(I+J+|M|)/2} \binom{(I+J+|M|)/2}{\sigma} \frac{(-1)^\sigma}{2\sigma+1+K+L-|M|-2v}, \quad (\text{C.8})$$

where the standard definition of the binomial coefficient is given by

$$\binom{a}{b} = \frac{a!}{(a-b)!b!}. \quad (\text{C.9})$$

The square brackets,  $[x]$ , denote the largest integer less than or equal to  $x$ , and  $(y)_p$  is Pochhammer's symbol,  $(y)_p = y(y+1)(y+2) \dots (y+p-1)$  for integers  $p$  and  $(y)_0 = 1$ . The index  $L$  in Eq. (C.4) decreases in steps of 2 from  $i+j+k$  to 1 or 0. These basic results permit the computation of all of the various types of integrals over a finite spherical volume needed for the  $\mathbf{K}$  matrix theory. From these expressions, one can evaluate overlap, kinetic, nuclear, and electron repulsion integrals analytically. The subsequent sections deal specifically with the tail integrals of one- and two-electron integrals of continuum orbitals.

## C.2 Overlap Integrals

The overlap tail integrals are obtained by integrating the product of two continuum CGOs from the  $\mathbf{K}$  matrix radius,  $R$ , to infinity. Since all the continuum CGOs are centered about the center of gravity,  $O$ , of the molecule, the product of two continuum CGOs is a single continuum CGO also located at the center of gravity,

$$\chi_{i,O}(p_i, q_i, r_i, a_i) \chi_{j,O}(p_j, q_j, r_j, a_j) = x^p y^q z^r e^{-ar^2}, \quad (\text{C.10})$$

where  $p = p_i + p_j$ ,  $q = q_i + q_j$ ,  $r = r_i + r_j$ , and  $a = a_i + a_j$ . Since the product of the two continuum CGOs is a Gaussian located at the center of gravity,  $R_P = 0$ , the following relations hold for this special case,

$$A_{ijk}^{pqr} = \delta_{i,p} \delta_{j,q} \delta_{k,r}, \quad (\text{C.11})$$

$$i_l(0) = \delta_{l,0}. \quad (\text{C.12})$$

Therefore, the expression for the radial function reduces to the following

$$\begin{aligned} C_{pqra}^{lm}(r) &= 4\pi e^{-ar^2} r^{p+q+r} Y_{0,0}^*(\mathbf{0}) \sum_{L,M} B_{pqr}^{LM} \langle Y_{l,m} | Y_{L,M} | Y_{0,0} \rangle \\ &= e^{-ar^2} r^{p+q+r} \sum_{L,M} B_{pqr}^{LM} \langle Y_{l,m} | Y_{L,M} \rangle \\ &= e^{-ar^2} r^{p+q+r} B_{pqr}^{lm}. \end{aligned} \quad (\text{C.13})$$

The calculation of the overlap tail integral involves the integration of Eq. (C.2) from  $R$  to infinity with the radial function given by Eq. (C.13)

$$S_{\text{tail}} = \sum_{l=0}^{\infty} \sum_{m=-l}^l \int_{r=R}^{r=\infty} e^{-ar^2} r^{p+q+r} B_{pqr}^{lm} Y_{l,m}(\hat{\mathbf{r}}) d\mathbf{r}. \quad (\text{C.14})$$

After integration over the angular variables, one obtains

$$\begin{aligned} S_{\text{tail}} &= \sqrt{4\pi} B_{pqr}^{00} \int_R^{\infty} r^{p+q+r+2} e^{-ar^2} dr \\ &= \sqrt{\pi} B_{pqr}^{00} \frac{\Gamma[1/2(p+q+r)+3/2, aR^2]}{a^{1/2(p+q+r)+3/2}}. \end{aligned} \quad (\text{C.15})$$

### C.3 Kinetic Energy Integrals

The kinetic energy tail integrals are defined by

$$\text{KE}_{\text{tail}} = -\frac{1}{2} \int_{r=R}^{r=\infty} \chi_{i,O}(p_i, q_i, r_i, a_i) \nabla^2 \chi_{j,O}(p_j, q_j, r_j, a_j) d\mathbf{r}. \quad (\text{C.16})$$

The action of the kinetic energy operator on a continuum CGO centered about the center of gravity  $O$  is given by

$$\begin{aligned} -\frac{1}{2} \nabla^2 \left( x^p y^q z^r e^{-ar^2} \right) &= a [2(p+q+r) + 3] x^p y^q z^r e^{-ar^2} \\ &\quad - 2a^2 [x^{p+2} y^q z^r + x^p y^{q+2} z^r + x^p y^q z^{r+2}] e^{-ar^2} \\ &\quad - \frac{1}{2} [p(p-1) x^{p-2} y^q z^r + q(q-1) x^p y^{q-2} z^r \\ &\quad + r(r-1) x^p y^q z^{r-2}] e^{-ar^2}. \end{aligned} \quad (\text{C.17})$$

Let  $S(p, q, r, a)$  denote the overlap tail integral between  $\chi_i(p_i, q_i, r_i, a_i)$  and  $\chi_j(p_j, q_j, r_j, a_j)$  where  $p = p_i + p_j$ ,  $q = q_i + q_j$ ,  $r = r_i + r_j$ , and  $a = a_i + a_j$ .

The kinetic energy tail integral is given by the sum of seven overlap tail integrals:

$$\begin{aligned} \text{KE}_{\text{tail}} &= a_j [2(p_j + q_j + r_j) + 3] S(p, q, r, a) \\ &\quad - 2a_j^2 [S(p+2, q, r, a) + S(p, q+2, r, a) + S(p, q, r+2, a)] \\ &\quad - \frac{1}{2} [p_j(p_j-1) S(p-2, q, r, a) + q_j(q_j-1) S(p, q-2, r, a) \\ &\quad + r_j(r_j-1) S(p, q, r-2, a)], \end{aligned} \quad (\text{C.18})$$

where the closed analytical forms for the seven different  $S$  integrals can be found from Eq. (C.15).

### C.4 Nuclear Attraction Integrals

For a nucleus centered about the point  $\mathbf{r}_C = (x_C, y_C, z_C)$ , the nuclear attraction tail integral is given by

$$\text{NAI}_{\text{tail}} = \int_{r=R}^{r=\infty} \chi_{i,O}(p_i, q_i, r_i, a_i) \frac{1}{|\mathbf{r} - \mathbf{r}_{\mathbf{C}}|} \chi_{j,O}(p_j, q_j, r_j, a_j) d\mathbf{r}. \quad (\text{C.19})$$

Using Eqs. (C.10) and (C.13), the number of Gaussians involved in the integration is reduced to one, and Eq. (C.19) takes the form

$$\text{NAI}_{\text{tail}} = \sum_{l=0}^{\infty} \sum_{m=-l}^l B_{pqr}^{lm} \int_{r=R}^{r=\infty} r^{p+q+r} e^{-ar^2} Y_{l,m}(\hat{\mathbf{r}}) \frac{1}{|\mathbf{r} - \mathbf{r}_{\mathbf{C}}|} dr. \quad (\text{C.20})$$

where  $p = p_i + p_j$ ,  $q = q_i + q_j$ ,  $r = r_i + r_j$ , and  $a = a_i + a_j$ . The Coulomb term can be expressed using the well-known multipolar expansion,

$$\frac{1}{|\mathbf{r} - \mathbf{r}_{\mathbf{C}}|} = 4\pi \sum_{l=0}^{\infty} \sum_{m=-l}^l \frac{1}{2l+1} \frac{r_{<}^l}{r_{>}^{l+1}} Y_{l,m}^*(\hat{\mathbf{r}}) Y_{l,m}(\hat{\mathbf{r}}_{\mathbf{C}}). \quad (\text{C.21})$$

Since the integration of Eq. (C.20) is from  $R$  to infinity and the  $\mathbf{K}$  matrix radius encloses all the nuclei, thus  $r_{>} = r$  and  $r_{<} = r_{\mathbf{C}}$ ; after integration over the angular variables, one obtains

$$\text{NAI}_{\text{tail}} = 4\pi \sum_{l=0}^{\infty} \sum_{m=-l}^l \frac{1}{2l+1} r_{\mathbf{C}}^l Y_{l,m}(\hat{\mathbf{r}}_{\mathbf{C}}) B_{pqr}^{lm} \int_R^{\infty} r^{p+q+r-l+1} e^{-ar^2} dr. \quad (\text{C.22})$$

Since the index  $l$  in Eq. (C.22) decreases by steps of 2 from  $p + q + r$  to 1 or 0, the exponent of  $r$  in the integral is always positive. Therefore

$$\text{NAI}_{\text{tail}} = 2\pi \sum_{l=0,1}^{p+q+r} \sum_{m=-l}^l \frac{1}{2l+1} r_{\mathbf{C}}^l Y_{l,m}(\hat{\mathbf{r}}_{\mathbf{C}}) B_{pqr}^{lm} \frac{\Gamma[1/2(p+q+r-l)+1, aR^2]}{a^{1/2(p+q+r-l)+1}}, \quad \mathbf{r}_{\mathbf{C}} \neq 0. \quad (\text{C.23})$$

Note that the original sum in Eq. (C.20) is finite because it is limited by the coefficient  $B_{ijk}^{lm}$  in Eq. (C.23). However, Eq. (C.23) is not applicable when a continuum CGO is centered about a nucleus located at the center of gravity of the molecule (i.e., this occurs in the equilibrium linear geometries of  $\text{CO}_2$  or  $\text{NO}_2^+$ ). In this special case, the

Coulomb term is simply  $1/r$ , and Eq. (C.20) reduces to

$$\text{NAI}_{\text{tail}} = \sum_{l=0}^{\infty} \sum_{m=-l}^l B_{pqr}^{lm} \int_{r=R}^{r=\infty} r^{p+q+r-1} e^{-ar^2} Y_{l,m}(\hat{\mathbf{r}}) d\mathbf{r}. \quad (\text{C.24})$$

After integration over the angular variables, one obtains

$$\begin{aligned} \text{NAI}_{\text{tail}} &= \sqrt{4\pi} B_{pqr}^{00} \int_R^{\infty} r^{p+q+r+1} e^{-ar^2} dr \\ &= \sqrt{4\pi} B_{pqr}^{00} \frac{\Gamma[1/2(p+q+r)+1, aR^2]}{a^{1/2(p+q+r)+1}}, \quad \mathbf{r}_{\mathbf{C}} = 0. \end{aligned} \quad (\text{C.25})$$

## C.5 Electron Repulsion Integrals

A general electron repulsion integral, evaluated over all space is given by

$$\begin{aligned} \text{ERI} &= \int \int \chi_{i,A1}(p_i, q_i, r_i, a_i) \chi_{j,B1}(p_j, q_j, r_j, a_j) \frac{1}{|\mathbf{r}_1 - \mathbf{r}_2|} \\ &\quad \times \chi_{k,C2}(p_k, q_k, r_k, a_k) \chi_{l,D2}(p_l, q_l, r_l, a_l) d\mathbf{r}_1 d\mathbf{r}_2, \end{aligned} \quad (\text{C.26})$$

where  $\chi_{i,Pn}$  is the  $i$ th unnormalized Cartesian Gaussian Orbital (CGO) for electron  $n$  centered at point  $\mathbf{R}_{n,\mathbf{P}} = (X_{n,P}, Y_{n,P}, Z_{n,P})$ . Since only one electron can occupy a continuum orbital in  $\mathbf{K}$  matrix theory, only the two-electron tail integrals where either  $\chi_i$  and  $\chi_j$  are continuum orbitals or  $\chi_k$  and  $\chi_l$  are continuum orbitals are required. The latter integral is given by

$$\begin{aligned} \text{ERI} &= \int \int \chi_{i,A1}(p_i, q_i, r_i, a_i) \chi_{j,B1}(p_j, q_j, r_j, a_j) \frac{1}{|\mathbf{r}_1 - \mathbf{r}_2|} \\ &\quad \times \chi_{k,O2}(p_k, q_k, r_k, a_k) \chi_{l,O2}(p_l, q_l, r_l, a_l) d\mathbf{r}_1 d\mathbf{r}_2, \end{aligned} \quad (\text{C.27})$$

where  $\chi_{i,A1}$  and  $\chi_{j,B1}$  are nucleus-centered CGOs, and  $\chi_{k,O2}$  and  $\chi_{l,O2}$  are continuum CGOs located at the center of gravity. By definition, this integral over all space can be expanded as

$$\begin{aligned}
\text{ERI} = & \int_{r_1=0}^{r_1=R} \int_{r_2=0}^{r_2=R} \chi_{i,A1} \chi_{j,B1} \frac{1}{|\mathbf{r}_1 - \mathbf{r}_2|} \chi_{k,O2} \chi_{l,O2} d\mathbf{r}_1 d\mathbf{r}_2 \\
& + \int_{r_1=0}^{r_1=R} \int_{r_2=R}^{r_2=\infty} \chi_{i,A1} \chi_{j,B1} \frac{1}{|\mathbf{r}_1 - \mathbf{r}_2|} \chi_{k,O2} \chi_{l,O2} d\mathbf{r}_1 d\mathbf{r}_2 \\
& + \int_{r_1=R}^{r_1=\infty} \int_{r_2=0}^{r_2=R} \chi_{i,A1} \chi_{j,B1} \frac{1}{|\mathbf{r}_1 - \mathbf{r}_2|} \chi_{k,O2} \chi_{l,O2} d\mathbf{r}_1 d\mathbf{r}_2 \\
& + \int_{r_1=R}^{r_1=\infty} \int_{r_2=R}^{r_2=\infty} \chi_{i,A1} \chi_{j,B1} \frac{1}{|\mathbf{r}_1 - \mathbf{r}_2|} \chi_{k,O2} \chi_{l,O2} d\mathbf{r}_1 d\mathbf{r}_2.
\end{aligned} \tag{C.28}$$

However, only the tail integral is required. If the nucleus-centered CGOs are assumed to have negligible contribution outside the  $\mathbf{K}$  matrix radius, the only contribution to the tail integral is

$$\begin{aligned}
\text{ERI}_{\text{tail}} = & \int_{r_1=0}^{r_1=R} \int_{r_2=R}^{r_2=\infty} \chi_{i,A1} (p_i, q_i, r_i, a_i) \chi_{j,B1} (p_j, q_j, r_j, a_j) \frac{1}{|\mathbf{r}_1 - \mathbf{r}_2|} \\
& \chi_{k,O2} (p_k, q_k, r_k, a_k) \chi_{l,O2} (p_l, q_l, r_l, a_l) d\mathbf{r}_1 d\mathbf{r}_2.
\end{aligned} \tag{C.29}$$

Using the multipolar expansion,

$$\begin{aligned}
\frac{1}{|\mathbf{r}_1 - \mathbf{r}_2|} &= 4\pi \sum_{l=0}^{\infty} \sum_{m=-l}^l \frac{1}{2l+1} \frac{r_{<}^l}{r_{>}^{l+1}} Y_{l,m}^* (\hat{\mathbf{r}}_1) Y_{l,m} (\hat{\mathbf{r}}_2) \\
&= 4\pi \sum_{l=0}^{\infty} \sum_{m=-l}^l \frac{1}{2l+1} \frac{1}{r_{>}^{2l+1}} r_1^l Y_{l,m}^* (\hat{\mathbf{r}}_1) r_2^l Y_{l,m} (\hat{\mathbf{r}}_2).
\end{aligned} \tag{C.30}$$

From Eq. (C.29) one can identify  $r_{>} = r_2$  and  $r_{<} = r_1$ ; therefore,

$$\begin{aligned}
&\text{ERI}_{\text{tail}} \\
&= 4\pi \sum_{l'=0}^{\infty} \sum_{m'=-l'}^{l'} \frac{1}{2l'+1} \left[ \int_{r_1=0}^{r_1=R} r_1^{l'} Y_{l',m'}^* (\hat{\mathbf{r}}_1) \chi_{i,A1} (p_i, q_i, r_i, a_i) \chi_{j,B1} (p_j, q_j, r_j, a_j) d\mathbf{r}_1 \right. \\
&\quad \left. \times \int_{r_2=R}^{r_2=\infty} \frac{1}{r_2^{l'+1}} Y_{l',m'} (\hat{\mathbf{r}}_2) \chi_{k,O2} (p_k, q_k, r_k, a_k) \chi_{l,O2} (p_l, q_l, r_l, a_l) d\mathbf{r}_2 \right].
\end{aligned} \tag{C.31}$$

Since the nucleus-centered CGOs are assumed to have negligible amplitude outside the  $\mathbf{K}$  matrix radius, the range of integration over  $\mathbf{r}_1$  can be extended to all space

$$\begin{aligned} & \text{ERI}_{\text{tail}} \\ &= 4\pi \sum_{l'=0}^{\infty} \sum_{m'=-l'}^{l'} \frac{1}{2l'+1} \left[ \int_{r_1=0}^{r_1=\infty} r_1^{l'} Y_{l',m'}^*(\hat{\mathbf{r}}_1) \chi_{i,A1}(p_i, q_i, r_i, a_i) \chi_{j,B1}(p_j, q_j, r_j, a_j) d\mathbf{r}_1 \right. \\ & \quad \left. \times \int_{r_2=R}^{r_2=\infty} \frac{1}{r_2^{l'+1}} Y_{l',m'}(\hat{\mathbf{r}}_2) \chi_{k,O2}(p_k, q_k, r_k, a_k) \chi_{l,O2}(p_l, q_l, r_l, a_l) d\mathbf{r}_2 \right]. \quad (\text{C.32}) \end{aligned}$$

First, consider the integration over  $\mathbf{r}_2$ . Using Eqs. (C.10) and (C.13), the number of Gaussians involved in this integration is reduced to one and

$$\begin{aligned} & \int_{r_2=R}^{r_2=\infty} \frac{1}{r_2^{l'+1}} Y_{l',m'}(\hat{\mathbf{r}}_2) \chi_{k,O2}(p_k, q_k, r_k, a_k) \chi_{l,O2}(p_l, q_l, r_l, a_l) d\mathbf{r}_2 \\ &= \sum_{l''=0}^{\infty} \sum_{m''=-l''}^{l''} B_{pqr}^{l''m''} \int_{r_2=R}^{r_2=\infty} r_2^{p+q+r-l'-1} e^{-ar_2^2} Y_{l',m'}(\hat{\mathbf{r}}_2) Y_{l'',m''}(\hat{\mathbf{r}}_2) d\mathbf{r}_2, \quad (\text{C.33}) \end{aligned}$$

where  $p = p_k + p_l$ ,  $q = q_k + q_l$ ,  $r = r_k + r_l$ , and  $a = a_k + a_l$ . After integration over the angular variables, one obtains

$$\begin{aligned} & \int_{r_2=R}^{r_2=\infty} \frac{1}{r_2^{l'+1}} Y_{l',m'}(\hat{\mathbf{r}}_2) \chi_{k,O2}(p_k, q_k, r_k, a_k) \chi_{l,O2}(p_l, q_l, r_l, a_l) d\mathbf{r}_2 \\ &= B_{pqr}^{l'm'*} \int_R^{\infty} r_2^{p+q+r-l'+1} e^{-ar_2^2} dr_2 \\ &= B_{pqr}^{l'm'*} \frac{\Gamma[1/2(p+q+r-l')+1, aR^2]}{2a^{1/2(p+q+r-l')+1}}. \quad (\text{C.34}) \end{aligned}$$

Now consider the integration over  $\mathbf{r}_1$ . Since the range of integration is over all space, it is easiest to calculate this integral using Cartesian coordinates. The transformation from Cartesian functions to spherical harmonic functions [161] is given by

$$r^l Y_{l,m}(\hat{\mathbf{r}}) = \sum_{l_x+l_y+l_z=l} \tilde{c}(l, m, l_x, l_y, l_z) x^{l_x} y^{l_y} z^{l_z}, \quad (\text{C.35})$$

where the complex constant  $\tilde{c}(l, m, l_x, l_y, l_z)$  for unnormalized CGOs with  $m > 0$  is given by

$$\begin{aligned}
& \tilde{c}(l, m, l_x, l_y, l_z) \\
&= (-1)^m \sqrt{\frac{(2l+1)(l-|m|)!}{4\pi(l+|m|)!}} \frac{1}{2^l l!} \\
&\times \sum_{i=0}^{(l-|m|)/2} \binom{l}{i} \binom{i}{(l_x+l_y-|m|)/2} \frac{(-1)^i (2l-2i)!}{(l-|m|-2i)!} \\
&\times \sum_{k=0}^{(l_x+l_y-|m|)/2} \binom{(l_x+l_y-|m|)/2}{k} \binom{|m|}{l_x-2k} (-1)^{(|m|-l_x+2k)/2},
\end{aligned} \tag{C.36}$$

which is modified from Schlegel and Frisch's original normalized expression to follow the phase choice for  $m > 0$ . The transformation to Cartesian functions for  $m < 0$  is obtained using the phase choice given in Eq. (C.3).

The following identity will be very helpful in simplifying all further calculations:

$$\begin{aligned}
\chi_{i,A}(0, 0, 0, a_i) \chi_{j,B}(0, 0, 0, a_j) &= e^{-a_i r_A^2} e^{-a_j r_B^2} \\
&= e^{-\frac{a_i a_j (\mathbf{A}-\mathbf{B})^2}{a_i + a_j}} e^{-(a_i + a_j) r_P^2},
\end{aligned} \tag{C.37}$$

where

$$\mathbf{r}_P = \mathbf{r} - \mathbf{P} = \mathbf{r} - \frac{a_i \mathbf{A} + a_j \mathbf{B}}{a_i + a_j}. \tag{C.38}$$

It is also helpful to express Eq. (C.35) in terms of the Cartesian components of  $\mathbf{r}_P$ :

$$r^l Y_{l,m}(\hat{\mathbf{r}}) = \sum_{l_x+l_y+l_z=l} \tilde{c}(l, m, l_x, l_y, l_z) (x_P + P_x)^{l_x} (y_P + P_y)^{l_y} (z_P + P_z)^{l_z}, \tag{C.39}$$

where  $x_P = x - P_x$ ,  $y_P = y - P_y$ , and  $z_P = z - P_z$ . Using Eqs. (C.37) and (C.39), the integral over  $\mathbf{r}_1$  is given by



$$\begin{aligned}
& \int_{r_1=0}^{r_1=\infty} r_1^{l'} Y_{l',m'}^* (\hat{\mathbf{r}}_1) \chi_{i,A1} (p_i, q_i, r_i, a_i) \chi_{j,B1} (p_j, q_j, r_j, a_j) d\mathbf{r}_1 \\
&= e^{-\frac{a_i a_j (\mathbf{A1}-\mathbf{B1})^2}{a_i+a_j}} \sum_{l_x+l_y+l_z=l'} \tilde{c}^* (l', m', l_x, l_y, l_z) \\
&\quad \times \int_{-\infty}^{\infty} \int_{-\infty}^{\infty} \int_{-\infty}^{\infty} (x_{P1} + P1_x)^{l_x} (y_{P1} + P1_y)^{l_y} (z_{P1} + P1_z)^{l_z} \\
&\quad \times x_{A1}^{p_i} y_{A1}^{q_i} z_{A1}^{r_i} x_{B1}^{p_j} y_{B1}^{q_j} z_{B1}^{r_j} e^{-(a_i+a_j)x_{P1}^2} e^{-(a_i+a_j)y_{P1}^2} e^{-(a_i+a_j)z_{P1}^2} dx_1 dy_1 dz_1.
\end{aligned} \tag{C.40}$$

The analysis is simpler if the other Cartesian components are also expressed in terms of  $\mathbf{r}_P$ . For example,

$$x_{A1} = x - A1_x = (x - P1_x) + (P1_x - A1_x) = x_{P1} + PA1_x, \tag{C.41}$$

where  $PA1_x \equiv P1_x - A1_x$ . Therefore

$$\begin{aligned}
& \int_{r_1=0}^{r_1=\infty} r_1^{l'} Y_{l',m'}^* (\hat{\mathbf{r}}_1) \chi_{i,A1} (p_i, q_i, r_i, a_i) \chi_{j,B1} (p_j, q_j, r_j, a_j) d\mathbf{r}_1 \\
&= e^{-\frac{a_i a_j (\mathbf{A1}-\mathbf{B1})^2}{a_i+a_j}} \sum_{l_x+l_y+l_z=l'} \tilde{c}^* (l', m', l_x, l_y, l_z) \\
&\quad \times \int_{-\infty}^{\infty} \int_{-\infty}^{\infty} \int_{-\infty}^{\infty} (x_{P1} + P1_x)^{l_x} (y_{P1} + P1_y)^{l_y} (z_{P1} + P1_z)^{l_z} \\
&\quad \times (x_{P1} + PA1_x)^{p_i} (y_{P1} + PA1_y)^{q_i} (z_{P1} + PA1_z)^{r_i} \\
&\quad \times (x_{P1} + PB1_x)^{p_j} (y_{P1} + PB1_y)^{q_j} (z_{P1} + PB1_z)^{r_j} \\
&\quad \times e^{-(a_i+a_j)x_{P1}^2} e^{-(a_i+a_j)y_{P1}^2} e^{-(a_i+a_j)z_{P1}^2} dx_1 dy_1 dz_1.
\end{aligned} \tag{C.42}$$

The notation of Eq. (C.42) can be condensed further and rewritten as

$$\begin{aligned}
& \int_{r_1=0}^{r_1=\infty} r_1^{l'} Y_{l',m'}^* (\hat{\mathbf{r}}_1) \chi_{i,A1} (p_i, q_i, r_i, a_i) \chi_{j,B1} (p_j, q_j, r_j, a_j) d\mathbf{r}_1 \\
&= e^{-\frac{a_i a_j (\mathbf{A1} - \mathbf{B1})^2}{a_i + a_j}} \sum_{l_x + l_y + l_z = l'} \tilde{c}^* (l', m', l_x, l_y, l_z) \\
&\quad \times \int_{-\infty}^{\infty} \int_{-\infty}^{\infty} \int_{-\infty}^{\infty} \sum_{\alpha=0}^{l_x + p_i + p_j} f_{\alpha} (l_x, p_i, p_j, P1_x, PA1_x, PB1_x) x_{P1}^{\alpha} e^{-(a_i + a_j) x_{P1}^2} \\
&\quad \times \sum_{\beta=0}^{l_y + q_i + q_j} f_{\beta} (l_y, q_i, q_j, P1_y, PA1_y, PB1_y) y_{P1}^{\beta} e^{-(a_i + a_j) y_{P1}^2} \\
&\quad \times \sum_{\gamma=0}^{l_z + r_i + r_j} f_{\gamma} (l_z, r_i, r_j, P1_z, PA1_z, PB1_z) z_{P1}^{\gamma} e^{-(a_i + a_j) z_{P1}^2} dx_1 dy_1 dz_1,
\end{aligned} \tag{C.43}$$

where  $f_{\alpha} (l_x, p_i, p_j, P1_x, PA1_x, PB1_x)$  is the coefficient of  $x_{P1}^{\alpha}$  in the expansion  $(x_{P1} + P1_x)^{l_x} (x_{P1} + PA1_x)^{p_i} (x_{P1} + PB1_x)^{p_j}$ . This coefficient is given by

$$\begin{aligned}
& f_{\alpha} (l_x, p_i, p_j, P1_x, PA1_x, PB1_x) \\
&= \sum_{a=0, l_x}^{a+b+c=\alpha} \sum_{b=0, p_i} \sum_{c=0, p_j} P1_x^{l_x - a} \binom{l_x}{a} PA1_x^{p_i - b} \binom{p_i}{b} PB1_x^{p_j - c} \binom{p_j}{c}.
\end{aligned} \tag{C.44}$$

Expressions for the other Cartesian components are similar. By symmetry, only the even powers of  $x_{P1}$ ,  $y_{P1}$ , and  $z_{P1}$  give nonzero contributions to the integral. The following integral is useful

$$\int_{-\infty}^{\infty} x^{2n} e^{-\alpha x^2} dx = \frac{(2n-1)!!}{(2\alpha)^n} \sqrt{\frac{\pi}{\alpha}}, \tag{C.45}$$

where  $n$  is a positive integer. The integral over  $\mathbf{r}_1$  becomes

$$\begin{aligned}
& \int_{r_1=0}^{r_1=\infty} r_1^{l'} Y_{l',m'}^*(\hat{\mathbf{r}}_1) \chi_{i,A1}(p_i, q_i, r_i, a_i) \chi_{j,B1}(p_j, q_j, r_j, a_j) d\mathbf{r}_1 \\
&= \left( \frac{\pi}{a_i + a_j} \right)^{3/2} e^{-\frac{a_i a_j (\mathbf{A1}-\mathbf{B1})^2}{a_i + a_j}} \sum_{l_x+l_y+l_z=l'} \tilde{c}^*(l', m', l_x, l_y, l_z) \\
&\quad \times \sum_{\alpha=0}^{[(l_x+p_i+p_j)/2]} f_{2\alpha}(l_x, p_i, p_j, P1_x, PA1_x, PB1_x) \frac{(2\alpha-1)!!}{[2(a_i+a_j)]^\alpha} \\
&\quad \times \sum_{\beta=0}^{[(l_y+q_i+q_j)/2]} f_{2\beta}(l_y, q_i, q_j, P1_y, PA1_y, PB1_y) \frac{(2\beta-1)!!}{[2(a_i+a_j)]^\beta} \\
&\quad \times \sum_{\gamma=0}^{[(l_z+r_i+r_j)/2]} f_{2\gamma}(l_z, r_i, r_j, P1_z, PA1_z, PB1_z) \frac{(2\gamma-1)!!}{[2(a_i+a_j)]^\gamma}.
\end{aligned} \tag{C.46}$$

Note that Eq. (C.32) is finite because it is limited by the coefficient  $B_{ijk}^{lm}$  in Eq. (C.34). Thus, the electron repulsion tail integral is given by summations over the product of Eqs. (C.34) and (C.46).



# Bibliography

- [1] P. Dupré, R. Jost, M. Lombardi, P. G. Green, E. Abramson, and R. W. Field. *Chem. Phys.*, 152:293, 1991.
- [2] G. Staszewska and L. Wolniewicz. *J. Mol. Spectrosc.*, 212:208, 2002.
- [3] M. Arif, Ch. Jungen, and A. L. Roche. *J. Chem. Phys.*, 106:4102, 1997.
- [4] B. Yoo and C. H. Greene. *Phys. Rev. A*, 34:1635, 1986.
- [5] Y. Chuang and D. G. Truhlar. *J. Chem. Phys.*, 112:1221, 2000.
- [6] J. K. G. Watson. *Mol. Phys.*, 15:479, 1968.
- [7] B. M. Wong, R. L. Thom, and R. W. Field. *J. Phys. Chem. A*, 110:7406, 2006.
- [8] J. T. Hougen, P. R. Bunker, and J. W. C. Johns. *J. Mol Spectrosc.*, 34:136, 1970.
- [9] D. P. Tew, N. C. Handy, and S. Carter. *Mol. Phys.*, 99:393, 2001.
- [10] B. M. Wong, A. H. Steeves, and R. W. Field. *J. Phys. Chem. B*, 110:18912, 2006.
- [11] C. Eckart. *Phys. Rev.*, 47:552, 1935.
- [12] D. P. Tew, N. C. Handy, S. Carter, S. Irle, and J. Bowman. *Mol. Phys.*, 101:3513, 2003.
- [13] W. H. Miller, N. C. Handy, and J. E. Adams. *J. Chem. Phys.*, 72:99, 1980.

- [14] K. N. Rao and C. W. Mathews. *Molecular Spectroscopy: Modern Research*. Academic Press: New York, 1972.
- [15] E. B. Wilson Jr., J. C. Decius, and P. C. Cross. *Molecular Vibrations: The Theory of Infrared and Raman Vibrational Spectra*. Dover Publications: New York, 1955.
- [16] C. C. Lin and J. D. Swalen. *Rev. Mod. Phys.*, 31:841, 1959.
- [17] P. Rabinowitz. *Numerical Methods for Nonlinear Algebraic Equations*. Gordon and Breach Science Publishers: New York, 1970.
- [18] <http://www.mathworks.com/matlabcentral/fileexchange/loadFile.do?objectId=14240&objectType=FILE>.
- [19] K. S. Pitzer and W. D. Gwinn. *J. Chem. Phys.*, 10:428, 1942.
- [20] K. S. Pitzer. *J. Chem. Phys.*, 14:239, 1946.
- [21] K. S. Pitzer and J. E. Kilpatrick. *J. Chem. Phys.*, 17:1064, 1949.
- [22] A. L. L. East and L. Radom. *J. Chem. Phys.*, 106:6655, 1997.
- [23] L. S. Kassel. *J. Chem. Phys.*, 4:276, 1936.
- [24] B. L. Crawford Jr. *J. Chem. Phys.*, 8:273, 1940.
- [25] M. J. Frisch, G. W. Trucks, H. B. Schlegel, G. E. Scuseria, M. A. Robb, J. R. Cheeseman, J. A. Montgomery, Jr., T. Vreven, K. N. Kudin, J. C. Burant, J. M. Millam, S. S. Iyengar, J. Tomasi, V. Barone, B. Mennucci, M. Cossi, G. Scalmani, N. Rega, G. A. Petersson, H. Nakatsuji, M. Hada, M. Ehara, K. Toyota, R. Fukuda, J. Hasegawa, M. Ishida, T. Nakajima, Y. Honda, O. Kitao, H. Nakai, M. Klene, X. Li, J. E. Knox, H. P. Hratchian, J. B. Cross, V. Bakken, C. Adamo, J. Jaramillo, R. Gomperts, R. E. Stratmann, O. Yazyev, A. J. Austin, R. Cammi, C. Pomelli, J. W. Ochterski, P. Y. Ayala, K. Morokuma, G. A. Voth, P. Salvador, J. J. Dannenberg, V. G. Zakrzewski, S. Dapprich, A. D.

- Daniels, M. C. Strain, O. Farkas, D. K. Malick, A. D. Rabuck, K. Raghavachari, J. B. Foresman, J. V. Ortiz, Q. Cui, A. G. Baboul, S. Clifford, J. Cioslowski, B. B. Stefanov, G. Liu, A. Liashenko, P. Piskorz, I. Komaromi, R. L. Martin, D. J. Fox, T. Keith, M. A. Al-Laham, C. Y. Peng, A. Nanayakkara, M. Challacombe, P. M. W. Gill, B. Johnson, W. Chen, M. W. Wong, C. Gonzalez, and J. A. Pople. Gaussian 03, Revision D.01. Gaussian, Inc., Wallingford, CT, 2004.
- [26] L. A. Curtiss, K. Raghavachari, P. C. Redfern, V. Rassolov, and J. A. Pople. *J. Chem. Phys.*, 109:7764, 1998.
- [27] P. Y. Ayala and H. B. Schlegel. *J. Chem. Phys.*, 108:2314, 1998.
- [28] A. Chung-Phillips. *J. Comput. Chem.*, 13:874, 1992.
- [29] Y. El Youssefi, M. Herman, and J. Liévin. *Mol. Phys.*, 94:461, 1998.
- [30] V. Hnizdo, A. Fedorowicz, H. Singh, and E. Demchuk. *J. Comput. Chem.*, 24:1172, 2003.
- [31] Y. El Youssefi, R. Georges, J. Liévin, and M. Herman. *J. Mol. Spectrosc.*, 186:239, 1997.
- [32] Y. El Youssefi, J. Liévin, J. Vander Auwera, and M. Herman. *Mol. Phys.*, 94:473, 1998.
- [33] S. Zou and J. M. Bowman. *Chem. Phys. Lett.*, 368:421, 2003.
- [34] S. Zou, J. M. Bowman, and A. Brown. *J. Chem. Phys.*, 118:10012, 2003.
- [35] L. Liu and J. T. Muckerman. *J. Chem. Phys.*, 107:3402, 1997.
- [36] D. Xu, G. Li, D. Xie, and H. Guo. *Chem. Phys. Lett.*, 365:480, 2002.
- [37] D. Xu, R. Chen, and H. Guo. *J. Chem. Phys.*, 118:7273, 2003.
- [38] R. A. Kendall, T. H. Dunning Jr., and R. J. Harrison. *J. Chem. Phys.*, 96:6796, 1992.

- [39] M. P. Jacobson, J. P. O'Brien, R. J. Silbey, and R. W. Field. *J. Chem. Phys.*, 109:121, 1998.
- [40] M. P. Jacobson, J. P. O'Brien, and R. W. Field. *J. Chem. Phys.*, 109:3831, 1998.
- [41] Matthew Paul Jacobson. *Spectroscopic Patterns Encode Unimolecular Dynamics*. PhD thesis, Massachusetts Institute of Technology, 1999.
- [42] Michelle Lee Silva. *Spectroscopic Investigations of the  $\tilde{X}$  and  $\tilde{A}$  State Dynamics of  $^{13}\text{C}_2\text{H}_2$* . PhD thesis, Massachusetts Institute of Technology, 2002.
- [43] Zicheng Duan. *Spectroscopic Study of the Acetylene Species*. PhD thesis, Massachusetts Institute of Technology, 2003.
- [44] R. L. Hayes, E. Fattal, N. Govind, and E. Carter. *J. Am. Chem. Soc.*, 123:641, 2001.
- [45] J. A. Bentley, R. E. Wyatt, M. Menou, and C. Leforestier. *J. Chem. Phys.*, 97:4255, 1992.
- [46] J. F. Stanton and J. Gauss. *J. Chem. Phys.*, 110:6079, 1999.
- [47] J. F. Stanton and J. Gauss. *J. Chem. Phys.*, 110:1831, 1999.
- [48] M. P. Jacobson, R. J. Silbey, and R. W. Field. *J. Chem. Phys.*, 110:845, 1999.
- [49] L. Halonen, M. S. Child, and S. Carter. *Mol. Phys.*, 47:1097, 1982.
- [50] L. Halonen. *Adv. Chem. Phys.*, 104:41, 1998.
- [51] S. F. Yang, L. Halonen, and A. Campargue. *Mol. Phys.*, 99:1303, 2001.
- [52] G. J. Scherer, K. K. Lehmann, and W. Klemperer. *J. Chem. Phys.*, 78:2817, 1983.
- [53] K. K. Lehmann. *J. Chem. Phys.*, 96:8117, 1992.



- [54] R. Prosmiti and S. C. Farantos. *J. Chem. Phys.*, 103:3299, 1995.
- [55] R. Prosmiti and S. C. Farantos. *J. Chem. Phys.*, 118:8275, 2003.
- [56] J. P. Rose and M. E. Kellman. *J. Chem. Phys.*, 105:10743, 1996.
- [57] E. L. Sibert and A. B. McCoy. *J. Chem. Phys.*, 105:469, 1996.
- [58] J. A. Barnes, T. E. Gough, and M. Stoer. *Chem. Phys. Lett.*, 237:437, 1995.
- [59] J. A. Barnes, T. E. Gough, and M. Stoer. *J. Chem. Phys.*, 114:4490, 2001.
- [60] J. S. Muentner and V. W. Laurie. *J. Am. Chem. Soc.*, 86:3901, 1964.
- [61] K. Matsumura, T. Tanaka, Y. Endo, S. Saito, and E. Hirota. *J. Phys. Chem.*, 84:1793, 1980.
- [62] J. M. Bowman, S. Irle, K. Morokuma, and A. Wodtke. *J. Chem. Phys.*, 114:7923, 2001.
- [63] C. Jung, H. S. Taylor, and M. P. Jacobson. *J. Phys. Chem. A*, 105:681, 2001.
- [64] S. Rainer and H. Köppel. *J. Chem. Phys.*, 115:7907, 2001.
- [65] M. Bittner and H. Köppel. *Phys. Chem. Chem. Phys.*, 5:4604, 2003.
- [66] V. Szalay. *J. Mol. Spectrosc.*, 128:24, 1988.
- [67] K. Fukui. *J. Phys. Chem.*, 74:4161, 1970.
- [68] K. Fukui. *Acc. Chem. Chem. Phys.*, 14:363, 1981.
- [69] Z. Bačić and J. C. Light. *J. Chem. Phys.*, 85:4594, 1986.
- [70] T. J. Lee and P. R. Taylor. *Int. J. Quantum Chem.*, page 199, 1989.
- [71] H.-J. Werner, P. J. Knowles, R. Lindh, F. R. Manby, M. Schütz, P. Celani, T. Korona, G. Rauhut, R. D. Amos, A. Bernhardsson, A. Berning, D. L. Cooper, M. J. O. Deegan, A. J. Dobbyn, F. Eckert, C. Hampel, G. Hetzer, A. W. Lloyd,

- S. J. McNicholas, W. Meyer, M. E. Mura, A. Nicklass, P. Palmieri, R. Pitzer, U. Schumann, H. Stoll, A. J. Stone, R. Tarroni, and T. Thorsteinsson. Molpro, version 2002.6, a package of ab initio programs. See <http://www.molpro.net>, Cardiff, UK, 2002.
- [72] P. G. Szalay and R. J. Bartlett. *Chem. Phys. Lett.*, 214:481, 1993.
- [73] M. I. El Idrissi, J. Lievin, A. Campargue, and M. Herman. *J. Chem. Phys.*, 110:2074, 1999.
- [74] K. Hoshina, A. Iwasaki, K. Yamanouchi, M. P. Jacobson, and R. W. Field. *J. Chem. Phys.*, 114:7424, 2001.
- [75] M. A. Tamsamani and M. Herman. *J. Chem. Phys.*, 102:6371, 1995.
- [76] M. A. Tamsamani, M. Herman, S. A. B. Solina, J. P. O'Brien, and R. W. Field. *J. Chem. Phys.*, 105:11357, 1996.
- [77] G. Strey and I. M. Mills. *J. Mol. Spectrosc.*, 59:103, 1976.
- [78] G. Hose and H. S. Taylor. *J. Chem. Phys.*, 76:5356, 1982.
- [79] P. L. Cummins, G. B. Bacskay, and N. S. Hush. *J. Phys. Chem.*, 89:2151, 1985.
- [80] H. B. G. Casimir. *Archives du Musée Teyler (III)*, 8:201, 1936.
- [81] B. T. Feld and W. E. Lamb Jr. *Phys. Rev.*, 67:15, 1945.
- [82] E. H. Roderick. *Nature*, 160:255, 1947.
- [83] R. Pd and P. Chandra. *J. Chem. Phys.*, 114:7450, 2001.
- [84] A. G. Maki, G. Ch. Mellau, S. Klee, M. Winnewisser, and W. Quapp. *J. Mol Spectrosc.*, 202:67, 2000.
- [85] A. G. Maki and G. Ch. Mellau. *J. Mol Spectrosc.*, 206:47, 2001.
- [86] H. A. Bechtel, A. H. Steeves, and R. W. Field. *ApJ.*, 649:L53, 2006.

- [87] R. L. Thom, B. M. Wong, R. W. Field, and J. F. Stanton. *J. Chem. Phys.*, 126:184307, 2007.
- [88] P. Dupré and P. G. Green. *Chem. Phys. Lett.*, 212:555, 1993.
- [89] P. Dupré, P. G. Green, and R. W. Field. *Chem. Phys.*, 196:211, 1995.
- [90] P. Dupré. *Chem. Phys.*, 196:239, 1995.
- [91] G. Vacek, C. D. Sherrill, Y. Yamaguchi, and H. F. Schaefer III. *J. Chem. Phys.*, 104:1774, 1996.
- [92] C. D. Sherrill, G. Vacek, Y. Yamaguchi, H. F. Schaefer III, J. F. Stanton, and J. Gauss. *J. Chem. Phys.*, 104:8507, 1996.
- [93] Selen Altunata. *Intersystem Crossing in Acetylene: A Mechanistic Study*. PhD thesis, Massachusetts Institute of Technology, 2001.
- [94] Kevin Laughton Cunningham. *The Surface Ejection of Electrons by Laser Excited Metastables Spectroscopy of Acetylene*. PhD thesis, Massachusetts Institute of Technology, 2000.
- [95] Ryan L. Thom. *Spectroscopic Investigations of Intersystem Crossing and Triplet State Structure in Acetylene*. PhD thesis, Massachusetts Institute of Technology, 2006.
- [96] A. P. Mishra, R. L. Thom, and R. W. Field. *J. Mol. Spectrosc.*, 228:565, 2004.
- [97] Q. Cui, K. Morokuma, and J. F. Stanton. *Chem. Phys. Lett.*, 263:46, 1996.
- [98] Q. Cui and K. Morokuma. *Chem. Phys. Lett.*, 272:319, 1997.
- [99] E. Ventura, M. Dallos, and H. Lischka. *J. Chem. Phys.*, 118:1702, 2003.
- [100] J. F. Stanton, J. Gauss, J. D. Watts, P. G. Szalay, and R. J. Bartlett. Aces2, mainz-austin-budapest version, a quantum-chemical program package for high-level calculations of energies and properties. See <http://www.aces2.de>.

- [101] G. Orlandi and F. Zerbetto. *J. Chem. Phys.*, 91:4238, 1987.
- [102] G. Orlandi, F. Zerbetto, and M. Z. Zgierski. *Chem. Rev.*, 91:867, 1991.
- [103] H. C. Longuet-Higgins. *Adv. Spectrosc.*, 2:42, 1961.
- [104] R. L. Fulton and M. Gouterman. *J. Chem. Phys.*, 35:1059, 1961.
- [105] W. H. Henneker, A. P. Penner, W. Siebrand, and M. Z. Zgierski. *J. Chem. Phys.*, 69:1884, 1978.
- [106] A. J. Merer, N. Yamakita, S. Tsuchiya, J. F. Stanton, Z. Duan, and R. W. Field. *Mol. Phys.*, 101:663, 2003.
- [107] J. D. Tobiasson, A. L. Utz, E. L. Sibert III, and F. F. Crim. *J. Chem. Phys.*, 99:5762, 1993.
- [108] T. E. Sharp and H. M. Rosenstock. *J. Chem. Phys.*, 41:3453, 1964.
- [109] P. T. Ruhoff and M. A. Ratner. *Int. J. Quant. Chem.*, 77:383, 2000.
- [110] A. Toniolo and M. Persico. *Int. J. Quant. Chem.*, 22:969, 2001.
- [111] F. Duschinski. *Acta Physicochim. URSS*, 7:551, 1937.
- [112] <http://www.mathworks.com/matlabcentral/fileexchange/loadFile.do?objectId=14992&objectType=FILE>.
- [113] I. M. Mills. *Molecular Spectroscopy: Modern Research*. Academic Press, 1972.
- [114] B. M. Wong, S. N. Altunata, and R. W. Field. *J. Chem. Phys.*, 124:014106, 2006.
- [115] M. J. Seaton. *Proc. Phys. Soc.*, 88:801, 1966.
- [116] M. J. Seaton. *Rep. Prog. Phys.*, 46:167, 1983.
- [117] U. Fano. *Phys. Rev. A*, 2:353, 1970.

- [118] Ch. Jungen. *Molecular Applications of Quantum Defect Theory*. IOP Publishing: Bristol, 1996.
- [119] C. H. Greene, A. R. P. Rau, and U. Fano. *Phys. Rev. A*, 26:2441, 1982.
- [120] S. Ross. An MQDT primer. In *AIP Conference Proceedings No. 225*, 1991.
- [121] Serhan N. Altunata. *Generalized Quantum Defect Methods in Quantum Chemistry*. PhD thesis, Massachusetts Institute of Technology, 2006.
- [122] P. G. Burke, I. Mackey, and I. Shimamura. *J. Phys. B*, 10:2497, 1977.
- [123] S. E. Branchett and J. Tennyson. *Phys. Rev. Lett.*, 64:2889, 1990.
- [124] L. A. Morgan, C. J. Gillan, J. Tennyson, and X. Chen. *J. Phys. B*, 30:4087, 1997.
- [125] S. F. Boys. *Proc. R. Soc. London, Ser. A*, 200:542, 1950.
- [126] H. Taketa, S. Huzinaga, and K. Oohata. *J. Phys. Soc. Jpn.*, 21:2313, 1966.
- [127] E. F. Valeev and H. F. Schaefer III. *J. Chem. Phys.*, 113:3990, 2000.
- [128] E. F. Valeev and C. L. Janssen. *J. Chem. Phys.*, 121:1214, 2004.
- [129] T. D. Crawford, S. S. Wesolowski, E. F. Valeev, R. A. King, M. L. Leininger, and H. F. Schaefer III. *Chemistry for the 21st Century*. Wiley-VCH: Weinheim, 2001.
- [130] M. Head-Gordon and J. A. Pople. *J. Chem. Phys.*, 89:5777, 1988.
- [131] T. D. Crawford, C. D. Sherrill, E. F. Valeev, J. T. Fermann, R. A. King, M. L. Leininger, S. T. Brown, C. L. Janssen, E. T. Seidl, J. P. Kenny, and W. D. Allen. *J. Comput. Chem.*, 28:1610, 2007.
- [132] A. Faure, J. D. Gorfinkiel, L. A. Morgan, and J. Tennyson. *Comput. Phys. Commun.*, 114:224, 2002.

- [133] W. M. Huo and F. A. Gianturco. *Computational Methods for Electron-Molecule Collisions*. Plenum Press: New York, 1995.
- [134] M. Yoshimine. *J. Comput. Phys.*, 11:449, 1969.
- [135] A. Szabo and N. S. Ostlund. *Modern Quantum Chemistry: Introduction to Advanced Electronic Structure Theory*. Dover Publications: New York, 1996.
- [136] C. J. Noble, P. G. Burke, and S. Salvini. *J. Phys. B*, 15:3779, 1982.
- [137] J. Tennyson, C. J. Noble, and S. Salvini. *J. Phys. B*, 17:905, 1984.
- [138] J. Tennyson, C. J. Noble, and S. Salvini. *J. Phys. B*, 29:6185, 1984.
- [139] P. G. Burke, C. J. Noble, and P. Scott. *Proc. R. Soc. Lond. A*, 410:289, 1987.
- [140] J. Tennyson, P. G. Burke, and K. A. Berrington. *Comput. Phys. Commun.*, 47:207, 1987.
- [141] J. Tennyson. *J. Phys. B*, 29:1817, 1996.
- [142] H. J. Monkhorst. *Int. J. Quantum Chem. Sym.*, 11:421, 1977.
- [143] S. Ghosh and D. Mukherjee. *Proc. Indian Acad. Sci.*, 93:947, 1984.
- [144] J. Geertsen, M. Rittby, and R. J. Bartlett. *Chem. Phys. Lett.*, 164:57, 1989.
- [145] H. Koch and P. Jørgensen. *J. Chem. Phys.*, 93:3333, 1990.
- [146] J. Vergès, C. Effantin, A. Bernard, A. Topouzkhanian, A. R. Allouche, J. D'Incan, and R. F. Barrow. *J. Phys. B*, 26:279, 1993.
- [147] A. Bernard, C. Effantin, E. Andrianavalona, J. Vergès, and R. F. Barrow. *J. Mol. Spectrosc.*, 152:174, 1992.
- [148] J. E. Murphy, J. M. Berg, A. J. Merer, N. A. Harris, and R. W. Field. *Phys. Rev. Lett.*, 65:1861, 1990.
- [149] Z. J. Jakubek and R. W. Field. *Phys. Rev. Lett.*, 72:2167, 1994.

- [150] N. A. Harris and Ch. Jungen. *Phys. Rev. Lett.*, 70:2549, 1993.
- [151] M. A. Iron, M. Oren, and J. M. L. Martin. *Mol. Phys.*, 101:1345, 2003.
- [152] D. J. Griffiths. *Introduction to Electrodynamics*. Prentice Hall: New Jersey, 1989.
- [153] M. Aubert, N. Bessis, and G. Bessis. *Phys. Rev. A*, 10:51, 1974.
- [154] Ch. Jungen and F. Texier. *J. Phys. B*, 33:2495, 2000.
- [155] A. Matzkin. *Phys. Rev. A*, 63:012103, 2001.
- [156] K. E. Thylwe and H. J. Korsch. *J. Phys. A*, 34:3497, 2001.
- [157] M. Hiyama and M. S. Child. *J. Phys. B*, 34:3935, 2001.
- [158] A. Matzkin and M. Lombardi. *Phys. Rev. E*, 66:037702, 2002.
- [159] H. Le Rouzo. *Int. J. Quant. Chem.*, 64:647, 1997.
- [160] R. J. Mathar. *Int. J. Quant. Chem.*, 90:227, 2002.
- [161] H. Schlegel and M. J. Frisch. *Int. J. Quant. Chem.*, 54:83, 1995.

## Curriculum Vitae

BIRTH DATE: August 3, 1979.

EDUCATION: Rice University, B.S. (2001);  
Massachusetts Institute of Technology, Ph.D. (2007).

### PUBLICATIONS:

Bryan M. Wong, Maria M. Fadri, and Sumathy Raman. “Thermodynamic Calculations for Molecules with Asymmetric Internal Rotors II – Application to the 1,2-Dihaloethanes.” *Journal of Computational Chemistry*, 28, in press, (2007).

Ryan L. Thom, Bryan M. Wong, Robert W. Field, and John F. Stanton. “Studies of Intersystem Crossing Dynamics in Acetylene.” *Journal of Chemical Physics*, 126, 184307-1–184307-7, (2007).

Bryan M. Wong and Sumathy Raman. “Thermodynamic Calculations for Molecules with Asymmetric Internal Rotors – Application to the 1,3-Butadiene.” *Journal of Computational Chemistry*, 28, 759–766, (2007).

Bryan M. Wong, Adam H. Steeves, and Robert W. Field. “Electronic Signatures of Large Amplitude Motions: Dipole Moments of Vibrationally Excited Local-Bend and Local-Stretch States of  $S_0$  Acetylene.” *Journal of Physical Chemistry B*, 110, 18912–18920, (2006).

Bryan M. Wong, Ryan L. Thom, and Robert W. Field. “Accurate Inertias for Large-Amplitude Motions: Improvements on Prevailing Approximations.” *Journal of Physical Chemistry A*, 110, 7406–7413, (2006).

Bryan M. Wong, Serhan N. Altunata, and Robert W. Field. “Analytical Calculations of Molecular Integrals for Multielectron R-Matrix Methods.” *Journal of Chemical Physics*, 124, 014106-1–014106-9, (2006).

INTERESTS: Alumni interviewer for Rice University admissions; Classical violinist; Enjoys New England clam chowder; Has a sister who once won a strawberry eating contest in Illinois.